

Sediment Transport Dynamics around an Emergent Vegetation Patch in Unsteady Flows

---

A Dissertation

Presented to  
The Faculty of the School of Engineering and Applied Science  
University of Virginia

---

In partial fulfillment  
of the requirements for the degree

Doctor of Philosophy  
Civil and Environmental Engineering

By

Kevin Alan Waters

May 2014

APPROVAL SHEET

This dissertation  
is submitted in partial fulfillment of the requirements  
for the degree of

Doctor of Philosophy  
Civil and Environmental Engineering

---

Kevin A. Waters, Author

The dissertation has been read and approved by the examining committee:

---

Joanna C. Curran, Advisor

---

Richard W. Miksad, Chair

---

Wu-Seng Lung

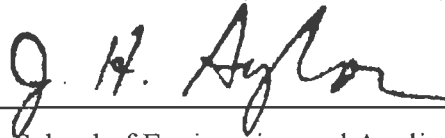
---

Matthew A. Reidenbach

---

Patricia L. Wiberg

Accepted for the School of Engineering and Applied Science:



---

Dean, School of Engineering and Applied Science

May 2014

*In loving memory of Edward Raffo,  
the first and best engineer I ever knew.*

## **ABSTRACT**

While recent efforts have promoted riverine vegetation because it can create habitats, enhance biodiversity, and improve nutrient dynamics and bank stability, its geomorphic impact when located in the main channel is not fully understood. This dissertation investigates the influence of an in-stream emergent vegetation patch on sediment transport rates and channel bed morphology for two sediment mixtures over repeated unsteady flows, with the overall goal being to assess the potential of vegetation patches as in-stream restoration measures. Three related groups of flume experiments were conducted that measured the steady flow hydraulics downstream of a sparse or dense model vegetation patch without a sediment bed, and the sediment transport and morphological adjustment during repeated hydrographs over sand/gravel and sand/silt bed mixtures with and without a patch. Differencing of digital bed elevation models before and after successive hydrographs enabled volumetric bed change calculations and evaluation of morphological adjustment over extended time scales.

Patch density and bed sediment distribution played dominant roles in determining conditions in which a patch was advantageous. For the sand/gravel mixture, the patch created a spatially variable bed surface that decreased entrainment thresholds and increased sediment yields. In the sand/silt mixture, patches reduced sediment yield by contributing to larger bedforms throughout the channel despite excessive scour adjacent to the patch location. Relationships for predicting bed load transport during unsteady flows were developed for no patch, sparse and dense patch conditions using a separate limb approach that captured temporal variability in grain entrainment and transport. These equations predicted reduced transport rates with a patch present relative to

reference shear stress values which were generally reduced by the patch. Changes in reach-scale morphology indicated that the channel would become dynamically stable with a sparse patch in either sediment mixture for low flow hydrograph sequences, which is a small subset of the conditions tested. Thus, this research provides a framework to expand vegetation studies through application of unsteady flow regimes that better simulate natural systems, but until a larger range of sediment, patch, and flow conditions are tested, in-channel vegetation patches should be used cautiously in restoration projects.

## **ACKNOWLEDGEMENTS**

Pursuing my Ph.D. has been a truly unique and humbling experience. I would not have been able to persevere through all of the unexpected obstacles and frustrating times without my faith in God. I feel incredibly blessed for the opportunities I have had in my life to continue my education. It is something I will never take for granted.

There are so many people I need to acknowledge that helped me get to this point. First, I would like to thank my research advisor, Dr. Joanna Curran, for all of her help over the past four years. She was a big reason why I chose to come to UVa and has been instrumental in my professional development. She provided the perfect balance of guidance, freedom, and funding that any graduate student would hope for in an advisor. I have learned so much from her and I am extremely grateful for all of her time and effort to help me achieve this goal. I would also like to thank my Ph.D. committee: Dr. Winston Lung and Dr. Richard Miksad of Civil and Environmental Engineering; and Dr. Matt Reidenbach and Dr. Pat Wiberg of Environmental Sciences. I appreciate all of their time and feedback during this process. In particular, our discussions following my proposal presentation definitely altered the direction of my research for the better.

I need to thank my lab assistants, Ellen Buckley, Rich Farella, Ameer Iqteit, and Juan Perez-Arango. Their availability and flexibility, particularly over the summer, is really what helped me push through my experiments at that pace that I wanted to. I also need to thank my former lab mates in the Sustainable Rivers Lab, Dr. Lu Tan, Dr. Kristen Cannatelli, and Stavros Calos. I learned a lot from both Lu and Kristen about the equipment in the lab, the various programs we use to collect and analyze data, and general lab procedures. Kristen's willingness to include me in various components of her

research was extremely beneficial for my work and I am grateful for that opportunity. Stavros' advice to build models within ArcGIS to automate analysis tasks saved me so much valuable time and enabled me to streamline a lot of the data analysis.

The unplanned setbacks that occurred during my lab work seemed endless at times. Without the constant help of Jim Danberg, I'm not sure if I ever would have completed my experiments. Jim was there for anything I needed. He fixed or repaired equipment issues, ordered parts I needed, helped me set up equipment, and even cleaned out the flume tank with me. His contributions were paramount in me conducting this research and I cannot thank him enough for all that he did for me.

I want to thank Dwight Dart in the Rapid Prototyping Lab at UVa for his help in developing and printing my vegetation patch model.

Every teacher I have had throughout my many years of school has helped me in one way or another and deserves some credit for helping me get this far. The great people in the Department of Civil and Environmental Engineering at Villanova University started me on this career path in engineering. I am so thankful for the time I spent there and the relationships that I built, both with faculty and fellow classmates.

There is no way I would be where I am today without the continued love and support of my family. Mom, Dad, Kim, and Kristen have always been there for me. I'm blessed to have such a great family. My parents have been tremendous role models throughout my life and I owe so much to them.

I appreciate the patience and support of my future in-laws. Joe in particular has always taken an interest in my work; it's a small thing, but it means a lot to me.

Thanks to all my friends for their support and not bothering me too much about

when I was going to finish and move back up north. Sharing a drink with my Brothers in Whiskey Friday was the ideal way to unwind each week. Lunchtime phone calls with my HLP were a welcomed distraction, as were detailed golf round recaps with Sabella.

It never mattered how bad of a day I had at lab, my little buddy Redick would always greet me at the door as if I did something brilliant. Playing fetch with her or taking her on walks kept me relaxed and centered. She was the perfect distraction whenever I needed one, which was often.

Last, but in no way least, I need to thank my wonderful fiancé, Kristin. She uprooted her life to move down to Virginia with me so I could pursue this dream. Things haven't always gone well for us down here, especially at first, but her patience and unselfishness have meant everything to me during my time at UVa. A graduate student has to make a lot of lifestyle sacrifices, and unfortunately for Kristin, so does their significant other. She had a lot of lonely nights while I was stuck working at lab, didn't get to go out nearly as much as we were accustomed to, and was forced to deal with my irrational mood swings based on how well my research was going. But through it all, she stuck with me. There is absolutely no way I would have been able to complete this dissertation without her unfaltering love and loyalty. Words cannot express how lucky I am to have her in my life. As this chapter closes in our lives, I'm so incredibly thankful for all she has done for me, and I'm excited to see what our future holds.

## TABLE OF CONTENTS

Abstract	i
Acknowledgements	iii
Table of Contents	vi
List of Tables	x
List of Figures	xii
List of Symbols	xv
<b><u>CHAPTER 1 – INTRODUCTION</u></b>	<b><u>1</u></b>
1.1 – Background	1
1.2 – Motivation	3
1.3 – Research Objective	4
1.4 – Dissertation Structure	5
<b><u>CHAPTER 2 – LITERATURE REVIEW</u></b>	<b><u>6</u></b>
2.1 – Introduction	6
2.2 – Flow through Vegetation	6
2.2.1 – Emergent Vegetation	6
2.2.2 – Vegetation Patches	7
2.3 – Sediment Transport	12
2.3.1 – Steady Flow	12
2.3.2 – Unsteady Flow	18
2.4 – Sediment Transport with Vegetation	29
2.4.1 – Emergent Vegetation	29
2.4.2 – Vegetation Patches	30
<b><u>CHAPTER 3 – EXPERIMENTAL METHODS</u></b>	<b><u>35</u></b>
3.1 – Introduction	35
3.2 – Equipment	35
3.2.1 – Flume	35
3.2.2 – Acoustic Doppler Velocimeter	37
3.2.3 - Laser Profiler	39
3.2.4 – Bed Monitoring System	39
3.3 – Data Processing	45
3.3.1 – Velocity Data	45
3.3.2 – Bed Scans	47
3.3.3 – Bed Monitoring System	49
3.4 – Model Vegetation	49
3.4.1 – Model Details	49
3.4.2 – Scaling	50

3.4.3 – Patch Characteristics	53
3.5 – Design Flows	55
3.5.1 – Steady Flows	55
3.5.2 – Unsteady Flows	56
3.6 – Sediment Distributions	60
3.7 – Experiment Details	61
3.7.1 – No Sediment (NS) Experiments	61
3.7.2 – No Patch (NP) Experiments	63
3.7.3 – Patch and Sediment (PS) Experiments	69
<b><u>CHAPTER 4 – EMERGENT VEGETATION PATCH HYDRAULICS</u></b>	<b>71</b>
4.1 – Introduction	71
4.2 – Results	73
4.2.1 – Wake Lengths	73
4.2.2 – Asymmetrical Flow Structure	76
4.2.3 – Stem Configuration	80
4.3 – Discussion	82
4.3.1 – Wake Length Predictions	82
4.3.2 – Implications of Asymmetrical Flow Structure	86
4.3.3 – Effect of Stem Configuration on Flow Field	88
4.4 – Summary	90
<b><u>CHAPTER 5 – MORPHOLOGICAL CHANGE IN UNSTEADY FLOWS</u></b>	<b>92</b>
5.1 – Introduction	92
5.2 – Analysis Methods	92
5.2.1 – Sediment Composition	92
5.2.2 – Semivariogram Analysis to Estimate Bedform Geometry	93
5.2.3 – Bed Adjustment Parameter	95
5.3 – Results: Sand/Gravel Sediment Mixture	96
5.3.1 – Surface and Active Layer Sediment Composition	96
5.3.2 – Bed Structure and Bedforms	97
5.4 – Results: Sand/Silt Sediment Mixture	99
5.4.1 – Active Layer Sediment Composition	99
5.4.2 – Bed Structure and Bedforms	100
5.5 – Discussion	101
5.5.1 – Role of Sediment Mixture on Bedform Geometry	101
5.5.2 – Topographic Variability and Bed Roughness	104
5.5.3 – Channel Adjustment and Stability	107
5.6 – Summary	109

<b><u>CHAPTER 6 – SEDIMENT TRANSPORT IN UNSTEADY FLOWS</u></b>	<b>111</b>
6.1 – Introduction	111
6.2 – Analysis Methods	111
6.2.1 – Shear Stress Calculation and Corrections	111
6.2.2 – Existing Transport Relationships	113
6.2.3 – Evaluation of Prediction Accuracy	114
6.3 – Results: Sand/Gravel Sediment Mixture	115
6.3.1 – Hydrograph Sediment Yield	115
6.3.2 – Fractional Transport	117
6.3.3 – Hysteresis of Sand/Gravel Mixture	117
6.3.4 – Sediment Transport Predictions: Sand/Gravel Mixture	118
6.4 – Results: Sand/Silt Sediment Mixture	120
6.4.1 – Hydrograph Sediment Yield	120
6.4.2 – Fractional Transport	122
6.4.3 – Hysteresis of Sand/Silt Mixture	122
6.4.4 – Sediment Transport Predictions: Sand/Silt Mixture	123
6.5 – Discussion	125
6.5.1 – Effect of Sediment Mixture on Bed Load Yield	125
6.5.2 – Hydrograph Bed Load Yield Prediction	126
6.5.3 – Transport Hysteresis of Bed and Wash Load	128
6.5.4 – Analysis of Sediment Transport Predictions in Unsteady Flows	131
6.6 – Summary	139
<b><u>CHAPTER 7 – IMPACT OF VEGETATION ON CHANNEL MORPHOLOGY</u></b>	<b>142</b>
7.1 – Introduction	142
7.2 – Analysis Methods	142
7.2.1 – Overview of Previously Introduced Methods	142
7.2.2 – Definition of Patch Mound Areas	143
7.3 – Results: Sand/Gravel Sediment Mixture	144
7.3.1 – Surface Sediment Composition and Active Layer Sorting	144
7.3.2 – Patch Channel Morphology	145
7.4 – Results: Sand/Silt Sediment Mixture	150
7.4.1 – Patch Channel Morphology	150
7.5 – Discussion	154
7.5.1 – Patch Hydraulics over Sediment Beds	154
7.5.2 – Channel Bed Structure and Topographic Variability	156
7.5.3 – Patch Mound Dynamics	161
7.5.4 – Influence of Vegetation on Morphological Adjustment and Stability	166
7.6 – Summary	170

<b>CHAPTER 8 – IMPACT OF VEGETATION ON SEDIMENT TRANSPORT</b>	<b>173</b>
8.1 – Introduction	173
8.2 – Analysis Methods	173
8.2.1 – Shear Stress Calculation	173
8.2.2 – Total Sediment Transport Predictions	174
8.2.3 – Reference Shear Stress Calculation	174
8.3 – Results: Sand/Gravel Sediment Mixture	175
8.3.1 – Hydrograph Sediment Yield	175
8.3.2 – Fractional Transport	177
8.3.3 – Hysteresis of Sand/Gravel Mixture	177
8.3.4 – Sand/Gravel Transport Predictions with Yang Equation	178
8.4 – Results: Sand/Silt Sediment Mixture	180
8.4.1 – Hydrograph Sediment Yield	180
8.4.2 – Hysteresis of Sand/Silt Mixture	181
8.4.3 – Sand/Silt Transport Predictions with Yang Equation	181
8.5 – Discussion	182
8.5.1 – Impact of Vegetation Patch on Bed Load Yield	182
8.5.2 – Transport Hysteresis with a Vegetation Patch	187
8.5.3 – Sediment Transport Predictions with a Vegetation Patch	190
8.6 – Summary	197
<b>CHAPTER 9 – CONCLUSIONS AND RECOMMENDATIONS</b>	<b>200</b>
<b>CHAPTER 10 – REFERENCES</b>	<b>205</b>
<b>APPENDICES</b>	<b>226</b>
Appendix A – Equipment Calibration	226
A.1 – Pump Calibration Curves	227
A.2 – Bed Monitoring System Calibration Curves	230
Appendix B – Data Processing	233
B.1 – ADV Processing MATLAB Code	234
B.2 – Bed Scan Processing MATLAB Code	238
B.3 – GIS Processing Flowcharts	242
B.4 – Bed Monitoring System Conversion MATLAB Code	244
Appendix C – Velocity Results	246
C.1 – Velocity and Turbulence Contour Plots (NS Experiments)	247
C.2 – Velocity and Bed Centerline Profiles (PS Experiments)	252
Appendix D – DEMs, Bed Change Maps, Panoramic Bed Photos	264
D.1 – No Patch (NP) Experiments	265
D.2 – Patch Sediment (PS) Experiments	277

## LIST OF TABLES

### *Chapter 2*

2.3.1. Ackers and White sediment transport coefficients	13
2.3.2. Van Rijn coefficient approximations from Shield's Curve	16
2.3.3. Yang sediment transport coefficients	17

### *Chapter 3*

3.2.1. Vectrino settings	38
3.2.2. Bed monitoring system calibration results	41
3.5.1. Baseflow parameters from unsteady flow, sediment transport studies	57
3.5.2. Design hydrograph characteristics	60
3.7.1. NS Experiment group summary	64
3.7.2. NP Experiment group summary	64
3.7.3. PS Experiment group summary	70

### *Chapter 4*

4.1.1. Experimental parameters and results for NS run group	72
---	----

### *Chapter 5*

5.3.1. Bedform geometry of sand/gravel beds	98
5.4.1. Bedform geometry of sand/silt beds	101

### *Chapter 6*

6.2.1. Existing sediment transport relationships	114
6.3.1. Hydrograph parameters and sediment yield (sand/gravel)	116
6.3.2. Transport prediction results for sand/gravel mixture	119
6.4.1. Hydrograph parameters and sediment yield (sand/silt)	121
6.4.2. Transport prediction results for sand/silt mixture	123
6.5.1. Conceptual framework to assess bedform related hysteresis	129
6.5.2. Reference shear stresses for each hydrograph and limb	135
6.5.3. Dimensionless transport coefficients	135
6.5.4. Dimensionless unsteady flow transport prediction results	136
6.5.5. Yang prediction results for combined sand/gravel and sand/silt data set	137

**Chapter 7**

7.3.1. Bedform geometry for sparse patch, sand/gravel sediment beds	147
7.3.2. Bedform geometry for dense patch, sand/gravel sediment beds	149
7.4.1. Bedform geometry for sparse patch, sand/silt sediment beds	151
7.4.2. Bedform geometry for dense patch, sand/silt sediment beds	153
7.4.3. Maximum scour depths around dense patch on sand/silt sediment beds	153

**Chapter 8**

8.2.1. Reference shear stresses for each hydrograph limb with patch	175
8.3.1. Hydrograph parameters and sediment yield for sand/gravel mixture	176
8.3.2. Maximum gravel fraction in transport with patch	177
8.3.3. Yang transport prediction results for sand/gravel mixture with patch	178
8.4.1. Hydrograph parameters and sediment yield for sand/silt mixture	180
8.4.2. Yang transport prediction results for sand/silt mixture with patch	182
8.5.1. Dimensionless transport coefficients with vegetation patch	192
8.5.2. Dimensionless transport prediction results with vegetation patch	192
8.5.3. Prediction results for combined patch-sediment data set	194

## LIST OF FIGURES

### *Chapter 2*

2.2.1. Patch-scale flow hydraulics	9
2.3.1. Example curves for the five common types of sediment transport hysteresis	21
2.4.1. Depositional patterns downstream of an emergent vegetation patch	34

### *Chapter 3*

3.2.1. SRL water and sediment recirculating flume	36
3.2.2. Acoustic Doppler velocimeter mounted in flume	38
3.2.3. Laser profiler collecting measurements over sediment bed	39
3.2.4. Bed monitoring system overhead view without sediment	40
3.2.5. Transducer calibration curve for flume segment 5 m (second calibration)	42
3.2.6. Transducer calibration errors (first calibration)	44
3.4.1. Stem and base model locking mechanism design	50
3.4.2. Preliminary scaling test results	53
3.4.3. Random stem configurations	55
3.4.4. Printed model patches	55
3.5.1. NRCS curvilinear dimensionless unit hydrograph	59
3.5.2. Experimental design hydrographs	60
3.6.1. Experimental sediment distributions	62
3.7.1. Velocity measurement schematics	65

### *Chapter 4*

4.2.1. Longitudinal profile comparison for role of stem density	75
4.2.2. Dimensionless wake lengths for range of flow conditions	76
4.2.3. Velocity and turbulence intensity contour plots for varying stem densities	78
4.2.4. Example asymmetry offset plots	79
4.2.5. Velocity contour plots for varying stem configurations	81
4.3.1. Comparison of predicted and measured wake lengths	83
4.3.2. Wake length predictions	85

### *Chapter 5*

5.2.1. Bed surface semivariogram examples	95
---	----

5.3.1. Surface sediment composition of sand/gravel beds	97
5.3.2. Active layer sediment composition for sand/gravel beds	98
5.3.3. Panoramic photo bed surface comparison for sand/gravel beds	99
5.4.1. Active layer sediment composition for sand/silt beds	100
5.4.2. Panoramic photo bed surface comparison for sand/silt beds	101
5.5.1. Bedform steepness adjustment for sand/silt mixture	103
5.5.2. Comparison of topographic variability	105
5.5.3. Standard deviation of bed elevations as a predictor of bedform height	106
5.5.4. Unit bed adjustment for sand/gravel mixture	108
5.5.5. Unit bed adjustment for sand/silt mixture	109

## ***Chapter 6***

6.3.1. Variation in sand/gravel bed load yield	116
6.3.2. Sediment transport hysteresis examples (sand/gravel)	118
6.3.3. Comparison of Ackers-White and Yang transport predictions (sand/gravel)	119
6.3.4. Prediction comparisons for low and high flow hydrographs (sand/gravel)	120
6.4.1. Variation in sand/silt bed load yield	121
6.4.2. Comparison of Laursen and Yang transport predictions (sand/silt)	124
6.4.3. Prediction comparisons for low and high flow hydrographs (sand/silt)	124
6.5.1. Relative bed load yield comparisons	125
6.5.2. Bed load yield prediction for no patch data set	128
6.5.3. Dimensionless bed load transport prediction	134
6.5.4. Separate limb fractional bed load transport relationships	136
6.5.5. Comparison of Yang and dimensionless bed load transport predictions	138

## ***Chapter 7***

7.2.1. Patch mound delineation using a DEM	143
7.3.1. Surface sand fraction for sand/gravel, patch beds	144
7.3.2. Sediment sorting around vegetation patch as measured by $D_{50}$	146
7.3.3. Characteristic sand/gravel bed morphology for sparse patch	147
7.3.4. Bedform steepness adjustment for sparse patch, sand/gravel beds	148
7.3.5. Characteristic sand/gravel bed morphology for dense patch	149
7.3.6. Bedform steepness adjustment for dense patch, sand/gravel beds	149

7.4.1. Characteristic sand/silt bed morphology for sparse patch	151
7.4.2. Bedform steepness adjustment for sparse patch, sand/silt beds	151
7.4.3. Characteristic sand/silt bed morphology for dense patch	153
7.5.1. Steady wake lengths with and without sediment beds	154
7.5.2. Velocity profile comparison over sediment bed	155
7.5.3. Comparison of shear conversion efficiency	156
7.5.4. Influence of vegetation patch on sand/gravel bed ripple heights	158
7.5.5. Influence of vegetation patch on sand/silt bed ripple heights	159
7.5.6. Topographic variability for patch beds of different sediment mixtures	160
7.5.7. Difference map of patch mound erosion	162
7.5.8. Patch mound area adjustment on sand/gravel beds	162
7.5.9. Patch mound adjustment models	164
7.5.10. Unit bed adjustment for sand/gravel beds with vegetation patch	166
7.5.11. Unit bed adjustment for sand/silt beds with vegetation patch	168

## ***Chapter 8***

8.3.1. Sand/gravel transport predictions with patch using Yang equation	179
8.3.2. Sand/gravel transport comparisons for flow magnitude and patch density	179
8.4.1. Sand/silt transport predictions with patch using Yang equation	182
8.4.2. Sand/silt transport comparisons for flow magnitude and patch density	183
8.5.1. Bed load yield comparison for two sediment mixtures and patch densities	183
8.5.2. Shear stress distributions for sand fraction in sand/gravel mixture	184
8.5.3. Bed load yield prediction for patch-sediment data set	186
8.5.4. Comparison of bed load yield prediction curves	187
8.5.5. Sediment bed weight as indicator of patch induced transport hysteresis	189
8.5.6. Dimensionless bed load transport relationships with patch	193
8.5.7. Dimensionless transport curves for patch and no patch flows	195
8.5.8. Differences in predicted sand transport rates for patch and no patch flows	196

## LIST OF SYMBOLS

The following list includes abbreviations and symbols used in this work, with corresponding units expressed in terms of length (L), time (T), and mass (M). Where symbols may take different meanings depending on context, specific chapters are listed for clarity. Remaining variables are defined within the text, where applicable.

$a$	Frontal patch area per unit volume [ $L^{-1}$ ] (Chapter 2)
	Transport coefficient [-] (Chapters 6 and 8)
$A_m$	Patch mound area [ $L^2$ ]
$A_{m,DS}$	Dynamically stable patch mound area [ $L^2$ ]
$A_{m,EQ}$	Patch mound area on equilibrium bed [ $L^2$ ]
$AO$	Asymmetry offset [-]
$b$	Transport exponent [-]
$B$	Flume width [L]
$c$	Semivariogram model sill [ $L^2$ ]
$C_D$	Patch drag coefficient [-] (Chapter 2)
	Bedform drag coefficient [-] (Chapter 6)
$C_s$	Sediment concentration [ $ML^{-3}$ ]
$d_{stem}, d$	Plant stem diameter [L]
$D$	Patch diameter [L] or sediment size [L] (as specified in text)
$D_p$	Patch diameter [L] (Chapter 3)
$D_x$	Grain size for which $x$ % of distribution is finer by weight [L]
$D_*$	Dimensionless grain diameter [-]
$DR$	Discrepancy ratio [-]
$E$	Modulus of elasticity [ $ML^{-1}T^{-2}$ ]
$f$	Darcy-Weisbach friction factor [-]
$F_B$	Buoyancy force [ $MLT^{-2}$ ]
$F_D$	Drag force [ $MLT^{-2}$ ]
$F_{gr}$	Dimensionless sediment mobility parameter [-]
$F_{gr,c}$	Critical dimensionless sediment mobility parameter [-]
$F_i$	Proportion of grain size $i$ on bed surface [-]
$Fr$	Froude number [-]

$F_R$	Resistance force due to stem rigidity [ $MLT^{-2}$ ]
$g$	Acceleration due to gravity [ $LT^{-2}$ ]
$G$	Stem spacing [L]
$h$	Water depth [L] Lag distance [L] (Chapter 5 and where specified)
$h_{bf}$	Baseflow water depth [L]
$h_p$	Water depth at peak flow rate [L]
$I$	Second moment of inertia [ $L^4$ ] (Chapter 3)
$k_s$	Total roughness length-scale [L]
$k_{s,bedform}$	Bedform roughness length-scale [L]
$k_{s,grain}$	Grain roughness length-scale [L]
$K$	Dimensionless Ackers-White transport coefficient [-] (Chapter 2)
$l$	Periodic function wavelength [L]
$L$	Total patch wake length [L]
$L_R$	Reach length [L]
$L_w$	Wake formation length [L]
$L_1$	Steady wake length [L]
$L_2$	Wake recovery length [L]
$m$	Dimensionless Ackers-White transport exponent [-] (Chapter 2) Number of stems per patch area [ $L^{-2}$ ] (Chapter 3)
$n$	Dimensionless Ackers-White transport exponent [-] (Chapter 2) Vortex shedding frequency [ $T^{-1}$ ] (Chapter 3)
$NRMSE$	Normalized root mean square error
$P, P_s$	Hydrograph unsteadiness parameter [-]
$q$	Unit discharge rate [ $L^2T^{-1}$ ]
$q_s$	Unit sediment transport rate [ $ML^{-1}T^{-1}$ ]
$q_{s,np}$	Unit sediment transport rate with no vegetation patch [ $ML^{-1}T^{-1}$ ]
$q_{s,p}$	Unit sediment transport rate with a vegetation patch [ $ML^{-1}T^{-1}$ ]
$Q$	Discharge rate [ $L^3T^{-1}$ ]
$Q_{BF}$	Baseflow discharge rate [ $L^3T^{-1}$ ]
$Q_P$	Peak flow discharge rate [ $L^3T^{-1}$ ]

$Q_s$	Sediment discharge rate [ $L^3T^{-1}$ ]
$r$	Semivariogram model range [L] (Chapters 5 and 7) Pearson's correlation coefficient (where specified)
$R$	Hydraulic radius [L]
$Re_d$	Stem Reynolds number [-]
$R^2$	Coefficient of determination [-]
$RMSE$	Root mean square error
$s$	Specific gravity of sediment
$S$	Flume slope [-]
$S_b$	Bed slope [-]
$S_e$	Energy slope [-]
$S_t$	Strouhal number [-]
$S_T$	Bed slope from transducer signal [-]
$SR$	Slope ratio [-]
$S_{\delta l}$	Empirical shear layer growth parameter [-]
$t$	Time [T]
$t_d$	Total hydrograph duration [T]
$t_p$	Time to hydrograph peak [T]
$t_r$	Duration of hydrograph rising limb [T]
$T$	Transport stage parameter [-]
$TKE$	Turbulent kinetic energy
$u_{rms}$	Turbulence intensity in $x$ -direction [ $LT^{-1}$ ]
$u_*$	Shear velocity [ $LT^{-1}$ ]
$u'_*$	Shear velocity due to grain resistance [ $LT^{-1}$ ]
$u_{*bf}$	Shear velocity at baseflow [ $LT^{-1}$ ]
$u_{*c}$	Critical shear velocity [ $LT^{-1}$ ]
$u_{*p}$	Shear velocity at peak flow [ $LT^{-1}$ ]
$u_{*,us}$	Unsteady flow shear velocity [ $LT^{-1}$ ]
$U$	Flow velocity [ $LT^{-1}$ ]
$\bar{U}$	Average velocity outside of shear layer, in steady wake [ $LT^{-1}$ ]
$U_{bf}$	Flow velocity at baseflow [ $LT^{-1}$ ]

$U_c$	Critical flow velocity for sediment motion [ $LT^{-1}$ ]
$U_p$	Flow velocity at peak flow [ $LT^{-1}$ ]
$U_0$	Unimpeded flow velocity upstream of patch [ $LT^{-1}$ ]
$U_1$	Flow velocity in steady wake [ $LT^{-1}$ ]
$U_2$	Flow velocity outside of shear layer [ $LT^{-1}$ ]
$volt$	Transducer voltage signal, in mV
$v_{rms}$	Turbulence intensity in $y$ -direction [ $LT^{-1}$ ]
$v_{rms,max}$	Maximum centerline turbulence intensity in $y$ -direction [ $LT^{-1}$ ]
$w_b$	Bedform width [L]
$w_l$	Bed monitoring system load [M]
$W_i^*$	Dimensionless bed load transport rate for size fraction $i$ [-]
$W_k$	Hydrograph flow work index [-]
$W_t$	Total bed load yield [M]
$Y_s^*, W_t^*$	Dimensionless total bed load yield [-]
$Y_s, W_t$	Total bed load yield [ $ML^{-1}$ ]
$x$	Streamwise flume distance [L]
$X$	Dimensionless transport rate [-] (Chapter 2)
$y$	Cross-stream flume distance [L]
$z$	Bed elevation, vertical flume distance [L]
$z_b$	Unit sediment bed depth [L]
$z_{s,max}$	Maximum bed scour depth [L]
$z_{0,sf}$	Zero velocity bed elevation associated with skin friction [L]
$\alpha$	Coefficient for Shield's Curve approximation [-] (Chapter 2) Patch mound area adjustment model coefficient [-] (Chapter 7)
$\beta$	Exponent for Shield's Curve approximation [-] (Chapter 2) Patch mound area decay coefficient [-] (Chapter 7)
$\gamma$	Model semivariance [ $L^2$ ]
$\delta_b$	Unit bed adjustment parameter [%]
$\varepsilon$	Shear conversion efficiency parameter [-]
$\zeta$	Scalar multiple for roughness analysis [-]
$\kappa$	von Karman's constant [-]

$\lambda$	Bedform spacing [L]
$\nu$	Kinematic viscosity of water [ $L^2S^{-1}$ ]
$\rho$	Water density [ $ML^{-3}$ ]
$\rho_s$	Sediment density [ $ML^{-3}$ ]
$\sigma_z$	Standard deviation of bed elevations [L]
$\tau_b$	Bed shear stress [ $ML^{-1}T^{-2}$ ]
$\bar{\tau}_b$	Weighted average bed shear stress [ $ML^{-1}T^{-2}$ ]
$\tau_c$	Critical shear stress [ $ML^{-1}T^{-2}$ ]
$\tau'$	Bed shear stress due to grain resistance/skin friction [ $ML^{-1}T^{-2}$ ]
$\tau^*$	Dimensionless shear stress [-]
$\tau_c^*$	Dimensionless critical shear stress [-]
$\tau_r^*$	Dimensionless reference shear stress [-]
$\phi$	Solid volume fraction [-]
$\chi$	Dimensionless hydrograph and channel descriptor variable [-]
$\omega$	Particle settling velocity [ $LT^{-1}$ ]
$\Delta$	Bedform height [L]
$\Delta U$	Velocity difference outside of shear layer, in steady wake [ $LT^{-1}$ ]
$\Delta V_b$	Volumetric bed change [ $L^3$ ]
$\Phi_A$	Bed load transport parameter [-]
$\Psi_A$	Flow intensity parameter [-]
$\forall$	Total volume of water under a hydrograph excluding baseflow [ $L^3$ ]

# CHAPTER 1

## *Introduction*

---

---

### 1.1 BACKGROUND

Aquatic vegetation falls into four categories: algae; floating plants not rooted in the channel bed; submerged plants where stems and leaves grow underwater; and emergent plants that grow to a height above the water surface. The most obvious impact of submerged and emergent vegetation in river channels is an increase in flow resistance and a reduction in conveyance capacity [e.g. *Kouwen and Unny*, 1973], so that for many years vegetation has been removed to accelerate the passage of peak flows. However, in-channel vegetation can positively influence fluvial systems. For instance, vegetation can improve water quality through nutrient removal and retention [e.g. *Chambers and Prepas*, 1994; *Schulz et al.*, 2003; *Mars et al.*, 1999], thus affecting chemical processes and in-stream nutrient dynamics. Specifically, carbon, nitrogen and phosphorus cycling is affected by aquatic vegetation through enhancement of nitrification and denitrification rates, organic matter mineralization, and uptake and release of nutrients from the soil to the water. Thus, in-stream vegetation links channel sediment to the water column [*Clarke and Wharton*, 2001], serving a unique role in riverine ecosystems [*Clarke*, 2002]. Additionally, vegetation promotes biodiversity by creating spatial flow heterogeneity, which provides a diversity of habitat conditions [*Kemp et al.*, 2000; *Crowder and Diplas*, 2000, 2002] and a range of in-stream functional habitats designated by spatially variable

substrate texture and macrophyte types [*Kemp et al.*, 1999].

In-channel vegetation affects sediment transport and storage. By baffling flow and reducing bed shear stress, vegetation creates regions of sediment retention [e.g. *Abt et al.*, 1994; *Lopez and Garcia*, 1998; *Cotton et al.*, 2006; *Gurnell et al.*, 2006; *Wharton et al.*, 2006]. Both riparian and in-channel vegetation act to retain sediment, which is critical in maintaining geomorphic channel form. In-channel vegetation has been shown to retain up to 80% of the sediment in transit downstream [*Sand-Jensen*, 1998], with varying sedimentation patterns linked to plants with different morphologies [*Sand-Jensen and Mebus*, 1996; *Sand-Jensen*, 1998], as well as initiate in-channel island formation [*Gurnell and Petts*, 2002]. The role of vegetation on channel planform adjustment has also been noted. *Tal and Paola* [2007] showed that single-thread channels are stabilized by bank vegetation. Similarly, *Braudrick et al.* [2009] showed that vegetation helps maintain a meandering channel form. It is now widely recognized that vegetation enhances both channel and bank stability [*Afzalimehr and Dey*, 2009; *Li and Millar*, 2011; *Wynn and Mostaghimi*, 2006; *Hung et al.*, 2007; *Murray and Paola*, 2004; *Pollen-Bankhead and Simon*, 2010].

The water quality, habitat, and stability benefits of in-stream vegetation suggest that planting or mowing could be useful in particular situations, rather than complete removal. Subsequently, researchers are now advocating replanting and ecological management of aquatic vegetation [e.g., *Mars et al.*, 1999, *Pollen and Simon*, 2005; *Vereecken et al.*, 2006]. However, extensive vegetation growth can lead to channel choking, which impedes flow [*Kemp et al.*, 1999; *Gurnell et al.*, 2010; *Liffen et al.*, 2011] and downstream transport of sediment and nutrients [*Zierholz et al.*, 2001], especially in

lower energy environments [Gurnell *et al.*, 2010]. Threshold conditions of sediment supply and stream power to control vegetation growth and prevent choking are unknown [Gurnell *et al.*, 2010]. If these thresholds can be determined for a range of hydrological conditions, vegetation can potentially be utilized to enhance select fluvial systems by broadly improving ecosystem functionality and channel stability.

## 1.2 MOTIVATION

Research into the interactions between vegetation, flow, and sediment transport in fluvial environments has important implications for river management, especially in terms of restoration. River restoration seeks to improve hydrologic, geomorphic, and ecological processes in a degraded fluvial system [Wohl *et al.*, 2005] while increasing natural riverine ecosystem production and protecting downstream environments [Palmer *et al.*, 2005]. Thus, it focuses on restoring biological functionality to degraded streams through improvement of habitats and enhanced channel bed and bank stability [Bennett *et al.*, 2002]. Because channel vegetation influences these processes, it may have a significant role in restoration; but commonly accepted river restoration standards have yet to be developed [Palmer *et al.*, 2005] and proper use of vegetation in restoration efforts is not fully understood and remains largely untested [Pollen, 2007]. Incorporating a thorough understanding of sediment transport processes around in-channel vegetation patches could prove valuable in improving restoration applications. In order to design restoration schemes that will be sustainable, extensive knowledge regarding the feedback between channel sediment, in-stream vegetation, and local hydraulics is necessary [Naden *et al.* 2006].

In-channel vegetation patches may possess utility as a method to reduce scour at

bridge piers, the most common cause of bridge failures [*Richardson and Davis, 2001*]. Understanding the flow field around piers and its erosion capacity is paramount in modeling scour and designing to prevent it [*Ettema et al., 2011*]. Wakes behind emergent vegetation patches are areas of decreased mean velocity and turbulence intensity [*Zong and Nepf, 2012*], and therefore, if strategically planted upstream of bridge piers, may contribute to lessen scour through flow deflection and reduction, while enhancing sediment accretion. Such an application would provide a natural way to inhibit scour, but requires a more comprehensive understanding of the nature and extent of flow field modification and corresponding geomorphic adjustments downstream of an emergent vegetation patch.

While numerous publications [e.g. *NRC, 2002*] and government policies [*CEC, 2003*] advocate fluvial vegetation as efficient traps for sediments and other pollutants, few studies have measured actual sediment storage rates [*Noe and Hupp, 2009*]. Such a description would enable future researchers and restoration managers to predict whether a given patch of pioneer (or planted) vegetation will grow into a stable channel feature or be erased by erosion, and how a particular distribution of vegetation would likely impact sediment storage and transport. Consequently, utilizing vegetation to provide for a more natural morphology and ecology could be considered in managing riverine environments [*Kemp et al., 1999*].

### **1.3 RESEARCH OBJECTIVE**

The overarching objective of this research is to gain a more complete understanding of how a patch of emergent vegetation alters flow patterns, sediment transport, and associated channel bed bathymetry changes over unsteady flows. This

work seeks to elucidate key hydraulic and geomorphic impacts of in-stream vegetation patches that can be directly applied to river restoration practices to enhance ecological functionality and channel bed stability. This central objective was investigated through physical experimentation focused on the interactions between an emergent vegetation patch, channel hydraulics, and sediment transport processes over a range of repeated unsteady flow conditions. Results from this research will form the necessary foundation to better understand and predict the impacts of an in-stream, emergent vegetation patch on flow and sediment transport over varying temporal scales.

#### **1.4 DISSERTATION STRUCTURE**

This dissertation is organized into nine primary chapters. The first chapter provides relevant background information, motivation, and objectives of this research. Chapter 2 is a comprehensive literature review focusing on three distinct areas of previous work: flow in and around vegetation, sediment transport in steady and unsteady flows, and sediment transport in and around vegetation. Chapter 3 details the experimental methods applied in this work, including equipment, data processing, experimental design, and procedures. Chapters 4 through 8 represent the core of this research, discussing results and analysis related to patch hydraulics (Chapter 4), channel bed morphology and stability (Chapters 5 and 7) and sediment transport in unsteady flows (Chapters 6 and 8). Specifically, the impact of a vegetation patch on bed morphology/stability and sediment transport is analyzed in Chapter 7 and Chapter 8, respectively. Chapter 9 is a summary of this work that places findings in a river restoration context and includes recommendations for future related research.

## CHAPTER 2

### *Literature Review*

---

---

#### **2.1 INTRODUCTION**

Linking sediment transport dynamics around a vegetation patch over a range of unsteady flow conditions requires understanding of the individual components of this system before a comprehensive analysis can be conducted. This chapter highlights previous research on flow through vegetation (Section 2.2), sediment transport in steady and unsteady flows (Section 2.3), and sediment transport around vegetation (Section 2.4), all of which serve as the foundation for this research.

#### **2.2 FLOW THROUGH VEGETATION**

##### **2.2.1 Emergent Vegetation**

Flow in open channels is governed by a balance of the gravitational forces driving the flow and drag forces at the channel boundary resisting flow. When emergent vegetation is present, drag acting on the vegetative elements reduces the mean flow velocity and the momentum equation simplifies to a balance between the pressure gradient and vegetative drag terms [*Nepf and Vivoni, 2000*]. Relative to unvegetated channel areas, flow velocity within an emergent canopy is reduced due to the contribution of drag forces induced by the plants on the flow as well as the turbulence generated in the wakes of individual plant stems [*Shi et al., 1995; Nepf and Vivoni, 2000; Asaeda et al.,*

2010]. Turbulence production within stem wakes is the primary source of turbulence generation within vegetated conditions [*Shucksmith et al.*, 2010], exceeding that of the bed shear production over most of the flow depth [*Nepf et al.*, 1997; *Nepf*, 1999].

Flow through and around vegetation is impacted by species specific plant characteristics [e.g. *Bouma et al.*, 2013]. In particular, stem density significantly alters flow patterns through emergent vegetation, with decreased flow velocity occurring through higher density stems [e.g. *Bennett et al.*, 2002; *Stern et al.*, 2001]. As stem density continually increases, a vegetative canopy will behave more like a porous-medium than an open channel [*Jadhav and Buchberger*, 1995], and beyond a certain blockage threshold, will behave like a solid body blocking all flow [e.g. *Zong and Nepf*, 2012]. Stem density affects turbulence properties, as well. In sparsely vegetated canopies, turbulence intensity is elevated due to stem wake production, experiencing minimal wake interference from adjacent stems. However, for denser canopies, turbulence intensity decreases as flow is further reduced. Changes in the turbulent kinetic energy budget in vegetated flow reflect the competing effects of reduced flow velocity and increased turbulence at the stem scale [*Nepf*, 1999].

### **2.2.2 Vegetation Patches**

Aquatic vegetation commonly grows as patches in rivers [*Naden et al.*, 2006; *Sand-Jensen and Mebus*, 1996]. Submerged plants tend to grow in distinct, monospecific patches varying in spatial distribution and channel cover [*Clarke*, 2002; *Sand-Jensen*, 1998; *Sand-Jensen and Pedersen*, 2008; *Sand-Jensen and Mebus*, 1996], while emergent vegetation forms patches of varying density [*Asaeda et al.*, 2010, 2005]. Vegetation patches affect flow at various scales, introducing spatial heterogeneity in the flow field

that impacts channel bathymetry and substrate sorting [*Sand-Jensen and Mebus, 1996*] which can result in distinctive in-stream morphology at the reach-scale [*Clarke, 2002*]. Within patches, flow velocity is reduced relative to unimpeded open channel flow [e.g. *Vandenbruwaene et al., 2011*]. Sparsely vegetated patches create minimal flow blockage, allowing some flow through the patch and thus, less flow accelerates around it [*Bouma et al., 2007*]. For patches of increasing stem density, flow is more restricted and subsequently diverted around the patch, causing flow acceleration in patch-adjacent areas [*Asaeda et al., 2010; Bouma et al., 2007; Vandenbruwaene et al., 2011*]. Reduced flow through a patch and the accelerated flow adjacent to it form velocity gradients which create shear layers at the edges of emergent vegetation patches. Vortices in shear layers increase turbulence flux and enhance momentum transport into a patch [*Zong and Nepf, 2011; Rominger and Nepf, 2011*].

Shear layers propagate downstream of a vegetation patch, contributing to distinct flow and turbulence characteristics at the patch-scale (Figure 2.2.1). For a solid body cylinder, a von Karman vortex street forms immediately downstream; however, because vegetation patches are porous, flow passing through the patch delays the onset of the vortex street. This produces a region of constant streamwise flow velocity downstream of a patch. Within this region, which is referred to as the steady wake, mean flow velocity is reduced relative to the unobstructed channel flow and turbulence intensity is diminished [*Zong and Nepf, 2012*]. The structure and length of the wake zone downstream of a patch is set by the shear layer growth, which is influenced by patch density and flow blockage [*Zong and Nepf, 2012; Chen et al., 2012; Nicolle and Eames, 2011*]. The steady wake length extends farther downstream for sparser patches [*Zong and Nepf, 2012*] because

more flow is able to pass through the patch, resulting in smaller velocity gradients and overall weaker shear layers. For dense patches, stems restrict flow penetration, causing more flow acceleration and stronger shear layers that grow quickly and meet closer to the trailing edge of the patch after a reduced steady wake length. The end of the steady wake and onset of the von Karman vortex street occurs when shear layers merge and the velocity begins to increase in the downstream direction [Ball *et al.*, 1996]. This zone of increasing velocity, referred to as the wake recovery region, is defined by a reduction in the spatial velocity gradient to a small value as the mean flow approaches the upstream velocity. Together, the steady wake and wake recovery regions are combined to form the total patch wake [Zong and Nepf, 2012], which describes the scale over which a vegetation patch influences the mean flow field.

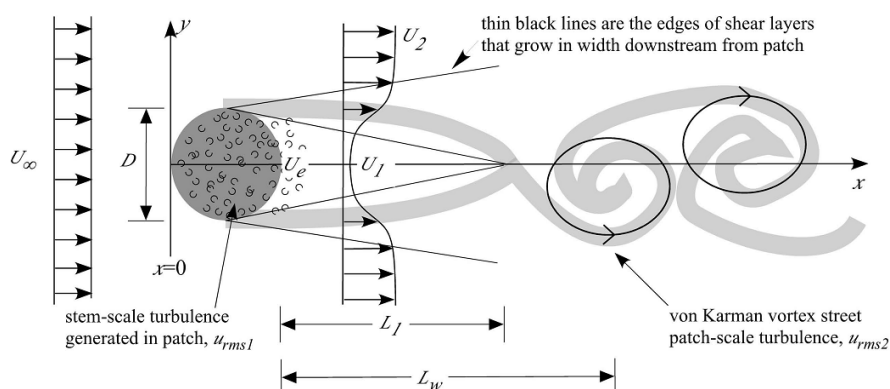


**Figure 2.2.1.** Patch-scale flow hydraulics (from *Chen et al.*, 2012).

A model defining the hydraulics around a circular patch of emergent vegetation with uniformly arranged stems was recently developed from flume experiments to predict the steady wake length,  $L_1$  [Zong and Nepf, 2012]. By utilizing the linear growth rate of individual shear layers and the patch diameter,  $L_1$  can be predicted with Equation 2.2.1:

$$L_1 \approx \frac{D/2 \bar{U}}{S_{\delta l} \Delta U} \quad (2.2.1)$$

where  $D$  is the patch diameter,  $\bar{U}$  is the average of the velocities in the steady wake and adjacent to the patch,  $\Delta U$  is the difference between these velocities, and  $S_{\delta l}$  is a dimensionless, empirical growth parameter associated with the shear layer downstream of a patch, which Zong and Nepf found to be constant and equal to 0.10 +/- 0.02. Using the average  $S_{\delta l}$  of 0.10, *Follett and Nepf* [2012] re-wrote this equation, in non-dimensional form, as Equation 2.2.2 below:

$$\frac{L_1}{D} = 2.5 \frac{(1 + U_1/U_2)}{(1 - U_1/U_2)} \quad (2.2.2)$$

where  $U_1$  is the flow velocity in the steady wake, and  $U_2$  is the flow velocity adjacent to the patch. Using Equation 2.2.2, the length of the steady wake region can be approximated using velocity measurements from two locations: downstream of the patch in the steady wake; and adjacent to the patch but outside of the shear layer. For channel widths much greater than the patch diameter, it can be assumed that  $U_2$  is equal to the velocity upstream of the patch,  $U_0$  [*Follett and Nepf*, 2012; *Chen et al.*, 2012], so  $L_1$  can be estimated from velocity measurements upstream and downstream of a patch. From the same data used to develop the above relationships, *Follett and Nepf* [2012] proposed an empirical relation to estimate the length of the wake recovery region,  $L_2$ , in non-dimensional form (Equation 2.2.3):

$$\frac{L_2}{D} = 13 \frac{U_1}{U_0} + 4 \quad (2.2.3)$$

Thus, the total wake,  $L$ , behind an emergent patch can be predicted by adding the steady wake and wake recovery lengths:  $L_1 + L_2 = L$ .

A distinct turbulence structure develops downstream of an emergent vegetation patch. Directly behind a patch, an initial peak in turbulence intensity occurs, representing the stem-scale turbulence [Chen *et al.*, 2012; Takemura and Tanaka, 2007], which dissipates quickly and has little effect on the flow field at larger spatial scales. Farther downstream of the patch, a second maximum in turbulence intensity occurs, coincident with patch-scale turbulence or vortices [Chen *et al.*, 2012; Takemura and Tanaka, 2007]. For high stem spacing (i.e. low density), the patch-scale von Karman vortex street may not form, leaving only the stem-scale turbulence present downstream [Chen *et al.*, 2012].

The distance from the trailing patch edge to the second turbulence intensity peak is termed the wake formation length,  $L_w$ , and corresponds to the von Karman vortex street (Figure 2.2.1). Chen *et al.* [2012] explored this length-scale behind porous, circular patches and found  $L_w$  to be a function of flow blockage, which is quantified as a dimensionless parameter,  $C_D a D$ , where  $C_D$  is the patch drag coefficient,  $a$  is the frontal area per volume ( $a = nd$ , or the number of stems multiplied by the stem diameter), and  $D$  is the patch diameter. When flow blockage is low ( $C_D a D < 4$ ), the stem-scale turbulence is greater than the patch-scale, with  $L_w$  shifting downstream and decreasing in magnitude as flow blockage decreases [Chen *et al.*, 2012; Zong and Nepf, 2012]. For higher flow blockage patches ( $C_D a D > 4$ ), the patch-scale turbulence peak is greater than the stem-scale. Using the reliance of turbulence behavior on flow blockage, Chen *et al.* [2012] proposed the following empirical relation to estimate  $L_w$  in non-dimensional form (Equation 2.2.4):

$$\frac{L_w}{D} = 1.2 + (25 \pm 10)C_D a D^{(-0.9 \pm 0.2)} \quad (2.2.4)$$

Taken together, the steady wake length, wake recovery length, wake formation length, and total wake length represent relevant scales for describing patch-scale hydraulics.

## 2.3 SEDIMENT TRANSPORT

### 2.3.1 Steady Flow

There is an extensive collection of existing relationships to predict sediment transport in steady flows that spans a variety of different approaches, theoretical bases, transport modes (i.e. bed, suspended, or total load), and applicable flow or sediment conditions. General approaches may include theoretical, regression, probabilistic, or deterministic consideration of sediment and/or flow parameters [Yang, 2006]. Many relationships use bed shear stress as the driving parameter, calculating transport rate proportionally to the excess shear stress above a critical value for sediment mobility [e.g. *Meyer-Peter and Muller*, 1948]. Others are based on the concept of stream power being directly linked to sediment transport [e.g. *Yang*, 1973]. While no consensus exists as to best method to predict sediment transport, it is important to apply transport equations only within their applicable ranges of flow and sediment characteristics for which they were developed. Selected sediment transport relationships that will be analyzed in Chapter 6 are detailed below. These include different approaches and applicable ranges of sediment size.

#### *Ackers and White*

*Ackers and White* [1973] developed an empirical function for total load transport using flume data. The relationship, which is applicable for sediment sizes between 0.4

and 7.0 mm, predicts transport rate as a function of dimensionless parameters for grain diameter ( $D_*$ ; Equation 2.3.1), sediment mobility ( $F_{gr}$ ; Equation 2.3.2), and transport rate ( $X$ ; Equations 2.3.3), using the  $D_{35}$  grain size.

$$D_* = D_{35} \left[ \frac{g(s-1)}{\nu^2} \right]^{1/3} \quad (2.3.1)$$

$$F_{gr} = \frac{u_*^n}{\sqrt{gD_{35}(s-1)}} \left[ \frac{U}{\sqrt{32} \log(10h/D_{35})} \right]^{1-n} \quad (2.3.2)$$

$$X = \frac{sD_{35}}{h} \left( \frac{u_*}{U} \right)^n K \left( \frac{F_{gr}}{F_{gr,c}} - 1 \right)^m \quad (2.3.3)$$

where  $s$  is specific gravity of the sediment,  $\nu$  is water viscosity,  $u_*$  is shear velocity,  $U$  is mean flow velocity, and  $h$  is water depth. Multiplying by water density and unit water discharge,  $q$ , converts  $X$  to unit transport rate,  $q_s$ , with units of kg/m-s. Values of  $F_{gr,c}$ ,  $K$ ,  $m$ , and  $n$  were developed using laboratory data and vary depending on sediment size. These coefficients were adjusted by *HR Wallingford* [1990] and are listed in Table 2.3.1.

**Table 2.3.1.** Ackers and White sediment transport coefficients.

Coefficient	$D_* \geq 60$ (Coarse)	$1 < D_* < 60$ (Fine)
$n$	0	$1.00 - 0.56 \log D_*$
$m$	1.78	$6.83/D_* + 1.67$
$K$	0.025	$10^{[-3.46 + 2.79 \log D_* - 0.98(\log D_*)^2]}$
$F_{gr,c}$	0.17	$0.23D_*^{-1/2} + 0.14$

*Proffitt and Sutherland* [1983] proposed a modification to include a hiding/exposure factor to the Ackers and White formula based on laboratory experiments. The correction is applied to the critical sediment mobility number ( $F_{gr,c}$ ) in Equation 2.3.3 for computing

transport rate in sediment mixtures.

### ***Einstein-Brown***

Proposing that bedload movement occurs as a series of steps and rest periods, *Einstein* [1942, 1950] developed a probabilistic function to predict bedload transport based on the probability of particle motion subject to given hydrodynamic forcing. *Brown* [1950] fit a new curve to Einstein's data, forming a revised relationship (Equation 2.3.4). The relationship is applicable for sand and gravels ranging in grain diameters of 0.30 mm to 29 mm.

$$q_s = \rho_s \sqrt{g(s-1)D_{50}^3} \left[ \sqrt{\frac{2}{3} + \frac{36\nu^2}{g(s-1)D_{50}^3}} - \sqrt{\frac{36\nu^2}{g(s-1)D_{50}^3}} \right] F(\tau^*) \quad (2.3.4)$$

where  $\tau^*$  is dimensionless shear stress given by Equation 2.3.5 and  $F(\tau^*)$  is a function of  $\tau^*$  given by Equation 2.3.6:

$$\tau^* = \frac{\tau_b}{(\rho_s - \rho)gD_{50}} \quad (2.3.5)$$

$$F(\tau^*) = \begin{cases} 2.15 \exp(-0.391/\tau^*) & \text{if } \tau^* \leq 0.18 \\ 40\tau^{*3} & \text{if } \tau^* > 0.18 \end{cases} \quad (2.3.6)$$

where  $\tau$  is shear stress and  $\rho$  is fluid density.

### ***Engelund and Hansen***

*Engelund and Hansen* [1967] proposed a semi-empirical formula (Equation 2.3.7) to predict total sand transport based on flume data and Bagnold's stream power concept. The applicable grain size range is between 0.15 and 1.6 mm and the median grain size should be used when applying this relationship to a unimodal sediment distribution.

$$q_s = \frac{0.1\rho_s}{f} \tau^{*5/2} \sqrt{g(s-1)D_{50}^3} \quad (2.3.7)$$

where  $\rho_s$  is sediment density and  $f$  is the Darcy-Weisbach friction factor, which can be calculated using Equation 2.3.8:

$$f = \frac{2gRS_e}{U^2} \quad (2.3.8)$$

where  $S_e$  is the energy slope and  $R$  is hydraulic radius.

### ***Laursen***

*Laursen* [1958] derived a bed-material load prediction relationship through a combination of qualitative analysis, experiments, and field measurements. The relationship predicts sediment concentration as a function of excess shear stress and Rouse number,  $u_*/\omega$  (Equation 2.3.9). It also explicitly accounts for the bed shear stress due to grain resistance,  $\tau'$ , using the Manning-Strickler equation (Equation 2.3.10).

$$q_s = 0.01\rho q \left(\frac{D_{50}}{h}\right)^{7/6} \left(\frac{\tau'}{\tau_c} - 1\right) F\left(\frac{u_*}{\omega}\right) \quad (2.3.9)$$

$$\tau' = \frac{\rho U^2}{58} \left(\frac{D_{50}}{h}\right)^{1/3} \quad (2.3.10)$$

where  $\tau_c$  is the critical shear stress for incipient motion,  $\omega$  is particle settling velocity, and  $F(u_*/\omega)$  is a functional relationship that can be approximated for bed load with Equation 2.3.11 [*Madden*, 1993]:

$$F\left(\frac{u_*}{\omega}\right) = 10.7378 \left(\frac{u_*}{\omega}\right)^{0.25301} \quad (2.3.11)$$

### Van Rijn

Van Rijn [1984a] developed a semi-empirical bed load transport relationship (Equation 2.3.12) based on saltation characteristics and motion of individual particles. The equation includes an excess shear stress term referred to as the transport stage parameter,  $T$  (Equation 2.3.13), and is applicable only for sand ( $0.2 \text{ mm} < D < 2.0 \text{ mm}$ ). Shear stress due to skin friction is explicitly accounted for through use of the Chezy resistance formula (Equation 2.3.14), and critical shear velocity,  $u_{*c}$ , is determined by piecewise functions that approximate the Shield's curve (Equation 2.3.15, Table 2.3.2).

$$q_s = 0.053\rho_s\sqrt{(s-1)gD_{50}^3}\frac{T^{2.1}}{D_*^{0.3}} \quad (2.3.12)$$

$$T = \frac{u_*'^2 - u_{*c}^2}{u_{*c}^2} \quad (2.3.13)$$

$$u_*' = \sqrt{g}\frac{U}{18\log\left(\frac{4R}{D_{90}}\right)} \quad (2.3.14)$$

$$u_{*c} = g(s-1)D_{50}[\alpha D_*^\beta] \quad (2.3.15)$$

**Table 2.3.2.** Van Rijn coefficient approximations from Shield's Curve.

$D_*$ Range	$\alpha$	$\beta$
$D_* \leq 4$	0.240	-1.00
$4 < D_* \leq 10$	0.140	-0.64
$10 < D_* \leq 20$	0.040	-0.10
$20 < D_* \leq 150$	0.013	0.29
$D_* > 150$	0.055	1.00

### Yang

From dimensional analysis with laboratory data, Yang [1973] developed a relationship to predict sand transport based on the concept of dimensionless unit stream

power,  $US_e/\omega$  (Equation 2.3.16), and a critical velocity for incipient motion,  $U_c$  (Equation 2.3.17):

$$\log C_s = I - J \log\left(\frac{\omega D_{50}}{\nu}\right) - K \log\left(\frac{u_*}{\omega}\right) + \left[ L - M \log\left(\frac{\omega D_{50}}{\nu}\right) - N \log\left(\frac{u_*}{\omega}\right) \right] \log\left(\frac{US_e}{\omega} - \frac{U_c S_e}{\omega}\right) \quad (2.3.16)$$

$$\frac{U_c}{\omega} = \begin{cases} \frac{2.5}{\log\left(\frac{u_* D_{50}}{\nu}\right) - 0.06} + 0.66 & \text{for } 1.2 < \frac{u_* D_{50}}{\nu} < 70 \\ 2.05 & \text{for } \frac{u_* D_{50}}{\nu} \geq 70 \end{cases} \quad (2.3.17)$$

where  $C_s$  is total sand concentration in ppm by weight and  $I$ ,  $J$ ,  $K$ ,  $L$ ,  $M$ , and  $N$  are coefficients given in Table 2.3.3. Sediment concentration can be converted to unit transport rate,  $q_s$ , using Equation 2.3.18:

$$q_s = \frac{\rho q 10^{\log C_s}}{10^6} \quad (2.3.18)$$

**Table 2.3.3.** Yang sediment transport coefficients.

Coefficient	Sand Transport ( $D < 2.0$ mm)	Gravel Transport ( $D \geq 2.0$ mm)
<i>I</i>	5.435	6.681
<i>J</i>	0.286	0.633
<i>K</i>	0.457	4.816
<i>M</i>	1.799	2.784
<i>N</i>	0.409	0.305
<i>O</i>	0.314	0.282

Yang [1984] extended the stream power relationship for sand calibrating the coefficients in Equation 2.3.16 with gravel data, resulting in modified coefficients to predict gravel transport (Table 2.3.3).

### 2.3.2 Unsteady Flow

#### *Hydrographs*

Flow that varies with respect to time is considered unsteady and although unsteadiness characterizes natural river flow, changing over various temporal scales, flume studies often employ steady flow to simplify experimental conditions. A small subset of studies investigating sediment transport in unsteady flows have implemented a range of approaches in the lab setting to simulate unsteady conditions, including experimental hydrographs with a triangular shape [e.g. *Guney et al.*, 2013; *Ahanger et al.*, 2008; *Lee et al.*, 2004; *De Sutter et al.*, 2001; *Yen and Lee*, 1995; *Phillips and Sutherland*, 1990], trapezoidal shape [*Bombar et al.*, 2011], a lognormal distribution [*Humphries et al.*, 2012], and stepped intervals of constant flow [e.g. *Mao*, 2012; *Hassan et al.*, 2006; *De Sutter et al.*, 2001; *Parker et al.*, 2008]. Both symmetric and asymmetric hydrograph shapes have been applied and in some cases the impact of hydrograph shape has been a primary area of interest [e.g. *Hassan et al.*, 2006].

Deriving relevant hydrograph characteristics for flume studies has been a challenge, resulting in large variations in hydrograph durations and flows used in previous research. Hydrograph durations have ranged from 70 seconds [*Bombar et al.*, 2011] to 64 hours [*Hassan et al.*, 2006], depending on the goals of the particular investigation. There is no widely accepted procedure for deriving flows to scale for use in unsteady flume experiments, and thus, several different approaches have been tested. For instance, *Lee et al.* [2004] applied Froude Number Law scaling with prototype flows taken from a typical storm hydrograph in their area to derive peak flow and hydrograph duration. In another approach, *Mao* [2012] did not specifically scale flows from a

prototype model. Rather, the author mimicked a range of hydrologic conditions, including high-magnitude, short-duration events and low-magnitude, long-duration snowmelt events, in an attempt to represent natural processes without following strict scaling procedures.

Several parameters have been used to characterize unsteady flow conditions in flume studies. The unsteadiness parameter initially proposed by *Graf and Suszka* [1985] quantified the unsteady nature of a hydrograph based on the change in water depth between base and peak flow conditions and the baseflow shear velocity (Equation 2.3.19):

$$P = \frac{h_p - h_{bf}}{t_d u_{*bf}} \quad (2.3.19)$$

where  $P$  is the dimensionless unsteadiness parameter,  $h_p$  is flow depth at the peak of the hydrograph (m),  $h_{bf}$  is flow depth at baseflow (m),  $t_d$  is duration of the hydrograph (s), and  $u_{*bf}$  is shear velocity at baseflow (m/s). This parameter has often been used to differentiate between hydrographs [e.g. *Yen and Lee*, 1995; *Song and Graf*, 1997; *Lee et al.*, 2004; *Bombar et al.*, 2011]. *De Sutter et al.* [2001] suggested that only the duration of the rising limb should be considered in hydrograph unsteadiness and proposed the following form of the unsteadiness parameter (Equation 2.3.20):

$$P = \frac{h_p - h_{bf}}{t_r [(U_{bf} + U_p)/2]} \frac{u_{*p}^2 - u_{*c}^2}{u_{*c}^2} \quad (2.3.20)$$

where  $t_r$  is duration of the rising limb (s),  $u_{*p}$  is shear velocity at peak flow (m/s),  $u_{*c}$  is critical shear velocity (m/s), and  $U_{bf}$  and  $U_p$  are measured velocities at base and peak flow (m/s), respectively. Another modification of this parameter used the concept of net

acceleration of flow on the rising limb to quantify hydrograph unsteadiness [Bombar *et al.*, 2011], as shown in Equation 2.3.21:

$$P_s = \frac{\left| gS_b - \left( \frac{U_p - U_{bf}}{t_r} \right) \right|}{g} \quad (2.3.21)$$

where  $P_s$  is a modified unsteadiness parameter,  $S_o$  is the bed slope, and  $g$  is the acceleration due to gravity. Total flow work, which is a measure of the total volume of water above baseflow in a hydrograph, has also been used to characterize experimental hydrographs, particularly in terms of the impact on sediment transport. *Lee et al.* [2004] defined this parameter as shown in Equation 2.3.22:

$$W_k = \frac{u_{*bf}^2 \forall}{(gh_{bf}^3 B)} \quad (2.3.22)$$

where  $W_k$  is a dimensionless total flow work index,  $\forall$  is total volume of water under the hydrograph excluding baseflow ( $m^3$ ), and  $B$  is the channel width (m).

### ***Hysteresis***

Sediment transport during unsteady flows often shows temporal variability during a flow event. This variability, in which sediment concentration differs for the same water discharge on the rising and falling limbs of a hydrograph, is referred to as hysteresis [Brownlie, 1981]. The existence of hysteresis means that sediment transport in unsteady flows generally cannot be approximated by quasi-steady flow conditions because there is no longer a one-to-one relationship between sediment and flow discharge [Ahanger *et al.*, 2008]. Different types of hysteresis transport exist. According to Williams [1989], there are five common classes of hysteresis loops: single-valued, clockwise, counter-clockwise, single-valued plus a loop, and figure-eight (Figure 2.3.1). The most common type of

hysteresis is clockwise, which occurs when more sediment transport is observed on the rising limb of a hydrograph than on the falling limb. Conversely, counterclockwise hysteresis occurs when greater sediment discharge occurs after the peak flow on the falling limb. While these two types of hysteresis are often classified based on whether peak sediment transport is observed prior to or after the peak flow, variable spreads and skewness of temporal sediment and water discharge graphs can result in hysteresis even for simultaneous peaks [Williams, 1989]. In general, hysteresis effects in sediment transport can result from a number of different factors and depend on type of river and transport mode, as discussed below.

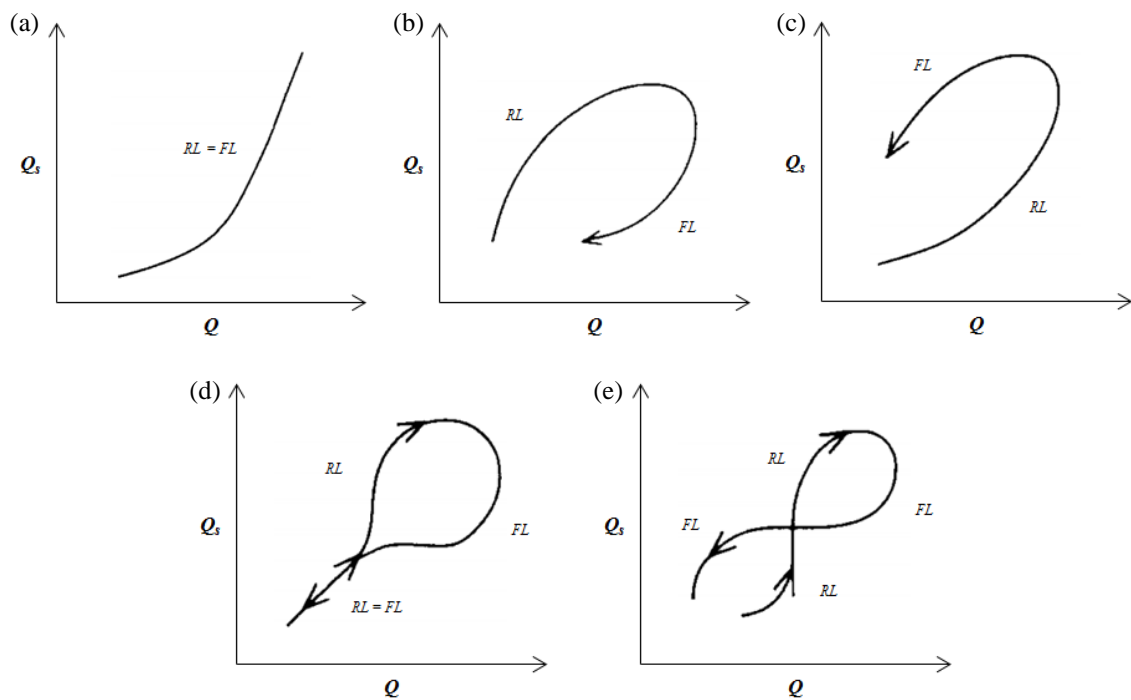


**Figure 2.3.1.** Example curves for the five common types of sediment transport hysteresis (adapted from Williams, 1989). Curves show qualitative loops for variation in transport rate ( $Q_s$ ) with flow rate ( $Q$ ). Arrows indicate flow direction, but RL and FL labels are provided for further clarification, indicating hydrograph rising and falling limbs, respectively. Curves correspond to following hysteresis behaviors: (a) single-valued (no hysteresis); (b) clockwise; (c) counterclockwise; (d) single-valued plus loop; and (e) figure-8 loop.

### ***Bed Load Transport***

Bed load transport in unsteady flow has commonly been reported to show counterclockwise hysteresis, with sediment transport lagging behind changes in flow [Humphries *et al.*, 2012]. Greater transport during the falling limb of a flood hydrograph has been attributed to a lag in the formation and destruction of bedforms between the rising and falling limbs in both sand [Lee *et al.*, 2004] and gravel-bed rivers [Kuhnle, 1992]. Differences in entrainment threshold resulting from variable flow conditions can also produce counterclockwise hysteresis. In the field, Reid *et al.* [1985] observed that sediment was more difficult to entrain during the rising limb of a flood because the bed had stabilized between large runoff events. Extended low flow periods preceding a flood event acted to consolidate the bed such that the rising limb loosened grains, but they were not fully entrained until after the flood peak. For sequential floods occurring with little time between them, grains were more easily entrained so greater bed load transport occurred during the rising limb [Reid *et al.*, 1985], highlighting the impact of antecedent hydrologic conditions on sediment transport.

Characteristics of an unsteady flow event can influence how much bed load is transported and potentially the hysteresis direction. Through an analysis of sediment yield, Bombar *et al.* [2011] showed that total sediment yield of uniform, small gravels increased linearly with total flow work but exponentially with increasing flow unsteadiness of triangular and trapezoidal hydrographs. Increasing sediment yields have been shown to correspond with hydrographs of a more unsteady nature over experimental sand beds [Lee *et al.*, 2004; Yen and Lee, 1995]. At sufficiently high peak flows, bed load transport rates may be greater on the rising limb of a hydrograph [Kuhnle, 1992], creating

a clockwise hysteresis that is contradictory to the expected pattern of bed load transport.

Channel complexity and sediment type further affects bed load hysteresis in unsteady flows and can contribute to clockwise hysteresis patterns. For instance, *Humphries et al.* [2012] reported a well-defined clockwise hysteresis of bed load transport through a forced bar flume morphology, attributing this to size-selective transport and potential pool-scour and fill during the hydrograph. *Mao* [2012] also reported clockwise hysteresis of bed load transport in a flume for a bimodal mix of sand and gravel subjected to a range of stepped hydrograph shapes. Consistent annual clockwise hysteresis was observed by *Moog and Whiting* [1998] for a range of sites with different channel morphologies, including riffle pools, planar beds, and step-pools, in which sediment stored after a previous storm event was diminished prior to a threshold discharge, producing higher transport earlier in the year.

Unsteady flow complicates bed load transport predictions and various approaches have been developed in an attempt to more accurately model such transport. Using flume data, regression analyses have modeled sediment yield as a function of an unsteadiness parameter and have obtained reasonable correlations. *Lee et al.* [2004] proposed a power law relationship to predict total bed load yield,  $W_t$ , based on their data (Equation 2.3.23):

$$W_t = 393.99P^{0.4189} \quad (2.3.23)$$

where  $P$  is defined in Equation 2.3.19. Similarly, *Bombar et al.* [2011] combined their data with *Qu* [2002] and found an exponential function (Equation 2.2.24) best fit the relationship between dimensionless total bed load,  $W_t^*$ , and unsteadiness parameter (as defined in Equation 2.3.21):

$$W_t^* = 1.04e^{983.66P_s} \quad (2.3.24)$$

where  $W_t^*$  is the dimensionless bed load yield given by Equation 2.3.25:

$$W_t^* = \frac{W_t}{\rho_s B D_{50}^2} \quad (2.3.25)$$

*Bombar et al.* [2011] also fit a linear relationship for dimensionless total bed load yield as a function of hydrograph flow work index (Equation 2.3.26):

$$W_t^* = 26.18W_k - 3.69 \quad (2.3.26)$$

In contrast to the use of regression analysis to derive transport relations based on hydrograph characteristics, direct corrections to theoretical, steady flow sediment transport relationships can be made for unsteady flows. One such example is based on the steady flow dimensionless bed load transport relationship described by Equations 2.3.27 through 2.3.29 [*Graf and Suszka*, 1987].

$$\Phi_A = 10.4K(\Psi_A)^{-1.5} \quad (2.3.27)$$

where  $\Phi_A$  is dimensionless bed load transport parameter and  $\Psi_A$  is the dimensionless flow intensity, given by Equations 2.3.28 and 2.3.29, respectively.

$$\Phi_A = \frac{(q_s/q)UR}{\sqrt{(s-1)gD^3}} \quad (2.3.28)$$

$$\Psi_A = \frac{(s-1)D}{S_e R} \quad (2.3.29)$$

where  $D$  is a representative grain diameter. The value of coefficient  $K$  is given for a range of flow intensities by Equation 2.3.30:

$$K = \begin{cases} \Psi_A^{-1} & \Psi_A \leq 14.6 \\ (1 - 0.045\Psi_A)^{2.5} & 14.6 < \Psi_A \leq 22 \\ 0 & \Psi_A > 22 \end{cases} \quad (2.3.30)$$

*Song and Graf* [1997] proposed a correction to this bed load transport by way of the unsteady flow shear velocity,  $u_{*,us}$ , which they applied to the dimensionless flow intensity, as shown in Equation 2.3.31:

$$\Psi_A = \frac{(s - 1)gD}{u_{*,us}^2} \quad (2.3.31)$$

When applying this correction to bed load transport rates measured in flume experiments, predicted rates showed good agreement with those measured.

### ***Suspended Load Transport***

Peak suspended load transport in unsteady flow commonly occurs prior to the peak discharge, resulting in clockwise hysteresis transport [*Humphries et al.*, 2012; *Asselman*, 1999; *Lenzi and Marchi*, 2000]. Clockwise hysteresis in suspended sediment transport is typically observed when the predominant sediment source is the channel alluvium [*Klein*, 1984], as sediment is initially eroded and entrained on the rising limb and settles out during the falling limb [*Asselman*, 1999; *Ahanger et al.*, 2008; *De Sutter et al.*, 2001]. Clockwise hysteresis also occurs due to early sediment supply from a tributary during a flood event, providing additional sediment to the main channel prior to the peak discharge [*Asselman*, 1999]. As with bed load, suspended load transport is linked to flow characteristics as hydrographs with higher unsteadiness will have larger suspended sediment transport capacity [*De Sutter et al.*, 2001]. The slope of the rising limb, analogous to flow unsteadiness, was also found to be an effective parameter in predicting suspended sediment yield [*Klein*, 1984]. As the unsteadiness of a hydrograph decreases,

the hysteresis loop closes, approaching transport conditions resembling those of constant flow [De Sutter *et al.*, 2001] or a single-valued loop in which sediment concentration is equal on the rising and falling limbs for the same discharge [Williams, 1989]. Though less common, counterclockwise hysteresis of suspended load transport can occur when the main sediment source is far from the channel [Klein, 1984; Lenzi and Marchi, 2000] or because of delayed bank failure following a flood wave [Ashbridge, 1995]. Different hysteresis patterns can even coexist during a single flood, depending on location and timing of sediment sources [Lenzi and Marchi, 2000].

Empirical relationships are often applied to predict suspended sediment transport rates for a specific set of flow and sediment conditions. These relationships are typically derived as rating curves, which represent the statistical relationship between suspended sediment concentration (SSC) and water discharge [Ahanger *et al.*, 2008]. Rating curves commonly take the form of a power law [e.g. Syvitski *et al.*, 2000; Walling, 1974, VanSickle and Beschta, 1983], as in Equation 2.3.32:

$$C_s = aQ^b \quad (2.3.32)$$

where  $C_s$  is suspended sediment concentration,  $Q$  is water discharge, and  $a$  and  $b$  are coefficients empirically derived through regression analysis. The suspended sediment discharge,  $Q_s$ , is related to the water discharge by the same rating coefficients [Ahanger *et al.*, 2008], as in Equation 2.3.33.

$$Q_s = aQ^{b+1} \quad (2.3.33)$$

Suspended sediment transports as a non-capacity load that displays temporal variation, making instantaneous transport rates a function of both the transport capacity of a river at a particular flow as well as sediment availability [Asselman, 1999]. VanSickle

and Beschta [1983] developed a supply-based model of suspended sediment concentration in time, expanding upon the standard power law function to incorporate a function to account for variable sediment supply (Equation 2.3.34):

$$C_s(t) = aQ(t)^b g[S(t)] \quad (2.3.34)$$

where  $g[S(t)]$  is a sediment supply function modeled as Equation 2.3.35:

$$g[S(t)] = p \exp \left[ r \frac{S(t)}{S_0} \right] \quad (2.3.35)$$

where  $S_0$  is initial sediment available for transport,  $S(t)$  is suspendable material present in channel at time  $t$ , and  $p$  and  $r$  are dimensionless calibration parameters determined empirically. The parameter  $r$  represents site sensitivity to hysteresis and accounts for bed composition and overall effectiveness of storages sites in retaining sediment [VanSickle and Beschta, 1983]. This model was applied to a site on the River Rhine over multiple floods spanning over approximately 3.5 years [Asselman, 1999]. Following calibration for the site, it was found that the supply-based model provided better instantaneous estimates of sediment concentration than a standard rating curve for higher discharges, but tended to underestimate concentrations in lower flows.

Doomen *et al.* [2008] used field data collected from the Meuse River to modify the traditional rating curve (Equation 2.3.32) by including a parameter the authors termed ‘sediment stock,’ which was designed to capture time-variable sediment storage in the channel. This sediment stock parameter,  $S$ , is a binary variable equal to zero when sediment stock is depleted and equal to one when sediment supply is available. The parameter is estimated using a flow threshold for sediment movement in the channel, with increasing stock for periods of low discharge, and depleting stock for higher flows

and flood events. The resulting rating curve (Equation 2.3.36) improved SSC predictions in comparison to the standard rating curve by 45%, and was found to be reliable over a range of discharge regimes, including single peak and multiple peak flood events.

$$C_s = (5.5 \times 10^{-5})Q^{0.245+1.96} + 7.8 \quad (2.3.36)$$

Suspended sediment transport hysteresis can be modeled by considering separate rating curves for the rising and falling limbs of a hydrograph in order to better describe temporal transport patterns. *Ahanger et al.* [2008] used this approach and expanded upon basic rating curves that depend solely on flow discharge, applying multivariate regression analysis to derive a rating curve for each limb as a function of flow and sediment characteristics. Following from a dimensional analysis, the authors proposed a final functional relationship for suspended sediment load (Equation 2.3.37):

$$\frac{q_s}{\rho_s g^{3/2} D^{3/2} \sqrt{\frac{\Delta \rho_s}{\rho}}} = f\left(\frac{U}{\Delta h / \Delta t}, \frac{S_e}{\Delta \rho_s / \rho}, \frac{h}{D}\right) \quad (2.3.37)$$

where  $\Delta \rho_s$  is  $(\rho_s - \rho)$  and  $\Delta h / \Delta t$  is rate of change of flow depth. Using flume experiments, regression relationships were developed for suspended sediment discharge on the rising (Equation 2.3.38) and falling (Equation 2.3.39) limbs:

$$\Psi = 5.316 \times 10^{-6} \left[ \frac{U}{\Delta h / \Delta t} \right]^{0.192} \times \left[ \frac{S_e}{\Delta \rho_s / \rho} \right]^{0.343} \times \left[ \frac{h}{D} \right]^{2.465} \quad (2.3.38)$$

$$\Psi = 8.510 \times 10^{-12} \left[ \frac{U}{\Delta h / \Delta t} \right]^{0.416} \times \left[ \frac{S_e}{\Delta \rho_s / \rho} \right]^{0.227} \times \left[ \frac{h}{D} \right]^{4.130} \quad (2.3.39)$$

where  $\Psi$  is the dimensionless sediment load parameter shown as the left-hand side of Equation 2.3.37. These regression relationships show the relative importance of various flow parameters on suspended sediment transport, as well as validate the prominent

clockwise hysteresis observed. In each case the relative flow depth,  $h/D$ , had the largest influence on transport rate [Ahanger *et al.*, 2008]. Although this approach did not explicitly include sediment storage, results were still able to satisfactorily predict suspended sediment transport in unsteady flows.

## **2.4 SEDIMENT TRANSPORT WITH VEGETATION**

### **2.4.1 Emergent Vegetation**

Vegetation-induced alterations to local hydraulics necessarily impact sediment transport dynamics, and do so at various scales. Reduced bed load transport capacity through simulated emergent vegetation has been attributed to increased drag from plant stems and the associated decrease in bed shear stress [Jordanova and James, 2003]. Transport rates can thus be calculated by incorporating the stem drag to account for the reduction in bed shear stress [e.g. Jordanova and James, 2003; James *et al.*, 2002]. Bottom shear stress reductions within vegetation are dependent on stem density [Bouma *et al.*, 2007] and as bed shear stress decreases, resuspension diminishes, promoting sediment retention within a canopy [Lopez and Garcia, 1998]. Additionally, reductions in turbulent kinetic energy due to increased biomass growth can enhance fine particle settling [Mudd *et al.*, 2010]. Thus, vegetated regions generally show a propensity for sediment trapping, deposition, and stabilization [Wu and He, 2009].

Sediment deposition and retention within vegetation has been measured in the field [e.g. Asaeda *et al.*, 2010; Gurnell *et al.*, 2006, 2010; Zierholz *et al.*, 2001], varying in volume with location and plant characteristics. For instance, Asaeda *et al.* [2010] documented a low sediment trapping efficiency for emergent stands of *Sparganium erectum* when compared to the sediment trapped by submerged or collapsed shoots in the

same lowland stream in Japan. In contrast, *Gurnell et al.* [2006] measured a larger average volume of fine sediment deposited around emergent plants than for submerged plants along the same river reach, finding that sediment retention in patchy vegetated areas is heavily influenced by species, arrangement, and biomass. In the case of in-stream wetlands, large amounts of fine sediment are trapped by plant stems, and accumulation volumes increase with wetland age [*Zierholz et al.*, 2001]. Due to the impact of vegetation on channel flow and fine sediment retention at the reach-scale, changes in growth patterns of in-channel vegetation can fundamentally affect stream morphology [*Asaeda et al.*, 2010].

#### **2.4.2 Vegetation Patches**

Sediment transport in and around emergent vegetation patches shows strong scale-dependent spatial effects. Localized sediment accretion generally occurs within the vegetation patch where flows and shear stresses are reduced, while flow acceleration around patches causes increased bed shear stresses and subsequent erosion in the adjacent unvegetated channel areas [e.g. *Bouma et al.*, 2009; *Temmerman et al.*, 2007; *Rominger et al.*, 2010; *Jones et al.*, 2011; *James et al.*, 2002]. Within a patch, bed load flux can vary spatially due to variations in near-bed turbulence intensities, resulting in scour zones near stems and depositional bedforms between them [*Yager and Schmeckle*, 2013].

Channel sediment sorting and changes in sediment size distribution are associated with patch-scale spatial processes, as finer sediment is typically predominant within patches [e.g. *Asaeda et al.*, 2010; *Cotton et al.*, 2006; *Sand-Jensen*, 1998; *Gurnell et al.*, 2006] and coarser sediment accumulates adjacent to patches where there are areas of increased flow velocity [*Sand-Jensen and Mebus*, 1996; *Gurnell et al.*, 2006]. Following

a flood event, *Tanaka and Yagisawa* [2010] documented grain size distributions upstream, inside, and downstream of clump-type vegetation *Salix subfragilis* on a gravel bar, finding that the finest material accumulated inside and downstream of the vegetation. The extent of sediment redistribution may be a direct function of stem density within the vegetated area [*Sharpe and James*, 2006; *Mudd et al.*, 2010], the bed sediment size distribution, and patch exposure [*van Katwijk et al.*, 2010]. Shear zones along the vegetation-water interface of longer emergent patches promote sediment influx into the patch by locally enhancing sediment diffusivity [*Sharpe and James*, 2006], although this enhanced turbulence can also result in diminished deposition at the patch edge [*Zong and Nepf*, 2010].

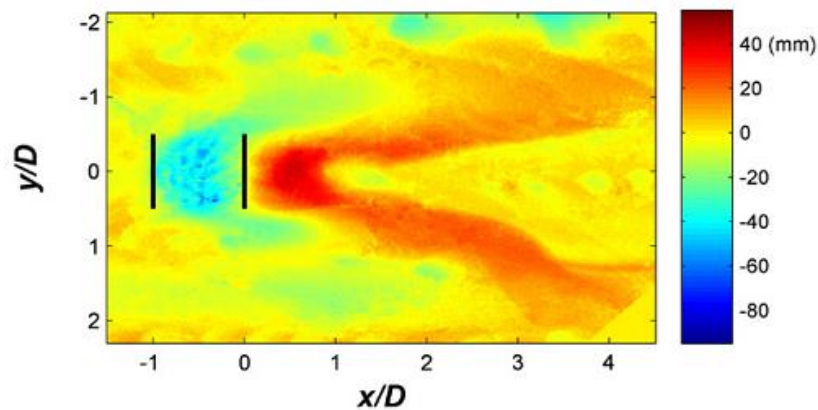
Several studies using simulated emergent stems documented a direct dependence of deposition on stem density within vegetation patches [*Sharpe and James*, 2006; *Zong and Nepf*, 2010, 2011; *Bouma et al.*, 2007]. Yet, erosion can also occur within a patch. Local bed scour can occur around individual stems that are irregularly distributed [*Asaeda et al.*, 2005] or where there are spatially variable bed load fluxes within the patch [*Yager and Schmeeckle*, 2013]. *Bouma et al.* [2007] measured net erosion at the leading edge of a dense patch as a result of elevated levels of turbulent kinetic energy, and a greater amount of within-patch erosion. Erosion at the seaward edge of an intertidal flat within a patch of *Spartina anglica* stems was also measured by *Widdows et al.* [2008], with the location of the erosion coinciding with enhanced turbulent kinetic energy and bed shear stresses. Scour can extend throughout an entire patch where higher turbulence levels are generated by increasing channel velocity and stem density [*Follett and Nepf*, 2012]. Thus, sediment transport through a vegetation patch is influenced by

vegetation density and type, as well as patch-averaged flow conditions [Yager and Schmeckle, 2013].

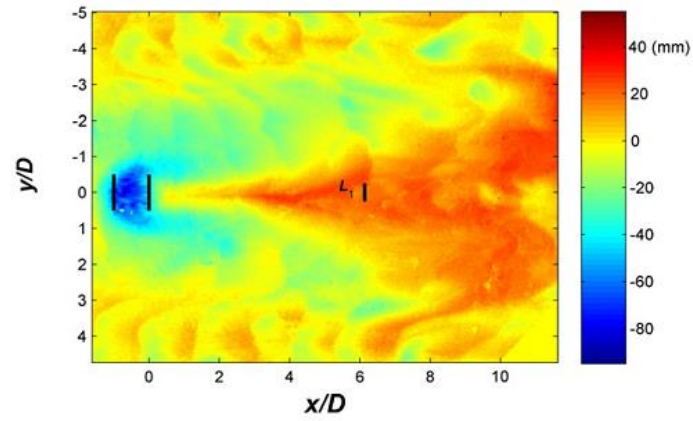
Deposition in the wake area downstream of isolated vegetation patches has been well documented. Fine sediment deposition encourages species succession [Zierholz *et al.*, 2001; Jones *et al.*, 2011] and sediment accretion downstream of patches is important to patch survival and longitudinal growth patterns [Sand-Jensen and Madsen, 1992]. Those species of emergent vegetation that grow in elongated patches aligned with the downstream flow direction are streamlined in shape, and thereby dissipate energy and reduce flow drag to remain intact [Asaeda *et al.*, 2005]. Deposition volumes downstream of patches vary with flow, sediment, and patch characteristics. James *et al.* [2002] reported from flume experiments that sediment volume in the lee of rectangular vegetation patches was inversely related to discharge such that increasing flow reduced the amount of deposited material. They proposed that an equilibrium volume of sediment exists around such patches, is determined by the discharge level, and is either approached via erosion or deposition depending on the upstream sediment supply. Field experiments by Bouma *et al.* [2007] confirmed enhanced sediment accretion in the area behind emergent patches and recent flume work has linked deposition in the lee of a circular emergent patch to wake length-scales for a range of stem densities [Follett and Nepf, 2012; Chen *et al.*, 2012].

Downstream of patches with varying stem density, Chen *et al.* [2012] found zones of net deposition approximately coinciding with the steady wake length,  $L_I$ , as defined by Zong and Nepf [2012]. However, beyond this scale net erosion zones were measured, roughly beginning at the patch wake formation length,  $L_w$ , which signifies the maximum

patch-scale turbulence. Thus, erosional and depositional zones were both present, with boundaries linked to the mean flow structure downstream of the patch. Testing patches in a uniform sand bed, *Follett and Nepf* [2012] found wake deposition patterns varied between two patch densities. For the sparser patch, the majority of sediment scoured from inside the patch was deposited within one patch diameter downstream. Additional deposition occurred downstream at the sides of the patch wake, showing a more diffuse depositional pattern reflective of the weak velocity gradients in that area, thus resulting in an open bed formation (Figure 2.4.1a). Conversely, a closed bed formation resulted from deposition in the wake of the denser patch, where the von Karman vortex street enhanced lateral transport, directing sediment towards the patch centerline to form a distinct mound-like depositional footprint (Figure 2.4.1b). Despite sediment redistribution around the patch, zero net deposition was measured over the reach-scale, defined as the patch diameter and total patch wake length [*Follett and Nepf*, 2012].



(a) Sparse patch.



(b) Dense patch.

**Figure 2.4.1.** Depositional patterns downstream of an emergent vegetation patch (from *Follett and Nepf, 2012*). Black horizontal lines indicate patch location and steady wake length,  $L_1$ . Distances are normalized by patch diameters. Color scales represent mean bed elevations.

## CHAPTER 3

### *Experimental Methods*

---

---

#### **3.1 INTRODUCTION**

The goals of this research were pursued through experimental flume work conducted in the Sustainable Rivers Laboratory (SRL) at the University of Virginia. This chapter describes the equipment used (Section 3.2), data collection and processing techniques and procedures (Section 3.3), experimental design and details (Sections 3.4 – 3.6), and experimental procedures (Section 3.7).

#### **3.2 EQUIPMENT**

##### **3.2.1 Flume**

Each experiment was conducted in a sediment and water recirculating flume (Figure 3.2.1), enabling controlled observation and direct measurements of scaled physical processes occurring through time between flow, vegetation, and sediment in an area analogous to the center of a natural channel. The flume is 11 m in total length, 0.6 m wide, and 0.5 m deep, with a working channel length of 9 m. The channel slope is adjustable up to a 5% grade and flow discharge is controlled by a variable frequency motor capable of flows up to 0.12 m<sup>3</sup>/s. Honeycomb meshes at the inlet dampen turbulence to facilitate flow adjustment. A downstream tailgate is used to control water depth in the channel. The sediment recirculation system used in each experiment is

controlled manually and utilizes a separate pump than the main water flow. This system recirculates slurry of water and sediment sizes finer than 16 mm from the downstream end of the flume back to the upstream inlet, where it reenters and is distributed across the channel width. Recirculation of sediment is restricted to grain sizes less than 16 mm in diameter; all sediment in these experiments was smaller than this threshold and thus, could be recirculated.



**Figure 3.2.1.** SRL water and sediment recirculating flume.

### ***Pump Calibration***

Flow rates were measured through the pump frequency with pump-flow calibration curves developed for these experiments. For a set pump frequency, velocity was measured at 3.5 m distance downstream from the flow entrance in the flume for 240 seconds at approximately 50% of the total water depth (+/- 2%) and was manually adjusted to maintain the relative measurement location during adjustments in flow rates and depths. This measurement depth was chosen to approximately correspond with the depth-averaged velocity of a vertical velocity profile taken over the smooth flume bottom. During calibration tests the tailgate height was fixed at a level that produced the desired baseflow depths. Flow depth was measured manually using a ruler on the side of

the flume at the same location as the velocity measurement for each pump frequency. Using these measurements pump frequency-flow discharge and water depth-pump frequency curves were developed for the range of flows to be tested. These calibration relationships (Appendix A.1) were used to set discharge throughout the experiments.

### **3.2.2 Acoustic Doppler Velocimeter**

Velocity measurements in these experiments were recorded using a Nortek Vectrino acoustic Doppler velocimeter (ADV). The Vectrino measures current velocity via the Doppler Effect; pulses are transmitted from the center transducer and the Doppler shift of particles in the water is registered by four probes to determine velocities [Nortek, 2009]. Thus, the device actually measures the velocity of the particles in the flow, rather than that of the flow itself [Nortek, 2009], but the assumption that the particle velocity is equal to the water velocity is valid for fine sediment traveling as washload [Hosseini *et al.*, 2006; Elci *et al.*, 2009]. ADV's have several advantages over other velocity measurement techniques, including robustness, capability to measure instantaneous 3D velocities at high sampling rates, a lack of calibration requirements, and portability [Khorsandi *et al.*, 2012]. Additionally, since the measurement sampling volume is approximately 5 cm below the probes [Nortek, 2009], measurements are collected non-intrusively in the flow [Nikora and Goring, 1998].

The primary ADV in the Sustainable Rivers Lab was mounted on a carriage platform above the flume (Figure 3.2.2a) which was controlled by three stepper motors, allowing for accurate placement in the streamwise, cross-stream, and vertical directions. The stepper motors were controlled through Velmex, Inc. COSMOS 3.1.6, which was automated using a LabVIEW program that also controlled ADV measurements. At each

measurement point, the ADV recorded instantaneous velocity at 25 Hz, which was later decomposed into time-averaged and fluctuating components to estimate mean and turbulent velocity statistics. Velocity range depended on the flow rate and sediment type, and was adjusted to maximize signal correlations. Specific ADV settings used for these experiments are given in Table 3.2.1.

**Table 3.2.1.** Vectrino settings.

Setting	Value
Sampling Rate (Hz)	25
Nominal Velocity Range (m/s)	0.3/1.0
Transmit Length (mm)	1.8
Sampling Volume Height (mm)	7.0



(a) Primary ADV on cart.



(b) Secondary ADV mounting.

**Figure 3.2.2.** Acoustic Doppler velocimeter mounted in flume.

For some experiments a secondary ADV was used and was located 1.5 m downstream of the first ADV (Figure 3.2.2b). The second ADV was attached to the side of the flume and, although the mounting system was stationary, the ADV was affixed to a manually adjustable vertical shaft with an electronic scale for reading relative distances. This ADV was operated independently of the primary ADV.

### 3.2.3 Laser Profiler

A Micro-Epsilon scanCONTROL laser profiler (Model LLT2800-100) was used to collect detailed measurements of the channel bed topography. This profilometer uses laser triangulation to determine distance to the bed, registering 1024 points per profile in the cross-stream direction. The vertical resolution of the profiler is 40  $\mu\text{m}$  [*Micro-Epsilon*, 2008] ensuring bed measurements detailed enough to develop high resolution digital elevation models (DEMs) for bed analysis and calculation of statistical metrics. In the SRL, this profiler is mounted to the same carriage as the primary ADV and, through LabVIEW automation, traverses the flume in a similar manner in order to collect the bed measurements over a specified area of the flume (Figure 3.2.3). Five individual scans are required to span the full flume width and are positioned to maintain approximately 1 cm of overlap between adjacent scans. All five scans are combined to create a full DEM of the channel bed using the post-processing techniques discussed in Section 3.3.2.



**Figure 3.2.3.** Laser profiler collecting measurements over sediment bed.

### 3.2.4 Bed Monitoring System

The flume was equipped with a continuous bed monitoring system, located beneath a false bottom constructed of 1 m by 0.60 m plexiglass boards (Figure 3.2.4).

This system provided for a complete analysis of sediment redistribution occurring during an experiment, especially when fine sediment in suspension precluded visual observation and measurement of the bed. The system operated in streamwise segments that were 1-meter long, with each segment comprised of a bicycle inner tube filled with water located beneath the plexiglass board and connected to a pressure transducer (Omegadyne, Inc., model no. PXM409-001BGV, pressure range 0-1 bar). Transducers at each location continuously recorded voltages that corresponded with pressure changes that were read into a data acquisition program in LabVIEW Signal Express 2012 (Version 6.0.0) as analog input. Measurements were collected at a frequency of 1000 Hz resulting in data output every 0.10 seconds. Signals were time-averaged using exponential weighting to a running average of 10 samples. Output data was processed in MATLAB (Section 3.3.3) to convert voltage to weight using calibration curves developed prior to the experiments.



**Figure 3.2.4.** Bed monitoring system overhead view without sediment.

### ***Transducer Calibration***

The bed monitoring system was calibrated prior to each group of experiments. Plates were placed on each 1-meter segment of the system in 27.2 kg increments and voltages recorded over 60 seconds for total weights ranging from 27.2 to 272.2 kg. Two

measurements were recorded for each weight and each transducer. The two time-averaged voltage outputs were plotted against the known weights to develop calibration relationships between load and voltage. Separate relationships were developed for each of the six transducers. Both linear and quadratic equations were fit to the data and it was determined that the quadratic calibration relationships produced slightly better regression correlations. Quadratic curves were of the form shown in Equation 3.2.1:

$$w_l = A(\text{volt})^2 + B(\text{volt}) + C \quad (3.2.1)$$

where  $w_l$  is load (kg),  $\text{volt}$  is voltage signal (mV), and  $A$ ,  $B$ , and  $C$  are calibration coefficients determined through least squares non-linear regression. In all cases the calibration curve fits were very high (Table 3.2.2).

**Table 3.2.2.** Bed monitoring system calibration results.

Flume Segment	<u>1st Calibration</u>				<u>2nd Calibration</u>			
	<i>A</i>	<i>B</i>	<i>C</i>	<i>R</i> <sup>2</sup>	<i>A</i>	<i>B</i>	<i>C</i>	<i>R</i> <sup>2</sup>
3m	38,674	9,175	-79.2	0.9997	-4,466	11,162	-119.8	0.9971
4m	48,093	9,040	-80.7	0.9998	59,579	8,958	-91.1	0.9990
5m	72,319	8,393	-69.7	0.9999	56,153	8,950	-119.2	0.9993
6m	22,328	9,994	-118.8	0.9998	35,514	9,573	-124.3	0.9999
7m	64,866	8,144	-99.4	0.9998	56,033	8,305	-121.0	0.9999
8m	41,550	9,533	-88.4	0.9999	35,010	9,638	-133.3	0.9996

Figure 3.2.5 shows an example load calibration curve for flume segment 5 m (second segment downstream of the patch location). This curve is typical of the calibration curves developed for the bed monitoring system (Appendix A.2).

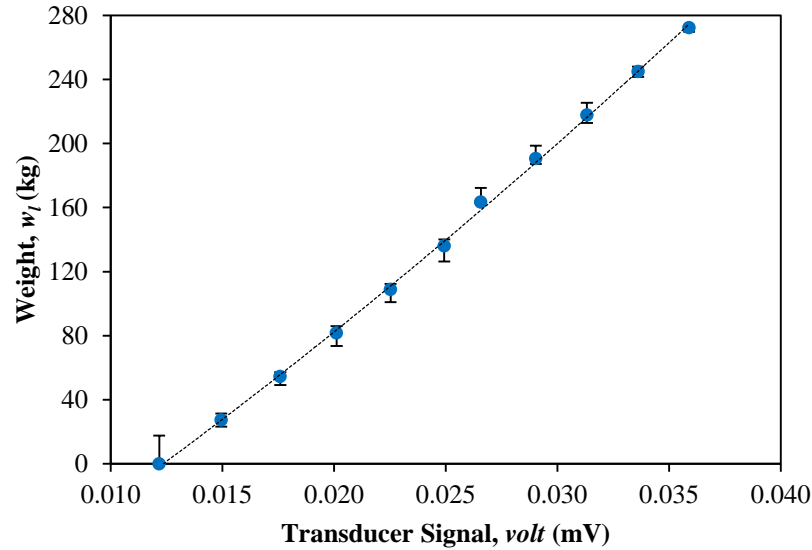
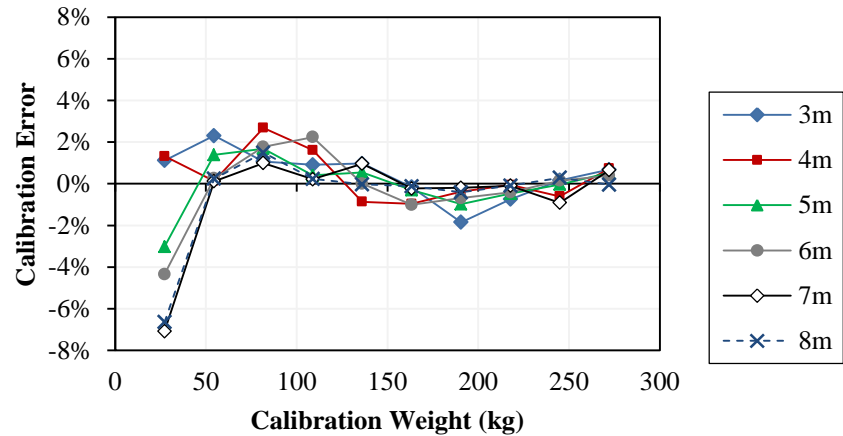


**Figure 3.2.5.** Transducer calibration curve for flume segment 5 m (second calibration). Error bars are determined by minimum and maximum signal measurements. Dashed line represents calibration curve given by equation:  $w_l = 56,153(\text{volt})^2 + 8,950(\text{volt}) - 119.2$ .

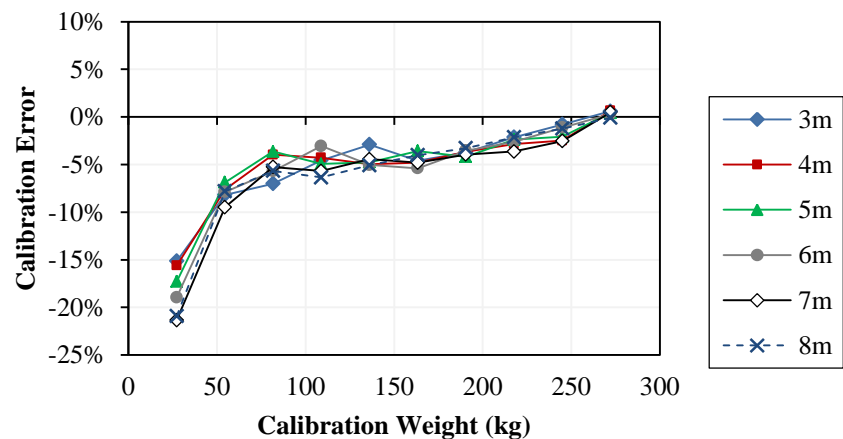
### *Error Analysis*

Because two signal records were recorded for each weight, the variability of the transducers in the bed monitoring system could be evaluated using each signal as a lower or upper uncertainty bound. These bounds were used to approximate the error associated with a given transducer reading across the range of weights tested. Mean voltage signals from the transducers predicted the load in the overlying system to within +/- 0.55% of the actual weight for the first calibration. This was reflective of the strong fit of the calibration curves to the mean data points. When the lower and upper voltages were applied to the calibration curves, the results were loads that were +/- 5.3% of the actual weight on a given flume segment. Calibration predictions improved as the weight on a given transducer increased (Figure 3.2.6a). For weights over 156 kg, which is roughly equal to the initial weight of sediment in the flume at each segment, the calibration curves showed strong predictive ability indicating reliable readings from the transducers. This

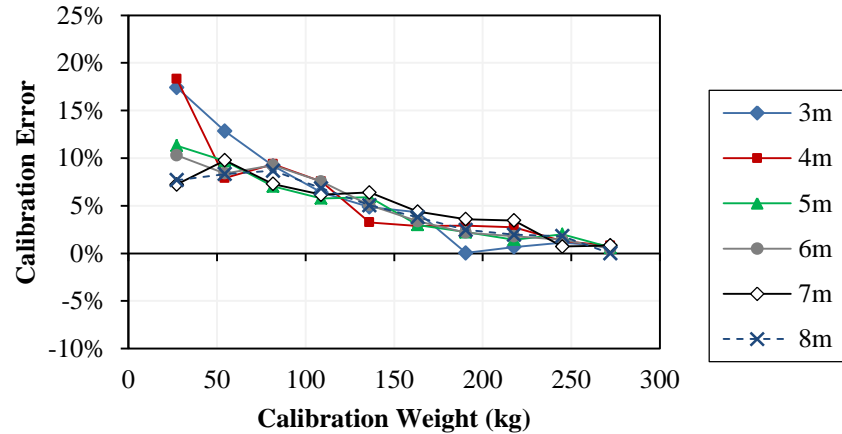
was true for both the mean signals used to develop the calibration curves as well as the upper and lower signals used to quantify predictive variability (Figure 3.2.6b-c). Considering only those predictions for weights over 156 kg, the error for the first transducer calibrations was approximated as -0.25% using the mean values, or between -2.5% and +2.0% according to the bounds. Error analysis for second round of transducer calibrations followed the same methodology and showed similar results, with error of -0.30% for the mean calibration curves and a range between -3.0% and +2.5% for the low and high signal predictions, respectively.



(a) Mean signals.



(b) Low signals.



(c) High signals.

**Figure 3.2.6.** Transducer calibration errors (first calibration).

### *Slope Calculation with Bed Monitoring System*

Transducer readings were converted to weight and broken into four minute segments to correspond with each constant flow interval. An averaging window from 2.83 min to 3.83 min was applied to each record to obtain a representative average weight while allowing for initial flow and bed slope adjustment. This window was selected following manual investigation of numerous transducer records that showed greatest signal change in the first 2 minutes of a record. Total sediment weights for each flume location and time interval were adjusted to account for overlying water weight then converted to mean sediment depth using sediment density and flume width. A linear regression of sediment depths over the downstream 6 m flume distance provided an estimate of reach bed slope for that flow interval.

Where water penetrated the bed monitoring system, water filled the area beneath the false flume bottom causing the false bottom to be supported in part by the water. Thus, calibration relationships did not provide accurate estimates of the total load because they were not developed under such conditions. However, they still provided

meaningful estimates in terms of relative changes through time, enabling calculation of slope ratios (Equation 3.2.2):

$$SR^j = \frac{S_T^j}{S_T^{j-1}} \quad (3.2.2)$$

where  $SR$  is slope ratio,  $S_T$  is bed slope from the transducer signal, and superscript  $j$  is flow interval ( $j = 2$  to 19). Slope ratios were applied in succession with Equation 3.2.3:

$$S_b^j = SR^j \times S_b^{j-1} \quad (3.2.3)$$

where  $S_b$  is bed slope. Known bed slope extracted from the DEM prior to a hydrograph was used as the initial starting point for the application of slope ratios. Thus, DEM bed slopes were essentially used as calibration points to scale the relative transducer signals into temporal estimates of bed slope. Overall, this method yielded improved estimates of bed slope over alternative methods (i.e. rulers on the side of the flume).

### 3.3 DATA PROCESSING

#### 3.3.1 Velocity Data

Raw velocity data measured by the ADV were recorded to binary files and converted to ASCII files using Nortek's Vectrino Plus software. The data were then processed in MATLAB using a script developed by the author (Appendix B.1). Data processing involved three filtering techniques: despiking, correlation filtering, and a low pass filter. Despiking was done using the 3D phase-space thresholding despiking algorithm proposed by *Goring and Nikora* [2002]. This method identifies spikes in the velocity time-series and fits a cubic polynomial to 12 points on either side of a spike, interpolating a new data point to replace it. The functions necessary to perform this

algorithm were obtained via the MATLAB Exchange [Mori, 2007]. The second filter was based on signal correlation of the ADV record. Data points in which the signal correlation was less than 70% in any of the four transducers were dropped and the time series shortened accordingly. Using a 70% correlation threshold is recommended by the manufacturer [Nortek, 2009]. To avoid aliasing errors the velocity records were also filtered with a third-order Butterworth low-pass filter, as done by Lacey and Roy [2007]. A half-power frequency of 8.53 Hz was applied, determined as the sampling frequency (25 Hz) divided by 2.93, as suggested by Roy *et al.* [1997]. The MATLAB code used to process the ADV data is summarized below:

- (a). Import raw data from text files for each measurement using directory search and cell creation at each measurement location.
- (b). Despikie raw data using *Goring and Nikora* [2002] method, outputting new velocity time series with spikes removed and percent of spikes detected.
- (c). Filter despiked data based on specified correlation threshold (70%), removing low correlation data and outputting new velocity time series and percentage of data removed.
- (d). Filter despiked, correlation-filtered data with third order Butterworth filter, outputting new velocity time series.
- (e). Calculate mean velocities and turbulence intensities in all three directions of filtered time series.
- (f). Combine results into a single output matrix that includes mean velocities, turbulence intensities, and filtering statistics (i.e. relative number of points filtered) for each measurement location.

### 3.3.2 Bed Scans

#### *Scan Processing*

Raw data from the laser profiler was the cross-stream distance ( $y$ ) and distance from the laser to the channel bed, which was inverted to determine bed elevation ( $z$ ). Scans were conducted with the flume at zero slope and scanner at a constant distance above the flume to maintain the same datum for each run set. Raw scanner data was first manually inspected and clipped at the upstream and downstream ends of the scans to eliminate any scan length outside the specified reach. These clipped data files were then pre-processed using a MATLAB script (Appendix B.2) using the following procedure:

- (a). Import raw  $y$  and  $z$  data from text files using a function developed through MATLAB code generation of the import data command, replacing empty cells with NaN (not-a-number) values.
- (b). Calculate number of profiles and points per profile.
- (c). Process scans individually to transform  $y$  and  $z$  data into useable formats and shift scans to proper location within flume relative to other scans.
- (d). Calculate  $x$ -coordinates for each scan based on the total number of profiles in the scan and the total distance covered, which was approximately 6.1 m.
- (e). Develop coordinates for each scan point by combining the  $x$ -points with the  $y$  and  $z$  data for each scan. Filter points using several criteria, including NaN points, low elevation outlier points, and high elevation outlier points (which include plant stems, where applicable).
- (f). Write remaining  $(x,y,z)$  points to separate comma-delimited text files for each individual scan.

Scan post-processing was performed in ArcGIS, utilizing several built-in tools. A model developed in Model Builder automated the scan processing tasks required to create a full DEM raster from the elevation data points pre-processed in MATLAB. A work flow diagram of the model is included in Appendix B.3 and the steps are summarized below:

- (a). Create point feature classes for each scan from the comma-delimited point files created through MATLAB pre-processing using “ASCII 3D to Feature Class” tool.
- (b). Assign coordinates to point features using “Add XY Coordinates” tool.
- (c). Create individual DEM rasters from point features using “Natural Neighbor Interpolation” tool with a cell size of 0.4 m in the  $x$ - and  $y$ -directions. Processing extents are specified as 13 m to include points nearer the center of the respective scans, remove outliers in the cross-stream direction, and allow for 1 m of overlap between adjacent scans.
- (d). Combine all five DEM rasters using “Mosaic to New Raster” tool with a “mean” mosaic operator. This option combines elevations in overlapping raster cells using the average cell value in the overlapping area.

### ***DEM Analysis***

DEM rasters were analyzed by subtracting one DEM from another in ArcGIS by means of the “Cut Fill” tool in the 3D Analyst Toolbox. This process produced difference maps between two DEMs and calculated changes in volumes on a per grid basis. A model was developed in Model Builder to automate this process, which was carried out in 1-m flume segments that coincided with the bed monitoring system (Section 3.2.4). A work

flow diagram of the cut/fill model is included in Appendix B.3 and summarized below:

- (a). Specify initial and final DEM rasters.
- (b). Run “Cut Fill” tool for each meter segment to create a new raster and data table with volume calculations. A  $z$ -factor of 0.001 is applied to convert the elevation data from units of millimeters to meters.
- (c). Select data table using the “Table Select” tool and export to a standalone table that is later analyzed using Microsoft Excel.

### **3.3.3 Bed Monitoring System**

Raw signal data recorded by the transducers in the bed monitoring system were post-processed in MATLAB using a function developed by the author (Appendix B.4), which is summarized below:

- (a). Import raw data text file.
- (b). Compute time array based on total recording time and output frequency.
- (c). Convert signals to weight using individual calibration curves for each flume segment of the monitoring system.
- (d). Plot results and write to a text file.

## **3.4 MODEL VEGETATION**

### **3.4.1 Model Details**

Vegetation used in these experiments modeled softstem bulrush (*Schoenoplectus tabernaemontani*), an emergent plant commonly found in rivers and marsh areas, and popular in river restorations [Hall, 2003]. Numerous past studies on sediment transport through emergent vegetation have used cylinders to model vegetation stems [e.g. Zong and Nepf, 2010, 2011; Sharpe and James, 2006; Jordanova and James, 2003], which are

geometrically similar to many reedy plant species, including softstem bulrush. Therefore, cylindrical stems were used here to maintain geometric similarity with actual bulrush as well as likeness with similar studies.

The model vegetation was created using a 3D printer in the Rapid Prototyping Lab in the Mechanical and Aerospace Engineering Department at the University of Virginia, and printed with ABS plastic (modulus of elasticity of  $E = 2.25 \cdot 10^9$  Pa). The patch was designed in AutoCAD prior to printing, with separate components for the stems and patch base. The stem model design included four small knobs on the stem bottom as part of a locking system to secure the stems in notches within the patch base (Figure 3.4.1). CAD design of the patch ensured direct control over stem location, density, and distribution.

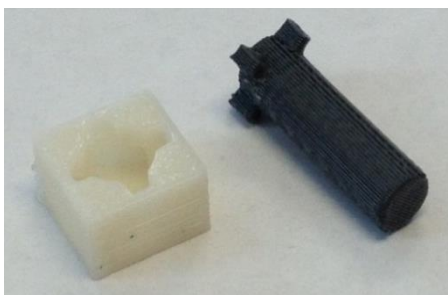


**Figure 3.4.1.** Stem (black) and base (white) model locking mechanism design.

### 3.4.2 Scaling

Three primary forces act on an emergent plant stem in flowing water. Drag force ( $F_D$ ) on the stem acts in the same direction of the flow, pushing the stem downstream. Stem buoyancy ( $F_B$ ) and rigidity ( $F_R$ ) forces counteract the drag force to keep the stem in place, whether erect or slightly bent in the flow. Scaling of artificial vegetation in the past has employed ratios of these three forces to determine a scaling factor for the model [i.e. *Nepf and Vivoni, 2000*]. To evaluate the relative contributions of forces for purposes of

dynamic scaling, buoyancy force and drag force were compared between field (prototype) and model conditions for constant flow velocity and variable water depth. Buoyancy was of greater magnitude than drag force across a range of flow depths for an average low flow velocity in the field, highlighting the importance of buoyancy in lower flows. However, higher drag forces were calculated as depth increased with flow. Because high flow conditions govern the stem scaling, buoyancy was neglected while stem rigidity was used as a critical design parameter. Dynamic similarity between the model patch and field conditions is achieved by matching the ratio of drag to stem rigidity, similar to the approach *Nepf and Vivoni* [2000] applied to submerged plant models. Initial sizing of the model plant stems was scaled based on this ratio (Equation 3.4.1).

$$\frac{\text{Drag}}{\text{Rigidity}} = \frac{F_D}{F_R} = \frac{U_p^2 d_p h_p^3}{E_p I_p} = \frac{U_m^2 d_m h_m^3}{E_m I_m} \quad (3.4.1)$$

where  $U$  is mean flow velocity (m/s),  $d$  is stem diameter (m),  $h$  is mean flow depth (m),  $E$  is stem modulus of elasticity (Pa) and  $I$  is second moment of inertia of the stem cross-section ( $\text{m}^4$ ), with subscripts  $p$  and  $m$  denoting prototype and model parameters, respectively. Measured values of stem modulus of elasticity from two field studies [*Chapman and Blickenderfer*, 2011; *Coops and Van der Velde*, 1996] were averaged to obtain a representative modulus of elasticity value of  $7.0 \times 10^8$  Pa. A softstem bulrush stem diameter of 10 mm, an average value reported in the field by *Coops and Van der Velde* [1996], was used for the prototype stem dimension. Flow velocity and depth values from areas in which emergent vegetation has been documented and studied [*Cotton et al.*, 2006; *Rominger et al.*, 2010; *Bouma et al.*, 2007] provided representative values for

scaling purposes ( $U = 0.6$  m/s;  $h = 0.4$  m). Applying the above methodology, model plant stem diameter for dynamic similarity was calculated as approximately 3.0 mm.

Preliminary tests with a 3.0 mm diameter model stem in flowing water revealed significant lateral stem oscillation. This oscillation is attributed to alternate vortex shedding at stem Reynolds numbers ( $Re_d = d_{stem}U/\nu$ ), greater than approximately 80 [Kundu and Cohen, 2008, p.370], which is the range within which field and experimental conditions fall. Consequently, a modified scaling analysis was conducted for similarity of stem oscillation and vortex shedding frequency based on the Strouhal number,  $S_t$ , which is defined as  $S_t = nd/U$ , where  $n$  is the frequency of vortex shedding and  $S_t$  is a function of  $Re_d$  [Kundu and Cohen, 2008, p.371]. To obtain kinematic similarity between experimental and natural stems,  $n$  for the prototype and model must be equal. Scaling based on Strouhal number reduces to ratios of stem diameter to flow velocity for the model and prototype (Equation 3.4.2):

$$\frac{d_p}{U_p} = \frac{d_m}{U_m} \quad (3.4.2)$$

Consistent with the initial scaling analysis, an average softstem bulrush stem diameter of 10 mm was used with average flow velocity in aquatic vegetation for the prototype. An experimental flow velocity of 0.34 m/s was assumed. Applying these values in Equation 3.4.2, the required model stem diameter was 5.4 mm.

The stem- and patch-scale turbulent structures generated by the model vegetation were emphasized in these experiments, making it more important to design the model plants to maintain similarity in wake and vortex behavior than to match model and prototype rigidity. Furthermore, neither natural nor model stems were bent during

preliminary tests (Figure 3.4.2), allowing the drag/rigidity scaling criterion to be relaxed. Thus, the model plant diameter used in these experiments was determined by the Strouhal number scaling analysis as 5.4 mm.



**Figure 3.4.2.** Preliminary scaling test results: vortex formation behind natural and model stems in flow.

### 3.4.3 Patch Characteristics

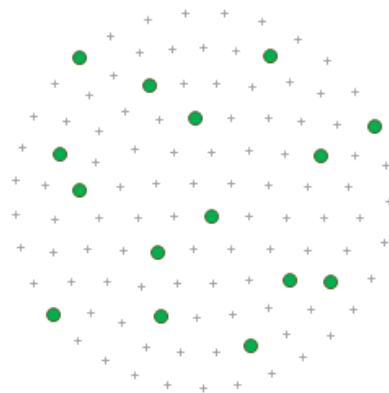
Patch diameter ( $D_p$ ) was held constant at 12 cm in all of the experiments, covering the middle 20% of the channel width. Stem density was characterized by the patch solid volume fraction,  $\varphi$ , which is calculated for a circular patch with Equation 3.4.3:

$$\varphi = \frac{m\pi d^2}{4} \quad (3.4.3)$$

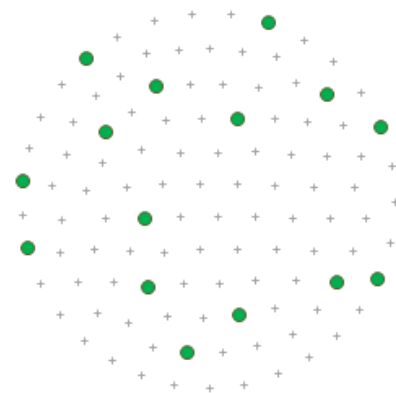
where  $m$  is the number of stems per patch area (stems/m<sup>2</sup>) and  $d$  is the stem diameter (0.0054 m). Two stem densities ( $\varphi = 0.03, 0.10$ ) were tested as these are consistent with a range of field conditions for plants with similar morphology as bulrush [e.g. *Asaeda et al.*, 2005] and are known to produce different wake structure [*Zong and Nepf*, 2012] and depositional patterns around patches [*Follett and Nepf*, 2012]. The number of stems per patch was determined by the required solid volume fraction, the stem diameter and the overall patch diameter of 12 cm. A circular mesh generator MATLAB code [*Persson and Strang*, 2004] was used to construct a grid within the patch diameter with approximately

equal point spacing. A random number generator was then utilized to determine stem locations within this grid (Figure 3.4.3). Using a criterion that each quadrant of the patch contained a minimum of 20% of the total amount of stems (3 and 10 stems per quadrant for the sparse and dense patches, respectively), random stem configurations were generated until this requirement was met. The final patches with  $\phi$  of 0.03 and 0.10 comprised 15 and 49 stems, respectively (Figure 3.4.4).

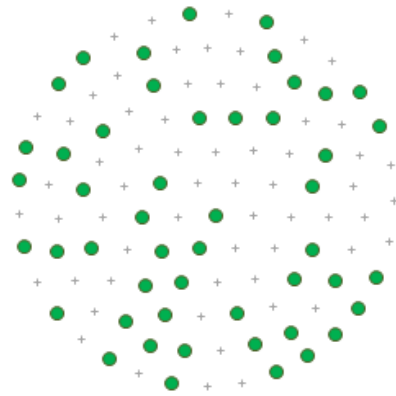
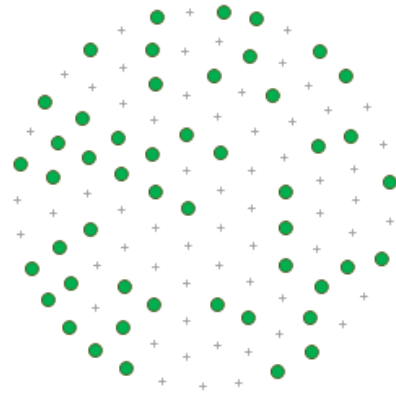
Due to the randomness of the stem locations and its potential impact on the flow field around the patch, two different configurations (designated as patch A and patch B) were tested in the no sediment (flow only) experiments for each stem density (Figure 3.4.3). For sparse patch B, the stem arrangement was developed as discussed above. Stem locations for the dense patches were the same, but patch B was rotated 90-degrees clockwise from dense patch A to provide a different configuration relative to the upstream flow (Figures 3.4.3c and 3.4.3d). This approach was taken because the stem locations for configuration A were specified within the base through the 3D printing process and therefore could not be changed once the model was printed.



(a) Sparse patch A ( $\phi = 0.03$ ).



(b) Sparse patch B ( $\phi = 0.03$ ).

(c) Dense patch A ( $\varphi = 0.10$ ).(d) Dense patch B ( $\varphi = 0.10$ ).

**Figure 3.4.3.** Random stem configurations (plan view; flow direction left to right). Green circles represent individual model plant stems; gray pluses represent grid points and potential stem locations.

(a) Sparse patch A ( $\varphi = 0.03$ ).(b) Dense patch A ( $\varphi = 0.10$ ).

**Figure 3.4.4.** Printed model patches.

### 3.5 DESIGN FLOWS

#### 3.5.1 Steady Flows

A series of experiments was conducted under steady flows without a sediment bed in the flume to allow for detailed hydraulic measurements over a range of four flow rates.

The first two steady flow rates tested had mean channel velocities of approximately  $U = 0.10$  and  $0.32$  m/s, Froude numbers ( $Fr$ )  $0.10$  and  $0.30$ , and were designated as low (L) and high (H) baseflows, respectively. These Froude numbers were selected to reflect flows observed in the field where emergent and submerged vegetation have been documented [ $Fr = 0.10$ : Wharton *et al.*, 2006; Cotton *et al.*, 2006; Hung *et al.*, 2007; Baattrup-Pedersen and Riis, 1999; Naden *et al.*, 2006; Nikora *et al.*, 2008; Gurnell *et al.*, 2006; Asaeda *et al.*, 2010; Lightbody and Nepf, 2006; Sand-Jensen and Mebus, 1996; Sand-Jensen and Pedersen, 2008; Rominger *et al.*, 2010; Bouma *et al.*, 2007; Wilcock *et al.*, 1999; Kemp *et al.*, 1999; Schulz *et al.*, 2003; Power, 1996;  $Fr = 0.30$ : Cotton *et al.*, 2006; Wharton *et al.*, 2006; Kemp *et al.*, 1999; Schulz *et al.*, 2003; Rominger *et al.*, 2010; Bouma *et al.*, 2007]. Flow depth for steady baseflow experiments was held constant at  $h = 11.0 \pm 0.2$  cm for both low and high conditions. The second two steady flows were derived as multiples of these baseflow rates, simulating peak flow conditions. Consistent tailgate height allowed for flow depth adjustment above the baseflow depth in both cases.

### **3.5.2 Unsteady Flows**

#### ***Baseflow***

Flow rates in unsteady flow, sediment transport flume studies are typically designed such that conditions of incipient motion of the median grain size are approximately satisfied at the baseflow rate and water depth [e.g. Lee *et al.*, 2004; Bombar *et al.*, 2011]. The baseflow for the unsteady experiments was designed to attain a small but measurable transport rate of the sand fraction. An additional criterion for these experiments was water depth large enough to collect representative velocity measurements with the ADV. This was a constraint because the sampling volume of the

ADV is approximately 5.0 cm below the probe, and under insufficient water depth velocity measurements would be taken too close to the bed to be reliable.

The baseflow rate ( $Q_{BF}$ ) for the unsteady flow experiments was set at  $Q_{BF} = 0.0174$  cms with a corresponding water depth of 8.0 cm +/- 0.2 cm. Velocity measurements at baseflow were recorded at approximately 40% of the water column depth, as measured from the bed, which was equal to 0.36 m/s for the design baseflow. The baseflow Froude number was 0.41, which is higher than the flows scaled from the field described in Section 3.5.1. This was partly due to an increase in flow velocity for an initial flume slope of 0.10% which was used to facilitate sediment movement. Ensuring sediment movement at baseflow was deemed more important than strict Froude number scaling given the emphasis on sediment transport. The design baseflow discharge, unit discharge, water depth, and Froude number all fall within ranges of previous unsteady transport studies (Table 3.5.1).

**Table 3.5.1.** Baseflow parameters from unsteady flow, sediment transport studies.

Study	$D_{50}$ (mm)	$Q$ (m <sup>3</sup> /s)	$q$ (m <sup>2</sup> /s)	$h$ (m)	$U$ (m/s)	$Fr$ (-)	$S$ (-)
<i>Bombar et al.</i> [2011]	4.80	0.0120	0.0150	0.040	0.38	0.60	0.005
	4.80	0.0120	0.0150	0.070	0.21	0.26	0.005
<i>Guney et al.</i> [2013]	3.40	0.0095	0.0119	0.050	0.24	0.34	0.006
	3.40	0.0095	0.0119	0.060	0.20	0.26	0.006
	3.40	0.0095	0.0119	0.072	0.16	0.20	0.006
	3.40	0.0095	0.0119	0.080	0.15	0.17	0.006
<i>Lee et al.</i> [2004]	2.08	0.0240	0.0400	0.088	0.45	0.49	0.002
<i>Mao</i> [2012]	6.20	0.0093	0.0310	0.051	0.61	0.86	0.010
<i>Yen and Lee</i> [1995]	1.00	0.0200	0.0250	0.054	0.46	0.63	0.002
This study	0.55	0.0174	0.0290	0.080	0.36	0.41	0.001
	0.27	0.0174	0.0290	0.080	0.36	0.41	0.001

### ***Hydrographs***

Stepped hydrographs are used to simulate unsteady flows in flumes [e.g. *Martin and Jerolmack*, 2013; *Mao*, 2012; *Hassan et al.*, 2006; *Parker et al.*, 2008; *De Sutter et al.*, 2001]. For this study, two stepped hydrographs were constructed with 17 flow intervals of constant flow rate: five intervals on the rising limb, one at the peak flow, and eleven intervals on the falling limb. Each flow interval lasted for four minutes, and the unsteady flow hydrographs had a total duration ( $t_d$ ) of 68 minutes with a time to peak ( $t_p$ ) of 22 minutes. An additional four minute baseflow period was run prior to and immediately following each hydrograph. Short flow duration intervals ensured that the stepped flow approach realistically modeled a natural hydrograph and its unsteady nature. Temporal characteristics of the two hydrographs were the same, isolating the effect of flow magnitude.

Relative flow magnitudes of each four minute interval were derived using the NRCS curvilinear dimensionless unit hydrograph [*NRCS*, 2007] over a duration from the onset of flow at  $t/t_p = 0$  to  $t/t_p = 3.0$ , where  $t$  is the experiment time (Figure 3.5.1). From the mass curve for the NRCS dimensionless unit hydrograph, which is a ratio of cumulative runoff volume to the total volume [*Jeng*, 2006], the end time corresponded to a hydrograph ordinate at which 97.7% of the total runoff volume has occurred. Flow has decreased to 5.5% of the peak flow at this time [*NRCS*, 2007] so the discretized hydrograph models the majority of an unsteady flow event and neglects the final low flow stages just prior to returning to baseflow. In addition to replicating the shape of the NRCS curvilinear unit hydrograph, the asymmetry represented by this stepped hydrograph model is consistent with Snyder's synthetic unit hydrograph and the NRCS

dimensionless triangular unit hydrograph, both of which use a longer duration for the falling limb than for that of the rising limb [Mays, 2011].

The two stepped hydrographs tested in this work (Figure 3.5.2) are differentiated by their respective flow magnitudes, with one representing a low flow hydrograph and the other a high flow hydrograph. Peak flows were defined to be 2.5 times and 4.5 times the baseflow rate (Table 3.5.2). Thus, the two experimental hydrographs tested distinct unsteady flow conditions applied to the same baseflow and provided some generality to the design flows and results. These particular scalar multiples were selected to ensure a range of sediment transport conditions in which fine gravel was partially mobile at the low flow peak and the larger gravel fractions were partially mobile at the high flow peak for the sand/gravel sediment. Unsteadiness parameters for the design hydrographs (Table 3.5.2), as calculated according to the definition put forth by *Bombar et al.* [2011] (Equation 2.3.21), highlights the difference in flow conditions.

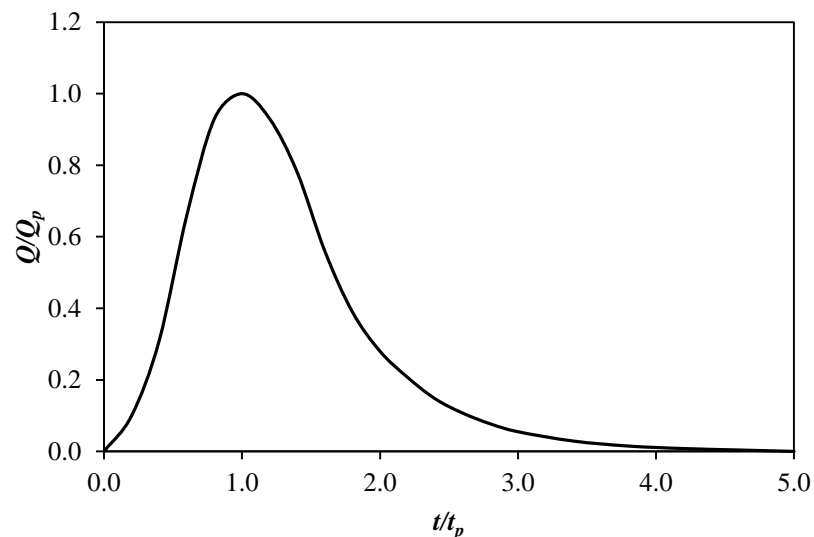
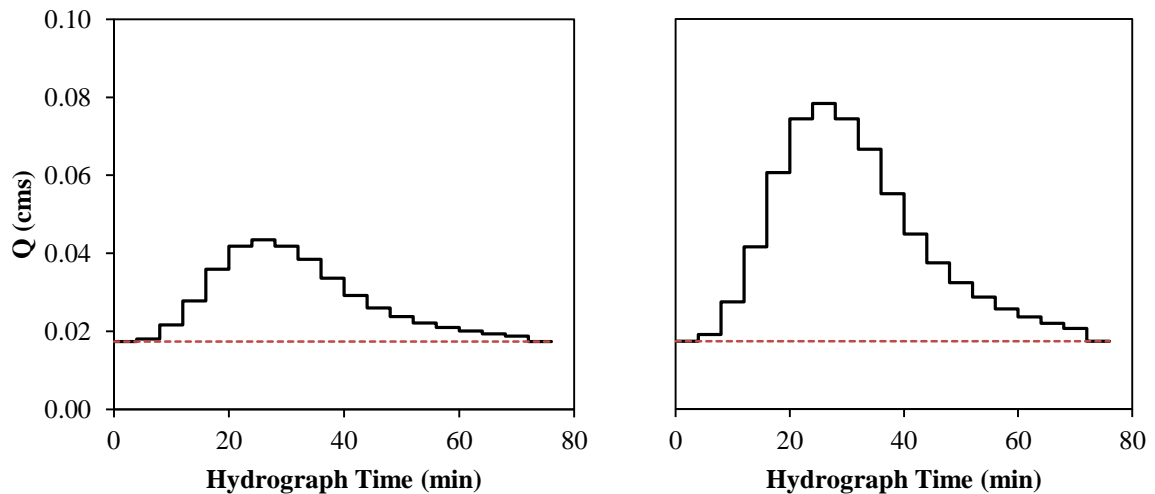


**Figure 3.5.1.** NRCS curvilinear dimensionless unit hydrograph.

**Table 3.5.2.** Design hydrograph characteristics.

Flow Characteristic	Hydrograph 1	Hydrograph 2
Flow Magnitude	Low	High
Baseflow, $Q_{BF}$ (cms)	0.0174	0.0174
Peak flow, $Q_P$ (cms)	0.0435	0.0783
Unsteadiness, $P_s$ (-)	$3.9 \cdot 10^{-4}$	$7.2 \cdot 10^{-4}$



(a) Hydrograph 1 – Low Flow.

(b) Hydrograph 2 – High flow.

**Figure 3.5.2.** Experimental design hydrographs. The red dashed line indicates baseflow.

### 3.6 SEDIMENT DISTRIBUTIONS

Channel vegetation is known to grow in substrates that range from predominantly gravels [Power, 1996] to exclusively sand and silt [French and Chambers, 1996]. Where plants favor coarse sediments, the gravel fraction varies from 29% to 79% [Sand-Jensen, 1998; Power, 1996]. There can be a significant sand content in these sediments [Baattrup-Pederson and Riis, 1999] and a maximum of 5% silt content [Gurnell et al., 2010; Power, 1996]. Submerged and emergent plants growing in finer substrates show a preference for sediment mixtures containing a maximum gravel fraction of up to 1.5%

[Zierholz *et al.*, 2001]. These fine substrates are dominated by sand sized sediments [French and Chambers, 1996; Sand-Jensen, 1998; Power, 1996] and typically contain between 20% and 50% silt sized sediment [Clarke and Wharton, 2001; Sand-Jensen, 1998; Zierholz *et al.*, 2001; Hung *et al.*, 2007; Gurnell *et al.*, 2010], though silt fractions have been shown to comprise nearly the entire substrate composition for certain aquatic species [French and Chambers, 1996].

From these ranges of typical field conditions with aquatic vegetation, two target grain size distributions were developed (Figure 3.6.1). Mix 1 was a graded mix of fine sand and small gravel, with grain sizes ranging from 0.063 mm to 6.3 mm. Bulk characteristics of this target mix were as follows: 70% sand, 30% gravel; median grain size  $D_{50}$  of 0.55 mm. Mix 2 was a graded mix from 0.001 mm to 1.4 mm, extending from silt to coarse sand. Bulk characteristics of this mix were as follows: 70% sand, 30% silt/clay; median grain size  $D_{50}$  of 0.27 mm. The different sediment types were colored (silt and fine sand: white; medium sand: dark brown; coarse sand and gravel: unpainted) to easily distinguish between relative fractions of each during transport and on the bed surface following hydrographs. Including one coarser mix and one finer mix enabled investigation of the influence of gravel and silt on both fractional and total transport rates.

### **3.7 EXPERIMENT DETAILS**

#### **3.7.1 No Sediment (NS) Experiments**

The first group of experiments did not involve any sediment and is referred to as the No Sediment (NS) runs. There were 12 individual runs in this group. Eight of these runs tested combinations of two stem densities ( $\varphi = 0.03, 0.10$ ) with each of four different steady flow rates. An additional four runs tested a secondary stem configuration

at each stem density and baseflow to evaluate the impact of stem arrangement on the flow field. Primary stem configurations, identified by the letter A in the run ID, were the arrangements used in subsequent experiments involving sediment. Secondary stem configurations are denoted by the letter B in the run ID.

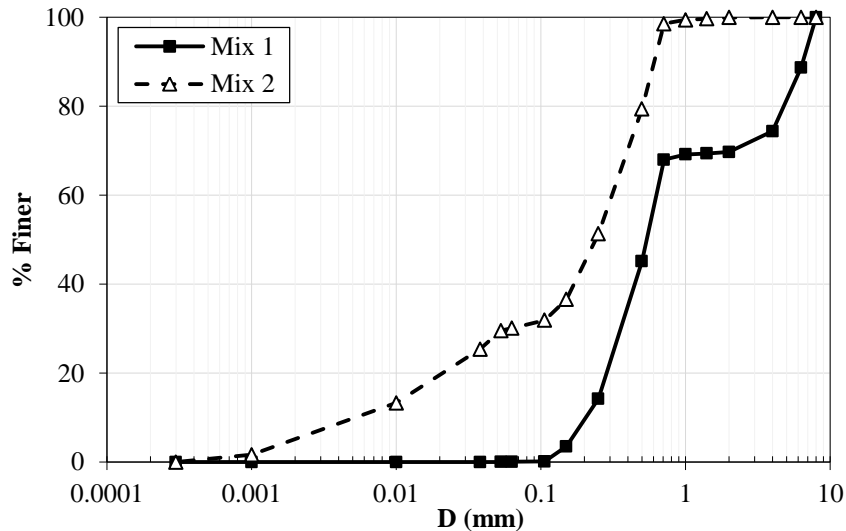


**Figure 3.6.1.** Experimental sediment distributions.

These experiments focused on fully characterizing the hydraulics downstream of the model emergent vegetation patch. Velocity measurement locations included streamwise (longitudinal) and cross-stream (transverse) profiles of velocity. NS runs details are summarized in Table 3.7.1. Information obtained during these runs provided necessary hydraulic details to link to geomorphic changes in the vicinity of the patch, including pertinent flow length-scales over which to analyze channel bed adjustment.

### ***Experimental Procedure***

The following procedure was used in all NS experiments:

- (a). The model patch base was glued to the flume bottom at flume location  $x = 288$  cm downstream of the inlet.

- (b). Stems were inserted or removed from the patch base to achieve the specified stem density.
- (c). The ADV was placed at flume location  $x = 224$  cm from the inlet to measure incoming flow over a period of 240 s. Mean velocity and discharge were calculated based on this record. If flow conditions did not match those specified for that given run, tailgate height and pump frequency were then adjusted to achieve the required flow rate and  $Fr$ .
- (d). The cart and ADV were placed in the initial position upstream of the patch and longitudinal velocity profiles were measured using LabVIEW automation in the locations shown in Figure 3.7.1(a). These measurements took approximately 6.5 hrs to complete.
- (e). The cart and ADV were placed in the initial position downstream of the patch and the transverse velocity profiles were measured using LabVIEW automation in the locations shown in Figure 3.7.1(b). These measurements took approximately 11.5 hrs to complete.

### 3.7.2 No Patch (NP) Experiments

The second group of experiments included sediment but not the model vegetation patch, and therefore is collectively referred to the No Patch (NP) run group. This group focused on sediment transport in unsteady flows in the absence of vegetation. Thus, these experiments provided a control against which to compare the impacts of vegetation on transport in subsequent runs. Experiments in this group were organized into “run sets,” testing two hydrographs (low and high flow) and two sediment mixtures for a total of four run sets. Run sets were comprised of individual experiments that were repeated

under approximately the same flow conditions until a dynamically stable equilibrium bed state was attained, as determined by minimal volumetric changes in the channel bed DEM difference analysis (Section 3.3.2). NP run sets details are summarized in Table 3.7.2.

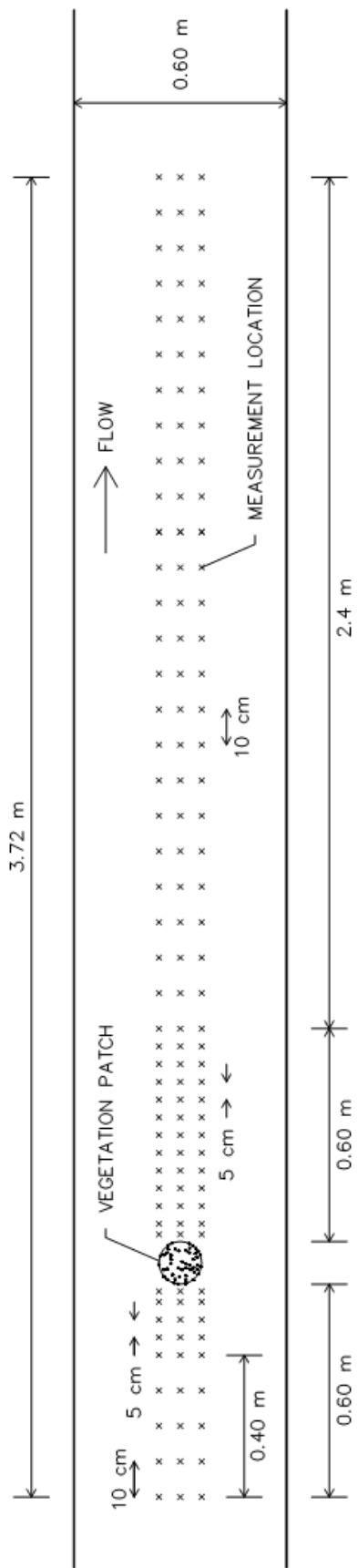
**Table 3.7.1.** NS Experiment group summary.

<b>Run</b>	<b>Patch</b>	<b>Solid Vol. Fraction</b>	<b>Steady Flow Level<sup>1</sup></b>	<b>Sediment</b>
NS-1A	Yes	0.03	L - BF	N/A
NS-1B	Yes	0.03	L - BF	N/A
NS-2A	Yes	0.03	L - P	N/A
NS-3A	Yes	0.03	H - BF	N/A
NS-3B	Yes	0.03	H - BF	N/A
NS-4A	Yes	0.03	H - P	N/A
NS-5A	Yes	0.10	L - BF	N/A
NS-5B	Yes	0.10	L - BF	N/A
NS-6A	Yes	0.10	L - P	N/A
NS-7A	Yes	0.10	H - BF	N/A
NS-7B	Yes	0.10	H - BF	N/A
NS-8A	Yes	0.10	H - P	N/A

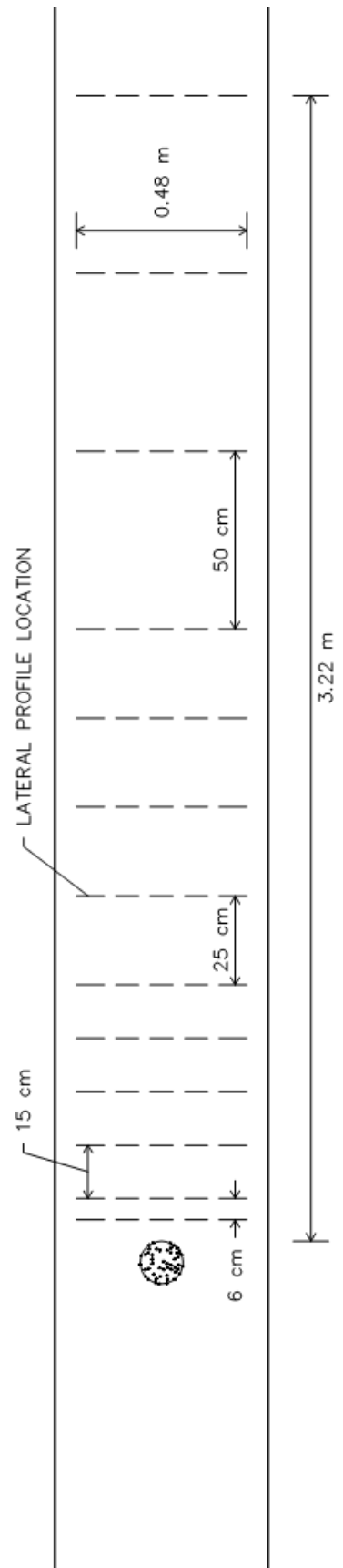
<sup>1</sup>BF denotes baseflow; P denotes peak flow

**Table 3.7.2.** NP Experiment group summary.

<b>Run Set</b>	<b>Patch</b>	<b>Solid Vol. Fraction</b>	<b>Hydrograph</b>	<b>Sediment</b>
NP-1	No	N/A	Low	Mix 1
NP-2	No	N/A	High	Mix 1
NP-3	No	N/A	Low	Mix 2
NP-4	No	N/A	High	Mix 2



(a) Longitudinal velocity profile measurement.



(b) Transverse velocity profile measurement.

Figure 3.7.1. Velocity measurement schematics.

### ***Experimental Procedure***

The following procedure was used in all NP experiments:

- (a). The sediment bed was prepared with the target grain size distribution. The bed was then manually mixed and sieve analysis was conducted on four active layer samples spaced at 2 m along the flume to verify bulk sediment distributions. The bed was then screeded flat.
- (b). Baseflow was run until the bed reached a condition of dynamic equilibrium. During this initial flow period, sediment transport samples were collected for 10 seconds at 10 minute intervals from the upstream end of the flume via the recirculation system. Samples were quickly weighed and returned to the flume. Following each transport sample, bed and water surface measurements were recorded from rulers placed every 0.5 meters on the flume walls. The bed monitoring system also recorded signal data throughout the run. These three data collection methods were used in combination to determine the equilibrium bed state as one in which the water and bed slopes were approximately equal and constant, the weight distribution of the bed showed minimal change having stabilized through time, and a steady sediment transport rate was observed.
- (c). Once equilibrium was reached, baseflow continued for 18 additional hours to provide a flow history consistent with the vegetation patch experiments in which detailed velocity measurements were collected.
- (d). Flow was slowly turned off and the flume drained.
- (e). After the flume had drained and there was no standing water on the bed

surface, an initial laser scan of the bed was collected. A camera scan of the initial bed was also collected, requiring individual photos taken 16-20 cm apart to cover the same 6 m flume area as the laser scan.

- (f). Flow was slowly restarted at the baseflow rate.
- (g). A 68-minute flow hydrograph was run in the flume, plus four minute baseflow periods before and after the unsteady flow intervals. The hydrograph required manual adjustment to the pump frequency every four minutes to approximate the design hydrograph flows outlined in Section 3.5.2. The required pump frequencies were obtained via flow calibration curves developed prior to the NP experiments. With each flow adjustment, the ADV probe height was also adjusted to ensure velocity measurement at roughly the same relative depth throughout the hydrograph. At the midpoint of each four minute constant flow interval, the following measurements were manually collected:

1. Bedload transport samples were collected with a double sieve stack (#10 sieve on top of #200 sieve; 20.5 cm in diameter) from the upstream end of the flume where the sediment and water slurry re-entered via the recirculation system. For the first sediment mix, gravel and sand were quickly separated, weighed, and returned to the flume. Samples collected at 10 min, 18 min, 26 min, 38 min, and 58 min were saved for later detailed grain size analysis. These times were selected to ensure two samples from similar flow rates on the rising and falling limbs, respectively, as well as a sample at

the peak flow.

2. Suspended sediment samples were collected as grab samples at the approximate location of the ADV.
3. Water and bed depth were recorded at the mid-point of each 1-m flume segment using rulers on the clear flume walls.

The following measurements were continuously collected throughout the hydrograph:

1. An ADV located at  $x = 244$  cm downstream from the flume inlet measured and recorded flow velocities throughout the flow period.
  2. The bed monitoring system recorded voltages from the pressure transducers throughout the flow period.
- (h). Flow was slowly turned off and the flume drained.
- (i). After roughly one to two hours of draining time, laser and camera scans of the bed were taken.
- (j). A difference analysis was conducted in ArcGIS to quantify volumetric change between the new channel bed and the bed prior to the hydrograph.
1. If the net change between successive beds was within an acceptable range (detailed in Section 5.2.3), no more hydrographs were required and the run set was completed.
  2. If the change between successive beds was large, the baseflow rate was run for two hours and steps (f) through (j) were repeated until minimal net volumetric change was observed or the maximum of six hydrographs was reached.

### 3.7.3 Patch and Sediment (PS) Experiments

The final group of experiments, which tested the impact of an emergent vegetation patch on sediment transport in unsteady flows, is collectively referred to as the Patch and Sediment (PS) runs. As in the NP run group discussed above, these experiments were organized into run sets because individual experiments were repeated until minimal volumetric bed change was measured between successive hydrographs of the same flow magnitude. In total, there were eight run sets within the PS group, testing the same combinations of sediment mixtures and hydrographs as tested for the NP group, with the same patch densities ( $\varphi = 0.03, 0.10$ ) as for the NS group. The primary focus of the PS experiments was to analyze transport and bed stability impacts from a vegetation patch over an extended period of time in which unsteady flows were repeated. Table 3.7.3 summarizes details of the PS experiments.

#### *Experimental Procedure*

The procedure used in the PS experiments was identical to the one used in the NP group of experiments, except for a few key differences to account for the vegetation patch, as highlighted below.

- (a). Once the sediment bed was properly prepared, the model vegetation patch was inserted approximately 3 m downstream from the flume inlet. The patch base was covered with 3 cm of sediment.
- (b). Once the bed had reached a dynamic equilibrium, detailed longitudinal and transverse velocity profiles were measured during 18 hours of baseflow in the same manner as in the NS runs discussed in Section 3.7.1.

- (c). Data collection during the hydrograph was identical to that in the NP experiments, with the only difference being that a secondary ADV was used. This secondary ADV was placed downstream of the patch in the approximate location of the steady wake region, as determined by detailed velocity measurements. The secondary ADV also continuously recorded velocity throughout the hydrograph.

**Table 3.7.3.** PS Experiment group summary.

<b>Run Set</b>	<b>Patch</b>	<b>Solid Vol. Fraction</b>	<b>Hydrograph</b>	<b>Sediment</b>
PS-1	Yes	0.03	Low	Mix 1
PS-2	Yes	0.03	High	Mix 1
PS-3	Yes	0.10	Low	Mix 1
PS-4	Yes	0.10	High	Mix 1
PS-5	Yes	0.03	Low	Mix 2
PS-6	Yes	0.03	High	Mix 2
PS-7	Yes	0.10	Low	Mix 2
PS-8	Yes	0.10	High	Mix 2

## CHAPTER 4

### *Emergent Vegetation Patch Hydraulics*

---

---

#### 4.1 INTRODUCTION

This chapter discusses results from the No Sediment (NS) group of experiments in which the mean flow field downstream of sparse and dense emergent vegetation patch models was investigated. Random stem configurations and a range of flow conditions were tested in order to expand on previous work developed for patches with regularly distributed stems in low flows. Detailed velocity measurements collected through streamwise and cross-stream transects provided the necessary hydraulic data to fully describe the flow field downstream of the model patch. Experimental parameters for all NS runs are given in Table 4.1.1.

Specific components of the hydraulics around a vegetation patch investigated in this chapter include patch wake length scales (Section 4.2.1), the asymmetrical nature of the downstream flow field (Section 4.2.2), and the role of stem configuration (Section 4.2.3), all of which are addressed in more detail in the discussion (Section 4.3). The goals of this chapter were to obtain full descriptions of the flow field downstream of sparse and dense patches with irregularly distributed stems and compare wake length-scales with those obtained downstream of patches with uniform stems.

**Table 4.1.1.** Experimental parameters and results for NS run group.

<b>Run ID</b>	$\phi$ (-)	$Q$ (m <sup>3</sup> /s)	$U_0$ (m/s)	$h$ (m)	$Fr$ (-)	$U_I$ (m/s)	$U_I/U_2$	$L_1$ (cm)	$L_2$ (cm)	$L$ (cm)	$L_w$ (cm)	$AO$ (-)
1A	0.03	0.0069	0.11	0.110	0.10	0.06	0.57	108	144	252	190	-0.008
1B	0.03	0.0069	0.10	0.110	0.10	0.07	0.59	100	140	240	220	0.008
2A	0.03	0.0242	0.27	0.152	0.22	0.18	0.65	130	161	291	240	-0.005
3A	0.03	0.0213	0.33	0.109	0.31	0.20	0.59	90	160	250	240	-0.009
3B	0.03	0.0214	0.32	0.110	0.31	0.22	0.65	110	180	290	-	0.011
4A	0.03	0.0641	0.61	0.175	0.47	0.36	0.54	100	140	240	190	-0.017
5A	0.10	0.0069	0.10	0.111	0.10	0.03	0.25	55	85	140	100	0.007
5B	0.10	0.0069	0.10	0.111	0.10	0.02	0.14	40	80	120	110	0.001
6A	0.10	0.0242	0.26	0.155	0.21	0.09	0.29	70	80	150	110	0.009
7A	0.10	0.0214	0.32	0.111	0.31	0.10	0.27	60	90	150	100	0.011
7B	0.10	0.0213	0.32	0.111	0.31	0.07	0.17	46	84	130	100	0.004
8A	0.10	0.0641	0.59	0.181	0.44	0.20	0.26	60	90	150	90	0.005

## 4.2 RESULTS

### 4.2.1 Wake Lengths

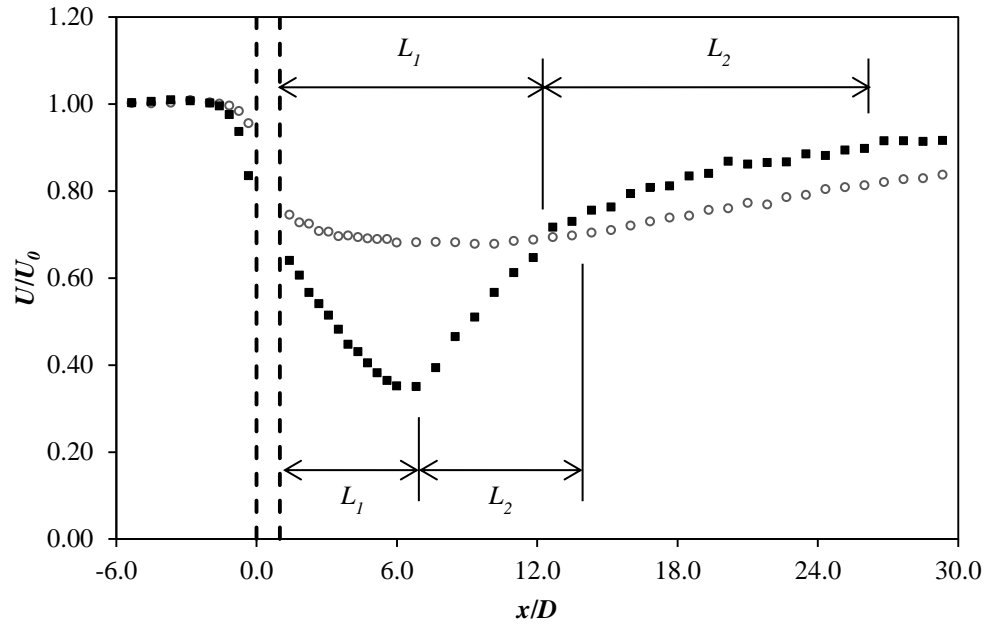
Wake length values of  $L_1$ ,  $L_2$ ,  $L$ , and  $L_w$  were estimated from longitudinal profiles of streamwise velocity and turbulence intensity (Table 4.1.1; Figure 4.2.1). In all experiments, a defined area of reduced velocity downstream of the patch was measured along the centerline, followed by a region of increasing flow velocity with distance downstream, signifying a characteristic flow modification caused by the emergent vegetation patch. The region of constant velocity immediately downstream of the vegetation patch defined the value of  $L_1$  for each experiment, while  $L$  was measured as the distance from the vegetation patch to the downstream point at which the velocity recovered, approximated by a break in the linear slope of velocity gradient.  $L_2$  was calculated as the difference between  $L$  and  $L_1$ .

Longitudinal velocity profiles defined the wake structure downstream of each patch, and these profiles were noticeably affected by the patch stem density. The differences between wake structures were distinct to patch density, as exemplified in Figure 4.2.1a by the centerline velocity measurements for the sparse and dense patches at a moderate flow rate. The decrease in longitudinal velocities downstream of the dense patches was more than 50% of the upstream, unaffected flow velocity in each run. In all cases, the velocity decrease was also greater downstream of the dense patch than the corresponding velocity decrease downstream of the sparse patches under the same flow rate. Over the range of flows tested,  $L_1$  for was between 53% and 150% higher for the sparse patches than the dense in the same flows. Downstream of the dense patches, flow velocities recovered more quickly than for corresponding sparse patches. This was

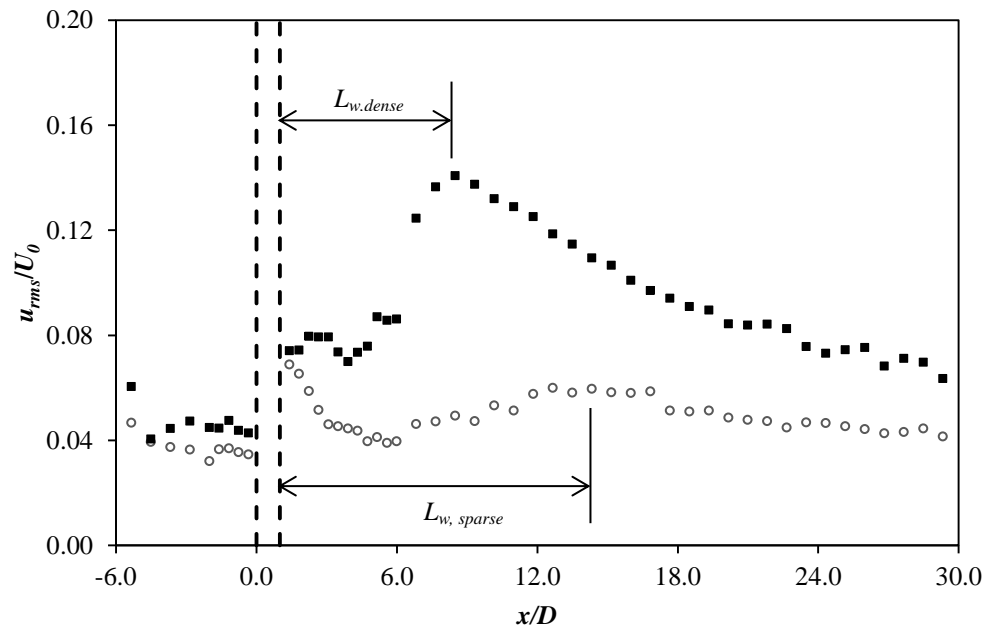
evident from comparison of velocity profiles which showed that  $L_2$  was 56-114% higher and the total wake length,  $L$ , was 60-123% longer for sparse patches.

Centerline profiles of turbulence intensity ( $u_{rms}$ ) confirmed two peaks in streamwise intensity downstream of patches, corresponding to the stem-scale and patch-scale turbulence, respectively [e.g. *Chen et al.*, 2012; *Takemura and Tanaka*, 2007]. The area between turbulence peaks was an area of diminished turbulence intensity and coincident with the steady wake region. Across all flow rates and patch densities, stem-scale turbulence was discernible in the vicinity immediately downstream of the patch. The second peak in  $u_{rms}$  defined patch-scale turbulence and the wake formation length,  $L_w$  (Table 4.1.1; Figure 4.2.1b). Flow blockage (i.e. stem density) controlled wake formation lengths and altered downstream turbulence structure. For each dense patch experiment,  $L_w$  was easily defined by a clear peak in  $u_{rms}$ , as in Figure 4.2.1b. However, the second peak in intensity was poorly defined downstream of all sparse patches and was difficult to estimate, which highlighted the reduced patch-scale turbulence relative to dense patches.

Because estimates of  $L_w$  were not reliable for the sparse patches, analysis of wake lengths focused on the  $L_1$ ,  $L_2$ , and  $L$ . For the same patch configuration (patch A), variation in these wake lengths was measured over a range of Froude numbers (Figure 4.2.2). Each of the three wake lengths peaked when the flow condition corresponded to  $Fr = 0.22$  for the sparse patches, before decreasing at higher flows. For the dense patches, wake lengths were less variable, with constant  $L$  for  $Fr$  between 0.21 and 0.44.



(a) Streamwise velocity ( $Q = 0.0242$ ,  $Fr = 0.21$ ).



(b) Streamwise turbulence intensity ( $Q = 0.0641$ ,  $Fr = 0.44-0.47$ ).

**Figure 4.2.1.** Longitudinal profile comparison for role of stem density. (a) Streamwise velocity,  $U$ ; and (b) turbulence intensity,  $u_{rms}$ . Downstream distance is normalized by the patch diameter,  $D$ , which is 12 cm for all experiments. Locations  $x/D = 0$  and  $x/D = 1.0$  correspond with the leading and trailing edges of the patch, respectively, and are denoted by dashed vertical lines.  $L_1$  and  $L_2$  for sparse and dense patches are labeled on the top and bottom of graph (a), respectively. Flow direction is from left to right.

Length scale variability for increasing flows was quantified using the range of observed values for each patch density. For the sparse patches, ranges in  $L_1$ ,  $L_2$ , and  $L$  were 38 cm, 21 cm, and 51 cm, respectively. In contrast, dense patch wake lengths were more consistent, shown by smaller ranges of 15 cm, 10 cm, and 10 cm for  $L_1$ ,  $L_2$ , and  $L$ , respectively. Greater wake length variability downstream of sparser patches suggested that as flow increased, patch-scale hydraulics were altered locally by individual stems in the sparse patch. Reductions in sparse patch wake lengths at higher flows indicated a lower steady wake velocity that was likely due to increased drag and stem-scale turbulence as a consequence of the increased upstream velocity.

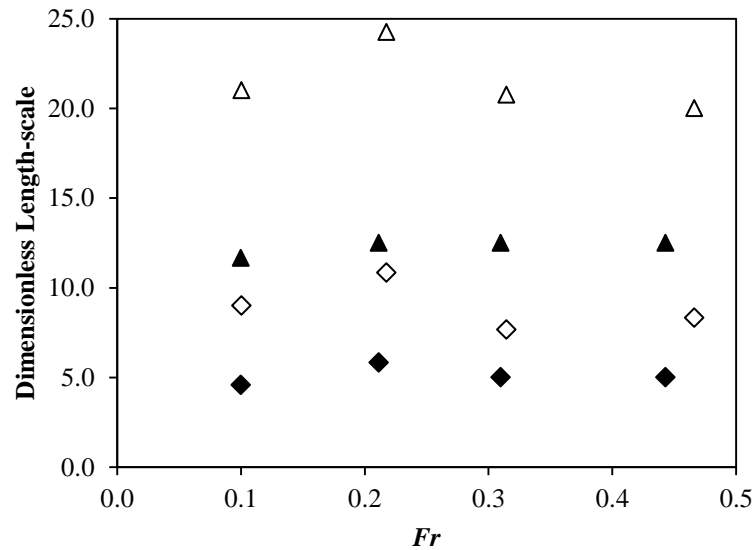


**Figure 4.2.2.** Dimensionless wake lengths for range of flow conditions. Diamonds are the steady wake length ( $L_1/D$ ) and triangles are the total wake length ( $L/D$ ). Wake recovery length ( $L_2/D$ ) is the difference between these two parameters and is not shown for clarity. Solid and empty symbols represent dense and sparse patches, respectively. Results shown are for patches with stem configuration-A only.

#### 4.2.2 Asymmetrical Flow Structure

The use of random stem arrangements within the patches led to asymmetrical flow patterns in the downstream flow field in all experiments. Using the measured lateral

profiles, velocity and turbulence intensity contour plots were created. These contour plots illustrated the dependence of flow structure and symmetry on stem density, flow rate, and stem configuration (Appendix C.1). For example, Figure 4.2.3a shows mean velocity downstream of the sparse patch for Run 3A ( $\phi = 0.03$ ,  $Fr = 0.31$ ; Table 4.1.1), normalized by the upstream flow velocity,  $U_0$ . The dark blue area downstream of the patch represents the region of greatest velocity reduction, which was offset from the patch centerline. The width of the total region of reduced velocity downstream of the patch was approximately equal to the patch width (lighter blue area in Figure 4.2.3a) and was roughly centered in line with the patch until a distance of approximately 14 patch diameters downstream ( $x/D = 15$ ). Beyond this location, the region of reduced velocity shifted so that it was no longer centered with the patch and asymmetry in the velocity reduction zone increased with increased downstream distance. A similar asymmetrical pattern was identified in the contour plot of streamwise turbulence intensity (Figure 4.2.3b), with greater turbulence intensity along the left edge (facing downstream) of the patch width extending downstream.

For the same flow rate, the flow field around the dense patch was also asymmetrical with minimum mean flow velocity to the right of the patch center. In contrast to the sparse patch case, asymmetry in velocity and turbulence fields extended only six patch diameters downstream (Figure 4.2.3c-d). Farther downstream, the mean flow field and turbulence intensity patterns shifted to be better aligned with the patch centerline. For this particular case, flow field asymmetry extended over larger scales for the sparse patch than for the dense, as it was stronger near the dense patch before adjusting towards a more symmetrical structure with distance downstream.

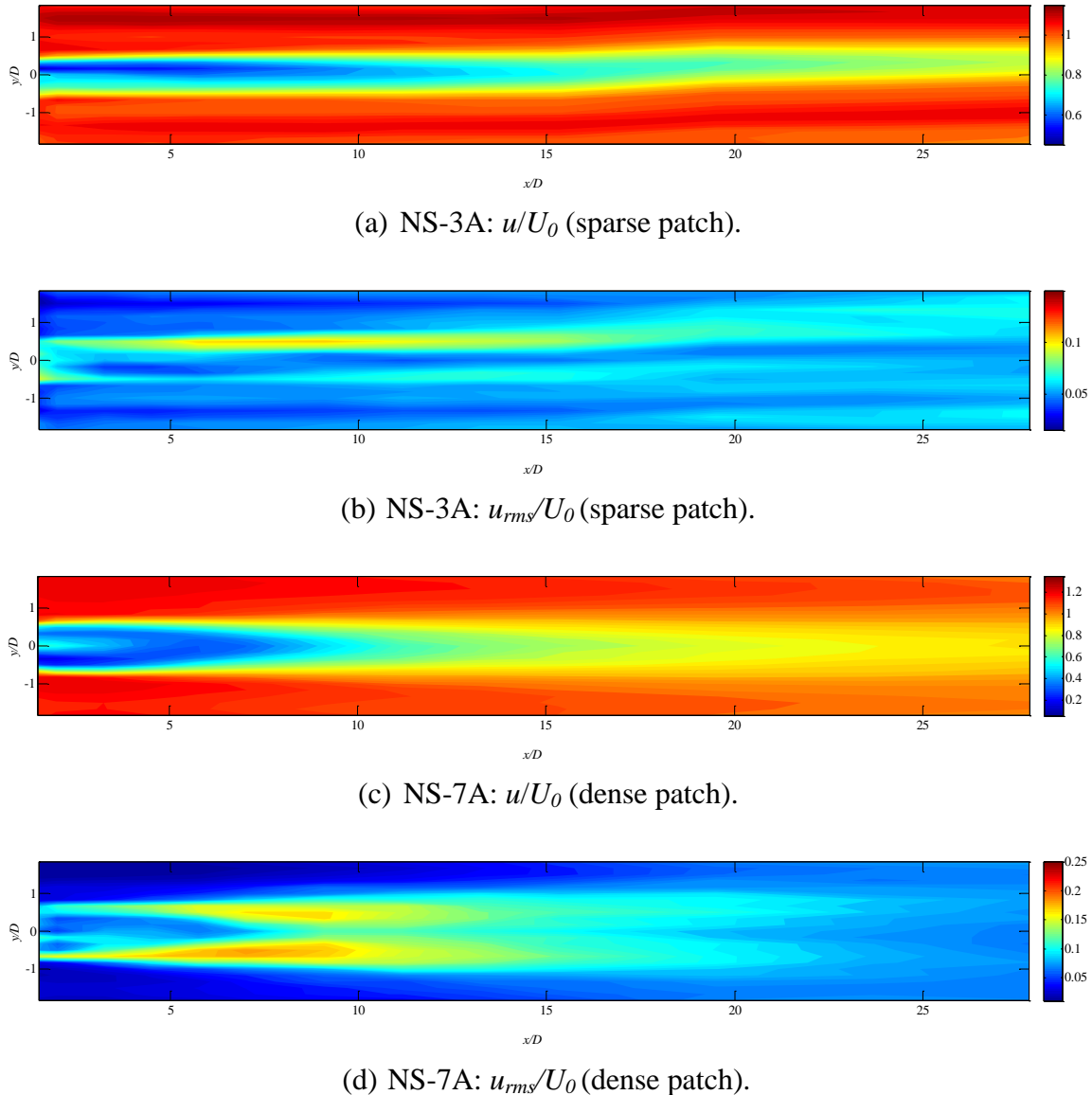
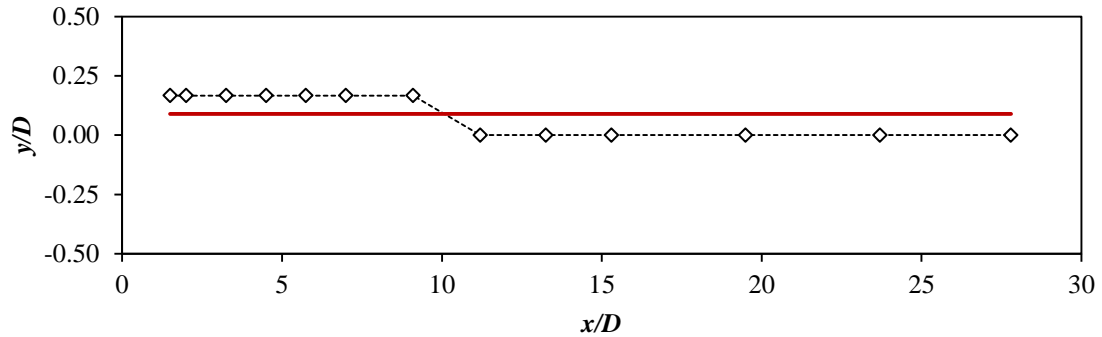


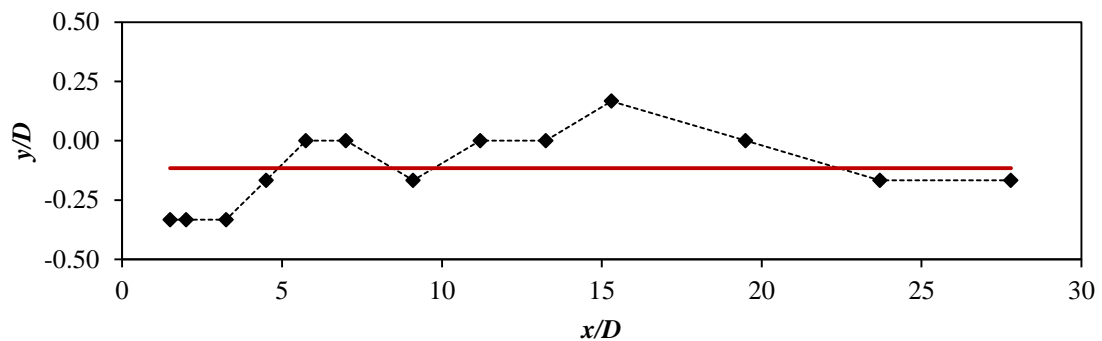
**Figure 4.2.3.** Velocity and turbulence intensity contour plots for varying stem densities. Color maps represent streamwise velocity (a, c) or turbulence intensity (b, d), normalized by upstream velocity,  $U_0$ . Note that for purposes of clarity, the contour scales change between velocity and turbulence intensity plots, as well as between sparse and dense patch densities. The trailing edge of the patch in each case is located just to the left of the plot at  $x/D = 1.0$ , with the patch width extending from  $-0.5 < y/D < 0.5$ . Flow is from left to right,  $Q$  is 0.0214 cms, and  $Fr$  equals 0.31 in all cases.

Asymmetry of the downstream flow field relative to the patch centerline was quantified by measuring the distance, normalized by the patch diameter, from the patch centerline to the minimum streamwise velocity location in each lateral profile. The result

was a low velocity path showing the deviation from the patch centerline over the measurement area downstream of the patch, as shown in Figure 4.2.4.



(a) Run NS- 3A ( $\phi = 0.03$ ). Solid, horizontal red line represents  $AO = 0.090$ .



(b) Run NS- 5A ( $\phi = 0.10$ ). Solid, horizontal red line represents  $AO = -0.115$ .

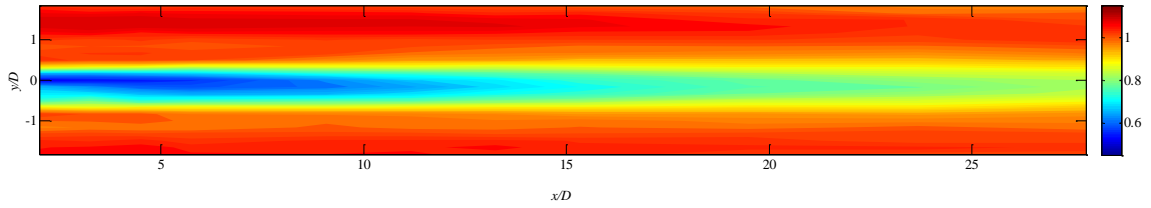
**Figure 4.2.4.** Example asymmetry offset plots. Plots start 6 cm downstream of patch, which extends from  $-0.5 > y/D > 0.5$ . Flow is from left to right.

Offsets at each profile were averaged to obtain a single value describing the amount of flow field asymmetry downstream of each patch, termed the asymmetry offset ( $AO$ ). Lower  $AO$  values indicated a more symmetrical flow field about the patch centerline, with a value of zero corresponding to a completely symmetrical flow structure. Asymmetry offsets, shown in Table 4.1.1 for each run, described overall asymmetry in velocity reduction areas downstream of an emergent patch, and thus, quantified the patch influence on flow symmetry for varying stem density and

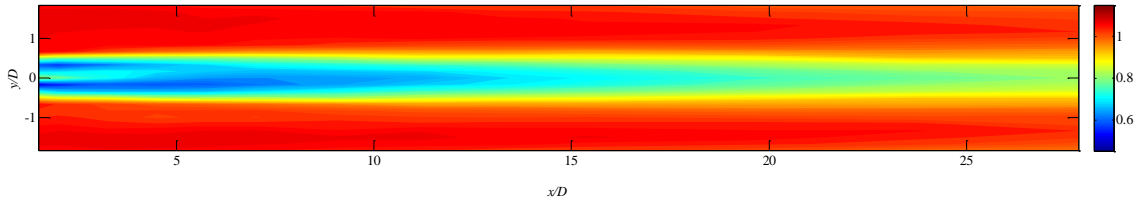
arrangement. For stem configuration-A, the average  $AO$  for the sparse patches was 0.029, compared with -0.094 for the dense patches, indicating that the sparse patches had less overall impact on asymmetry of the downstream flow field. The negative average  $AO$  value for the dense patches corresponded to flow that was asymmetrically skewed such that the flow pattern was shifted toward the right flume wall. Conversely, the positive  $AO$  for the sparse patches indicated regions of minimum velocity tended towards the left flume wall. This discrepancy in principal offset of reduced flow regions demonstrated the importance of stem density on spatial patterns and symmetry of the mean flow field.

### **4.2.3 Stem Configuration**

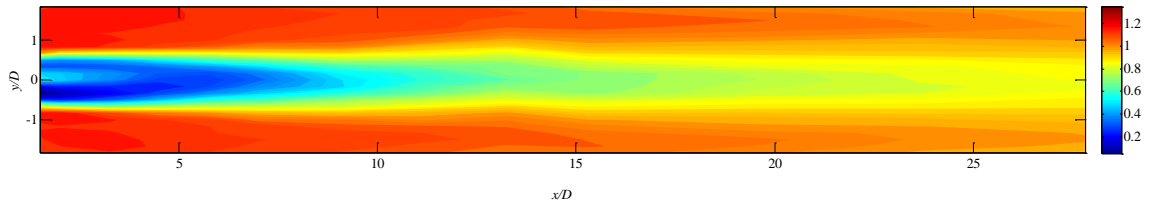
Tests using multiple stem configurations for the same patch stem density (Figure 3.4.3), illustrated the impact of stem arrangement on patch-scale hydraulics. Two configurations for each of the sparse and dense patch densities were tested against the low ( $Fr = 0.10$ ) and high ( $Fr = 0.31$ ) baseflows obtained through  $Fr$  scaling with field conditions (Section 3.5.1), therefore forming four comparison cases. Results indicated that individual stem location within the patch relative to incoming flow influenced the downstream flow field at both local and reach spatial scales. Contour plots of the downstream velocity fields revealed that those areas of a patch with a higher stem concentration created a greater local flow blockage, a region of reduced velocity immediately downstream of the concentrated stems, and consequently an asymmetrical flow field at a scale roughly equal to the steady wake length measured from the centerline profiles (Table 4.1.1; Figure 4.2.5).



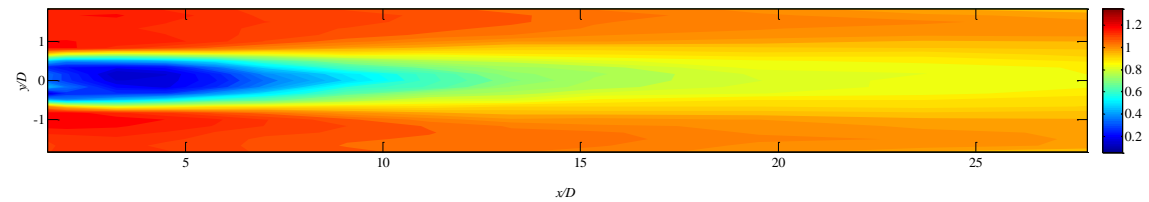
(a) NS-1A:  $u/U_0$  (sparse patch, stem configuration-A).



(b) NS-1B:  $u/U_0$  (sparse patch, stem configuration-B).



(c) NS-5A:  $u/U_0$  (dense patch, stem configuration-A).



(d) NS-5B:  $u/U_0$  (dense patch, stem configuration-B).

**Figure 4.2.5.** Velocity contour plots for varying stem configurations. Color maps indicate streamwise velocity normalized by upstream velocity. Different color scales are used for the sparse and dense patches for clarity. The trailing edge of the patch in each case is located just to the left of the plot at  $x/D = 1.0$ , with the patch width extending from  $-0.5 < y/D < 0.5$ . Flow is from left to right,  $Q$  is 0.0069 cms, and  $Fr$  is 0.10 in all cases.

The irregular stem locations within a patch clearly impacted the spatial patterns and symmetry of the downstream flow field (Figure 4.2.5), as the direction and amount of asymmetry varied significantly between stem configurations.  $AO$  values were positive for sparse patch configuration-A, but negative for sparse configuration-B. Sparse stem

configuration-B increased the level of flow asymmetry (average  $AO$  from 0.029 to -0.051). Conversely, dense configuration-A patches had negative  $AO$  values while the configuration-B patches had positive  $AO$  values. For the dense patches, stem configuration-B resulted in a more symmetrical flow field (average  $AO = 0.026$ ) than that of stem configuration-A (average  $AO = -0.094$ ).

Variation in the wake structure for different stem configurations was identified in the wake lengths measured from centerline velocity profiles. In three of the comparison cases, wake length scales decreased when stem configuration changed from A to B. The single case in which the wake length scales increased was the sparse patch under flow conditions with  $Fr = 0.31$ . In this particular case, the ratio  $U_1/U_2$  was higher in stem configuration-A than in configuration-B, suggesting that the reduced flow blockage by the stems in configuration-A was emphasized in the higher flow conditions, which in turn increased steady and total wake lengths. During lower flows,  $U_1/U_2$  was similar for both sparse patch configurations, making it reasonable to infer that differences in the wake lengths resulted from the impact of individual stem arrangements on the local flow field. Larger  $L$  values were consistently measured for dense stem configuration-A over configuration-B, indicating that there was less flow blockage by stem arrangement A. Discrepancies between the wake lengths for the different stem configurations in sparse and dense patches demonstrated that although stem-scale flow impacts are local, stem arrangements can also impact the patch-scale flow field.

## **4.3 DISCUSSION**

### **4.3.1 Wake Length Predictions**

Wake lengths were calculated for each set of experimental parameters using the

equations developed by *Zong and Nepf* [2012] (Equation 2.2.2) and *Follett and Nepf* [2012] (Equation 2.2.3). Calculated values were compared to the values measured from the centerline velocity profiles from these experiments (Table 4.1.1) to evaluate the applicability of Equations 2.2.2 and 2.2.3 in predicting the steady and wake recovery length scales downstream of patches with randomly distributed stems.

The steady wake length was greater downstream of the sparse patches and was reduced downstream of dense patches, confirming the expected flow pattern and the findings of *Zong and Nepf* [2012]. However, the ability of Equations 2.2.2 and 2.2.3 to accurately predict the wake length varied with stem density and specific length scale (i.e.  $L_1$ ,  $L_2$ , and  $L$ ), as shown in Figure 4.3.1.

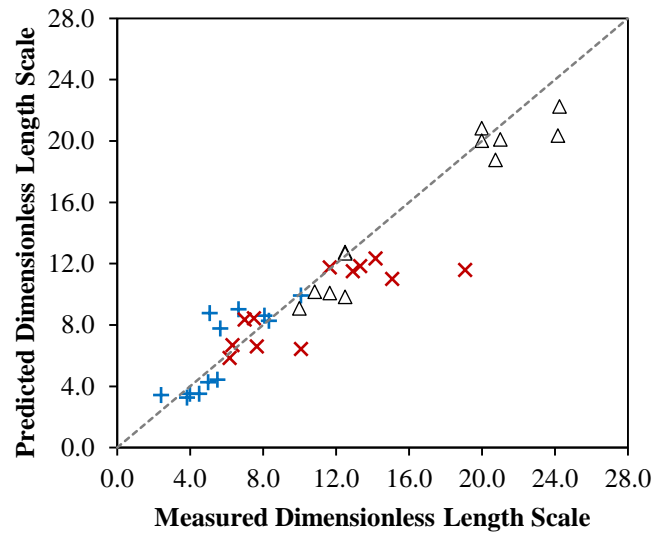


**Figure 4.3.1.** Comparison of predicted and measured wake lengths. Dashed gray line represents perfect agreement between predicted and measured length-scales.

$L_1$  was under-predicted in all cases for the dense patches, but overpredicted for the sparse ones. An opposite pattern occurred in the comparison of calculated to measured  $L_2$  values, for which  $L_2$  was overpredicted by Equation 2.2.3 for dense patches but

underpredicted for sparse ones. With these contradicting results for steady wake and wake recovery lengths, the total wake length scale, which is the sum of  $L_1$  and  $L_2$ , showed the best agreement between predicted and measured values (Figure 4.3.1).

Measured and calculated length scales are plotted together in Figure 4.3.2, along with predicted values from Equation 2.2.2 (Figure 4.3.2a) and Equation 2.2.3 (Figure 4.3.2b). Regression analyses were applied to optimize the fit of the predictive equations to the combined data set that included both the data collected in this study and the data collected by *Zong and Nepf* [2012]. For the  $L_1$  regression analysis, the leading coefficient of 2.5 in Equation 2.2.2 was adjusted to minimize the sum of the squares of the residuals, thereby maximizing the regression fit including the NS data. A new coefficient of 2.36 resulted in a slightly improved fit ( $R^2 = 0.80$  from  $R^2 = 0.78$ ), which is also plotted in Figure 4.3.2a. Because the coefficient in Equation 2.2.2 is not strictly empirical, a change in this coefficient suggests a shear layer growth parameter,  $S_{\delta l}$ , for these experiments different than the 0.10 average assumed from Zong and Nepf's data. Based on the derived best-fit coefficient, a marginally increased value of  $S_{\delta l}$  of 0.106 is more appropriate. The impact on the flow conditions in these experiments was minor and this value falls within the uncertainty bounds proposed by Zong and Nepf for this parameter (0.10 +/- 0.02).

The  $L_2$  length scale was calculated with Equation 2.2.3, adjusted using regression analysis to provide an improved fit to the combined dataset. The leading coefficient (slope) of 13 and the constant (y-intercept) of 4 were lowered to 12.9 and 3.9, respectively. These changes (Figure 4.3.1b) and do not offer an improvement in the  $R^2$  value of the prediction for the combined dataset ( $R^2 = 0.86$ ). In each case, the revised equations for  $L_1$  and  $L_2$  were not significantly different than the original relationships.

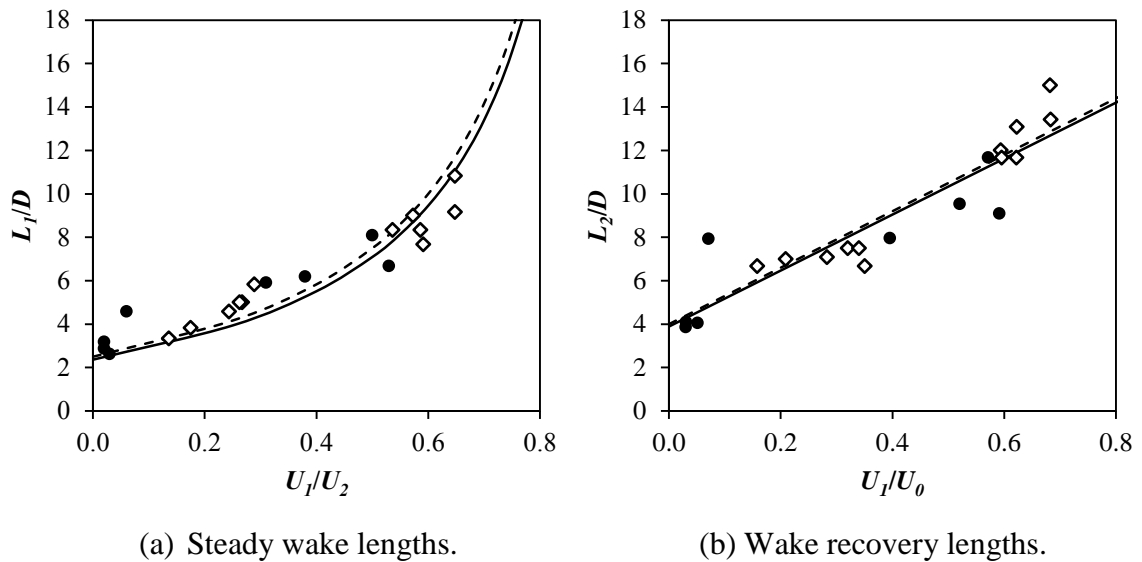


**Figure 4.3.2.** Wake length predictions. (a) Steady wake lengths are compared to Equation 2.2.2; (b) Wake recovery lengths compared to Equation 2.2.3. In both plots, black circles are data from previous researchers and white diamonds are data from the new data set. Dashed and solid black lines represent previous and new fitted relationships, respectively.

The range of flow conditions tested in this study was larger than what was tested previously by *Zong and Nepf* [2012], expanding especially into higher flows and water depths. Inclusion of a greater range of flow conditions expanded the boundaries of the predictive equations and likely resulted in some of the small discrepancies between predicted and measured wake lengths. Testing patches with randomly arranged stems provided additional complexity to the flow measurements relative to previous work involving patches with uniformly distributed stems. Expanding the applicable range of these prediction relationships helps narrow the gap between translating wake lengths measured in idealized flume conditions and those that may be expected in nature, as changing flows and non-uniform vegetation distributions can impact patch-scale hydraulics.

### 4.3.2 Implications of Asymmetrical Flow Structure

A patch of regularly distributed cylinders has been shown to create a symmetrical flow field about the patch centerline [e.g. *Zong and Nepf, 2012; Takemura and Tanaka, 2007; Tanaka and Yagisawa, 2010*]. When stem locations were randomly distributed within a patch, the wake structure downstream changed, impacting flow patterns over the patch and wake length scales. Flow asymmetry developed downstream of the patch with the amount of asymmetry a function of stem density and stem arrangement within the patch.

To investigate more thoroughly the spatial patterns in flow field asymmetry, the  $AO$  values corresponding to the end of the steady wake ( $L_1$ ) and end of the wake recovery ( $L_2$ ) were compared. The asymmetry offsets measured near the patch at the  $L_1$  scale were greater downstream of dense patches with an average offset of -0.170, while for sparse patches the average offset was 0.031. However, at the larger spatial scale roughly corresponding to the  $L_2$  distance, the flow field downstream of dense patches was nearly symmetrical about the patch centerline (average  $AO = -0.007$ ). These scale-dependent and asymmetrical flow field alterations enhance flow heterogeneity around and downstream of vegetation patches, which increases habitat diversity [e.g. *Crowder and Diplas, 2000; 2002*]. Near and far flow field  $AO$  comparisons indicated that a dense vegetation patch creates an asymmetrical flow field at the scale of several patch diameters, or approximately over the steady wake length. The wake area and velocity gradients resulting from non-uniform flow distributions downstream of a patch are analogous to the flow complexity introduced by other in-channel obstructions, such as boulders. Changes in local flow patterns can be critical in enhancing habitat for flora and

fauna within a stream [Crowder and Diplas, 2000]. Thus, based on flow considerations, dense vegetation patches appear to create an environment more favorable to biodiversity.

Enhanced sediment deposition has been indicated in the wake region downstream of vegetation patches by several researchers [e.g. Follett and Nepf, 2012; Chen et al., 2012], making it reasonable to assume that asymmetrical flow fields will impact spatial patterns of sediment deposition and scour around a patch. For a patch with randomly distributed stems, which would be a common occurrence in a natural system, an asymmetrical downstream flow field suggests that maximum deposition may not occur along the patch centerline. Rather, more deposition is likely to occur in localized reduced flow areas that are offset from the centerline, such as the dark blue region shown around  $y/D$  of -0.333 in Figure 4.2.3c, with an increased potential for scour away from this location. For this reason, sediment changes downstream of patches with irregularly arranged stems should be quantified over an area corresponding to at least the patch width, thereby providing more representative volumes of sediment deposition or erosion than can be obtained by only using measurements along the patch centerline. Measuring or predicting changes in sediment depth over a patch centerline will not fully account for spatial patterns of asymmetrical flow and localized low flow areas, which would be expected to impact sedimentation patterns in field applications. The asymmetrical flow field downstream of vegetation may also influence the transport of suspended constituents. Where the hydraulic patterns within a channel or wetland are important in dissolved constituent degradation [e.g. Ng and Eheart, 2008; Hancock et al., 2010], an ability to predict the asymmetrical flow patterns downstream of plant patches takes on a large importance.

Because flow patterns downstream of vegetation patches with irregular stem spacing were asymmetrical, a full description of the flow field required lateral velocity profiles in addition to the longitudinal ones. In these experiments, detailed lateral velocity transects were measured at 13 pre-selected positions downstream with variable streamwise spacing. The asymmetrical nature of the spatial flow structure was represented in a way not possible using a single centerline profile, or even multiple longitudinal profiles. While this approach in itself is not new for studying the flow field downstream of a patch [e.g. *Tanaka and Yagisawa, 2010; Takemura and Tanaka, 2007*], it provided valuable information regarding downstream flow adjustment, wake structure, and symmetry at various scales. Contour plots revealed localized areas and spatial patterns of reduced velocity and turbulence intensity, and when combined with data from longitudinal profiles, a full description of the downstream flow field was possible.

#### **4.3.3 Effect of Stem Configuration on Flow Field**

The comparison cases used to test different stem configurations for the same patch density revealed that relative stem placement within a patch affected the downstream flow structure. Variable stem locations altered relative stem spacing, which in turn, altered flow blockage. *Takemura and Tanaka [2007]* studied the flow field around an emergent patch model similar to the one studied here, varying the spacing between regularly distributed stems in both the streamwise and cross-stream directions. They found that differences in relative stem spacing, especially in the cross-stream direction, strongly influenced downstream flow structure. Approximate stem spacing for the patches tested here was estimated by measuring the spacing from each stem to its nearest neighboring stems in all directions, then calculating the average of these values to

obtain a representative spacing,  $G$ , for the patch. Relative stem spacing was quantified by the ratio of  $G/d$ , where  $d$  is the stem diameter. The  $G/d$  ratio of 2.6 was the same for each dense patch because the patch was merely rotated between stem configurations A and B. Relative stem spacing ratios of 5.6 and 6.0 were calculated for sparse patch stem configurations A and B, respectively.

Takemura and Tanaka tested relative stem spacing ranging from 0.25 to 5.0 in the streamwise direction, and from 0.1 to 4.2 in the cross-stream. Although stem spacing of the sparse patches studied here was higher than their ranges, alterations in the flow field for the different stem arrangements were measured. For sparse stem configuration-B, the steady wake length increased relative to that downstream of configuration-A because the ratio of steady wake velocity to patch-adjacent velocity,  $U_1/U_2$ , was greater. The difference in  $U_1/U_2$  ratio was consistent with a larger  $G/d$  ratio for stem configuration-B. A greater  $G/d$  ratio created less local flow blockage and consequently, longer steady and total wake lengths. Despite identical relative stem spacing, a decrease in  $L_I$  was observed between dense patch stem configurations A and B. Average stem spacing, as estimated here, may not be fully representative of local stem concentrations within a densely vegetated patch that can influence patch wake lengths.

The effect of varying stem configuration within a single patch on the downstream flow field may have application to the broad evaluation of the impact of multiple patches on reach-scale hydraulics, with each stem being analogous to a different patch or clump of vegetation. Although local flow characteristics would vary with the change in porous flows between stems and full patches, the larger scale flow alterations and asymmetry

resulting from different configurations could provide meaningful insight into the expected flow heterogeneity through reaches with multiple vegetation patches.

#### 4.4 SUMMARY

Experiments without sediment were carried out to investigate the mean flow and turbulence structure downstream of sparse and dense emergent vegetation patch models. Random stem configurations and a range of flow conditions were tested in order to expand previous work developed for patches with regularly distributed stems in low flows. Results showed that the downstream flow field displayed varying levels of asymmetry about the patch centerline, depending on stem density and individual stem arrangement within the patch. Dense patches created an asymmetrical near flow field that approached a more symmetrical spatial pattern at larger downstream distances. Steady wake ( $L_1$ ), wake recovery ( $L_2$ ) and total wake ( $L$ ) lengths were estimated to quantify descriptive length-scales of vegetation patch hydraulics. Consistent with previous work, these length scales were influenced by patch stem density and were longer for sparse patches. Stem configuration and relative stem spacing within a patch impacted the symmetry of the downstream flow fields as well as the characteristic wake lengths. Relative stem configuration and spacing in the sparse patches, measured by the  $G/d$  ratio, influenced both the velocity gradients in flows around the patches and wake lengths, which were longer for higher values of  $G/d$  because more flow was able to pass directly through the patch. The dense patches tested had constant  $G/d$  ratios but different stem configurations relative to the incoming flow. Wake lengths downstream of these dense patches varied due to locally higher stem concentrations, which highlighted the role of stem configuration on patch-scale hydraulics.

Regression analyses were conducted on previously developed prediction equations for steady wake and wake recovery lengths. Incorporating the NS data set with that of *Zong and Nepf* [2012] required minor modifications to the previous relationships in order to account for irregular stem distributions and higher flow conditions. However, velocity contour plots revealed localized areas and spatial patterns of reduced velocity and turbulence that were not fully captured by simple longitudinal velocity profiles or patch wake length-scales, thus elucidating the asymmetrical nature of the flow field downstream of patches with variable stem configurations.

## CHAPTER 5

### *Morphological Change in Unsteady Flows*

---

---

#### 5.1 INTRODUCTION

This chapter discusses experiments without vegetation but with a sediment bed, referred to as the No Patch (NP) group of experiments. Sand/gravel and sand/silt/clay sediment beds were each tested under repeated low and high flow hydrographs. Digital elevation models (DEMs) were created of the bed surface after it reached dynamic equilibrium and after each successive hydrograph. DEMs were analyzed in several ways, including differencing of subsequent DEMs to calculate volumetric channel change and statistical analysis to evaluate bed surface structure and bedform geometry. The goals of this chapter are to gain a comprehensive understanding of how channel morphology adjusts to repeated unsteady flow events and evaluate how the grain size distribution of the sediment mixture impacts these changes.

#### 5.2 ANALYSIS METHODS

##### 5.2.1 Sediment Composition

Sediment samples were collected from the top 2-3 cm of the initial channel bed prior to the equilibrium portion of each experiment, as well as after each run set. Samples were approximately 250-350 g and were collected from the center of the flume at locations 19%, 44%, 69%, and 94% of the flume length. These samples were dried and sieved. Grain size distributions (GSDs) were averaged into a single composite GSD to

describe the active layer composition.

Samples were not collected between hydrographs within a run set as collection would have interfered with channel bed adjustment. Panoramic photos of the bed surface were instead created and analyzed after each hydrograph (Appendix D.1). Six grids comprised of 144 points per grid were superimposed on the photos, spaced equally along the downstream 6 m of the flume. The modified grid by number method [Wolman, 1954] was used to approximate relative percent gravel and sand on the channel bed surface from 864 individual grid points on each sand/gravel bed in between unsteady flow events. Relative surface fractions were not determined for the sand/silt/clay mixture because the finest sand fraction and the silt fractions were both white, and reliably distinguishing between the two sediment types from photos was extremely difficult. Active layer samples, combined with suspended sediment sampling, showed that the majority of the silt and clay fractions were quickly entrained into the water column, resulting in a primarily sand bed. The clay fraction is therefore dropped from descriptions of the second sediment distribution, which is hereafter referred to as the sand/silt mixture.

### **5.2.2 Semivariogram Analysis to Estimate Bedform Geometry**

Thirteen longitudinal profiles were extracted from each DEM, spaced 4 cm apart in the lateral direction and spanning the center 48 cm of the flume. Profile points were filtered in the  $x$ -direction to obtain 1-mm point spacing. These profiles were used to determine DEM bed slopes and spatial correlations of bed elevations with semivariogram analysis. Experimental semivariograms for each profile were computed in MATLAB with lags of 1 mm and maximum lag between data points of 1.65 m, or approximately 1/3 of each profile's total record. Semivariograms were fit with an empirical model

consisting of an exponential and periodic component [Robert, 1988; Robert and Richards, 1988], described by Equations 5.2.1 - 5.2.3:

$$\gamma(h) = \gamma_1(h) + \gamma_2(h) \quad (5.2.1)$$

with:

$$\gamma_1(h) = c \left[ 1 - \exp\left(-h/r\right) \right] \quad (5.2.2)$$

$$\gamma_2(h) = \sum_{i=1}^2 a_i \cos\left(2\pi h/l_i\right) + b_i \sin\left(2\pi h/l_i\right) \quad (5.2.3)$$

where  $\gamma(h)$  is the model semivariance at lag distance  $h$ ,  $\gamma_1(h)$  and  $\gamma_2(h)$  are exponential and periodic components of the empirical semivariogram model, respectively,  $c$  is model sill,  $r$  is model range,  $l_i$  is wavelength of periodic function  $i$ , and  $a_i$  and  $b_i$  are Fourier coefficients representing periodic amplitudes for function  $i$ . Models of this form were fit to experimental semivariograms using a sum of least squares non-linear regression, adjusting model parameters to minimize error between fitted and computed semivariance.

In the presence of bedforms, semivariogram model parameters are used to estimate bedform geometry [Robert 1988; Robert and Richards, 1988]. Bedform spacing ( $\lambda$ ) is estimated as the dominant periodic function wavelength ( $l_1$ ) and bedform height,  $\Delta$ , is estimated with Equation 5.2.4:

$$\Delta = 2(\hat{A}^{1/2} + c^{1/2}) \quad (5.2.4)$$

where  $\hat{A}$  is the amplitude of the dominant periodic function calculated from  $a_1$  and  $b_1$ . A dimensionless regularity parameter,  $\sqrt{c}/r$ , quantifies the regularity of a bedform sequence based on model sill and range. High regularity indicates dominance of periodicity in the semivariogram and a prevalence of bedforms on the surface [Robert, 1988; Robert and

Richards, 1988]. Figure 5.2.1 shows example semivariograms for a bed surface with and without bedforms, and a model fitted to the bedform surface.

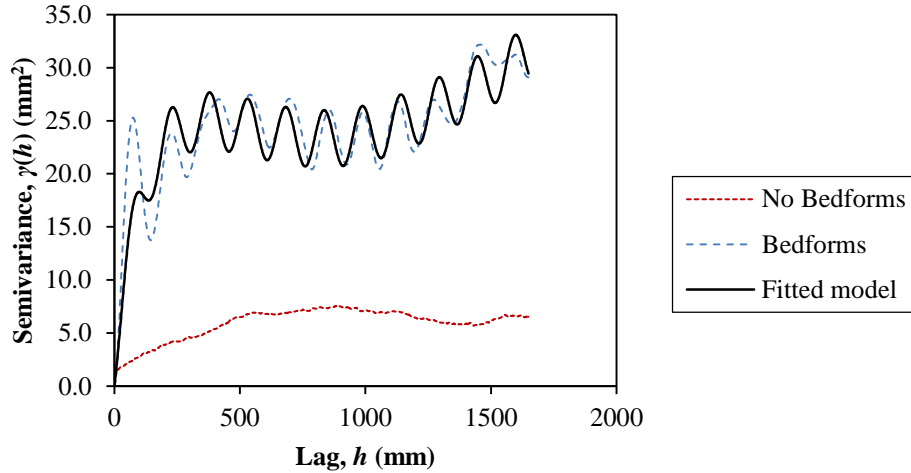


**Figure 5.2.1.** Bed surface semivariogram examples.

### 5.2.3 Bed Adjustment Parameter

Morphological channel adjustment was analyzed between successive unsteady flow hydrographs. This analysis was possible through DEM differencing (Section 3.3.2), which calculated volumetric channel change and created bed change maps of the spatial distribution of erosion and deposition between subsequent DEMs (Appendix D.1). A unit bed adjustment parameter,  $\delta_b$ , was developed to evaluate net morphological adjustment over the reach-scale after each hydrograph (Equation 5.2.5):

$$\delta_B = \frac{1}{L_R B z_b} \sum_{j=1}^N \Delta V_{bj} \quad (5.2.5)$$

where  $\delta_B$  is unit bed adjustment (%),  $N$  is number of 1-m flume segments considered in the reach (5 for these experiments),  $L_R$  is reach length ( $N \cdot 1 \text{ m} = 5 \text{ m}$ ),  $B$  is flume width (0.60 m),  $z_b$  is unit sediment bed depth (1 cm), and  $\Delta V_{bj}$  is volumetric bed change for

flume segment  $j$  calculated from DEM differencing. As the bed adjusts to unsteady flow events, the amount of change in the reach-scale morphology will reduce until there is no net aggradation or degradation between successive flow events, indicating that the reach can be considered dynamically stable. The unit bed adjustment parameter is considered a surrogate for this reach-scale dynamic stability, and should approach zero as the bed reaches a dynamically stable state. Because  $\delta_B$  considers net morphological change over a specified reach, smaller scale bed adjustments such as bedform migration are incorporated into the stability calculation, thereby accounting for the active nature of a mobile bed. A bed adjustment threshold of  $|\delta_B| \leq 0.5\%$  was assumed to be adequately low in order to classify the channel as being dynamically stable, which was also used as a criterion to stop the repetition of hydrographs for a given run set. Because the parameter quantifies bed change relative to a unit bed thickness of 1 cm, the percentage value of  $\delta_B$  approximates the reach-averaged adjustment in bed elevation; the 0.5% threshold corresponds to a mean bed elevation adjustment of 0.5 cm. Quantifying bed adjustment as a unit value allows its application in more general situations because  $\delta_B$  can be scaled to the active layer thickness.

## **5.3 RESULTS: SAND/GRAVEL SEDIMENT MIXTURE**

### **5.3.1 Surface and Active Layer Sediment Composition**

The grain size distributions of the bed surface and active layer adjusted with the flow magnitudes of the hydrograph sequence. Surface sand content decreased from 64% on the equilibrium bed surface to 50% of the final bed surface after a progression of five low flow hydrographs (Figure 5.3.1). Conversely, the relative sand fraction of the bed surface increased nearly 20% following two high flow hydrographs (Figure 5.3.1). These

changes in surface sand-gravel fractions were not reflected in the active layer grain size distributions, which experienced modest adjustments from the initial to the final hydrograph-worked beds (Figure 5.3.2). For the low flow hydrograph sequence, the  $D_{50}$  and  $D_{16}$  grain sizes remained nearly constant, the  $D_{84}$  increased by only 11%, and the sand fraction decreased by approximately 3% (Figure 5.3.2a). As in the surface composition, active layer adjustments in grain size distribution were greater for the higher flow hydrographs (Figure 5.3.2b). Following the high flow hydrograph sequence, the  $D_{84}$  and  $D_{50}$  grain sizes decreased by 20% and 5%, respectively, relative to the initial bed composition, and active layer sand content increased by 7%.

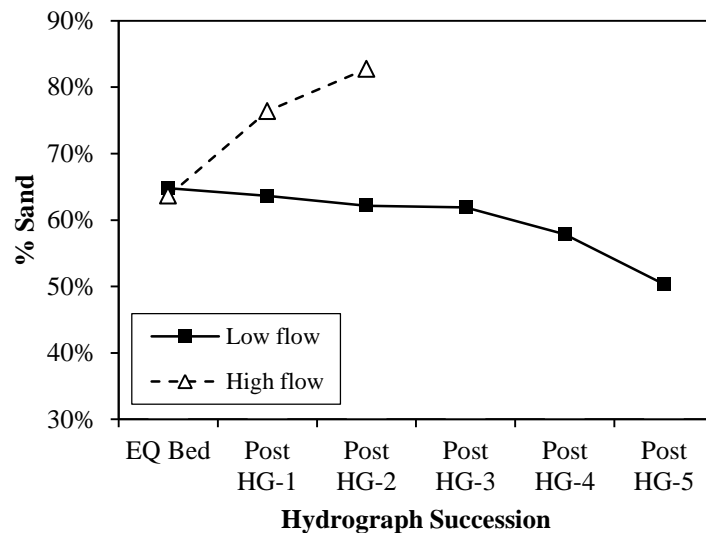
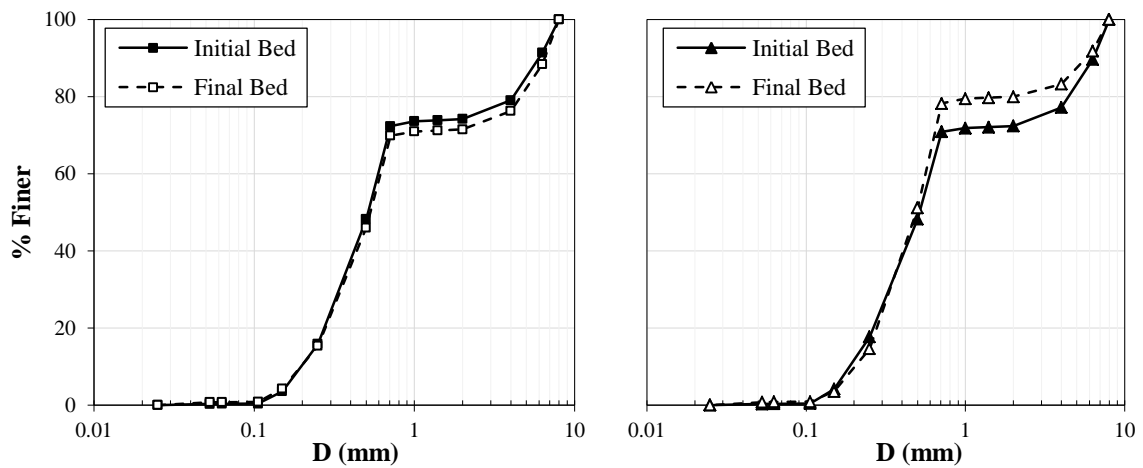


**Figure 5.3.1.** Surface sediment composition of sand/gravel beds.

### 5.3.2 Bed Structure and Bedforms

For the sand/gravel sediment mixture, no defined bedforms developed on beds during the five low flow hydrographs (Appendix D.1: NP-1), but ripple formation was observed along the flume center following the high flow hydrographs (Appendix D.1: NP-2). Estimates of bedform geometry for these beds indicated that ripple formation was

not substantial (Table 5.3.1), with average regularity of 0.049 between the two bed surfaces. Ripple height was approximately 8.5 mm with average spacing of 298 mm. Bedform geometry was laterally irregular and poorly defined in the sand/gravel beds following the high flow hydrographs (Appendix D.1). The two panoramic bed photos in Figure 5.3.3 show differences between the sand/gravel bed surfaces formed during low and high flow hydrographs.



(a) Low flow hydrographs.

(b) High flow hydrographs.

**Figure 5.3.2.** Active layer sediment composition for sand/gravel beds.**Table 5.3.1.** Bedform geometry of sand/gravel beds.

Hydrograph Magnitude	Hydrograph Progression	$\sqrt{c}/r$ (-)	$\Delta$ (mm)	$\lambda$ (mm)	$\Delta/\lambda$ (-)
Low	EQ Bed	0.016	-	-	-
	Post HG-1	0.013	-	-	-
	Post HG-2	0.011	-	-	-
	Post HG-3	0.011	-	-	-
	Post HG-4	0.022	-	-	-
	Post HG-5	0.012	-	-	-
High	EQ Bed	0.048	-	-	-
	Post HG-1	0.059	8.3	348	0.024
	Post HG-2	0.040	8.6	247	0.035



(a) After one low flow hydrograph.



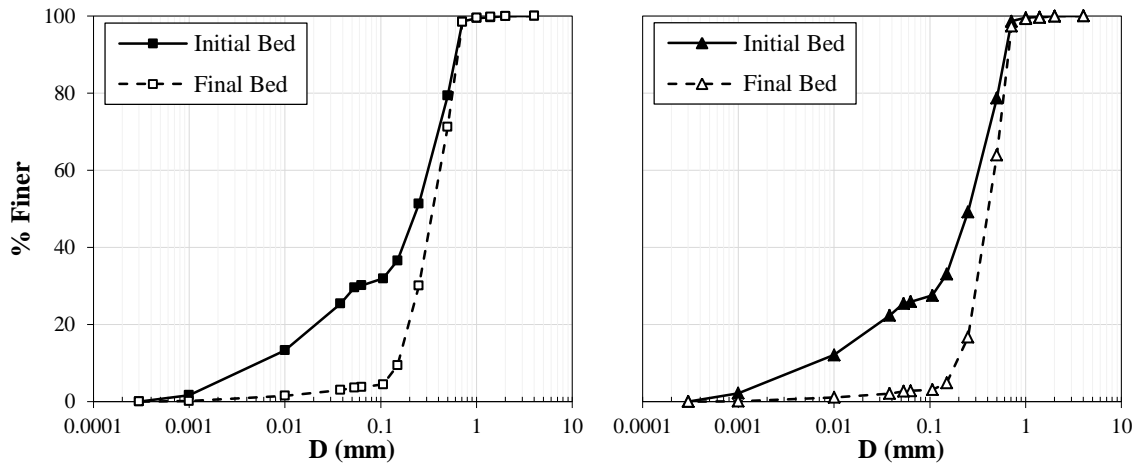
(b) After one high flow hydrograph.

**Figure 5.3.3.** Panoramic photo bed surface comparison for sand/gravel beds. Sand fractions are dark brown/red color.

## 5.4 RESULTS: SAND/SILT SEDIMENT MIXTURE

### 5.4.1 Active Layer Sediment Composition

The grain size distribution of the active layer was greatly altered upon application of the hydrographs. The silt/clay content of the active layer decreased by 22% and 20% during the low and high flow hydrographs, respectively (Figure 5.4.1). This decrease in the content of finer fractions within the bed indicated the majority of the finest material in the active layer was entrained once flows began, and therefore was largely removed from the active bed material. During the experiments, it was observed that most of the fine sediment was entrained very quickly and often before the flow rate in the flume reached the baseflow rate. Corresponding  $D_{50}$  values increased by 54% and 66% for the low and high flow hydrograph sequences, respectively (Figure 5.4.1), while the sorting coefficient decreased to about 31% of its initial value in both cases. The removal of most of the silt/clay fractions produced more uniform and poorly sorted bed sediment composed of primarily sand.



(a) Low flow hydrographs.

(b) High flow hydrographs.

**Figure 5.4.1.** Active layer sediment composition for sand/silt beds.

## 5.4.2 Bed Structure and Bedforms

Bedforms developed on all sand/silt beds during both low and high flow hydrograph sequences, but varied in regularity and geometry with flow magnitude. In each case, ripples developed as a response to the unsteady flows as there were no distinct bedforms present on the equilibrium bed surface. Ripples formed during the low flow hydrographs had greater regularity (mean 0.109), but with smaller heights and spacing (Table 5.4.1; Figure 5.4.2), indicating a highly mobile bed in which the large amount of material in transport enhanced bedform migration and adjustment during the high flow hydrographs. There was large streamwise and cross-stream topographic variability in the high flow hydrograph beds, but much of this was not explicitly due to a consistent bedform structure (Figure 5.4.2b). The DEMs and panoramic bed photos in Appendix D.1 (NP-3 and NP-4) show the bedforms and bed surface variability that was observed.

**Table 5.4.1.** Bedform geometry for sand/silt beds.

Hydrograph Magnitude	Hydrograph Progression	$\sqrt{c}/r$ (-)	$\Delta$ (mm)	$\lambda$ (mm)	$\Delta/\lambda$ (-)
Low	EQ Bed	-	-	-	-
	Post HG-1	0.118	5.3	114	0.047
	Post HG-2	0.105	9.9	124	0.080
	Post HG-3	0.104	10.5	137	0.077
	Post HG-4	0.085	12.4	153	0.081
	Post HG-5	0.107	13.1	154	0.085
	Post HG-6	0.135	13.0	170	0.076
High	EQ Bed	-	-	-	-
	Post HG-1	0.056	13.6	174	0.078
	Post HG-2	0.070	13.2	202	0.065
	Post HG-3	0.061	15.9	220	0.072
	Post HG-4	0.058	14.0	186	0.075
	Post HG-5	0.054	18.3	193	0.095
	Post HG-6	0.049	18.1	220	0.082



(a) After five low flow hydrographs.



(b) After five high flow hydrographs.

**Figure 5.4.2.** Panoramic photo bed surface comparison for sand/silt beds.

## 5.5 DISCUSSION

### 5.5.1 Role of Sediment Mixture on Bedform Geometry

The formation of bedforms during successive hydrographs was a function of both hydrograph flow rates and sediment mixture, with the sediment type having an apparent dominant effect. For the sand/gravel beds, a lack of bedform formation during the low flow hydrograph sequence indicated that the flow was not sufficient to create a strongly

bimodal transport regime with a highly mobile sand fraction. In contrast, the surface sand fraction decreased with additional hydrographs, indicating winnowing into the subsurface (Figure 5.3.1). Bedforms only developed during the high flow hydrographs, but not in a well-defined or regular configuration. The preferential transport of the sand fraction relative to the gravels led to an accumulation of sand on the bed surface, creating a supply sufficient to form ripples [Carling *et al.*, 2000; Kleinhans *et al.*, 2002; Kuhnle *et al.*, 2006]. For the high flow hydrograph succession, more of the gravel fraction was mobilized, exposing a larger fraction of the sand to entrainment, increasing the surface sand content (Section 5.3.1). Surface sand supply remained limited enough to restrict bedform heights relative to a purely sand system [Tuijnder *et al.*, 2009]. There was a contrast in transport of the sand fraction with hydrograph flow rate as the low flows created limited overall transport and sand winnowed into the subsurface, while during the higher flows, bimodal transport occurred with active sand transport sufficient to enable ripple formation over the gravel fraction on the surface. Thus, surface sand supply likely prevented bedform development in the sand/gravel mixture during the low flow hydrographs and restricted bedform growth during the high flow hydrographs.

Bedforms developed on all sand/silt beds during both low and high flow hydrographs and bedform geometry was related to flow magnitude (Table 5.4.1; Appendix D.1). Bedform heights and spacings were greater for the higher flow hydrograph beds, but ripples were more regular for the lower flow repetitions, which is consistent with the finding of Robert and Richards [1988] who observed decreased bedform regularity for increasing flow velocity. Increases in post-hydrograph ripple height and spacing were monotonic for the low flows (Pearson's  $r = 0.90$  and  $0.99$  for  $\Delta$

and  $\lambda$ , respectively), but more variable for the high flow hydrographs. Accordingly, bedform steepness, quantified as  $\Delta/\lambda$ , also adjusted during hydrograph sequences (Figure 5.5.1). During the second low flow hydrograph,  $\Delta/\lambda$  reached an average value of 0.080 that was maintained over the following four unsteady flow events. Conversely,  $\Delta/\lambda$  was variable for the higher flows and continued to increase during the hydrograph sequence.

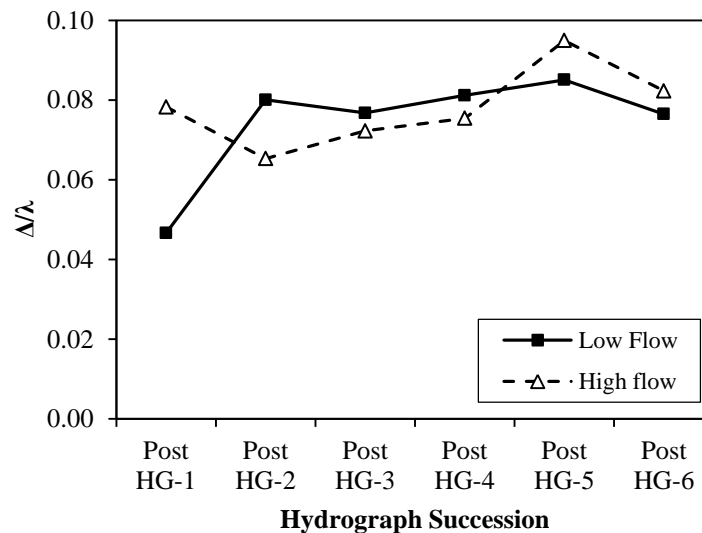


**Figure 5.5.1.** Bedform steepness adjustment for sand/silt mixture.

Adjustments in bedform height, spacing, and steepness during low floods were similar to what has been measured with flood discharge in the Meuse River and Rhine River, both large sand-bed systems [Julien and Klaassen, 1995]. The continued increase in ripple geometry over repeated floods is consistent with the idea that bedform adjustment lags behind flow changes [Martin and Jerolmack, 2013; Lee et al., 2004]. More pronounced bedform lag and hysteresis has been documented for shorter floods [Wijbenga and Van Nes, 1986], but because low and high flow hydrographs tested here were the same duration, increased variability in  $\Delta/\lambda$  adjustment during the higher flow sequence highlights the importance of flow magnitude on the ability of bedforms to

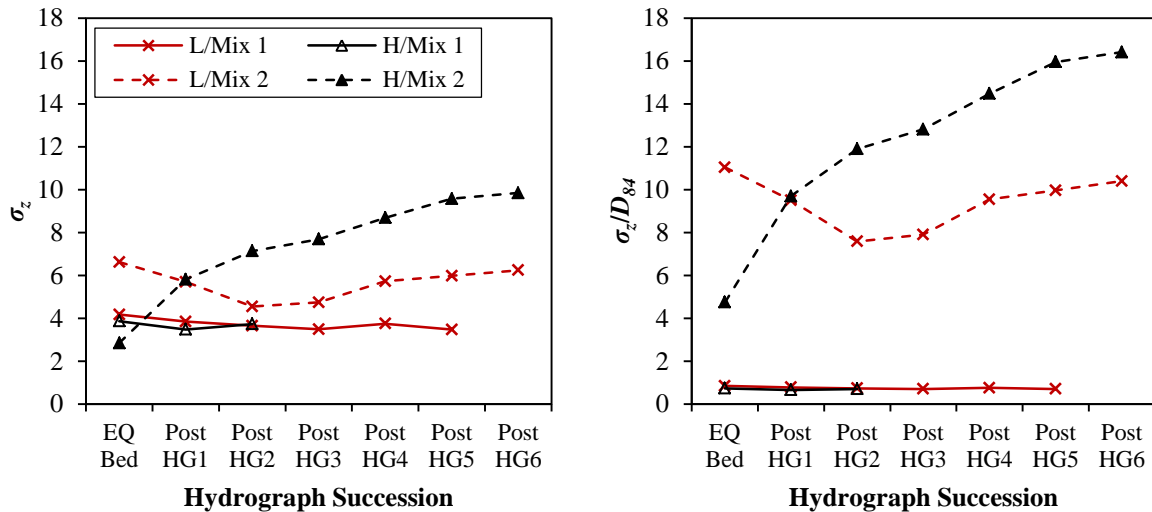
adjust during unsteady flows. Estimating bedform geometry prior to and following each hydrograph masked some of the hysteresis that likely occurred during each hydrograph [Martin and Jerolmack, 2013], but still provided information on bedform adjustment over temporal scales of repeated unsteady flow conditions.

Equilibrium bedform geometry in steady flows is predicted using relationships derived theoretically or from laboratory data [e.g. Yalin, 1964; Van Rijn, 1984b; Karim, 1999], and so application of such relationships to more natural conditions assumes quasi-steadiness [Martin and Jerolmack, 2013]. On average, the Van Rijn [1984b] relations overpredicted measured ripple heights and spacing by factors of 2.8 and 4.8, respectively. Van Rijn's approach assumed that bedform spacing scales with the flow depth. In contrast, ripple spacing scales with  $D_{50}$  in the Yalin [1964] relation. This approach overpredicted measured values by an average factor of 2.4. Whether bedform spacing scales with the flow depth or grain size, large overprediction of geometries indicates that the short duration of each hydrograph was insufficient for bedforms to approach their equilibrium geometry. Bedform heights tend to adjust more quickly than spacing [Nelson et al., 2011; Wilbers and Ten Brinke, 2003; Wjibenga and Van Nes, 1986], so better predictions of heights in unsteady flows were possible. However, applying existing relationships will overpredict bedform geometry due to the unsteady nature of hydrographs and lags in bedform adjustment behind flow changes.

### **5.5.2 Topographic Variability and Bed Roughness**

The standard deviation of bed elevations ( $\sigma_z$ ) has been used as a characteristic vertical roughness length scale of gravel bed surfaces [e.g. Nikora et al., 1998; Aberle and Smart, 2003; Aberle and Nikora, 2006] and linked to bedform height in sand beds

[e.g. *Robert and Richards, 1988*]. It provides a measure of topographic variability and a reference for bed roughness length scale. In these experiments, the value of  $\sigma_z$  was strongly related to the bed sediment. For the sand/gravel mixture,  $\sigma_z$  had minimal variation with flow rate or hydrograph repetition (Figure 5.5.2a). Variability in these bed surfaces was due largely to the presence of the gravels on the surface rather than differences in sediment mobility between different magnitude flows, suggesting that the gravel was a controlling factor in bed surface structure despite the moderate proportions present during hydrograph sequences (17-50% for all beds and flows).



(a) Standard deviation of bed elevations.

(b)  $\sigma_z$  normalized by  $D_{84}$ .

**Figure 5.5.2.** Comparison of topographic variability. Low (L) and high (H) flow hydrographs are denoted by red X's/lines and black triangles/lines, respectively. Sand/gravel (Mix 1) and sand/silt (Mix 2) beds shown by solid and dashed lines, respectively.

Bed surface variability was substantially greater for the sand/silt beds (Figure 5.5.2a). Adjustment in  $\sigma_z$  was significant through each hydrograph succession, changing over a wide range of values, and was impacted by hydrograph magnitude. The  $\sigma_z$  after six high flow hydrographs was 58% greater than after the low flow sequence. This large

difference in bed variability illustrated the mobile nature of the sand/silt beds, but also the strong influence of flow rate over bedform geometry in the channel.

Normalizing  $\sigma_z$  by the  $D_{84}$  grain size for all beds emphasizes the impact of grain size on topographic variability and bed roughness (Figure 5.5.2b). For the sand/gravel beds, values of  $\sigma_z$  were on the order of 0.65-0.85 times the  $D_{84}$  grain size, indicating a bed roughness estimate set at the scale of the gravel grains. Conversely,  $\sigma_z/D_{84}$  was much greater than 1.0 for all sand/silt beds, showing that bedform geometry was the dominant factor in setting bed roughness in the unsteady flows. Bedform height has been shown to scale as  $3\sigma_z$ , providing a means to approximate bed roughness scale [Robert and Richards, 1988]. A scaling factor of 1.9 was more appropriate for the sand/silt beds studied here (Figure 5.5.3) because of the time-lag of bedform growth and the limitation set by hydrograph duration. Maximum bed roughness scale can be approximated at the end of each hydrograph succession as 10.0 mm and 15.7 mm for the low and high flow sequences, respectively, which are significantly larger than on the sand/gravel beds.

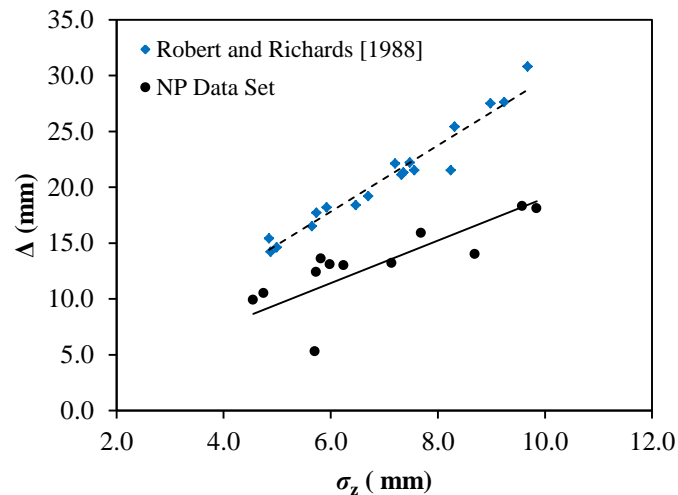


**Figure 5.5.3.** Standard deviation of bed elevations as a predictor of bedform height. Solid and dashed best-fit lines are shown for the no patch data set (slope = 1.9) and Robert and Richards [1988] data set (slope = 3.0), respectively.

### 5.5.3 Channel Adjustment and Stability

Morphological channel adjustment was linked to changes in bedform geometry and topographic variability for the two sediment mixtures. The sand/gravel reaches stabilized in fewer hydrographs than for the sand/silt cases, as measured by the unit bed adjustment parameter,  $\delta_B$ . Reach-scale channel morphology for the sand/gravel beds varied with hydrograph flow magnitude (Figure 5.5.4). Values of  $\delta_B$  varied over the five low flow hydrographs, but stayed within a range of +/- 5% before dropping below 0.5% after the fifth hydrograph. In this case, the  $\delta_B$  parameter illustrated the dynamic processes of net channel erosion and deposition that occurred over a series of unsteady, lower magnitude flow events. The lack of large variability in  $\delta_B$  over these extended time scales showed the limited impact of the lower magnitude flows on altering the reach-scale channel morphology. After the first high flow hydrograph, the channel largely aggraded relative to the equilibrium bed, but after the second hydrograph, the channel stabilized and  $\delta_B$  dropped below the stability threshold. This was an unexpected result given the large magnitude and unsteadiness of the high flow hydrographs, but indicated the widespread aggradation that occurred after the first hydrograph was largely eroded out by the second high flow hydrograph, allowing the bed to adjust back towards a mean condition similar to its reach-scale equilibrium. Gravel acted as a channel stabilizer in the sand/gravel beds, maintaining much of the channel bed morphology as sand was transported through the reach. Thus, these beds experienced smaller net morphological change at the reach-scale over the unsteady flow sequences.

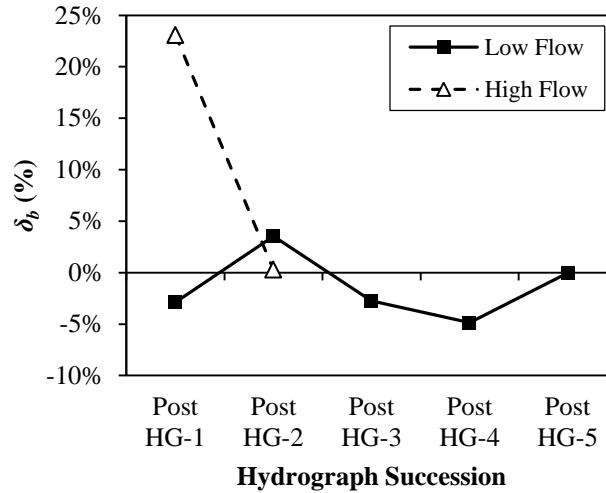


**Figure 5.5.4.** Unit bed adjustment for sand/gravel mixture.

Active bedform adjustment and migration on the sand/silt beds caused a large degree of bed surface change that inhibited the channel's ability to attain a dynamically stable reach condition. These beds experienced large variability between hydrographs, as reflected by the unit bed adjustment parameter. The amount of bed adjustment was greater with initial hydrographs and decreased as the bed approached dynamic stability. As shown in Figure 5.5.5,  $\delta_B$  was initially high following the first low and high flow hydrograph, indicative of net channel aggradation. With subsequent hydrographs, the channel transitioned into a state of net channel erosion, shown by negative values of  $\delta_B$ , which occurred following the second and third hydrographs for the low and high flow conditions, respectively. In the case of the low flow hydrograph sequence, the reach adjusted toward stability from a state of maximum degradation after the 4<sup>th</sup> hydrograph, reaching a dynamically stable  $\delta_B$  value of -0.16% following the sixth hydrograph. The bed adjusted in a similar fashion for the high flow hydrographs. Values of  $\delta_B$  stayed within a smaller range (+/- 5.2%) following the first hydrograph, but based on the stability threshold of 0.5% set in this study, the channel did not stabilize after six high

flow events. However, the trend towards zero (Figure 5.5.5) and the relatively small final  $\delta_B$  of -1.4% do suggest that the channel was adjusting towards a more stable reach and if an additional hydrograph was run,  $\delta_B$  would likely have been closer to, if not below, the 0.5% threshold.

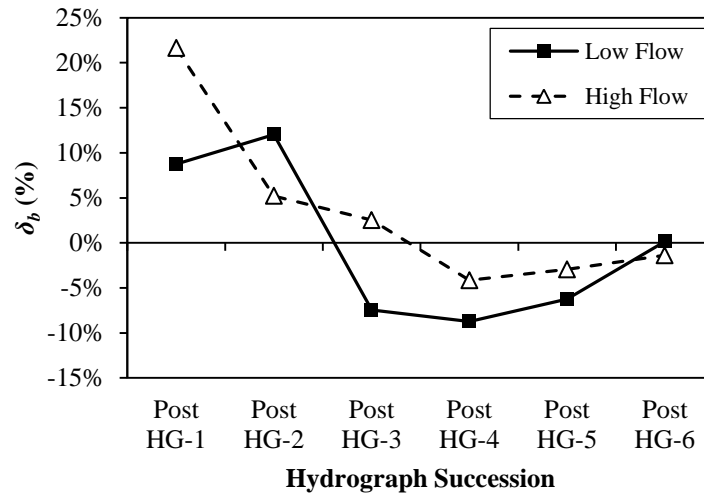


**Figure 5.5.5.** Unit bed adjustment for sand/silt mixture.

For the low flow hydrograph succession on these beds, bedform steepness approximately leveled off after the second hydrograph (Figure 5.5.1). Although the reach did not stabilize until after the sixth hydrograph, a constant value of  $\Delta/\lambda$  appears to indicate reach-scale equilibrium of a mobile sand bed over repeated unsteady flows. The continued increase in bedform steepness for the high flow hydrograph succession was consistent with the dynamic and unstable conditions of the sand/silt beds in the higher unsteady flows.

## 5.6 SUMMARY

Sediment composition greatly influenced channel morphology and how sand/gravel and sand/silt beds adjusted over temporal scales of multiple unsteady flow

events. Sediment mixture grain size distribution controlled bed surface roughness, structure, and topographic variability. For the sand/gravel beds, roughness scaled with the gravel grain size. For the higher flow hydrographs, bimodal transport of the sand/gravel mixture enabled limited sand ripple migration over the gravel surface. In the absence of gravel, substantial ripples formed on the sand/silt beds, which increased in both height and spacing over hydrograph sequences. Ripples were more regular in the low flow hydrograph successions, but ripple heights and spacings were greater for the higher flow repetitions. In both cases, bedform geometry set the surface roughness scale and topographic variability of these sand/silt beds.

A unit bed adjustment parameter, introduced to quantify volumetric bed change over the reach-scale, was used to assess morphological change and classify dynamically stable channel conditions based on a threshold value. The sand/gravel beds reached this threshold for the low and high flows in repetitions of five and two hydrographs, respectively. The sand/silt beds adjusted more variably over time as the stability threshold was reached after six low flow hydrographs but not at all after six high flow hydrographs. Widespread changes over the respective hydrograph successions occurred in the sand/silt channels due to enhanced sediment mobility and the presence, adjustment, and migration of bedforms on the surface. The sand/silt sediment beds had a more variable response to the hydrographs that made adjustments toward dynamic stability more extensive than for the sand/gravel beds, which were able to stabilize at the reach-scale due to the presence of gravel.

## CHAPTER 6

### *Sediment Transport in Unsteady Flows*

---

#### 6.1 INTRODUCTION

This chapter discusses sediment transport in the No Patch (NP) group of experiments. Sand/gravel and sand/silt sediment beds were each tested under repeated low and high flow hydrographs. Bed load and suspended sediment samples were collected during each hydrograph to monitor sediment transport rates for comparison with predictions from six existing transport relationships. Total hydrograph sediment yield was also calculated from these samples and related to hydrograph and sediment characteristics. The primary goal of this chapter is to gain a comprehensive understanding of sediment transport rates, yield, and hysteresis in unsteady flows, and evaluate how well existing relationships and approaches can predict sediment transport in these flow conditions.

#### 6.2 ANALYSIS METHODS

##### 6.2.1 Shear Stress Calculation and Corrections

Bed shear stress ( $\tau_b$ ) was initially calculated using the depth-slope product, with hydraulic radius and energy slope (Equation 6.2.1), and corrected for sidewall effects using the *Vanoni and Brooks* [1957] procedure.

$$\tau_b = \rho g R S_e \quad (6.2.1)$$

Stresses calculated in this manner were directly compared with shear stresses obtained by assuming a logarithmic velocity profile in fully rough flow, and applying the depth-averaged form to estimate shear velocity,  $u_*$ . For the sand/gravel sediment mixture, the roughness length scale,  $k_s$ , was estimated to be a scalar multiple of the  $D_{84}$  grain size. A non-linear regression analysis was run in which this multiple was varied to minimize error between shear stresses calculated with the two different methods. It was found that  $k_s = 0.80 * D_{84}$  was an appropriate roughness scale to provide a suitable trend match between depth-slope and log-law calculated stresses. *Kleinhans and Van Rijn* [2001] approximated  $k_s$  equal to the  $D_{75}$  grain size for bimodal sand/gravel beds. For the sand/gravel beds tested here,  $D_{75}$  was 2.0 mm for Run Set NP-1 (low flows) and 3.1 mm for Run Set NP-2 (high flows), or 41% and 59% of the  $D_{84}$ , respectively. Given the higher sand content (~70%) of these beds relative to those with a higher gravel fraction tested by *Kleinhans and Van Rijn*, a roughness scale of  $0.8 * D_{84}$  is reasonable because it still accounts for the gravel grains. Thus, the depth-slope product was assumed as suitable for shear stress estimates in the unsteady flows.

A similar analysis was conducted for the sand/silt beds, but including bedform geometry as well as grain roughness to estimate total roughness scale (Equation 6.2.2):

$$k_s = k_{s,grain} + k_{s,bedform} \quad (6.2.2)$$

where  $k_{s,grain}$  was estimated to be  $3 * D_{84}$ , consistent with typical grain-scale roughness estimates for sand beds [e.g. *Van Rijn*, 1984b; *Kamphuis*, 1974; *Hey*, 1979], and  $k_{s,bedform}$  was approximated by Equation 6.2.3:

$$k_{s,bedform} = \zeta \frac{\Delta^2}{\lambda} \quad (6.2.3)$$

where  $\zeta$  is a scalar multiple. Bedform height ( $\Delta$ ) and spacing ( $\lambda$ ) prior to and after each hydrograph were obtained from fitted semivariogram model parameters (Table 5.4.1); and the values of each were linearly interpolated during the hydrographs when direct measurements were not possible. With application of these bedform estimates,  $\zeta$  equal to 2.1 was determined from a similar non-linear regression analysis as for the sand/gravel experiments and the total roughness length,  $k_s$ , was determined from Equation 6.2.2. Using the total roughness length, there was good trend and value agreement between calculated shear stresses, so depth-slope product was also utilized for the sand/silt sediment mixture.

Shear stresses for the sand beds were corrected to account for bedform geometry using the *Smith and McLean* [1977] relationship to approximate the skin friction component,  $\tau'$ , of the total shear stress (Equation 6.2.4):

$$\tau' = \tau_b \left\{ 1 + \frac{C_D}{2\kappa^2} \frac{\Delta}{\lambda} \left[ \ln \left( \frac{\Delta}{z_{0,sf}} \right) - 1 \right]^2 \right\}^{-1} \quad (6.2.4)$$

where  $C_D$  is bedform drag coefficient (assumed equal to 0.2),  $\kappa$  is von Karman's constant (0.41), and  $z_{0,sf}$  is the zero velocity bed elevation associated with the skin friction, approximated as  $k_s/30$  for fully rough flow.

## 6.2.2 Existing Transport Relationships

Existing transport equations tested spanned a range of theoretical bases, including excess shear stress, stream power, probabilistic, and empirically-based derivations in order to explore the validity of different approaches in unsteady flows. These relationships were applied within their range of applicable sediment sizes, and therefore, not every relationship was applied to each sediment mixture. Selected transport equations

and their application in this study are listed in Table 6.2.1. Full descriptions of each equation were given in Section 2.3.1.

**Table 6.2.1.** Existing sediment transport relationships.

Relationship	ID	Equations	Sediment Mixture
<i>Ackers and White</i> [1973]	A-W	2.3.1 – 2.3.3	Sand/gravel, Sand/silt
<i>Einstein and Brown</i> [1950]	E-B	2.3.4 – 2.3.6	Sand/gravel, Sand/silt
<i>Engelund and Hansen</i> [1967]	E-H	2.3.7 – 2.3.8	Sand/silt
<i>Laurson</i> [1958]	L	2.3.9 – 2.3.11	Sand/silt
<i>Van Rijn</i> [1984a]	VR	2.3.12 – 2.3.15	Sand/silt
<i>Yang</i> [1973]	Y	2.3.16 – 2.3.18, Table 2.3.3 sand coefficients	Sand/gravel (sand), Sand/silt
<i>Yang</i> [1984]	Y	2.3.16 – 2.3.18, Table 2.3.3 gravel coefficients	Sand/gravel (gravel)

### 6.2.3 Evaluation of Prediction Accuracy

Transport prediction accuracy relative to the new data set was evaluated using several metrics: root mean square error (*RMSE*), discrepancy ratio (*DR*), percent of predictions within an order of magnitude, and percent of predictions within a factor of two. The root mean square error of a data set quantifies differences in measured and predicted values of a given parameter, calculated for unit sediment transport rate ( $q_s$ ) according to Equation 6.2.5:

$$RMSE = \sqrt{\frac{\sum_{i=1}^N (q_s - \hat{q}_s)^2}{N}} \quad (6.2.5)$$

where  $\hat{q}_s$  is the unit sediment transport rate predicted by a given transport equation and  $N$  is the total number of data points. Normalized root mean square error (*NRMSE*) accounts

for data scatter, calculated as the *RMSE* divided by the range of measured values. The discrepancy ratio, or ratio of predicted to measured values ( $\hat{q}_s/q_s$ ), is commonly applied to evaluate the performance of sediment transport equations [e.g. *Yang, 1996; Yang, 2006; Recking et al., 2012*]. Percentage of predictions within a specified range quantifies prediction accuracy while accounting for inherent variability in sediment transport measurements. The transport rates predicted by each equation were compared separately for the high and low flow hydrographs and also as a combined data set for each sediment mixture. The data were used to evaluate the predictive ability of each equation and identify any systematic trends in transport prediction.

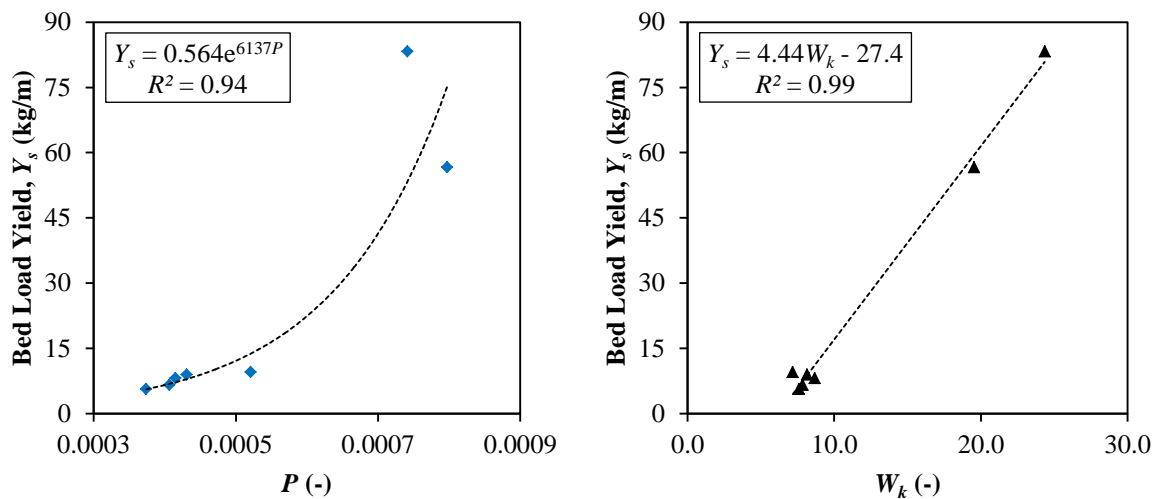
## **6.3 RESULTS: SAND/GRAVEL SEDIMENT MIXTURE**

### **6.3.1 Hydrograph Sediment Yield**

Sediment transport was measured during five low flow and two high flow hydrographs for the sand/gravel sediment mixture. Hydrograph characteristics varied both within a hydrographs series, as well as between low and high flow repetitions. Table 6.3.1 shows the ranges in unsteadiness parameters (Equation 2.3.19) and total flow work (Equation 2.3.22) for each hydrograph. Average flow work of the high flow hydrographs was 2.8 times greater than for the low flow hydrographs. As a result, substantially more transport occurred during the higher flow repetitions, with mean bed load yield ( $Y_b$ ) approximately 9 times greater than for the low flow hydrographs (Table 6.3.1). Across all hydrographs, bed load yield increased exponentially with hydrograph unsteadiness and linearly with total flow work (Figure 6.3.1).

**Table 6.3.1.** Hydrograph parameters and sediment yield (sand/gravel).

Hydrograph Magnitude	Hydrograph Number	$D_{50}$ (mm)	$P$ (-)	$W_k$ (-)	$h_p$ (m)	$Y_s$ (kg/m)	$Y_s/W_k$ (kg/m)
Low	1	0.52	0.00052	7.2	0.129	9.5	1.32
	2	0.52	0.00041	8.7	0.126	8.1	0.93
	3	0.52	0.00041	7.8	0.124	6.6	0.84
	4	0.52	0.00043	8.1	0.127	8.9	1.09
	5	0.52	0.00037	7.6	0.123	5.6	0.74
High	1	0.52	0.00074	24.4	0.164	83.2	3.42
	2	0.52	0.00084	19.6	0.164	56.6	2.90



(a) Hydrograph unsteadiness.

(b) Hydrograph flow work.

**Figure 6.3.1.** Variation in sand/gravel bed load yield with: (a) hydrograph unsteadiness,  $P$ ; and (b) total hydrograph flow work,  $W_k$ . Best fit equations with  $R^2$  coefficients are given and plotted on each graph.

Sediment yield was normalized by the total flow work of each hydrograph to quantify dimensionless relative sediment yield ( $Y_s/W_k$ ) and enable a more direct comparison between hydrographs. Relative bed load yield ranged between 0.74 and 1.32 for the low flow hydrographs, and between 2.90 and 3.42 for the higher flows (Table 6.3.1). Based on mean values, the high flow hydrographs moved approximately 3.2 times more bed load than the low flow hydrographs, relative to each hydrograph's flow work

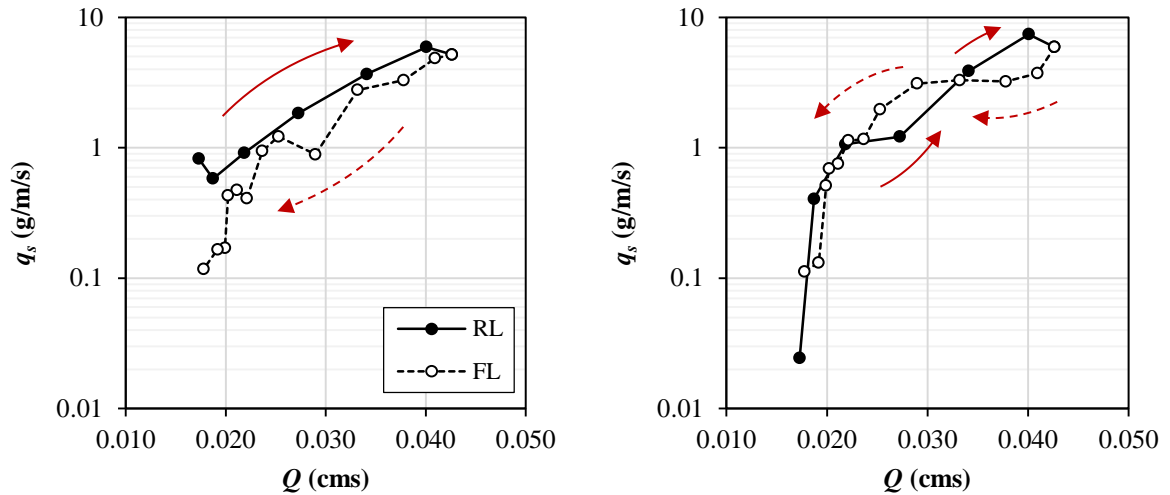
index. Over hydrograph sequences,  $Y_s/W_k$  decreased as successive hydrographs were run. This change was especially measurable for the lower flows, as  $Y_s/W_k$  during the fifth low flow hydrograph was 56% of that during the first hydrograph.

### **6.3.2 Fractional Transport**

Minimal gravel transported during the low flow hydrographs, reaching a maximum fraction of only 1% by weight across the five events. In the two high flow hydrographs, a much larger fraction of gravels was mobilized by comparison, which reached a maximum of 23% by weight of the collected bed load samples. Gravel was mobile during hydrograph intervals around the peak flow, spanning a maximum of 59% of the hydrograph duration. In terms of transport mechanisms, a large amount of suspended material was measured with this sediment mixture, which transported as wash load. The average fraction of wash load was 41% for the low flow hydrograph succession and 37% for the higher flows.

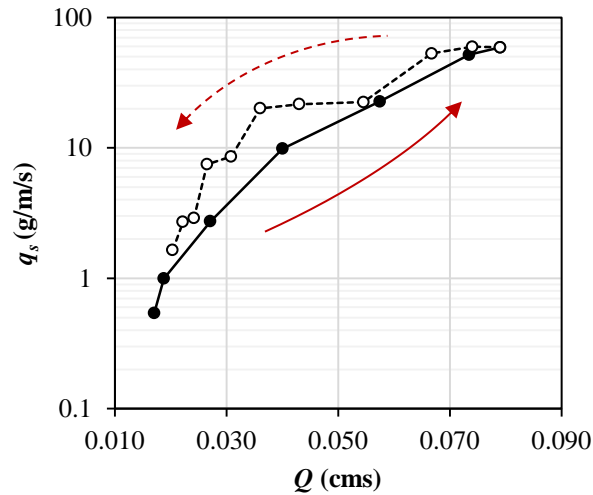
### **6.3.3 Hysteresis of Sand/Gravel Mixture**

Sediment transport hysteresis occurs when different transport rates are measured on the rising and falling limbs of a hydrograph for the same discharge. In these seven hydrographs, hysteresis was measured with a range of behaviors for the total load, bed load, and wash load data sets. Three hydrographs exhibited counterclockwise hysteresis of total load, three showed the figure-eight hysteresis pattern, and one had clockwise hysteresis. Bed load transport patterns included one single-value case (i.e. no hysteresis) and three with clockwise hysteresis of bed load. Wash load transported predominantly with a counterclockwise hysteresis pattern (6 of 7 hydrographs). Example bed load hysteresis curves are shown in Figure 6.3.2.



(a) Clockwise hysteresis (low flow).

(b) Figure-8 hysteresis (low flow).



(c) Counterclockwise hysteresis (high flow).

**Figure 6.3.2.** Sediment transport hysteresis examples (sand/gravel). In all plots, the solid black line with black circles is the rising limb (RL) and the dashed black line with empty circles is the falling limb (FL). Red arrows indicate hysteresis direction, with solid and dashed lines indicating RL and FL, respectively.

### 6.3.4 Sediment Transport Predictions: Sand/Gravel Mixture

Three equations were tested with the sand/gravel sediment (Table 6.3.2). In general, the Yang and Ackers-White equations performed equally well with similar *RMSE* and *DR* within factors of 2.0 and 10. However, the Yang equation provided better

overall fit to the transport data, with a lower median (Table 6.3.2) and narrower range in  $DR$  (Figure 6.3.3), and so for the transport data from the sand/gravel mixture, the Yang equation performed the best.

**Table 6.3.2.** Transport prediction results for sand/gravel mixture.

Equation	$RMSE$	$NRMSE$	Median $DR$	$0.1 \leq DR \leq 10$	$0.5 \leq DR \leq 2.0$
<i>A-W</i>	12.2	20.5%	2.9	97.7%	32.6%
<i>E-B</i>	14.3	24.0%	3.5	91.5%	21.7%
<i>Y</i>	14.6	24.5%	2.4	96.9%	33.3%

However, all three equations for this sand/gravel mixture consistently overpredicted transport rates for the unsteady flows, especially for the lower flow hydrographs (Figure 6.3.4). Predictions for the high flow hydrographs were much more accurate, suggesting that the existing relationships tested here are more appropriately applied to unsteady flow conditions in which the flow magnitudes are higher.

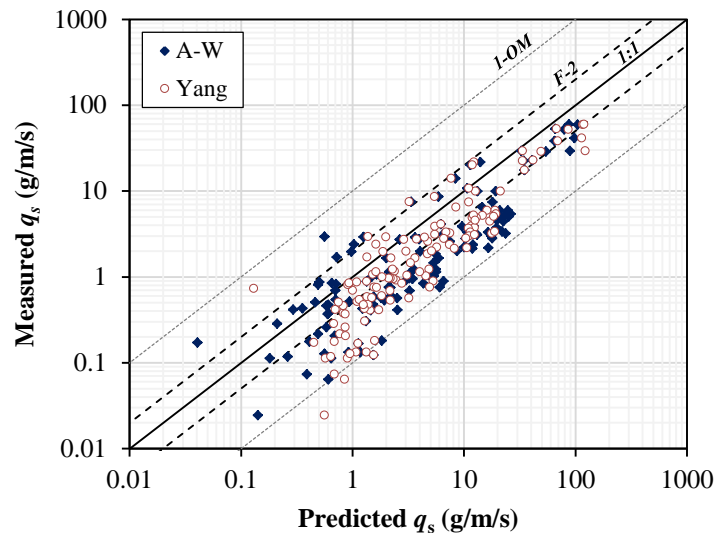


**Figure 6.3.3.** Comparison of Ackers-White and Yang transport predictions (sand/gravel). Lines in the plot correspond to perfect agreement between measured and predicted rates (1:1 line), prediction ranges within one order of magnitude in either direction (1-OM), and prediction ranges within a factor of two in either direction (F-2). These lines maintain the same meanings for all subsequent plots of a similar nature.

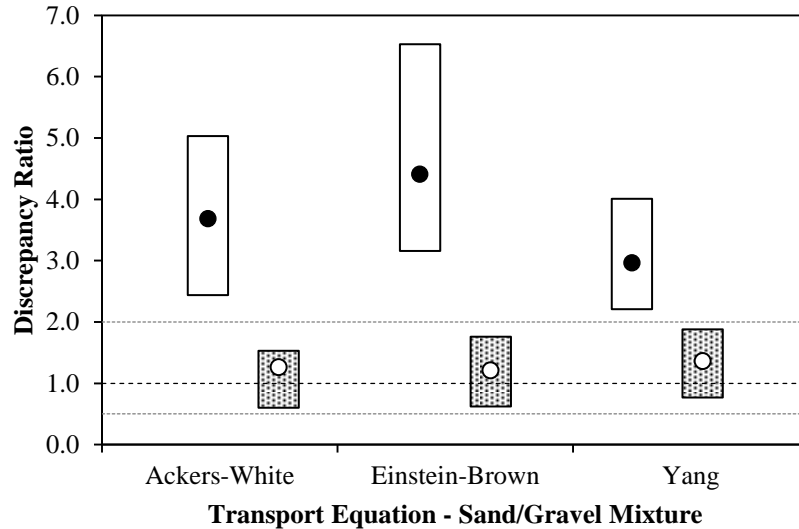


**Figure 6.3.4.** Prediction comparisons for low and high flow hydrographs (sand/gravel). White and hatched boxes indicate the middle 50% of discrepancy ratios (i.e. from 25<sup>th</sup> to 75<sup>th</sup> percentiles) for the low and high flow hydrographs, respectively. Circles within each box indicate the median *DR* values.

## 6.4 RESULTS: SAND/SILT SEDIMENT MIXTURE

### 6.4.1 Hydrograph Sediment Yield

A total of 12 hydrographs (6 each for low and high flows) were run for the second sediment distribution containing sand and silt fractions. Individual hydrographs within each sequence varied in terms of unsteadiness and total flow work parameters (Table 6.4.1). Average flow work for the six high flow hydrographs was approximately 3.9 times greater than for the lower flows. Relative bed load yield showed a similar, but less pronounced discrepancy as on average 1.8 times more bed material transported during a high flow hydrograph. Bed load yield increased with both hydrograph unsteadiness and total flow work (Figure 6.4.1), although fitted relationships did not show strong correlations in either case. No well-defined relationship of  $Y_s/W_k$  over hydrograph succession was observed (Pearson's correlation coefficient  $r = -0.13$  and  $r = 0.07$  for low

and high flow hydrographs, respectively), indicating a highly active and mobile bed over the temporal scales of repeated flow events.

**Table 6.4.1.** Hydrograph parameters and sediment yield (sand/silt).

Hydrograph Magnitude	Hydrograph Number	$D_{50}^a$ (mm)	$P$ (-)	$W_k$ (-)	$h_p$ (m)	$Y_s$ (kg/m)	$Y_s/W_k$ (kg/m)
Low	1	0.37	0.00085	2.1	0.128	6.8	3.23
	2	0.37	0.00078	2.9	0.129	6.7	2.34
	3	0.37	0.00075	3.5	0.131	14.2	4.12
	4	0.37	0.00075	3.2	0.131	13.3	4.17
	5	0.37	0.00050	6.5	0.129	12.3	1.88
	6	0.37	0.00050	4.7	0.128	14.5	3.05
High	1	0.43	0.00101	12.3	0.166	57.3	4.65
	2	0.43	0.00094	14.7	0.169	99.5	6.78
	3	0.43	0.00093	15.1	0.168	99.3	6.56
	4	0.43	0.00068	23.8	0.166	59.5	2.50
	5	0.43	0.00113	8.7	0.167	69.9	8.07
	6	0.43	0.00114	15.6	0.168	80.6	5.18

<sup>a</sup>Final bed values due to drastic changes in bed composition measured (see Section 5.4.1).

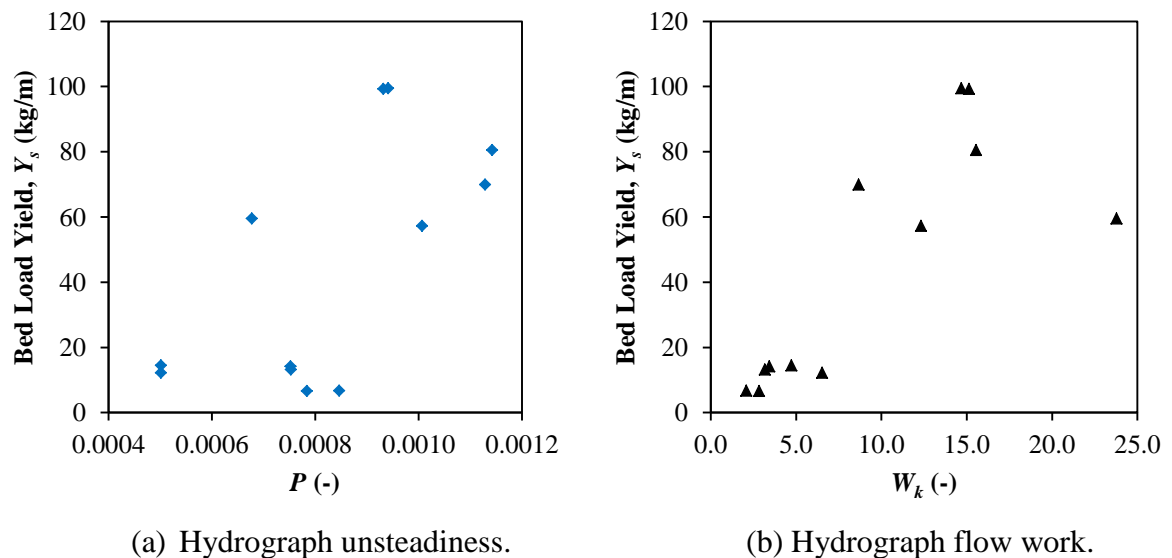


**Figure 6.4.1.** Variation in sand/silt bed load yield with: (a) hydrograph unsteadiness,  $P$ ; and (b) total hydrograph flow work,  $W_k$ . Fitted relationships were not strong, and therefore, are not plotted in either graph.

### **6.4.2 Fractional Transport**

A distinct trait of the transport measured for this sediment mixture was the dominance of suspended material relative to the total sediment transport. The finer fractions in the initial bed were entrained rapidly when flow started and stayed in the system as wash load. For the low flow hydrographs, the wash load fraction varied between 85 and 96% of the total load. Similarly, wash load comprised 84-93% of the total load for the high flow hydrographs. The amount of sediment in suspension drastically increased total yield estimates for hydrographs of this sediment mixture. When considering only bed load yield, high flow hydrographs moved an average of 7.1 times more sediment than the low flow hydrographs.

### **6.4.3 Hysteresis of Sand/Silt Mixture**

The prevalence of wash load for this sediment mixture was reflected in the hysteresis patterns measured during the different hydrographs. In each of the 12 hydrographs, wash load transport showed counterclockwise behavior, with more sediment transported following the hydrograph peak. Because of the high proportion of wash load, the total load hysteresis also had a counterclockwise hysteresis pattern for each hydrograph. However, total load behavior stemming from high suspended sediment for these experiments masked the variation in bed load transport. Of the 12 hydrographs, each of the five major classes of hysteresis was measured for bed load transport at least once, including single-value, or no hysteresis. The 8-loop pattern was measured most often (5 out of 12 hydrographs), followed next by counterclockwise transport. In general, temporal patterns of bed load transport were much more variable than suspended load transport.

#### 6.4.4 Sediment Transport Predictions: Sand/Silt Mixture

Transport was predicted for the sand/silt mixture using six different equations (Table 6.4.2). The Laursen and Yang equations performed the best, with the lowest *NRMSE* and highest percentage of predictions within a factor of 2.0 of the measured transport rates. Direct comparison of these two methods reveals that 58% of predictions with the Yang relationship were within a factor of 2.0, as opposed to 49% for the Laursen. Additionally, the median *DR* for Yang predictions was nearly 1.0, signifying better accuracy than the Laursen method (median *DR* = 2.0), even though Laursen predictions had a lower root mean square error. Figure 6.4.2 highlights the scatter associated with predictions obtained using each method and the higher accuracy of the Yang equation, as indicated by closer grouping of points along the measured/predicted equals 1.0 line, particularly for larger transport rates.

**Table 6.4.2.** Transport prediction results for sand/silt mixture.

Equation	<i>RMSE</i>	<i>NRMSE</i>	Median <i>DR</i>	$0.1 \leq DR \leq 10$	$0.5 \leq DR \leq 2.0$
<i>A-W</i>	14.8	15.1%	0.5	68.0%	33.3%
<i>E-B</i>	15.1	15.4%	0.2	65.4%	18.9%
<i>E-H</i>	16.0	16.3%	0.5	97.4%	39.0%
<i>L</i>	10.0	10.2%	2.0	90.0%	48.7%
<i>VR</i>	21.1	21.5%	1.0	80.7%	41.7%
<i>Y</i>	13.6	13.9%	1.1	95.2%	57.9%

Unlike with the sand/gravel mixture, there was no systematic overprediction in transport rates for the sand/silt beds (Figure 6.4.3). The Ackers-White, Einstein-Brown, and Engelund-Hansen all underpredicted transport rates, while overprediction was more common with the Laursen, Van Rijn, and Yang formulas. Additionally, the discrepancy in prediction accuracy between the low and high flow hydrographs for the sand/gravel

beds was not measured for the sand/silt mixture (Figure 6.4.3). Median  $DR$  values were slightly improved for higher flow hydrographs, but the improvement was not as drastic as with the sand/gravel mixture (Figure 6.3.4).

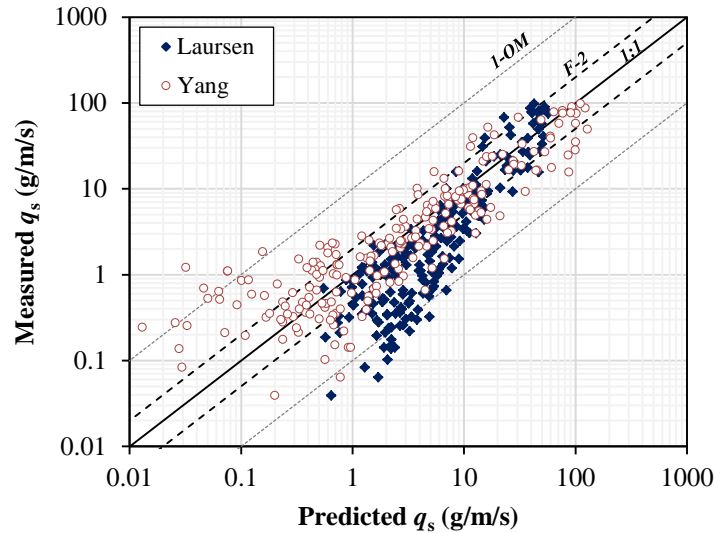


**Figure 6.4.2.** Comparison of Laursen and Yang transport predictions (sand/silt).

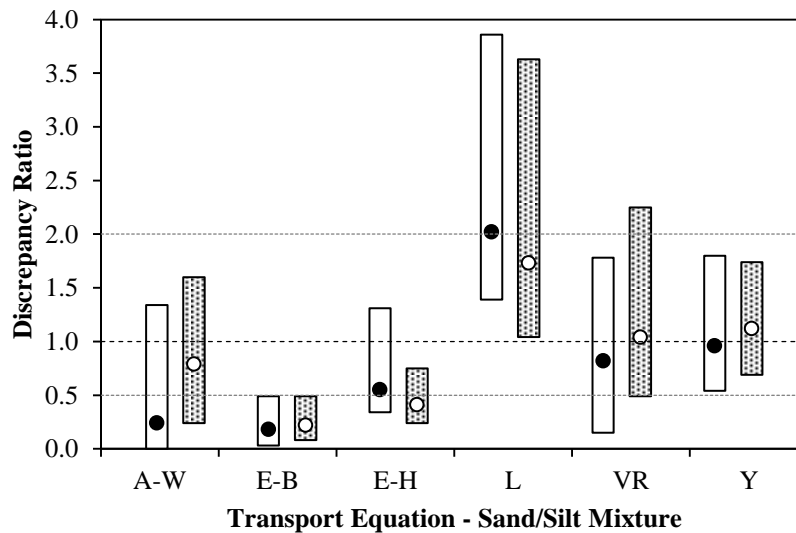


**Figure 6.4.3.** Prediction comparisons for low and high flow hydrographs (sand/silt). White and hatched boxes indicate the middle 50% of discrepancy ratios (i.e. from 25<sup>th</sup> to 75<sup>th</sup> percentiles) for the low and high flow hydrographs, respectively. Circles within each box indicate the median  $DR$  values.

## 6.5 DISCUSSION

### 6.5.1 Effect of Sediment Mixture on Bed Load Yield

Flow magnitude and bulk bed sediment distribution impacted the cumulative bed load yield during the unsteady flow hydrographs (Figure 6.5.1). For each sediment mixture, mean relative bed load yield ( $Y_s/W_k$ ) for the high flow hydrographs was more than double that of the low flow hydrographs. For similar flow magnitude hydrographs, relative yield was greater for the sand/silt sediment than for the sand/gravel. Additionally, larger variability in bed load yield was measured for the sand/silt mixture, as indicated by the range in yield values illustrated in Figure 6.5.1.

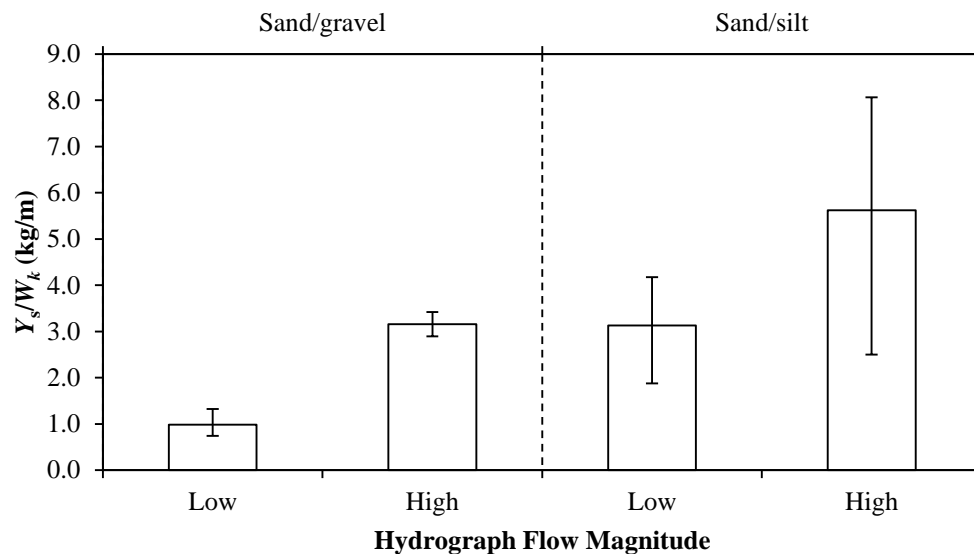


**Figure 6.5.1.** Relative bed load yield comparison. Columns represent mean bed load yield normalized by hydrograph flow work for a given combination of hydrograph flow magnitude and sediment mixture. Bars represent minimum and maximum values, relative to the mean.

In the sand/gravel mixture, sand was largely sheltered by gravel grains, making it more difficult for the sand to be entrained. With the gravel fraction absent from the sand/silt beds, the surface sheltering was also removed. Therefore, increased yield for the

sand/silt beds was the result of increased mobility of the sand grains when gravel was no longer present in the channel. Greater variability in the sand/silt yield can be attributed to this increased mobility, and also the prevalence and irregularity of bedforms on the surface. In the sand/gravel cases, there was limited gravel transport which allowed gravel to persist on the channel surface. Bedforms did not form during the low flow hydrographs, and were limited in size and extent of bed coverage during the high flows. The lack of bedforms for this sediment mixture reduced variability in the measured sediment yields relative to the predominantly sand beds in which bedforms developed, migrated, and adjusted due to sediment transport during the unsteady flow hydrographs.

### **6.5.2 Hydrograph Bed Load Yield Prediction**

The ability to predict how much sediment will be transported during a flood event is useful in assessing potential channel change and downstream impacts in unsteady flow conditions. Dimensional analysis conducted by past researchers has related sediment transport rates to dimensionless hydrograph characteristics, specifically its unsteadiness ( $P$ ) and total flow work ( $W_k$ ). *Lee et al.* [2004] found that total bed load yield increased with hydrograph unsteadiness according to a power law (Equation 2.2.23). *Bombar et al.* [2011] non-dimensionalized the total bed load (Equation 2.2.25) and developed an exponential relation with a modified unsteadiness parameter (Equation 2.2.24) and linear relationship with total flow work (Equation 2.3.26). While the impacts of hydrograph unsteadiness and total flow work on sediment yield have been documented separately, these parameters have yet to be combined in a predictive capacity, especially for finer bed material. Thus, a non-dimensional descriptor variable,  $\chi$ , is proposed here that takes into consideration both the unsteadiness and total flow work of a hydrograph, as well as

peak flow depth ( $h_p$ ) and channel bed  $D_{50}$  (Equation 6.5.1):

$$\chi = \frac{PW_k h_p}{D_{50}} \quad (6.5.1)$$

Although not derived from a strict dimensional analysis,  $\chi$  is dimensionless and can be approximated using representative values for a given channel and flow event, and therefore, may provide some basic applicability for estimating bed load yield. A regression analysis showed that  $\chi$  estimated non-dimensional bed load yield well ( $R^2 = 0.83$ ) for the NP data set with the power law relationship given in Equation 6.5.2 and shown in Figure 6.5.2.

$$Y_s^* = 22,762\chi^{1.072} \quad (6.5.2)$$

By combining hydrograph unsteadiness and flow work index, this regression equation expands on previous experimental work that individually linked these parameters to total bed load yield [Lee *et al.*, 2004; Bombar *et al.*, 2011], while also incorporating peak flow depth and median channel grain size. Variability in the yield prediction is on the order of 17%, which is somewhat substantial when considered relative to the large magnitudes of  $Y_s^*$  measured with the fine material used in the present study. However, this proposed relation is meant to provide initial estimates of how much sediment might be expected to move for a given storm event, as well as serve as a reference to compare the influence of vegetation on hydrograph yield. Efforts to combine the NP data set with that of previous researchers were unsuccessful, likely because of the large discrepancy in grain sizes and the presence of heterogeneous mixtures in these experiments. Therefore, Equation 6.5.2 is presented with the caveat that it may be more applicable for finer grained channels, with median grain sizes below 1 mm.

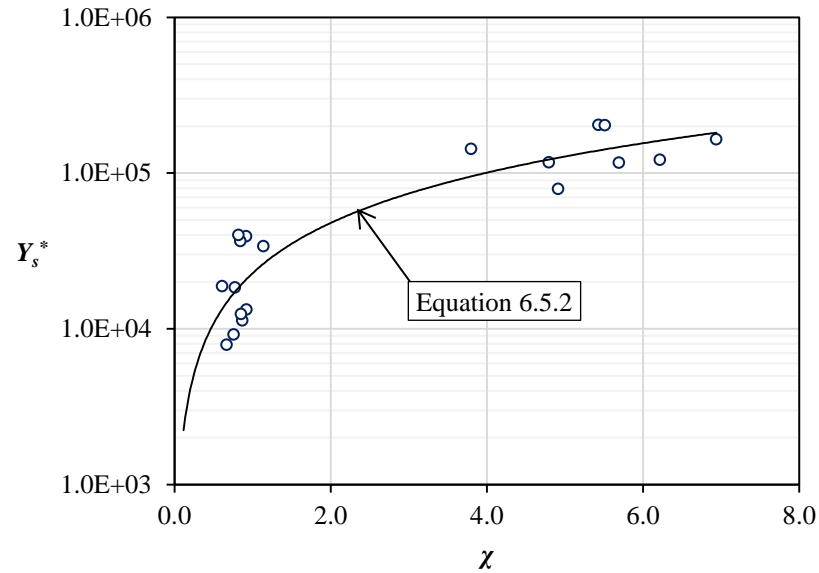


**Figure 6.5.2.** Bed load yield prediction for no patch data set.

### 6.5.3 Transport Hysteresis of Bed and Wash Load

#### *Bed Load Hysteresis*

Sediment transport hysteresis was measured in the majority of hydrographs for each sediment mixture. Although bed load hysteresis typically shows counterclockwise transport, a range of patterns occurred in these experiments, including clockwise, counterclockwise, and figure-8 loops, as detailed in Chapter 2. Hysteretic transport has often been linked to lags in bedform development relative to changes in flow [e.g. *Martin and Jerolmack*, 2013; *Lee et al.*, 2004; *Griffiths and Sutherland*, 1977]. Using this lag concept, a conceptual framework for explaining the hysteresis in these experiments is presented based on estimates of bedform geometry prior to and following a given hydrograph (Sections 5.3.2 and 5.4.2). The framework summarized in Table 6.5.1 is based on the idea that if bedform steepness ( $\Delta/\lambda$ ) increases during a hydrograph, much of the geometric adjustment is likely to lag behind the peak flow, and therefore, sediment transport should decrease corresponding to a reduction in skin friction shear stress and

thus, clockwise hysteresis should occur. The opposite is assumed true for a reduction in steepness, resulting in more transport after the peak flow rate and counterclockwise hysteresis.

**Table 6.5.1.** Conceptual framework to assess bedform related hysteresis.

$\Delta/\lambda$ Change	Transport Comparison	Hysteresis Pattern
Increases	$q_{s-RL} > q_{s-FL}$	Clockwise (CW)
Decreases	$q_{s-RL} < q_{s-FL}$	Counterclockwise (CCW)

This conceptual framework was applied to the three run sets for which bedforms developed (NP-2: high flows, sand/gravel; NP-3: low flows, sand/silt; NP-4: high flows, sand/silt). The framework matched the measured hysteresis for only 3 of the 7 CW or CCW cases. However, when including hydrographs in which figure-8 transport hysteresis transport occurred, the agreement dramatically improved. Because 8-loop patterns contain both CW and CCW hysteresis, bedform adjustment and lags should also impact this type of sediment transport. Considering all hydrographs in the three run sets, the conceptual framework and measured transport hysteresis agreed in 67% of the hydrographs in which hysteresis occurred. Without detailed, temporal bedform geometry estimates during each hydrograph, this conceptual framework remains somewhat rudimentary in nature. However, it does support the idea that bedform adjustment and lag can cause variable sediment transport over a flow event, inferring hysteresis behavior based on estimates of bedform steepness from before and after a flood event, or vice versa.

Bed load hysteresis in these experiments was also influenced by antecedent hydrologic conditions in that the first hydrograph of each series showed a CCW transport

pattern or a figure-8 loop in which more material was moved during the lower loop, analogous to initial CCW hysteresis. An antecedent low flow can consolidate bed material [Reid *et al.*, 1985]. The preceding 18-hour baseflow period in these experiments likely acted to consolidate and, in part, stabilize the bed such that grains were harder to entrain on the rising limb of the first hydrograph, thus creating a counterclockwise hysteresis transport pattern.

When no bedforms developed during the hydrograph, as in the first run set of experiments (NP-1: low flows, sand/gravel), bed load hysteresis was most likely caused by lags in transport distance as a result of patchy bed sediment sources along the reach creating temporal fluctuations of bed load movement [e.g. Lisle and Madej, 1992]. Appendix D.1 (NP-1) illustrates some of the sand patchiness on the bed surfaces in this run set.

### ***Suspended and Wash Load Hysteresis***

The consistent counterclockwise hysteresis of the suspended sediment samples was contradictory to the expected behavior of suspended sediment concentration (SSC) in unsteady flows in which more material is transported in suspension on the rising limb of a hydrograph [e.g. Asselman, 1999; Ahanger *et al.*, 2008]. Because suspended sediment transport is a non-capacity load [Asselman, 1999], instantaneous transport rates are functions of sediment supply. Therefore, SSC behavior in the unsteady experiments indicated that the fine sediment supply in the recirculation system set the suspended load transport, rather than entrainment from and deposition onto the channel bed. Particularly for the sand/silt mixture, material in suspension during the unsteady experiments was much finer than the bed sediment, which is characteristic of wash load [Einstein and

*Chien*, 1953]. Additionally, the silt and clay fractions of sediment for this mixture had Rouse numbers ( $\omega/\kappa u_*$ ) less than 0.8, a typical limit for wash load [e.g. *Hearn*, 2008; *Yuill and Nichols*, 2011]. In a recirculation system, the sediment supply is constant, so it is reasonable to conclude that the samples collected during the experiments monitored wash load more than suspended sediment load. Thus, for purposes of calculating sediment transport rates and yield, results are focused on bed load rather than total load.

#### **6.5.4 Analysis of Sediment Transport Predictions in Unsteady Flows**

##### ***Total Transport Relationships***

Prediction accuracy varied with existing transport relationship, sediment mixture, and hydrograph flow magnitude. For the sand/gravel mixture, predictions of transport rates during the high flow hydrograph sequences were more accurate than for the lower flows for each sediment transport equation. Improved transport prediction at higher flows is common [e.g. *Recking et al.*, 2012], especially for equations that include incipient motion thresholds. Such relationships are susceptible to how critical shear stress is defined and wide variations in  $\tau_c^*$  values have been reported [*Buffington and Montgomery*, 1997]. Of the three equations tested, the Yang relationship includes critical velocity for threshold motion while Ackers-White equation relies on a critical sediment mobility parameter based on grain size. In both equations, these thresholds were developed for uniform sediments, and therefore, could overpredict sand transport rates in a mixture. Although the Ackers-White equation was applied to the sand/gravel mixture with the *Proffitt and Sutherland* [1983] hiding factor to account for mixture properties, transport was still widely overpredicted for the low flow hydrographs.

Systematic overprediction was in part due to the application of total load transport equations to predominantly bed load data. Suspended sediment samples collected during hydrographs more accurately reflected wash load in the recirculation system, and therefore, were not included in calculation of total load transport. Thus, some overprediction of transport rates was expected. However, consistent overprediction was not measured for the sand/silt beds (Figure 6.4.3) as accuracy varied across the six transport models applied, suggesting diminished reliance on incipient motion criterion for a more poorly sorted bed.

Of the existing relationships tested, the Yang equation gave the most accurate transport predictions for both sediment mixtures. This equation was derived using the concept that total bed-material load must be directly related to unit stream power, which is the product of flow velocity and energy slope [Yang, 1973]. It is sensitive to settling and shear velocities, making it necessary to use bedform-corrected shear stresses to calculate  $u_*$  in the sand/silt mixture in which ripples were prevalent on the bed surface. Yang predictions that did not directly account for bedforms had higher *RMSE* and median *DR* values (15.0 and 1.4, respectively) than those reported in Table 6.4.2. Although the Yang relationship does include a critical velocity component developed for uniform sediment, its stream power basis appears to make it applicable for the unsteady flow conditions and sediment distributions tested here.

### ***Fractional Bed Load Transport Relationships***

Fractional transport during unsteady flows was evaluated using a dimensionless, reference shear stress approach in which the dimensionless bed load transport,  $W_i^*$ , is calculated with Equation 6.5.3:

$$W_i^* = \frac{(s-1)gq_s}{F_i u_*^3} \quad (6.5.3)$$

where  $s$  is specific gravity of the sediment and  $F_i$  is the fraction of grain size  $i$  on the bed surface. Reference dimensionless shear stress ( $\tau_{ri}^*$ ) was estimated for three sediment fractions: the sand and gravel fractions separately in the sand/gravel mixture, and the sand in sand/silt mixture. Similar to the approach taken by *Guney et al.* [2013], a regression analysis was applied in which the reference shear stress for fraction  $i$  was adjusted to minimize the error between measured transport rates and those predicted by Equation 6.5.4, which represents the *Einstein* [1950] relation as interpreted by *Parker* [1979]. In this manner,  $\tau_{ri}^*$  was used as a similarity parameter to collapse fractional transport rates for each grain fraction to the Parker-Einstein equation, providing a single transport relation for multiple grain sizes. Reference shear stresses were calculated as 0.079, 0.014, and 0.019 for the sand/gravel sand fraction ( $\tau_{r,S/G-s}^*$ ), gravel fraction ( $\tau_{r,S/G-g}^*$ ), and sand/silt sand fraction ( $\tau_{r,S/S}^*$ ), respectively.

$$W_i^* = 11.2 \left( 1 - 0.8531 \frac{\tau_{ri}^*}{\tau_i^*} \right)^{4.5} \quad (6.5.4)$$

Once reference shear stresses were estimated, a dimensionless equation of the form shown in Equation 6.5.4 was used with modified coefficients to estimate transport rate as a function of excess shear stress above the reference value for each respective grain fraction (Equation 6.5.5).

$$W_i^* = a \left( 1 - 0.8531 \frac{\tau_{ri}^*}{\tau_i^*} \right)^b \quad (6.5.5)$$

The coefficients  $a$  and  $b$  were derived using non-linear regression to first

minimize the *RMSE* with the unsteady flow data set, then obtain a median discrepancy ratio of 1.0. Using this approach, the regression produced values of  $a = 12.3$  and  $b = 4.73$ , resulting in the curve shown in Figure 6.5.3 for fractional bed load transport rate,  $W_i^*$ . While there is much scatter in the data set, transport predictions using the dimensionless transport relationship with the fitted coefficients are comparable to those with the total transport equations tested, predicting transport rates with *RMSE* and *NRMSE* of 10.8 and 11.1%, respectively. Additionally, 88.5% of the predicted transport rates fall within one order of magnitude of the measured rates, 47.6% fall within a factor of 2.0.

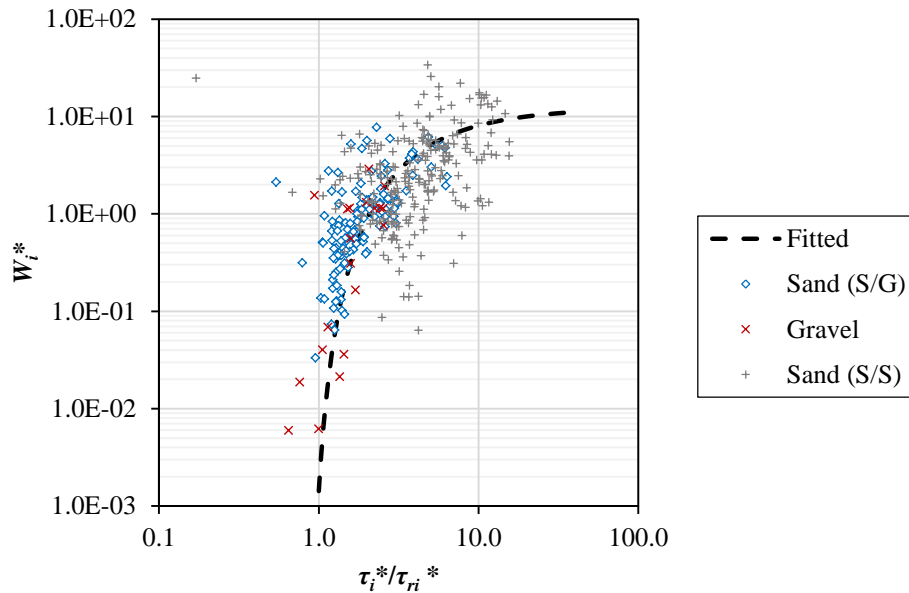


**Figure 6.5.3.** Dimensionless bed load transport prediction ( $R^2 = 0.58$ ).

An additional dimensionless transport relationship was developed to better account for the temporal variability in bed load transport that occurred during individual hydrographs, as well as over a series of repeated unsteady flow events. Specifically, reference shear stresses for the three size fractions were estimated separately for each limb of each individual hydrograph using Equation 6.5.4 and the regression approach

described above. The unsteady flow data sets were divided according hydrograph limb and, using the detailed reference shear stresses given in Table 6.5.2, regression coefficients  $a$  and  $b$  in Equation 6.5.5 were derived for hydrograph rising and falling limbs separately. Coefficients determined using this methodology, termed the separate limb approach, are given in Table 6.5.3 and the relationships are plotted in Figure 6.5.4.

**Table 6.5.2.** Reference shear stresses for each hydrograph and limb.

Flow Magnitude	Hydrograph	$\tau_{r,S/G-s}^*$		$\tau_{r,S/G-g}^*$		$\tau_{r,S/S}^*$	
		RL	FL	RL	FL	RL	FL
Low	1	0.083	0.076	0.016	0.016	-	-
	2	0.089	0.091	0.016	0.016	-	-
	3	0.104	0.105	0.015	0.015	-	-
	4	0.083	0.065	0.013	0.013	-	-
	5	0.092	0.105	0.013	0.013	-	-
High	1	0.075	0.041	0.015	0.014	-	-
	2	0.087	0.099	0.011	0.016	-	-
Low	1	-	-	-	-	0.085	0.076
	2	-	-	-	-	0.077	0.041
	3	-	-	-	-	0.010	0.025
	4	-	-	-	-	0.029	0.023
	5	-	-	-	-	0.017	0.014
	6	-	-	-	-	0.022	0.026
High	1	-	-	-	-	0.024	0.027
	2	-	-	-	-	0.004	0.013
	3	-	-	-	-	0.005	0.014
	4	-	-	-	-	0.026	0.027
	5	-	-	-	-	0.008	0.014
	6	-	-	-	-	0.010	0.023

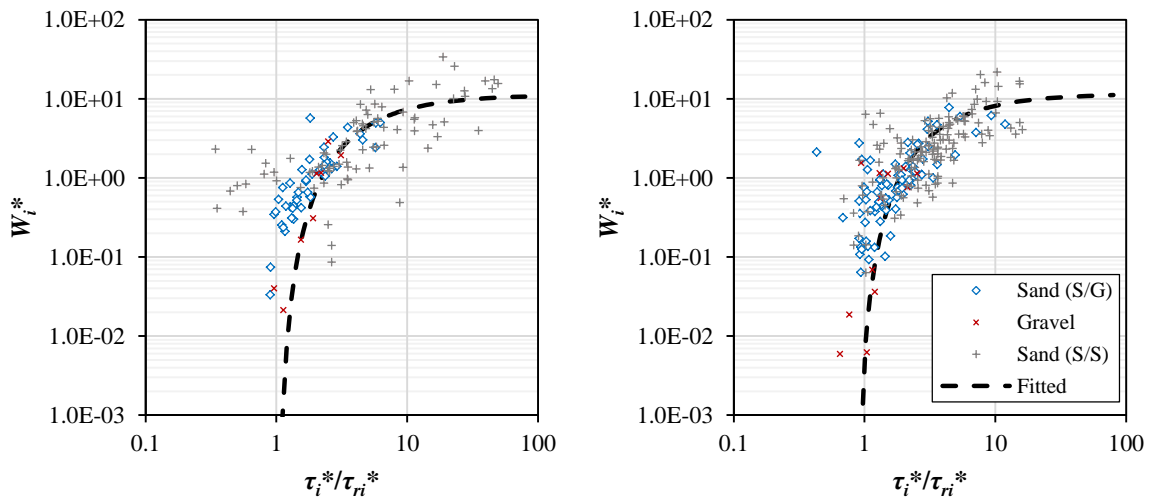
**Table 6.5.3.** Dimensionless transport coefficients.

Data Subset	$a$	$b$
All	12.3	4.73
Rising Limb (RL)	11.3	4.06
Falling Limb (FL)	11.7	3.98

Predictions obtained using the separate limb approach had improved accuracy when compared to what was obtained for the full hydrographs, which used the same fractional reference shear stresses for both rising and falling limbs across the collection of hydrographs. All accuracy metrics were improved for the separate limb relationships (Table 6.5.4), and the decreased root mean square error was reflective of reduced scatter in the transport predictions.

**Table 6.5.4.** Dimensionless unsteady flow transport prediction results.

Approach	RMSE	NRMSE	Median DR	$0.1 \leq DR \leq 10$	$0.5 \leq DR \leq 2.0$
Full Data Set	9.5	9.7%	1.0	82.6%	51.0%
Separate Limb	7.3	7.4%	1.0	84.0%	55.7%



(a) Rising Limb ( $R^2 = 0.61$ ).

(b) Falling Limb ( $R^2 = 0.71$ ).

**Figure 6.5.4.** Separate limb fractional bed load transport relationships.

### *Comparison of Transport Approaches*

For direct comparison with predictions using the Yang Equation, fractional unit transport rates,  $q_{si}$ , were calculated by combining Equations 6.5.3 and 6.5.5 to form Equation 6.5.6:

$$q_{si} = a \frac{F_i u_*^3}{(s-1)g} \left( 1 - 0.8531 \frac{\tau_{ri}^*}{\tau_i^*} \right)^b \quad (6.5.6)$$

with the appropriate  $a$  and  $b$  coefficients obtained from regression (Table 6.5.3). Because the dimensionless relationships were derived for the full data set using a fractional transport approach, Yang predictions for the sand/gravel and sand/silt data sets were combined to evaluate the accuracy of each transport model against one another for the full range of sediment conditions tested.

Overall, the fractional dimensionless bed load relationships provided more accurate transport predictions than the Yang equation for the unsteady flow data set (Tables 6.5.4 and 6.5.5; Figure 6.5.5), especially when using the separate limb, fractional approach. Bed load transport is a temporally variable process due to its stochastic nature, the presence of bedforms, grain sorting, hysteresis, and supply limitation [Recking *et al.*, 2012]. Thus, the separate limb relationships in which 55.7% of transport predictions were within a factor of two was encouraging given the scatter in the unsteady flow transport measurements. The only accuracy metric in which the Yang was superior to the dimensionless separate limb relationships was the percent of predictions within an order of magnitude. Most of these poor predictions were at low transport rates (Figure 6.5.5) and should not impact the prediction accuracy when considering unsteady flow events in which increased sediment transport is expected.

**Table 6.5.5.** Yang prediction results for combined sand/gravel and sand/silt data set.

Approach	RMSE	NRMSE	Median DR	$0.1 \leq DR \leq 10$	$0.5 \leq DR \leq 2.0$
Yang	14.0	14.3%	1.4	95.8%	49.0%

Predicting sediment transport with different relationships on the rising and falling limbs was previously applied to suspended sediment concentrations in flume experiments [Ahanger *et al.*, 2008], but has not been as widely used or successful for bed load transport during unsteady flows. A single relationship adequately predicted bed load on both limbs for flash floods in an ephemeral stream [Cohen *et al.*, 2010], suggesting that transport on each hydrograph limb can be grouped together in some cases. Yet, widespread observation of transport hysteresis implies that treating each hydrograph limb independently might better capture unsteady flow transport dynamics.

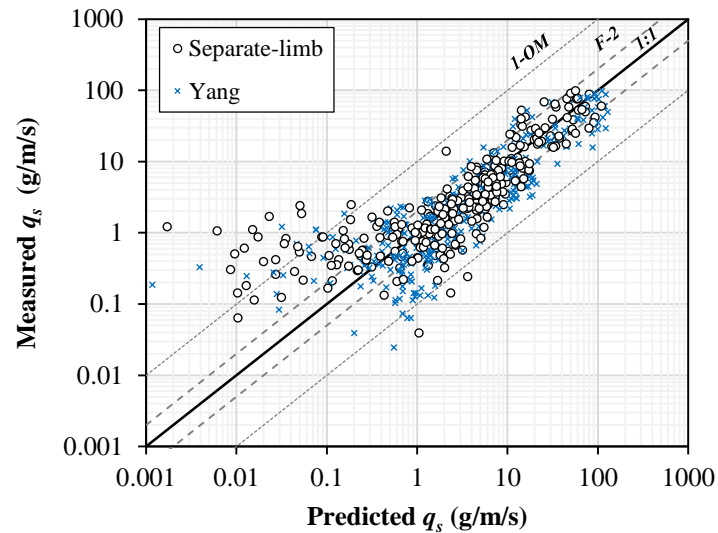


**Figure 6.5.5.** Comparison of Yang and dimensionless bed load transport predictions. Predictions from the separate limb dimensionless relationships are shown.

Application of different reference shear stresses prior to and following the hydrograph peaks incorporated information about sediment mobility and bed structure changes during an unsteady flow sequence that in part contributed to hysteresis. Different entrainment thresholds on rising and falling limbs have previously been attributed to surface rearrangement for gravel bed rivers [e.g. Mao, 2012]. The same concept appears

to be present here for both the sand/gravel beds in which the gravel added surface complexity and sand patchiness was observed, as well as for the sand/silt beds in which bedforms were widely present. In particular, differences in reference shear stresses between hydrograph limbs for the sand/gravel mixture agreed with the measured transport hysteresis during all hydrographs. Thus, regression coefficients developed with consideration of temporally varying reference shear stresses implicitly accounted for unsteady flows and variable transport behavior.

While varying hysteresis patterns were measured in these experiments, the derived separate limb relationships imply counterclockwise hysteresis in all cases, which is consistent with typical observations of bed load transport. This lack of full agreement can partly be attributed to inherent variability in sediment transport and uncertainty in its measurement, especially in unsteady flow conditions. However, a separate limb transport approach does appear to have some merit because it captures part of the temporal variability in transport. Separate limb analysis could potentially provide better estimates of sediment transport in unsteady flows if applied more broadly, including a possible extension to existing formulas such as the *Yang* [1973] equation, which would require reanalysis of original data sets used in equation formulation with perhaps inclusion of new ones.

## **6.6 SUMMARY**

Sediment composition was a dominant factor in sediment transport and yield over repeated unsteady flows. Larger bed load yields were measured from the sand/silt beds, which were predominantly comprised of sand as most of the silt and clay fractions of the mixture were entrained as wash load. Increased mobility and bedform development

resulted in larger variability in yield and transport rates for the sand beds that wasn't present in the sand/gravel beds because the gravel fraction acted to partly shelter sand grains and inhibit entrainment, while providing a sort of stabilizing impact on the channel morphology. A predictive relationship for hydrograph bed load yield was proposed based on a dimensionless descriptor variable,  $\chi$ , which incorporates channel grain size with peak hydrograph flow depth, unsteadiness, and total flow work. The relationship did an adequate job of predicting bed load yield, but because it is subject to large uncertainty for finer sediment sizes, should be applied only for generating initial yield estimates.

Some type of bed load transport hysteresis was measured during most hydrographs, including clockwise, counterclockwise, and figure-8 loops. Using the basis that bedform adjustment often lags behind changes in flow, a conceptual hysteresis-bedform framework was developed utilizing bedform geometry estimates prior to and after a hydrograph. The framework adequately agreed with the measured hysteresis patterns, but other factors such as bed surface patchiness and antecedent hydrologic conditions were also shown to impact temporal patterns of transport.

Evaluation of six existing sediment transport relationships showed that total transport predicted with the *Yang* [1973] equation best matched the unsteady transport measurements in these experiments for each sediment mixture. This suggests that a transport relationship based on stream power may have the most applicability for predicting transport in unsteady flows relative to existing transport models that incorporate excess shear stress or probabilistic components. Total transport predictions with the Yang equation were especially good for the sand/silt mixture, likely because these beds were poorly sorted and the equation was derived for uniform sediment. For all

equations tested, transport predictions were more accurate for the high flow hydrographs, highlighting the importance of incipient motion definition as well as the inherent variability of transport measurements in lower flows.

Dimensionless fractional bed load transport rates were computed using an alternate form of the Parker-Einstein transport equation for which the coefficients were fit to the measured dataset and reference shear stresses calculated for the grain size fractions. Evaluating the transport fractionally gave improved predictions relative to those calculated with the Yang equation. Additional dimensionless transport relationships were developed by dividing the unsteady flow data set by hydrograph limb and estimating reference shear stresses for each limb of each individual hydrograph to account for temporal disparities in grain entrainment. This approach was termed separate limb transport and produced different dimensionless bed load transport equations for each limb. Using the separate limb approach improved transport predictions over the hydrographs, with reduced *RMSE*, a median *DR* of unity, and 55.7% of predictions within a factor of two. The separate limb approach quantified some of the entrainment variability associated with bed surface patchiness, complexity, and bedforms that contributes to hysteresis, and therefore, may provide physical basis for using time-dependent transport prediction equations for an unsteady flow event.

## CHAPTER 7

### *Impact of Vegetation on Channel Morphology*

---

---

#### 7.1 INTRODUCTION

This chapter discusses experiments with a patch of emergent vegetation in a sediment bed, referred to as the Patch Sediment (PS) group of experiments. Sand/gravel and sand/silt beds were tested under repeated low and high flow hydrographs with either a sparse or dense vegetation patch. Changes in bed morphology were measured in terms of sediment composition and sorting, bedform geometry, and volumetric bed adjustment. Findings are based on analysis of detailed digital elevation models (DEMs), which were created from accurate laser scans of the channel bed prior to and after each successive hydrograph. Data obtained from panoramic bed photos and sediment sampling supplemented the DEMs. The experiments build on the results from Chapter 5, emphasizing the role of an in-channel vegetation patch and the impacts of flow magnitude, patch stem density, and sediment mixture. The goals of this chapter are to more fully understand how an emergent vegetation patch of a certain stem density alters channel bed morphology over multiple unsteady flow events and evaluate what these morphological changes mean in terms of reach-scale channel stability.

#### 7.2 ANALYSIS METHODS

##### 7.2.1 Overview of Previously Introduced Methods

Sediment composition data collection/analysis and application of the unit bed

adjustment parameter to DEM differencing results followed the procedures described in Section 5.2. Sediment was collected from locations on each side of the patch and approximately 15 cm downstream along the patch centerline in addition to the established bed surface sediment sampling. Semivariogram analysis was carried out in the same manner as in Chapter 5, estimating bedform geometry from select elevation profiles. All DEMs, bed change maps, and panoramic bed photos for patch-sediment experiments are in Appendix D.2.

### 7.2.2 Definition of Patch Mound Areas

Vegetation patches have been shown to induce sediment accretion in the downstream wake area, creating a mound-type morphology that varies with stem density [e.g. *Follett and Nepf, 2012*], herein termed the patch mound. Formation of a patch mound occurred in these experiments and was quantified by the DEMs. In order to study changes occurring in response to unsteady flows, the patch mound was defined as the bed area encompassed by  $1\sigma_z$  above the mean bed elevation. This elevation was classified on each DEM using ArcGIS (Figure 7.2.1) and traced with polygons to delineate patch mound boundaries.

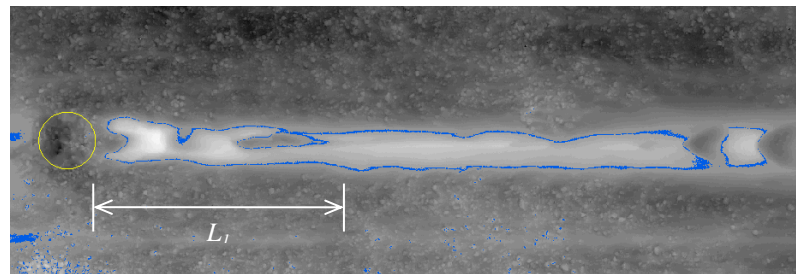


**Figure 7.2.1.** Patch mound delineation using a DEM. Blue boundaries are  $1\sigma_z$  above mean bed elevation. Yellow circle is the approximate patch location. The DEM portion shown is a sand/gravel equilibrium bed surface with a dense patch. White and black areas correspond to higher and lower elevations, respectively. The approximate location of the steady wake,  $L_1$ , at the baseflow rate is also shown.

Mound area and volume were calculated using the “Calculate Geometry” and “Cut/Fill” tools within GIS. Bedform initiation, which occurred downstream of some patches around the centerline, was assumed as a limit to the patch mound extent in the streamwise direction to emphasize the area in which a patch would be expected to grow.

### 7.3 RESULTS: SAND/GRAVEL SEDIMENT MIXTURE

#### 7.3.1 Surface Sediment Composition and Active Layer Sorting

Surface composition for the various sand/gravel patch beds was most impacted by initial hydrographs in each sequence, which created the single largest changes in surface sand fraction in each hydrograph set. After an initial increase, surface sand content decreased throughout the rest of the low flow hydrograph sequences. During the high flow hydrographs, the amount of sand on the surface continually increased with successive hydrographs (Figure 7.3.1). Patch stem density also affected the amount of sand on the bed surface. This effect was greater for sediment beds during the high flow hydrograph sequences, as there was a greater disparity between patch densities.

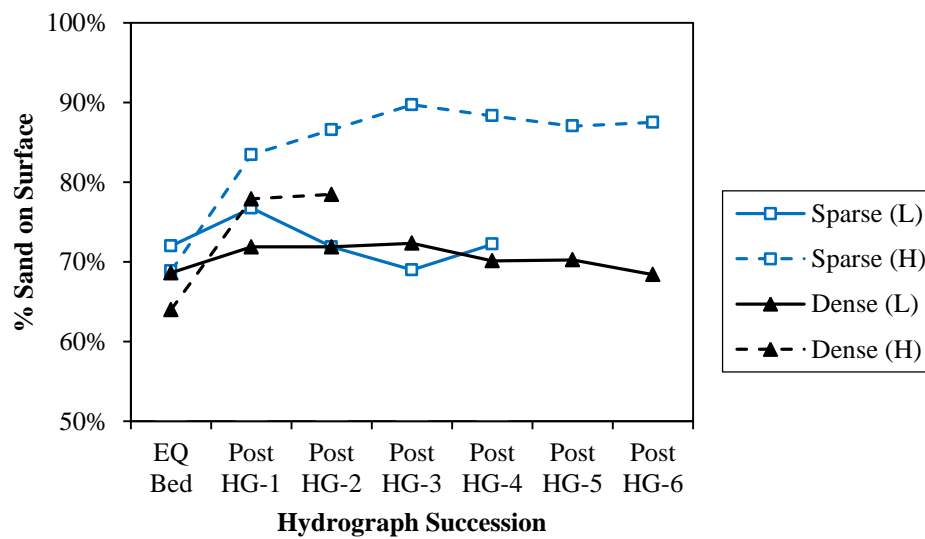


**Figure 7.3.1.** Surface sand fraction for sand/gravel, patch beds.

Sediment sorting within the active layer of the sand/gravel mixture occurred around vegetation patches as a function of patch density and hydrograph flow magnitude. The  $D_{50}$  grain size was used as a metric to evaluate sorting in the active layer sediments. Figure 7.3.2 shows changes in  $D_{50}$  from the initial bed composition to the final bed following a full hydrograph sequence, highlighting spatial variability in sediment sorting. In all cases, active layer fining was measured in the downstream wakes of the patches (Figure 7.2.1). Reductions in  $D_{50}$  were greater downstream of the dense patch than for the sparse and also for the high flow hydrograph sequence during which fine sediment accumulated in the wake area. Farther downstream of the patches, changes in active layer sediment composition were limited such that  $D_{50}$  remained within a range of +/- 5% relative to the initial bed value. Adjacent to the patches, hydrograph flow rates strongly impacted how the sediment composition changed. The greatest change in  $D_{50}$  occurred for the sparse patch during the low flow hydrograph sequence, coarsening by an average of 21% adjacent to the patch. Coarsening of  $D_{50}$  around the sparse patch during the higher flows was less pronounced at 4.1%. Adjacent to dense patches, there was a slight increase in average  $D_{50}$  during the low flow succession, although one side of the patch coarsened while the other underwent fining, and consistent decreases in  $D_{50}$  around 10% for the high flow sequence.

### **7.3.2 Patch Channel Morphology**

As unsteady flows were applied, characteristic bed morphologies developed in the vegetated sand/gravel channels that were largely impacted by stem density and hydrograph flow magnitude. Scour occurred within each patch, so the analysis is focused on those channel areas adjacent to and downstream of the patches.

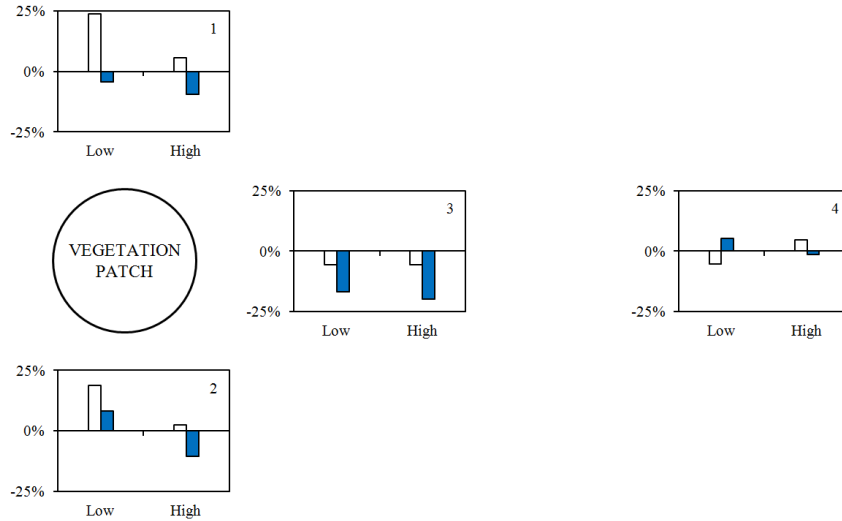


**Figure 7.3.2.** Sediment sorting around vegetation patch as measured by  $D_{50}$ . Flow direction is from left to right. Four sampling locations are shown: (1) left patch-adjacent; (2) right patch-adjacent; (3) 15 cm downstream of patch; and (4) 2.5 m downstream of patch. Bar graphs represent changes in  $D_{50}$  from the initial active layer GSD to the final GSD after the full low or high flow hydrograph sequence. White and solid blue bars represented sparse and dense patches, respectively.

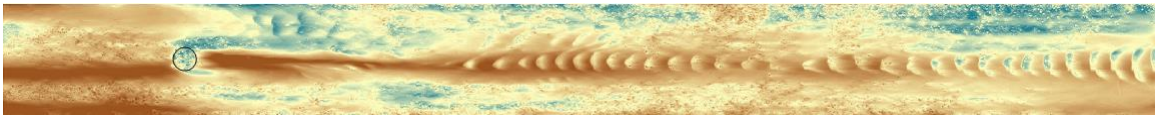
### *Sparse Patches*

A sand mound formed downstream of the sparse patch on the equilibrium beds prior to the low and high flow hydrograph successions. In each case, the mound extended approximately 2.7 m, or 22 patch diameters ( $D$ ), downstream of the trailing patch edge. Once hydrographs were begun, the patch mound decreased in area and volume. Adjacent to patches, scour depths ranged between 1.6 and 2.0 cm below the mean bed elevation for the high flow hydrographs (darker blue color in Figure 7.3.3b), but minimal scour was measured in these locations for the lower flows (Figure 7.3.3a). For the low flow hydrographs, fairly regular ripples formed beyond the patch mound, initiated around 1.3 m ( $11D$ ) downstream of the patch. Ripples were maintained throughout the flow succession and were laterally constrained to the middle 20 cm of the channel (Appendix D.2). Bedforms developed closer to the patch for the high flow hydrographs (Figure

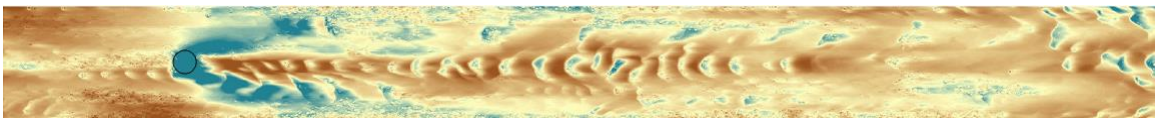
7.3.3b) with greater ripple heights ( $\Delta$ ) and spacing ( $\lambda$ ). Mean ripple regularity was comparable for each flow sequence (Table 7.3.1), while bedform steepness ( $\Delta/\lambda$ ) increased during both hydrograph successions (Figure 7.3.4).

**Table 7.3.1.** Bedform geometry for sparse patch, sand/gravel sediment beds.

Hydrograph Magnitude	Patch Density	Hydrograph Succession	$\sqrt{c}/r$ (-)	$\Delta$ (mm)	$\lambda$ (mm)	$\Delta/\lambda$ (-)
Low	Sparse	EQ Bed	-	-	-	-
		Post HG-1	0.024	7.0	124	0.056
		Post HG-2	0.118	7.3	131	0.056
		Post HG-3	0.132	7.5	133	0.056
		Post HG-4	0.130	8.6	118	0.073
High	Sparse	EQ Bed	0.062	5.9	124	0.048
		Post HG-1	0.101	11.8	149	0.079
		Post HG-2	0.082	12.6	148	0.085
		Post HG-3	0.126	12.1	171	0.071
		Post HG-4	0.138	15.2	202	0.075
		Post HG-5	0.172	15.5	150	0.103
		Post HG-6	0.135	15.1	161	0.094



(a) Bed surface DEM after first low flow hydrograph.



(b) Bed surface DEM after first high flow hydrograph.

**Figure 7.3.3.** Characteristic sand/gravel bed morphology for sparse patch. DEM color scale is given in Appendix D.2; brown and blue correspond to higher and lower bed elevations, respectively. The black circle represents patch location on all DEM images, unless otherwise indicated.

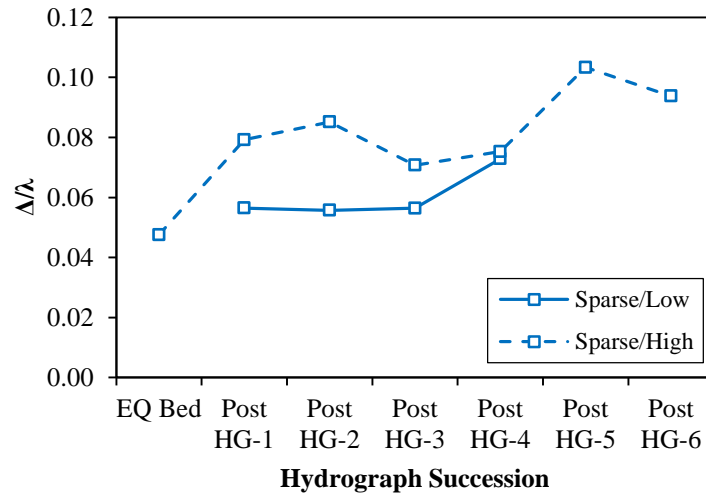
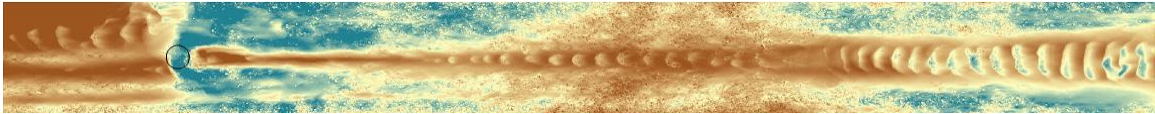


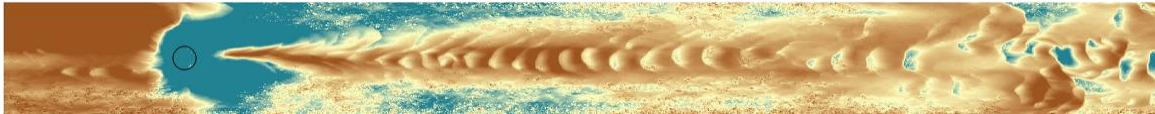
**Figure 7.3.4.** Bedform steepness adjustment for sparse patch, sand/gravel beds.

### ***Dense Patches***

The sand mounds that formed downstream of dense patches on the equilibrium beds extended approximately 2.1 m ( $17.5D$ ) and 1.2 m ( $10D$ ) downstream prior to the low and high flow hydrograph successions, respectively. Once the hydrograph sequences were begun, the patch mound decreased sharply in area and volume. The dense patch induced adjacent bed scour for both flow successions (Figure 7.3.5), reaching maximum scour depths ( $z_{s,max}$ ) of 2.2 cm and 5.6 cm below the mean bed elevation for the low and high flow hydrographs, respectively. Not only was  $z_{s,max}$  2.5 times greater for the high flows, but the scour footprint extended up to 0.5 m downstream from the patch in a horseshoe shape (Figure 7.3.5b), reflective of an erosive bed morphology around the patch. Ripples developed beyond the patch mound and remained present throughout each flow sequence, with larger heights and spacing for the high flow hydrograph beds, but greater regularity for the lower flows (Table 7.3.2). Bedform steepness increased during the low flow hydrograph succession, but decreased during the high flow hydrograph sequence (Figure 7.3.6).



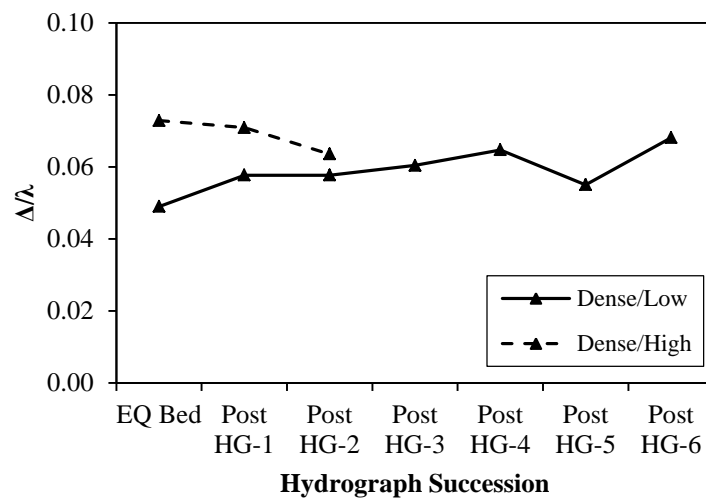
(a) Bed surface DEM after first low flow hydrograph.



(b) Bed surface DEM after first high flow hydrograph.

**Figure 7.3.5.** Characteristic sand/gravel bed morphology for dense patch.**Table 7.3.2.** Bedform geometry for dense patch, sand/gravel sediment beds.

Hydrograph Magnitude	Patch Density	Hydrograph Succession	$\sqrt{c}/r$ (-)	$\Delta$ (mm)	$\lambda$ (mm)	$\Delta/\lambda$ (-)
Low	Dense	EQ Bed	0.121	9.7	198	0.049
		Post HG-1	0.121	9.0	156	0.058
		Post HG-2	0.121	9.0	156	0.058
		Post HG-3	0.128	8.7	144	0.060
		Post HG-4	0.148	8.8	136	0.065
		Post HG-5	0.127	9.3	169	0.055
		Post HG-6	0.130	9.4	138	0.068
High	Dense	EQ Bed	0.032	10.2	140	0.073
		Post HG-1	0.044	11.7	165	0.071
		Post HG-2	0.068	12.4	195	0.064

**Figure 7.3.6.** Bedform steepness adjustment for dense patch, sand/gravel beds.

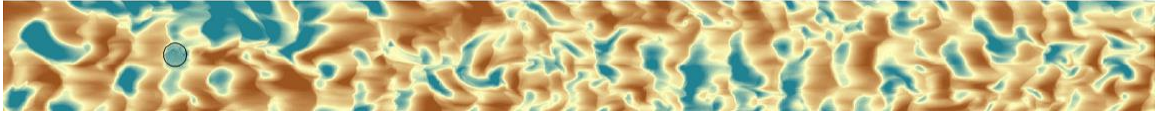
## 7.4 RESULTS: SAND/SILT SEDIMENT MIXTURE

### 7.4.1 Patch Channel Morphology

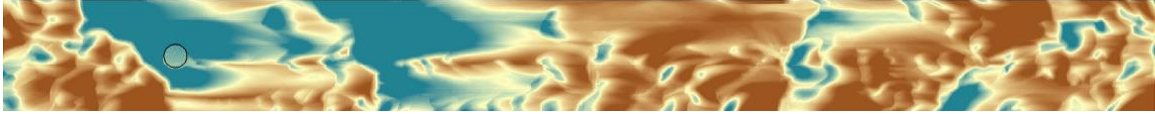
In the vegetated sand/silt channels, characteristic bed morphologies developed that were largely impacted by stem density and hydrograph flow magnitude.

#### *Sparse Patches*

Patch mounds downstream of the sparse patches on each equilibrium sand/silt bed were small in area, only extending a maximum of 0.25 m ( $2D$ ) from the patch trailing edge with a maximum local elevation of 2.0-2.8 mm above the mean bed elevation. For each equilibrium bed, substantial bedforms developed over the reach upstream and downstream of the sparse patch and spanned most of the channel width. These ripples dominated the bed surface structure during both the low and high flow hydrograph sequences (Figure 7.4.1; Appendix D.2), adjusting their geometry across individual hydrographs and decreasing in regularity with additional flow events (Table 7.4.1). Ripples developed during the hydrographs were more regular for the low flow sequence (mean  $\sqrt{c}/r = 0.15$ ) than for the high flow (mean  $\sqrt{c}/r = 0.08$ ). Bedform height was several millimeters larger on the high flow hydrograph beds than for the lower flows, but larger ripple spacing resulted in similar bedform steepness values after the first two hydrographs of either magnitude (Figure 7.4.2). Steepness values were variable during the second and third low flow hydrographs, but returned to the post hydrograph-1 value for the remainder of the sequence. High flow hydrographs beds were best classified by large and spatially variable bed features, with extensive scour ( $z_{s,max} = 6.7$  cm) adjacent to the patch following the second high flow hydrograph (Figure 7.4.1b).



(a) Bed surface DEM after second low flow hydrograph.



(b) Bed surface DEM after second high flow hydrograph.

**Figure 7.4.1.** Characteristic sand/silt bed morphology for sparse patch. DEM color scale is different than for the images in Section 7.3.2 to account for the different sediment mixture. The scale is given in Appendix D.2; brown and blue correspond to higher and lower bed elevations, respectively.

**Table 7.4.1.** Bedform geometry for sparse patch, sand/silt sediment beds.

Hydrograph Magnitude	Patch Density	Hydrograph Succession	$\sqrt{c}/r$ (-)	$\Delta$ (mm)	$\lambda$ (mm)	$\Delta/\lambda$ (-)
Low	Sparse	EQ Bed	0.179	26.1	209	0.125
		Post HG-1	0.161	23.0	204	0.113
		Post HG-2	0.215	23.0	243	0.095
		Post HG-3	0.106	26.6	181	0.147
		Post HG-4	0.169	25.3	216	0.117
		Post HG-5	0.115	24.3	213	0.114
High	Sparse	EQ Bed	0.146	21.9	237	0.092
		Post HG-1	0.058	29.5	245	0.120
		Post HG-2	0.100	29.0	302	0.096

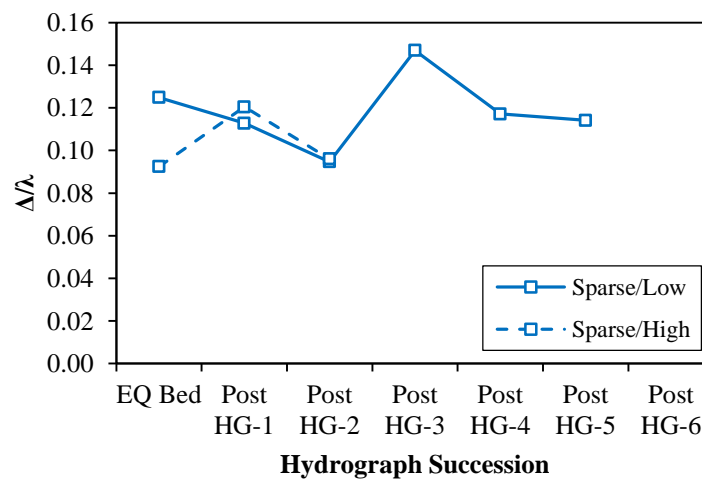


**Figure 7.4.2.** Bedform steepness adjustment for sparse patch, sand/silt beds.

### ***Dense Patches***

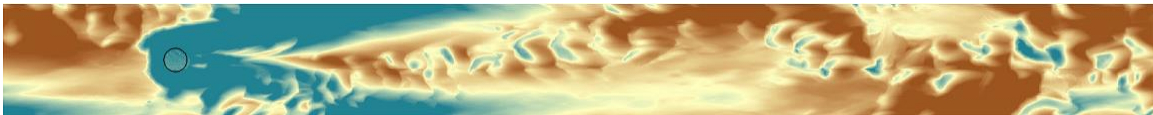
Bed morphology with the dense patch differed between sand/silt beds prior to and during each hydrograph sequence. The equilibrium bed patch mound areas were up to six times larger prior to the low flow sequence than for the high flow, extending approximately 1.85 m (15.4*D*) and 0.80 m (6.7*D*) downstream of the patch, respectively. In the low flow case, the mound was highly asymmetrical, extending farther downstream on the right patch edge (relative to the flow direction). As hydrographs of either magnitude were applied, the patch mound area and volume reduced sharply and the shapes of the mounds became triangular at the upstream end, then diffusing outward with downstream distance (Figure 7.4.3; Appendix D.2). Bedforms developed downstream of the patch mound on all beds with geometries and extents varying with flow magnitude. Ripples on low flow succession beds were more regular with larger spacing, but ripple height was greater for the high flow beds (Table 7.4.2). In both cases, bedform height and steepness increased with additional hydrographs. Bedforms extended laterally over the bed surface for the low flow sequence beds only after the second hydrograph (Figure 7.4.3a). Bedforms were present on all high flow hydrographs beds, with variable lateral bed coverage during the hydrograph sequence (Figure 7.4.3b).

Scour adjacent to the dense patch was characteristic of the sand/silt mixture. Scour developed during the equilibrium baseflow and persisted through each hydrograph succession (Figure 7.4.3) with scour depths and footprints impacted by hydrograph flow magnitude and succession (Table 7.4.3). The scour footprint increased during the low flow hydrograph sequence until it spanned over half the flume width, extended 0.40 m (3.3*D*) downstream of the patch, and reached a  $z_{s,max}$  of 4.8 cm after the second

hydrograph. Conversely,  $z_{s,max}$  decreased during the high flow sequence and the maximum scour footprint was observed following the first high flow hydrograph (Appendix D.2).



(a) Bed surface DEM after second low flow hydrograph.



(b) Bed surface DEM after second high flow hydrograph.

**Figure 7.4.3.** Characteristic sand/silt bed morphology for dense patch.

**Table 7.4.2.** Bedform geometry for dense patch, sand/silt sediment beds.

Hydrograph Magnitude	Patch Density	Hydrograph Succession	$\sqrt{c}/r$ (-)	$\Delta$ (mm)	$\lambda$ (mm)	$\Delta/\lambda$ (-)
Low	Dense	EQ Bed	0.012	12.1	224	0.054
		Post HG-1	0.010	16.8	219	0.077
		Post HG-2	0.093	17.9	234	0.076
High	Dense	EQ Bed	0.104	12.9	196	0.066
		Post HG-1	0.052	20.1	191	0.105
		Post HG-2	0.073	22.8	193	0.118

**Table 7.4.3.** Maximum scour depths around dense patch on sand/silt sediment beds.

Hydrograph Magnitude	Hydrograph Succession	$z_{s,max}$ (cm)
Low	EQ Bed	4.1
	Post HG-1	4.6
	Post HG-2	4.8
High	EQ Bed	6.7
	Post HG-1	6.4
	Post HG-2	6.1

## 7.5 DISCUSSION

### 7.5.1 Patch Hydraulics over Sediment Beds

Much of the wake structure downstream of an emergent vegetation patch has been defined in flumes without a sediment bed [e.g. *Zong and Nepf, 2012; Chen et al., 2012*]. In these experiments, velocity profiles measured along the patch centerlines during steady, low flows before and after hydrographs revealed that steady wake lengths were reduced over rough mobile beds of two different grain size distributions (Figure 7.5.1). Total wake length predictions calculated by summing  $L_1$  (Equations 2.2.2) and  $L_2$  (Equation 2.2.3) overpredicted measured total wake lengths by an average of 78%. Thus, the patch influence on the downstream flow field was shorter for rough, mobile beds, resulting in a shift in patch-scale hydraulics and lesser downstream influence on the mean flow field (Figure 7.5.2).

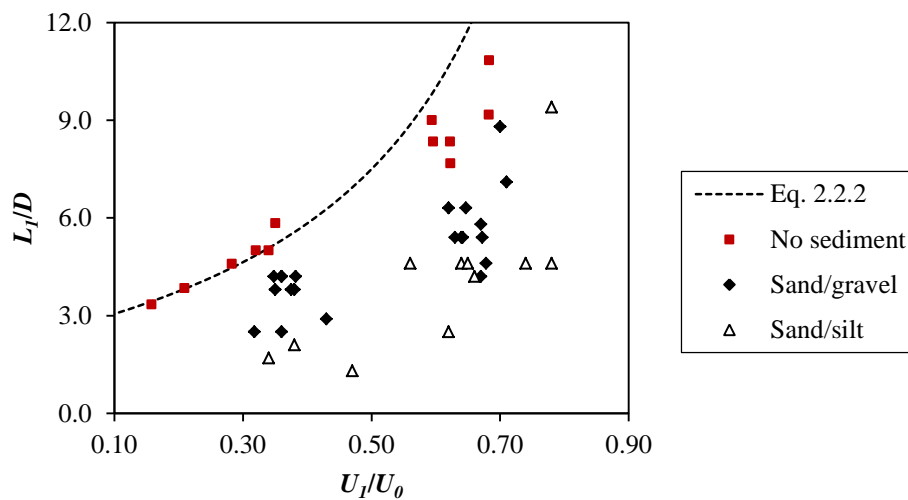


**Figure 7.5.1.** Steady wake lengths with and without sediment beds.

Because the steady wake length is controlled by shear layer growth [*Zong and Nepf, 2012*], a possible cause of reduced patch wake lengths over rough, mobile beds can

be explained in terms of the conversion of shear to turbulence downstream of patches by applying concepts from a turbulent energy budget. The shear production term of the turbulent kinetic energy (*TKE*) equation represents the generation of *TKE* from mean kinetic energy based on the interaction of Reynolds stress and lateral velocity gradient (Equation 7.5.1; *Kundu and Cohen*, 2008, pg. 558):

$$\text{Shear Production} = -\overline{u_{rms}v_{rms}} \frac{dU}{dy} \quad (7.5.1)$$

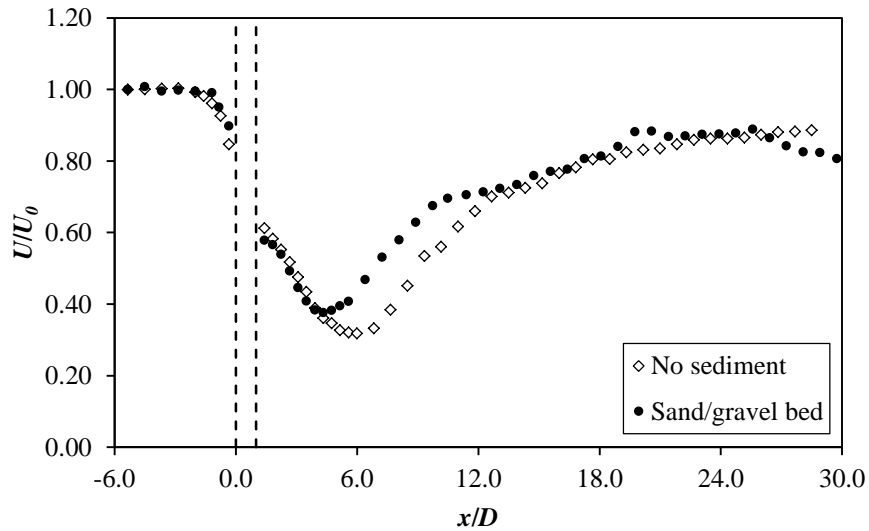


**Figure 7.5.2.** Velocity profile comparison over sediment bed.

In the case of the flow field downstream of a patch, shear layers develop on each side of the patch, growing with downstream distance until they converge to form the patch-scale turbulence [*Zong and Nepf*, 2012]. Therefore, decreased steady wake lengths over sediment beds signify more rapid shear layer growth. Relative to the no sediment velocity measurements, the velocity gradients over sediment beds were similar for all patches in the sediment beds, which suggests that the increased turbulence intensities and Reynolds stresses due to the rougher bed boundary condition enhanced the efficiency

with which mean kinetic energy was converted to turbulent kinetic energy. *Zong and Nepf* [2012] used the ratio of maximum lateral turbulence intensity ( $v_{rms,max}$ ) to the difference between velocities in the steady wake and outside the shear layer ( $\Delta U = U_2 - U_1$ ) to quantify the efficiency of shear conversion to turbulence. They found that this ratio increased with stem density because a larger velocity gradient occurred around denser patches. Applying the same concept here to compare the conversion efficiency for flows over a smooth bottom and sediment beds, it was found that this ratio is higher for rougher beds (Figure 7.5.3), supporting the idea that shear layers grow faster as the result of more efficient conversion to patch-scale *TKE* over a rougher boundary. Reduced patch wake lengths should decrease the extent of channel bed morphology changes due to a patch.

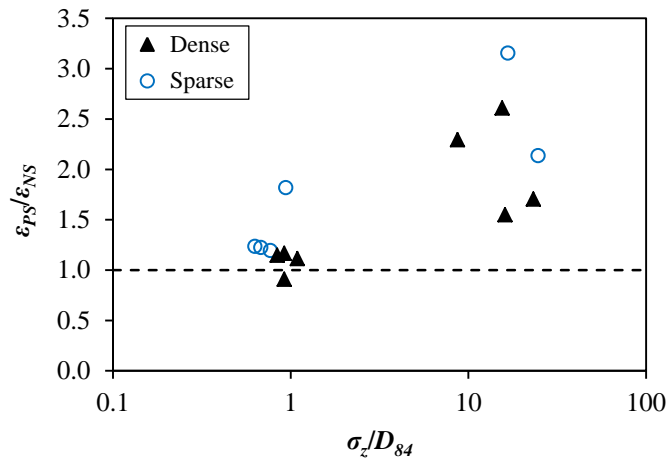


**Figure 7.5.3.** Comparison of shear conversion efficiency. The parameter  $\varepsilon$  is used for efficiency, equal to  $v_{rms,max}/\Delta U$ . Subscripts denote patch-sediment (PS) and no sediment (NS) runs, so a ratio of  $\varepsilon_{PS}/\varepsilon_{NS}$  greater than 1.0 indicates greater efficiency for the sediment beds. Bed roughness is parameterized as  $\sigma_z/D_{84}$ .

## 7.5.2 Channel Bed Structure and Topographic Variability

### *Sediment Sorting*

Bed structure for the sand/gravel beds is related to the spatial distribution of

sediment on the surface and in the active layer. Sediment sorting in the vicinity of the vegetation patches depended on patch density and flow magnitude for the sand/gravel beds. The finer sand fraction formed a mound on top of the gravel fraction in the patch wake for each hydrograph sequence and patch density. Accumulation of finer sediment directly downstream of the patches has been observed in the field following a flood event [Tanaka and Yagisawa, 2010] as well as in a flume where fine sediment deposited from suspension [Follett and Nepf, 2012]. Patch-adjacent areas experienced primarily surface coarsening, which was expected for these areas due to flow acceleration and increased shear stresses. The exception was the high flow sequence and the dense patch where the active layer  $D_{50}$  decreased relative to the initial bed. This sediment fining was consistent with results from the no patch channel in which surface sand content increased during the high flow hydrograph sequence (Figure 5.3.1). The consistency in results with and without vegetation suggests that the increased sand fraction in transport during the high flow hydrographs had a greater influence over bed sediment composition than local patch-hydraulics that typically cause coarsening adjacent to a patch.

### ***Bedform Geometry***

Ripple formation on the sand/gravel beds was enhanced by the presence of a vegetation patch (Figure 7.5.4). Ripples were constrained to the center portion of each channel that corresponded with the patch width where patch hydraulics induced preferential deposition. Sand fraction accumulation in the patch wake led to a surface supply adequate for ripple formation that was restricted elsewhere in the channel by the surface structure created by the gravel fraction [Tuijnder *et al.*, 2009], which was discussed in Chapter 5 for no patch beds. Ripples formed downstream of the steady wake

length where the flow velocity began to recover, creating increased sediment transport locally and bedform development. Ripples formed beyond the steady wake in all cases except for the sparse patch in the high flow hydrograph sequence, where the combination of high flow rates and reduced flow blockage appeared to inhibit a steady wake from persisting during the hydrographs, which allowed for ripples to develop immediately downstream of the patch.

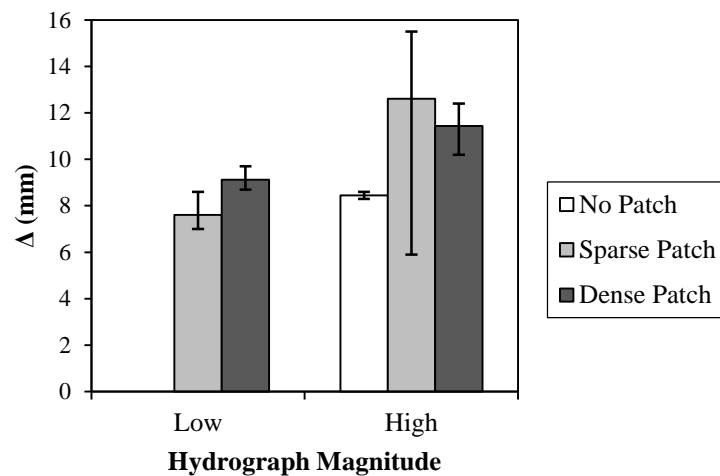


**Figure 7.5.4.** Influence of vegetation patch on sand/gravel bed ripple heights. Columns correspond to mean values; error bars correspond to minimum and maximum values. All plots of a similar nature follow this convention.

Ripples developed with larger heights on the sand/silt beds when a patch was present and grew to their largest for the sparse patch (Figure 7.5.5). Sand/silt ripples did not show the same spatial restrictions as those on the sand/gravel beds because they were not supply limited. Bedforms often spanned the full flume width (Appendix D.2), and in cases where the steady wake length was minor, ripples developed adjacent to the patches in areas of flow acceleration. Turbulent ejections of low momentum fluid over dune crests and recirculation cells forming in the leeside affect the mean flow field over bedforms [e.g. *Best*, 2005]. Thus, ripples likely inhibited well-defined patch wakes from

forming over the sand/silt beds and contributed to reduced length scales (Section 7.5.1).

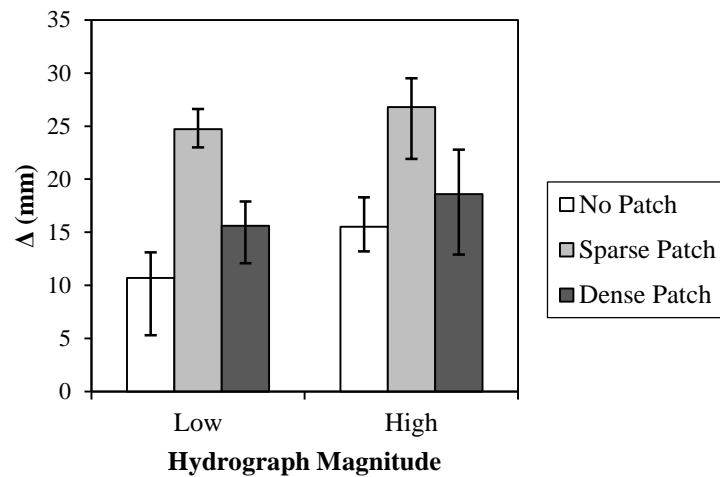


**Figure 7.5.5.** Influence of vegetation patch on sand/silt bed ripple heights.

### *Topographic Variability*

Topographic variability was measured through sediment sorting, bedform development, and spatial variability in bed surface structure. Both sparse and dense vegetation patches increased topographic variability in the channel relative to the no patch cases. Sediment mixture, patch density, and hydrograph flow magnitude all influenced the degree of variability, which was quantified as the standard deviation of bed elevations,  $\sigma_z$  (see Section 5.5.2), calculated over the downstream 5 m reach for the patch beds. In the case of the sand/gravel sediment, there was minimal difference in  $\sigma_z$  resulting from the presence of the sparse patch in low flow hydrographs (Figure 7.5.6a), but differences in  $\sigma_z$  were statistically significant at the 5% level for the higher flows. The dense patch produced a more topographically complex bed surface for this sediment mixture that was significantly different than the no patch beds for both flow magnitudes (Figure 7.5.6a). Much of the reach-scale topographic variability was set by the gravel fraction of the bed for this sediment mixture, and patch induced hydraulics affected

spatial patterns of surface gravel distribution. Using the reach-scale  $\sigma_z$  value as a single metric of bed variability does not fully account for some of the spatial variation in bed surface structure that may have important implications for habitat creation. For example, scour in patch-adjacent areas or ripples on the bed surface downstream of patches may provide refuge for small fish [Gerstner, 1998].

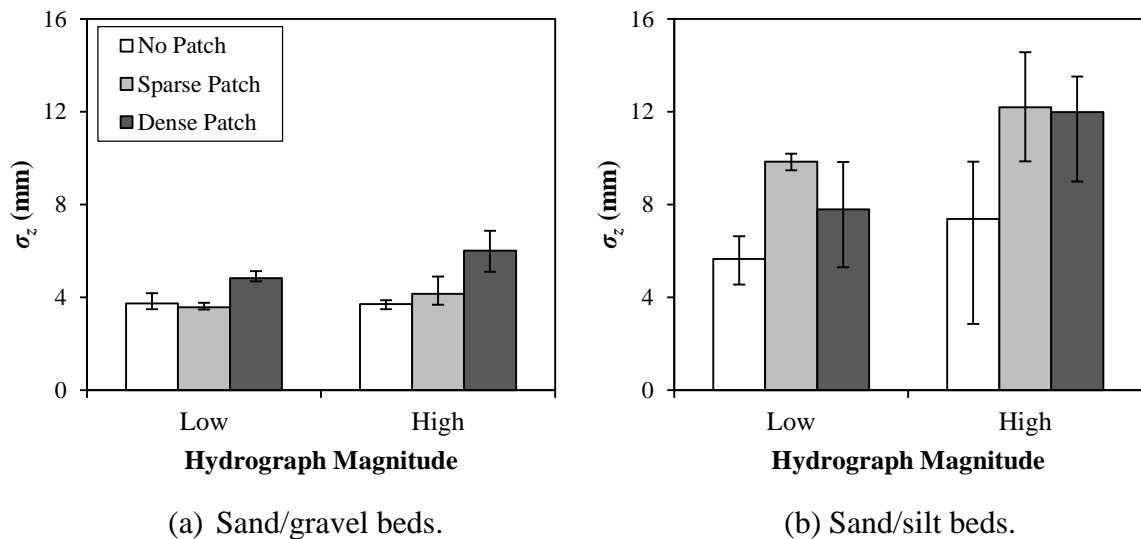


**Figure 7.5.6.** Topographic variability for patch beds of different sediment mixtures.

Both sparse and dense patches increased the surface variability of the sand/silt beds through the formation of larger bedforms (Figure 7.5.6b). Unlike the sand/gravel beds, bedforms developed across the full channel width downstream of the sparse patch for both hydrograph sequences, with increased heights relative to a non-patch bed that produced a statistically significant difference in bed surface structure. Thus, much of the variability in the bed surface was in the vertical direction rather than through a spatial distribution of preferential deposition locations. Greater lateral topographic variability was measured downstream of the dense patches due to enhanced flow heterogeneity induced by increased flow blockage. This resulted in spatial bedform formation similar to

the sand/gravel cases, with bedforms more concentrated towards the center of the channel, but with larger ripple heights because sand supply was not limited. Reach-scale  $\sigma_z$  increased for the dense patch compared to the no patch beds (Figure 7.5.6b), although bed surface differences were only statistically significant for the higher flow sequences.

### 7.5.3 Patch Mound Dynamics

Patch induced sediment mound formation on the equilibrium beds was consistent with observed sediment accretion downstream of patches in both field [Bouma *et al.*, 2007] and flume experiments where a steady, low flow has been applied to a uniform sediment bed [James *et al.*, 2002; Follett and Nepf, 2012]. However, the asymmetrical mean flow fields created by the randomly distributed stems within each patch (Chapter 4) resulted in asymmetrical patch mounds that differed in shape relative to those documented downstream of patches with regularly distributed stems [Follett and Nepf, 2012]. Downstream accumulation of finer sediment is important in terms of longitudinal patch growth [Sand-Jensen and Madsen, 1992; Corenblit *et al.*, 2009], thus asymmetrical patch mound development may impact patch growth patterns, the ability of a patch to streamline its shape to reduce drag [Asaeda *et al.*, 2005], and depending on vegetation biomass and patch encroachment, may increase channel blockage and local flow depths.

Unsteady flow conditions control patch sediment mound size and geometry over extended time scales. Although a well-defined sand mound developed downstream of the sparse and dense patches following the equilibrium flow (Appendix D.2), when the first hydrograph was applied patch mound area and volume reduced by over 50% regardless of flow magnitude or stem density. The bed surface difference map in Figure 7.5.7 illustrates this initially large change in mound morphology following a single low flow

hydrograph in which mound volume was reduced by 51%. Mound adjustment during the rest of the hydrographs in a sequence was much slower, and in some cases appeared to approach a constant geometry (Figure 7.5.8).

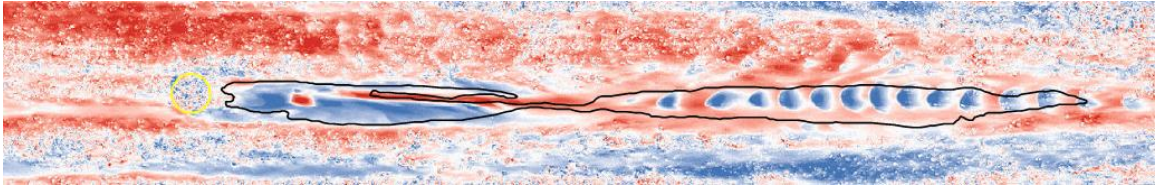


**Figure 7.5.7.** Difference map of patch mound erosion. Bed shown is a comparison between equilibrium bed and post hydrograph-1 bed for the sand/gravel mix and sparse patch. Vegetation patch location is shown in yellow and the equilibrium bed patch mound area is the solid black line. Red areas indicate aggradation; blue areas indicate erosion.

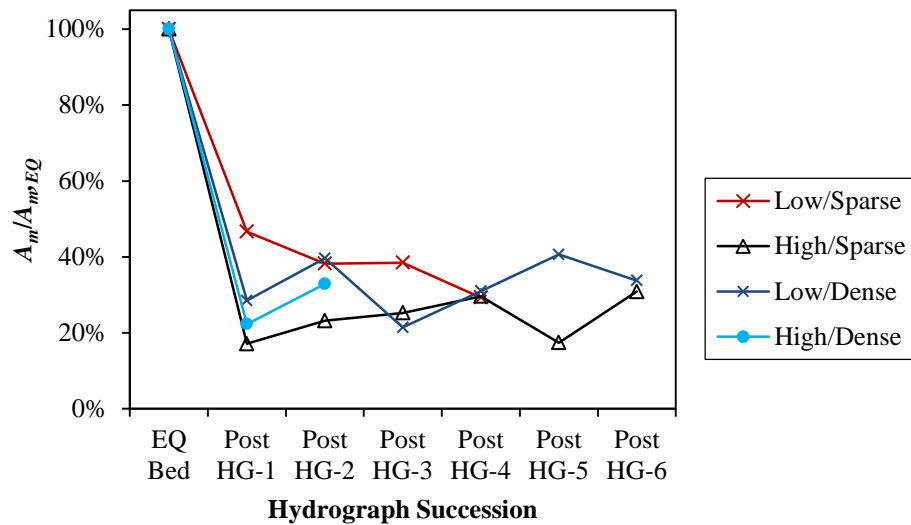


**Figure 7.5.8.** Patch mound area adjustment on sand/gravel beds. Adjustment is shown as a percentage of the equilibrium bed patch mound area,  $A_{m,EQ}$ .

This general trend of a decreasing rate of mound adjustment over sequential hydrographs was measured over all sand/gravel patch beds and hydrographs, as well as for both hydrograph sequences with the dense patch density in the sand/silt beds. For the sparse patch, sand/silt beds, patch mounds were much smaller and did not represent

distinctive bed features. As a result, both area and volume increased during the first hydrograph prior to decreasing with subsequent hydrographs, similar to the other beds. This bed response was measured only for the sand/silt beds with the sparse vegetation patch, and was likely the result of minimal flow alterations induced by the sparse stems and the highly active nature of the sand/silt mixture. Because the sediment mounds from this run set were poorly defined based on the mound area definition in Section 7.2.2, they were not considered in the overall patch mound analysis.

Using measured patch mound geometries, a model was developed to capture mound dynamics over temporal scales of repeated flood events. Experimenting under steady flow conditions, *James et al.* [2002] found that the volume and area of a sediment deposit in the wake of an emergent patch was inversely related to discharge. To incorporate that idea into the present analysis, changes in patch mound area were quantified relative to hydrograph characteristics using the dimensionless descriptor variable,  $\chi$ , introduced in Chapter 6 for predicting sediment yield as a function of hydrograph unsteadiness, flow work, peak flow depth, and channel  $D_{50}$ . Because the time scales of interest extended over multiple flow events, cumulative values of  $\chi$  were calculated to represent the cumulative impact of changing flow regime on the patch mound morphologies.

An exponential decay relationship was applied to model the change in relative sediment mound area over unsteady flows. The exponential decay function best represented the measured trend of mound area adjustment with an initially sharp decrease that levels off and approaches a constant value asymptotically (Figure 7.5.8). The proposed model is given as Equation 7.5.2, estimating patch mound area,  $A_m$ , at time  $t$

during a hydrograph sequence relative to the equilibrium bed mound area,  $A_{m,EQ}$ , which is reached under a steady baseflow rate prior to any flood events. The constant value added to the decay function represents the dynamically stable patch mound area,  $A_{m,DS}$ , that is approached through time as additional flow events occur.

$$\frac{A_m(t)}{A_{m,EQ}} = \alpha e^{-\beta[\Sigma\chi(t)]} + A_{m,DS} \quad (7.5.2)$$

where  $\alpha$  and  $\beta$  are dimensionless coefficients. Through non-linear regression the following model was derived with separate relationships for the sparse (Equation 7.5.3; Figure 7.5.9a) and dense (Equation 7.5.4; Figure 7.5.9b) patch densities:

$$\frac{A_m(t)}{A_{m,EQ}} = 0.74e^{-1.27[\Sigma\chi(t)]} + 0.260 \quad (7.5.3)$$

$$\frac{A_m(t)}{A_{m,EQ}} = 0.76e^{-2.07[\Sigma\chi(t)]} + 0.238 \quad (7.5.4)$$

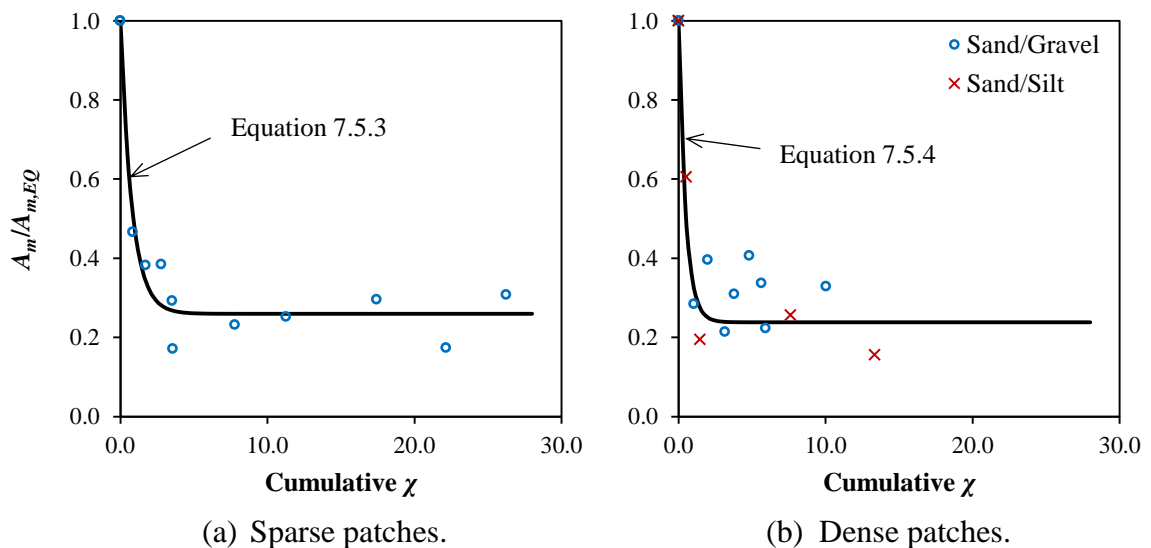


**Figure 7.5.9.** Patch mound adjustment models.

The model extends the steady flow findings of *James et al.* [2002] to unsteady

flows, showing that as unsteady flow events are cumulatively applied, a patch mound will decay from its equilibrium bed geometry to a new, dynamically stable geometry. For the beds tested here,  $A_{m,DS}$  was 26% and 24% of the area of the equilibrium patch mound for the sparse and dense patches, respectively. Separate sparse and dense patch models were developed in order to best represent the more rapid decay of the mounds downstream of dense patches and the larger dynamically stable mound areas downstream of sparse patches.

These patch mound decay models provide the basis for how sediment mounds downstream of emergent patches adjust over time when subjected to changing flows, and therefore, can be applied as a surrogate for patch expansion. Sediment mixture, flow magnitude, and patch density all impacted patch mound geometry and adjustment. Patch density appeared to have a dominant role in patch mound dynamics as the mound area decay coefficient ( $\beta$ ) differed between the sparse (-1.27) and dense (-2.07) patch models. A smaller  $A_{m,DS}$  downstream of the dense patch reflects the reduced scale over which the dense patch alters downstream hydraulics relative to a sparse patch.

These patch mound adjustment models are a significant step toward realistic models of natural systems. Future work to improve them could include testing of different flow sequences to alter flow magnitudes, hydrograph unsteadiness, and timing between flow events. In particular, prolonged low flow periods in between hydrographs would likely result in some degree of patch mound re-growth, altering the dynamics over extended time scales and perhaps introducing a cyclical growth-decay element. Inconsistent patch densities representative of seasonal vegetation growth and dieback would add further complexity to the issue of modeling patch growth dynamics. Because

the models presented here are functions of cumulative measures of flow strength and unsteadiness, it is hypothesized that their form can be expanded to handle such flow and timing complexities, maintaining decay in patch mound geometry but occurring over longer time scales.

#### 7.5.4 Influence of Vegetation on Morphological Adjustment and Stability

##### *Sand/Gravel Beds*

Channel adjustment for the sand/gravel beds, as quantified by the unit bed adjustment parameter,  $\delta_b$ , was impacted by both hydrograph flow magnitude and stem density. Of the four run sets with this sediment mixture, the channel stabilized with the sparse patch only after four low flow hydrographs (Figure 7.5.10).

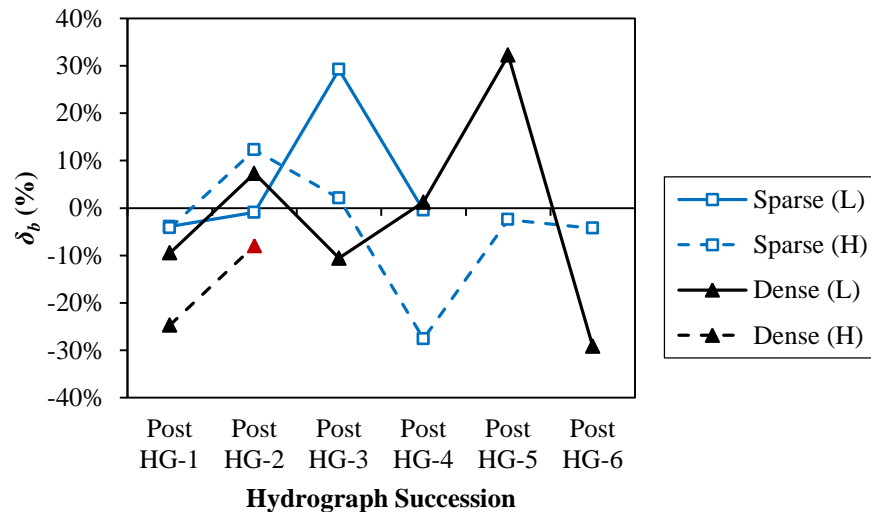


**Figure 7.5.10.** Unit bed adjustment for sand/gravel beds with vegetation patch. Red markers indicate excessive scour around patch resulting in hydrograph sequence termination.

The channel nearly reached a dynamically stable condition after the same number of low flow hydrographs for the dense patch (minimum  $\delta_b = 1.24\%$ ), but additional flow events led to large changes in the bed morphology at the reach-scale. Adjustment to high

flow hydrograph sequences showed instances of net channel bed aggradation and degradation for each patch density, but in neither case was dynamic stability reached. For the dense patch, substantial scour was measured adjacent to the patch in the high flow hydrograph series such that the patch base anchor was exposed. The hydrograph succession was terminated because this excessive scour exposed the patch anchor, creating a local bed obstruction that altered the hydraulics immediately downstream.

The channel conditions with the lowest amount of variability in the path of channel adjustment were for the sparse patch in the low flow hydrograph series. During this series,  $\delta_b$  stayed within a net erosional range of less than 4.2%, with the exception being after the third hydrograph when large net aggradation was measured. The sparse vegetation patch had a stabilizing impact on the channel morphology as the dynamic stability threshold of  $|\delta_B| \leq 0.5\%$  was reached in one fewer low flow hydrograph than for the channel without a patch (Section 5.5.3). The influence of the sparse patch on dynamic stability correlated with the slower rate of patch mound decay observed for the low flow hydrograph sequence (Figure 7.5.8), suggesting a link between patch mound dynamics and reach stability.

### ***Sand/Silt Beds***

Morphological adjustment for the sand/silt beds was complicated by the high mobility of the bed material during the hydrograph successions. In three of the four run sets (sparse/high flow, dense/low flow, dense/high flow), excessive scour occurred around the patch that uncovered the patch anchor forcing termination of the flow sequence after two hydrographs. Scour in patch-adjacent areas is not uncommon as flow acceleration due to patch flow blockage increases local bed shear stresses that can result

in erosion [Rominger *et al.*, 2010; Bouma *et al.*, 2007; 2009]. Scour was also widely measured within the patch itself, consistent with previous work testing finite patch sizes [Follett and Nepf, 2012]. In the cases tested here, it was difficult to draw any conclusions about the reach-scale stability given that the patch location was itself unstable and erosion prone.

The sparse patch stabilized the sand/silt reach for the low flow hydrograph succession (Figure 7.5.11) in one fewer hydrograph than when no patch was present (Section 5.5.3), suggesting that in a finer bed with no gravel, a patch in which stem density is controlled may enhance reach-scale stability in low flow unsteady regimes.

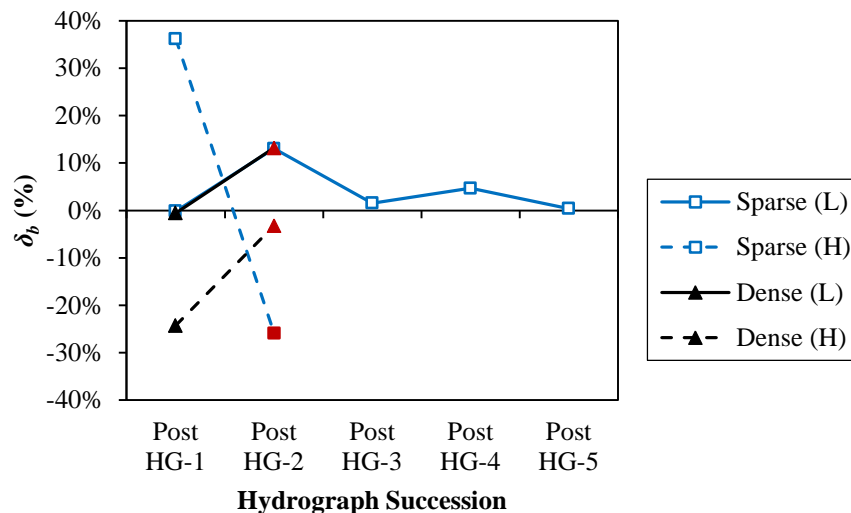


**Figure 7.5.11.** Unit bed adjustment for sand/silt beds with vegetation patch. Red markers indicate excessive scour around patch resulting in termination of that hydrograph sequence.

An interesting component of the sparse patch in the sand/silt bed was the widespread presence of bedforms on the surface (Figure 7.4.1a; Appendix D.2) and the apparent connection between bedform steepness and reach-scale morphological stability. The  $\delta_b$  following the first low flow hydrograph was actually below the stability threshold

(-0.17%) and had a corresponding bedform steepness of approximately 0.11. As additional hydrographs were run, the bed morphology adjusted outside the  $\delta_b$  stability range and bedform steepness varied. The adjustment of bedform steepness back near 0.11 following the fourth and fifth hydrographs (Figure 7.4.2) corresponded to a decreased  $\delta_b$  below the stability threshold after the fifth hydrograph, indicative of a dynamically stable channel. Thus, for the low flow hydrographs over the sand/silt sediment bed, a stable bedform steepness existed downstream of the sparse patch.

For the same sediment mixture and low flow hydrograph sequence without a patch, a similar connection between bedform steepness and morphological stability was determined at the slightly lower  $\Delta/\lambda$  of 0.080. This suggests that the sand/silt beds stabilized over repeated unsteady flows as their bedforms adjusted towards an equilibrium geometry for those particular flow conditions. Because the sparse patch altered the downstream flow field, bedforms adjusted toward a different geometry, one that was reached quicker but still corresponded with a dynamically stable reach for the patch channel. Morphological adjustments with the sparse patch in this sand/silt mixture suggest that the definition of dynamic stability may need to include a cyclical component over extended time scales because low  $\delta_b$  values were measured twice during the hydrograph sequence, but with several hydrographs applied in between.

### ***Discussion of Channel Stability with a Vegetation Patch***

Vegetation is widely accepted as a means to enhance bank stability and control channel planform adjustment [Tal and Paola, 2007; Braudrick et al., 2009; Gran and Paola, 2001] but the impact of in-channel vegetation patches is less understood. Flume work focused on bed changes downstream of an in-channel emergent vegetation patch

showed no net deposition within the total patch wake length [Follett and Nepf, 2012], but those experiments tested lower flow conditions and uniform sediment. When repeated unsteady flow events were run over heterogeneous sediment beds, DEM differencing showed that in-stream patches promoted reach-scale stability within a small subset of patch, flow, and sediment conditions. Specifically, the sparse patch in each sediment mixture accelerated morphological adjustment of the reach towards a dynamically stable state in which no net aggradation or degradation of the bed occurred after successive low flow hydrographs. In all other cases, either the threshold for dynamic stability was not reached within six hydrographs, or excessive scour at the patch forced termination of a run set because of altered local hydraulics and the assumption that the patch itself would likely be destabilized. Thus, in-stream patches do not appear to widely enhance reach-scale channel stability for flashy flow regimes like those simulated in these experiments.

## **7.6 SUMMARY**

The introduction of an emergent vegetation patch in the channel created characteristic bed morphologies that depended on patch density, sediment mixture, and hydrograph flow magnitude. For the sand/gravel beds, distinct mounds of sand developed downstream of both sparse and dense patches. These mounds decreased in area and volume by over 50% upon the first hydrograph, regardless of flow magnitude, with much slower adjustments during successive flow events. Ripples formed within the center 20 cm of the flume, coincident with increased surface sand supply downstream of the patch, and a limited amount of sediment sorting adjacent to the patch. For the sand/silt beds, patch induced sediment mounds were less distinct and these beds were better classified by the extensive scour adjacent to the patches and increased bedform formation. Ripples

were larger and not as spatially variable as for the sand/gravel beds, especially for the sparse patch where they extended across the entire channel width. In all experiments, channels with a patch contained larger ripples than those without a patch, which enhanced topographic variability.

An exponential decay model was presented to quantify patch mound area adjustment over time relative to the geometry following a low, steady flow rate. The model was a function of  $\chi$ , a dimensionless descriptor variable based on hydrograph characteristics and channel  $D_{50}$ . Using cumulative values of this parameter modeled patch mound adjustment over repeated unsteady flow conditions and extended time scales. Different model coefficients were determined for sparse and dense patches, including a slightly larger dynamically stable patch mound area downstream of the sparse patch. The basis of the model should be applicable to different flow conditions, including variable timing between unsteady flow events.

Morphological adjustment of the different patch beds was evaluated using the unit bed adjustment parameter. For both the sand/gravel and sand/silt beds, only the sparse patch in the low flow succession accelerated adjustment toward dynamic stability relative to the beds without a patch. There was an apparent connection between bedform steepness and reach-scale stability in the sand/silt beds such that when ripples adjusted toward a constant steepness over multiple unsteady flow events, the reach morphology stabilized. When there was a sparse patch in the channel, dynamic stability was achieved in one fewer hydrograph and with larger bedform steepness. The patch location was a region of scour for several experiments, particularly those testing the highly mobile sand/silt bed mixture and a dense patch. Vegetation patches enhanced reach-scale channel

stability only when the patch was sparsely vegetated and the unsteady flows simulated smaller floods. Given these results, a single emergent vegetation patch should not be considered equal to bank vegetation in its ability to enhance sediment stability for unsteady flow regimes similar to those tested in this work.

## CHAPTER 8

### *Impact of Vegetation on Sediment Transport*

---

#### 8.1 INTRODUCTION

This chapter discusses the Patch Sediment (PS) group of experiments in which sediment transport was studied in unsteady flows with a patch of emergent vegetation present in the channel. Sparse and dense patches were each tested in sand/gravel and sand/silt sediment beds subjected to either low or high flow hydrograph repetitions. The analysis presented here builds on Chapter 6, with the primary goal of quantifying the effect of a vegetation patch on predicting sediment transport rates and yield in unsteady flow conditions for various sediment mixtures and patch stem densities.

#### 8.2 ANALYSIS METHODS

##### 8.2.1 Shear Stress Calculation

Shear stresses were calculated using the depth-slope product with energy slope and hydraulic radius (Equation 6.2.1) and corrected using the *Vanoni and Brooks* [1957] approach, as described in Section 6.2.1. When bedforms were present, the *Smith and McLean* [1977] equation was used (Equation 6.2.4) to estimate skin friction as a function of bedform geometry. In the case of the sand/gravel beds with a patch, bedforms often did not extend across the full flume width. When this was the case, a representative bed shear stress ( $\bar{\tau}_b$ ) was calculated as a weighted average of the total, sidewall-corrected

shear stress ( $\tau_b$ ) and the bedform-corrected skin friction ( $\tau'$ ) using an approximate bedform width,  $w_b$ , relative to the flume width,  $B$  (Equation 8.2.1):

$$\bar{\tau}_b = \left(1 - \frac{w_b}{B}\right) \tau_b + \left(\frac{w_b}{B}\right) \tau' \quad (8.2.1)$$

## 8.2.2 Total Sediment Transport Predictions

Based on its accuracy for the no patch data set (Chapter 6), the *Yang* [1973] relationship (Equations 2.3.16-2.3.18) was applied to the patch-sediment data set to evaluate its applicability to predict sediment transport rates in unsteady flows when a vegetation patch is present. Prediction accuracy was quantified using the same metrics as in Chapter 6: root mean square error (*RMSE*; Equation 6.2.5), discrepancy ratio (*DR*), percentage of predictions within one order of magnitude of measured values ( $0.1 \leq DR \leq 10$ ), and percentage of predictions within a factor of two of measured values ( $0.5 \leq DR \leq 2.0$ ). Predictions were made for full data sets of each sediment mixture, separately for the sparse and dense patches, and for the low and high flow hydrograph data sets.

## 8.2.3 Reference Shear Stress Calculation

Using transport measurements and non-linear regression of the Parker-Einstein relationship (Equation 6.5.4), reference shear stresses were estimated for the sand fraction ( $\tau_{r,S/G-s}^*$ ) and gravel fraction ( $\tau_{r,S/G-g}^*$ ) of the sand/gravel mix, and for the sand/silt sand fraction ( $\tau_{r,S/S-s}^*$ ). As done in Chapter 6 for the no patch data set, reference stresses were determined separately for each limb of each individual hydrograph. Results are given in Table 8.2.1 for the range of patch densities, hydrographs, and sediment mixtures tested.

**Table 8.2.1.** Reference shear stresses for each hydrograph and limb with patch.

Flow Magnitude	Patch Density	Hydrograph	$\tau_{r,S/G-s}^*$		$\tau_{r,S/G-g}^*$		$\tau_{r,S/S}^*$	
			RL	FL	RL	FL	RL	FL
Low	Sparse	1	0.035	0.031	0.011	0.013	-	-
		2	0.013	0.041	0.011	0.013	-	-
		3	0.040	0.029	0.013	0.013	-	-
		4	0.015	0.025	0.013	0.013	-	-
High	Sparse	1	0.026	0.027	0.006	0.010	-	-
		2	0.020	0.027	0.010	0.008	-	-
		3	0.032	0.024	0.008	0.009	-	-
		4	0.029	0.036	0.006	0.008	-	-
		5	0.031	0.014	0.009	0.009	-	-
		6	0.018	0.006	0.007	0.008	-	-
Low	Dense	1	0.039	0.041	0.010	0.006	-	-
		2	0.051	0.056	0.013	0.012	-	-
		3	0.043	0.046	0.013	0.014	-	-
		4	0.043	0.053	0.014	0.013	-	-
		5	0.039	0.050	0.013	0.012	-	-
		6	0.040	0.059	0.011	0.012	-	-
High	Dense	1	0.050	0.056	0.008	0.011	-	-
		2	0.080	0.038	0.013	0.009	-	-
Low	Sparse	1	-	-	-	-	0.010	0.004
		2	-	-	-	-	0.014	0.015
		3	-	-	-	-	0.022	0.016
		4	-	-	-	-	0.009	0.011
		5	-	-	-	-	0.018	0.017
High	Sparse	1	-	-	-	-	0.007	0.010
		2	-	-	-	-	0.012	0.017
Low	Dense	1	-	-	-	-	0.076	0.060
		2	-	-	-	-	0.052	0.046
High	Dense	1	-	-	-	-	0.051	0.013
		2	-	-	-	-	0.008	0.008

### 8.3 RESULTS: SAND/GRAVEL SEDIMENT MIXTURE

#### 8.3.1 Hydrograph Sediment Yield

Sediment transport was measured during 18 hydrographs for the sand/gravel sediment mixture, including 10 for the sparse patch and 8 for the dense patch (Table 8.3.1). Both low and high flow hydrograph repetitions were tested for each vegetation patch density. Hydrograph characteristics varied within each sequence, and the mean

flow work of the high flow hydrographs was 2.4 times greater than for the low flow hydrographs. The range in flow conditions resulted in a range of measured sediment yields (Table 8.3.1). Mean relative bed load yield ( $Y_s/W_k$ ) with the sparse patch was 7.9 times greater over the high flow hydrograph sequence than for the low flow hydrographs. Less discrepancy was measured for the dense patch as the mean  $Y_s/W_k$  was 4.25 times greater for the high flow hydrograph sequence. Relative bed load yield during successive hydrographs within a set was variable, increasing with hydrographs during both dense patch cases, but was more variable for the sparse patch cases where there was no defined trend with hydrograph number (Pearson's  $r$ -coefficient of 0.02 and -0.07, for low and high flow sequences, respectively). Correlations between bed load yield, hydrograph unsteadiness, and total hydrograph flow work were poor with both vegetation densities.

**Table 8.3.1.** Hydrograph parameters and sediment yield for sand/gravel mixture.

Hydrograph Magnitude	Stem Density	Hydrograph Number	$D_{50}$ (mm)	$P$ (-)	$W_k$ (-)	$h_p$ (m)	$Y_s$ (kg/m)	$Y_s/W_k$ (kg/m)
Low	Sparse	1	0.55	0.0007	5.4	0.128	24.5	4.5
		2	0.55	0.0014	2.7	0.128	25.5	9.4
		3	0.55	0.0005	8.6	0.128	27.1	3.1
		4	0.55	0.0009	3.6	0.128	24.0	6.8
High	Sparse	1	0.52	0.0012	8.8	0.169	101.5	11.5
		2	0.52	0.0010	13.1	0.166	106.5	8.1
		3	0.52	0.0014	8.0	0.166	89.8	11.3
		4	0.52	0.0008	24.3	0.166	104.6	4.3
		5	0.52	0.0010	14.7	0.167	102.7	7.0
		6	0.52	0.0013	9.9	0.168	125.6	12.7
Low	Dense	1	0.56	0.0005	9.1	0.128	25.1	2.7
		2	0.56	0.0005	7.6	0.128	26.3	3.5
		3	0.56	0.0005	10.6	0.129	28.9	2.7
		4	0.56	0.0011	2.5	0.130	23.1	9.1
		5	0.56	0.0007	5.9	0.133	23.9	4.0
		6	0.56	0.0008	4.3	0.131	19.5	4.5
High	Dense	1	0.54	0.0008	25.1	0.166	66.9	2.7
		2	0.54	0.0011	12.2	0.166	56.8	4.7

### 8.3.2 Fractional Transport

The amount of gravel in transport during the hydrographs varied with flow magnitude and patch density (Table 8.3.2). Maximum gravel fraction did not exceed 5% by weight for any transport sample collected during the low flow hydrographs with either patch present. Fractional transport was more significant during high flow hydrographs, as gravel was mobile for 47-63% of the hydrograph duration for the sparse patch and for 52.5% of the hydrograph duration for the dense patch runs. As described in Chapter 6, suspended sediment samples were more reflective of wash load than suspended sediment transport and are not considered in detail for this analysis.

**Table 8.3.2.** Maximum gravel fraction in transport with patch.

<b>Hydrograph Magnitude</b>	<b>Sparse Patch</b>	<b>Dense Patch</b>
Low	4.2%	3.1%
High	30.1%	43.6%

### 8.3.3 Hysteresis of Sand/Gravel Mixture

Sediment transport hysteresis was variable for the 18 hydrographs tested with the sand/gravel sediment mixture. The dominant bed load pattern was clockwise hysteresis (50.0% of all hydrographs), followed by counterclockwise (16.7%) and figure-eight loop transport (5.6%). No defined hysteresis was measured during five hydrographs, or 27.8% of the total hydrographs tested. The only discernible difference in hysteresis patterns for different patch densities was a higher occurrence of counterclockwise transport with the dense patch (25%) than with the sparse (10%). As in the no patch experiments, counterclockwise hysteresis of suspended sediment was dominant, showing a dependence on sediment supply that was reflective of wash load (Chapter 6).

### 8.3.4 Sand/Gravel Transport Predictions with Yang Equation

The *Yang* [1973] relationship slightly overpredicted the transport rates for the sand/gravel, patch data set (Table 8.3.3). For the data set including both patch densities, total sediment transport predictions had a *NRMSE* of 13.5% with a median *DR* of 1.8. Nearly every predicted transport rate was within an order of magnitude of the corresponding measured value and 57.3% were within a factor of two. Prediction accuracy was improved for the sparse patch runs (median *DR* = 1.5) relative to the dense patch (median *DR* = 2.1) (Table 8.3.3; Figure 8.3.1).

**Table 8.3.3.** Yang transport prediction results for sand/gravel mixture with patch.

Flow Magnitude	Patch Density	<i>RMSE</i>	<i>NRMSE</i>	Median <i>DR</i>	$0.1 \leq DR \leq 10$	$0.5 \leq DR \leq 2.0$
All	Both	16.4	13.5%	1.8	99.4%	57.3%
	Sparse	14.8	12.2%	1.5	98.9%	66.8%
	Dense	18.2	40.9%	2.1	100.0%	45.4%
Low	Both	6.9	29.4%	1.9	98.9%	54.2%
	Sparse	4.9	20.7%	1.6	97.4%	63.2%
	Dense	8.0	34.6%	2.0	100.0%	48.2%
High	Both	23.4	19.2%	1.6	100.0%	61.2%
	Sparse	18.7	15.4%	1.5	100.0%	69.3%
	Dense	33.7	76.7%	2.2	100.0%	36.8%

Transport prediction accuracy also varied with hydrograph flow magnitude. Sparse patch predictions were more accurate for the higher flow hydrographs, with a lower median *DR* and 69.3% of predictions within a factor of two (Table 8.3.3; Figure 8.3.2). Conversely, dense patch predictions were more accurate for the lower flow hydrographs, showing less scatter, a lower median *DR*, and greater percentage within acceptable ranges. Overall, discrepancies between the predicted and measured transport data were greater with changes in patch density than for flow magnitude with the same density.

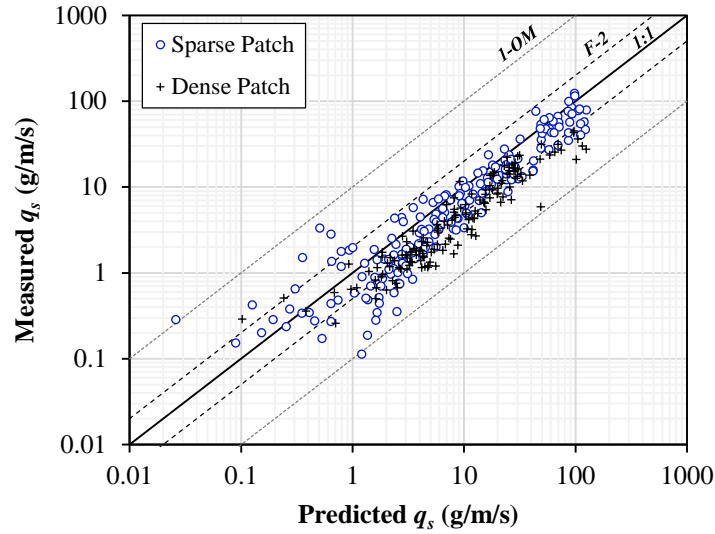


**Figure 8.3.1.** Sand/gravel transport predictions with patch using Yang equation. Lines in the plot correspond to perfect agreement between measured and predicted rates (1:1 line), predictions within one order of magnitude in either direction (1-OM), and predictions within a factor of two in either direction (F-2). These lines maintain the same meanings for all subsequent plots of a similar nature.

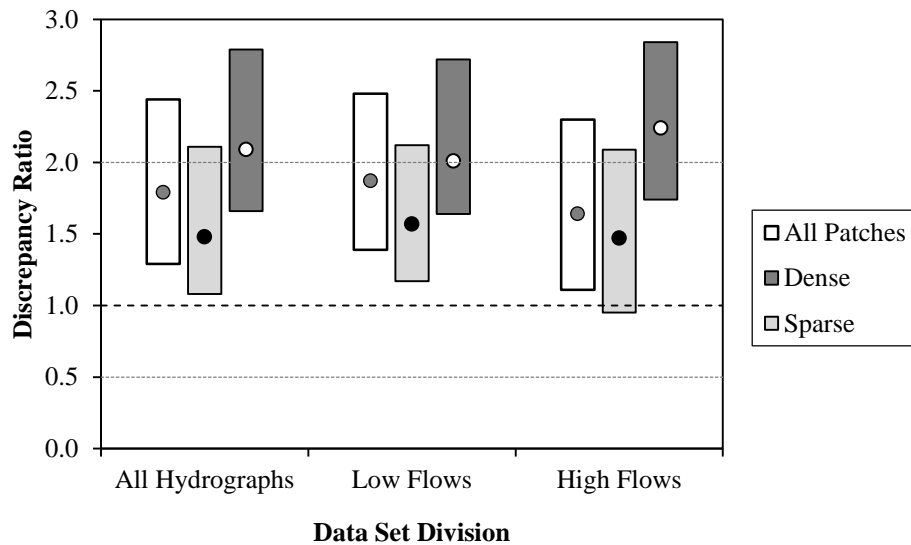


**Figure 8.3.2.** Sand/gravel transport comparisons for flow magnitude and patch density. Boxes indicate the middle 50% of discrepancy ratios (i.e. from 25<sup>th</sup> to 75<sup>th</sup> percentiles). Circles within each box indicate the median *DR* values.

## 8.4 RESULTS: SAND/SILT SEDIMENT MIXTURE

### 8.4.1 Hydrograph Sediment Yield

A total of 11 hydrographs were run for the sand/silt sediment beds, including 7 and 4 each for the sparse and dense patches, respectively. Both low and high flow hydrograph repetitions were tested for each vegetation patch density, with mean flow work of the high flow hydrographs 2.8 times greater than for the lower flows. Individual hydrographs of the same magnitude varied in unsteadiness and total flow work within each hydrograph sequence, which resulted in variable sediment yield measurements (Table 8.4.1). Patch density affected yield such that mean relative bed load yield ( $Y_s/W_k$ ) was 1.75 times greater for the dense patch than for the sparse patch. There was no consistent trend in  $Y_s/W_k$  during a hydrograph succession as relative yield increased with additional hydrographs for the sparse patch/low flow and dense patch/high flow cases, but decreased for the other two run sets.

**Table 8.4.1.** Hydrograph parameters and sediment yield for sand/silt mixture.

Hydrograph Magnitude	Stem Density	Hydrograph Number	$D_{50}$ (mm)	$P$ (-)	$W_k$ (-)	$h_p$ (m)	$Y_s$ (kg/m)	$Y_s/W_k$ (kg/m)
Low	Sparse	1	0.38	0.0004	11.3	0.132	15.0	1.3
		2	0.38	0.0005	6.1	0.136	12.4	2.0
		3	0.38	0.0004	9.7	0.133	12.7	1.3
		4	0.38	0.0005	11.1	0.133	13.2	1.2
		5	0.38	0.0005	5.0	0.139	14.7	3.0
High	Sparse	1	0.38	0.0009	13.6	0.166	63.4	4.6
		2	0.38	0.0006	31.1	0.167	101.9	3.3
Low	Dense	1	0.38	0.0011	1.3	0.130	5.4	4.1
		2	0.38	0.0007	4.0	0.131	7.4	1.9
High	Dense	1	0.37	0.0007	22.6	0.170	80.8	3.6
		2	0.37	0.0012	10.5	0.168	76.5	7.3

### 8.4.2 Hysteresis of Sand/Silt Mixture

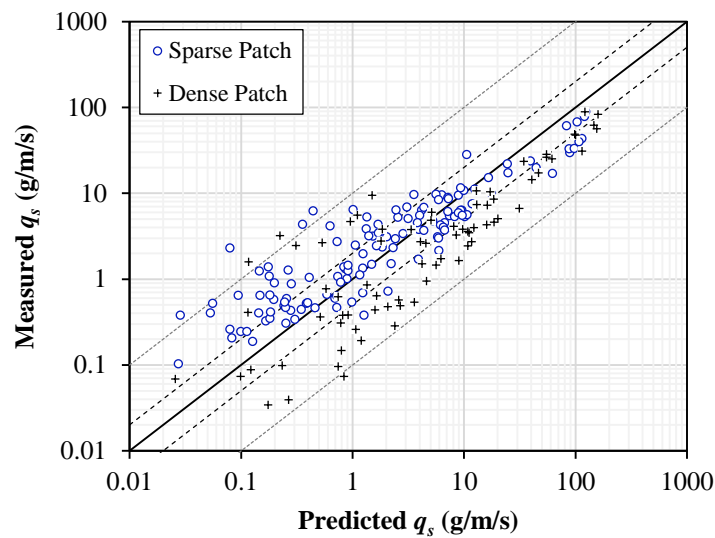
Each of the five major types of sediment transport hysteresis was measured during hydrographs with the sand/silt beds, although none could be considered a dominant transport pattern. Of the 11 total hydrographs, clockwise, counterclockwise, and figure-8 bed load hysteresis each occurred three times (27.3%), single-value plus a loop was measured once, and the fourth hydrograph in the low flow sequence for the sparse patch did not show any hysteresis. Overall, temporal bed load transport for the sand/silt mixture was highly variable with patches of either stem density present, precluding identification of a consistent trend in hysteresis.

### 8.4.3 Sand/Silt Transport Predictions with Yang Equation

The Yang relationship provided reasonable predictions of transport rates for the sand/silt, patch data set (Table 8.4.2), with a median  $DR$  of 1.1 and 95.7% percent of predictions within one order of magnitude of the measured values. However, there was large scatter in the predictions ( $NRMSE = 21.2\%$ ; Figure 8.4.1) and less than 50% were within a factor of two of the measured rates. Predicted rates were biased according to patch density and hydrograph flow magnitude. For the subset of low flow hydrographs, transport was slightly underpredicted with the sparse patch but vastly overpredicted for the dense (Table 8.4.2; Figure 8.4.2). For both patch densities, transport rates were overpredicted for the high flow hydrographs, with larger scatter for the dense patch. In general, transport was more accurately predicted with the sparse patch in the lower flow hydrographs, while predictions with the dense patch were more accurate in the higher flow hydrographs.

**Table 8.4.2.** Yang transport prediction results for sand/silt mixture with patch.

Flow Magnitude	Patch Density	<i>RMSE</i>	<i>NRMSE</i>	Median <i>DR</i>	$0.1 \leq DR \leq 10$	$0.5 \leq DR \leq 2.0$
All	Both	18.7	21.2%	1.1	95.7%	47.4%
	Sparse	15.0	17.0%	0.8	95.5%	59.4%
	Dense	23.9	27.0%	2.4	96.1%	26.3%
Low	Both	3.3	28.4%	0.9	97.0%	46.6%
	Sparse	1.8	15.4%	0.7	96.8%	61.1%
	Dense	5.4	75.8%	3.8	97.4%	10.5%
High	Both	30.7	34.9%	1.5	93.4%	48.7%
	Sparse	27.8	31.8%	1.5	92.1%	55.3%
	Dense	33.4	37.9%	1.6	94.7%	42.1%

**Figure 8.4.1.** Sand/silt transport predictions with patch using Yang equation.

## 8.5 DISCUSSION

### 8.5.1 Impact of Vegetation Patch on Bed Load Yield

The presence of a vegetation patch impacted hydrograph bed load yield differently in each sediment mixture (Figure 8.5.1). In the sand/gravel beds, the patch increased relative sediment yield in all cases. Conversely, relative bed load yield for hydrographs run over the sand/silt beds decreased with either patch (Figure 8.5.1).

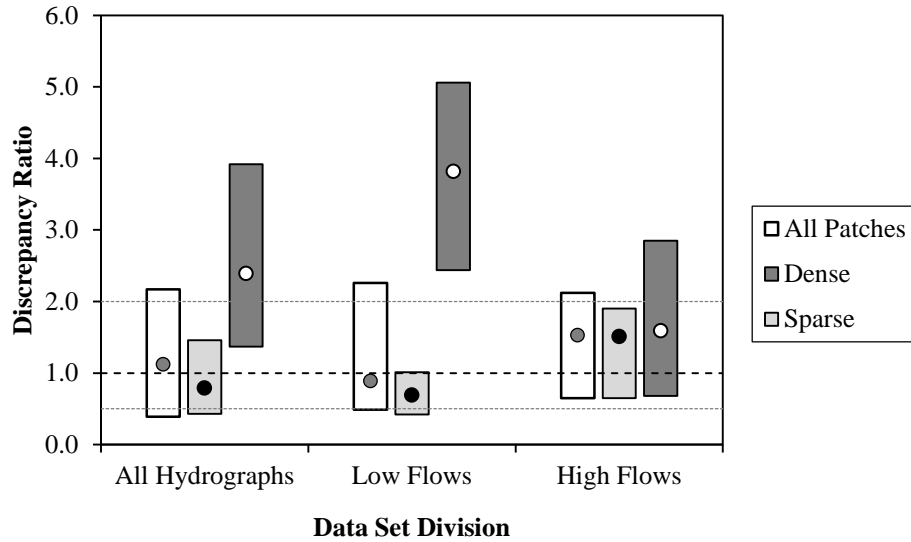


**Figure 8.4.2.** Sand/silt transport comparisons for flow magnitude and patch density. Boxes indicate the middle 50% of discrepancy ratios (i.e. from 25<sup>th</sup> to 75<sup>th</sup> percentiles). Circles within each box indicate the median  $DR$  values.

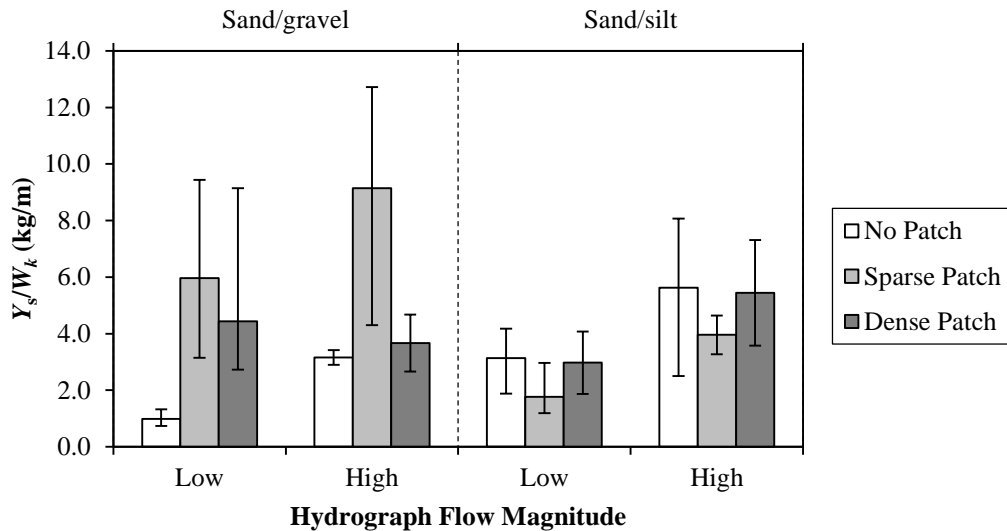
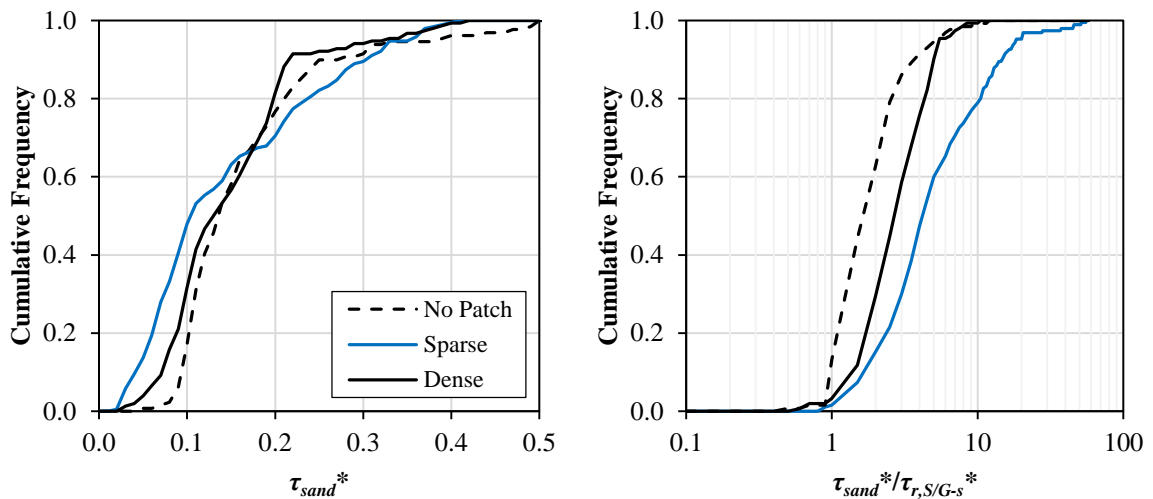


**Figure 8.5.1.** Bed load yield comparison for two sediment mixtures and patch densities.

Sediment yields were affected by several factors related to the characteristic patch bed morphology and surface structure (Chapter 7). The high surface sand content during the sparse patch, high flow hydrograph sequence (Figure 7.3.1) created a sand supply on top of the less mobile gravel grains, which lowered the reference shear stress for the sand

fraction ( $\tau_{r,S/G-s}^*$ ) and produced large values of total sediment yield that were 89-97% sand. When the dense vegetation patch was present, increases in surface sand content over the hydrograph sequences were more modest (Figure 7.3.1) and reference shear stresses were higher, so sediment yields were lower than those measured for the sparse patch with gravel comprising 9 to 15% of the total yield. Figure 8.5.2 highlights the differences in reference shear stresses estimated for all the sand/gravel beds. For similar distributions of shear stress (Figure 8.5.2a), differences in excess shear stress distributions for the sand fraction resulted from variable reference stresses (Figure 8.5.2b), which were reflected in the measured bed load yields (Figure 8.5.1).



(a) Dimensionless shear stress.

(b) Excess shear stress.

**Figure 8.5.2.** Shear stress distributions for sand fraction in sand/gravel mixture.

Patchy surface distributions in which sand preferentially accumulated on top of gravel in the center portion of the channel downstream of the vegetation patch did not occur to the same extent when there was no patch present, making the sand fraction more difficult to entrain due to the sheltering effect of the surface gravels. Reference shear

stress of the sand fraction in a sand/gravel mixture has been shown to decrease as surface sand content increases until approximately 40%, after which the reference stress remains constant [Wilcock and Kenworthy, 2002]. However, variable values of  $\tau_{r,S/G-s}^*$  for sediment beds with a vegetation patch indicated that the distribution and patchiness of the sand content, as well as the patch-induced alterations to the flow field, can cause reductions in the reference shear stresses beyond this threshold in unsteady flows.

In the sand/silt beds, the change in relative bed load yields was related to the patch density (Figure 8.5.1). When the dense patch was present, bed load yields were comparable to the experiments without a patch. With the sparse patch in the bed, relative bed load yield was reduced. Topographic variability of the sand/silt beds was entirely due to ripple formation. Ripples were present with and without vegetation in the channel, but when a patch was present, larger ripples were measured (Figure 7.5.5). The increase in ripple size indicates that these beds had increased form drag, reducing the amount of skin friction available to transport sediment and resulting in reduced bed load yields. In addition to extensive bedforms, part of the characteristic bed morphology with a dense patch in these finer sediment beds was excessive scour around the patch. Scour around the dense patch entrained and transported additional sediment, increasing sediment yields for the dense patch when compared to beds with sparse patches where scour was much less. Overall, the patch influenced bed yield through the feedback between patch hydraulics and bed morphology.

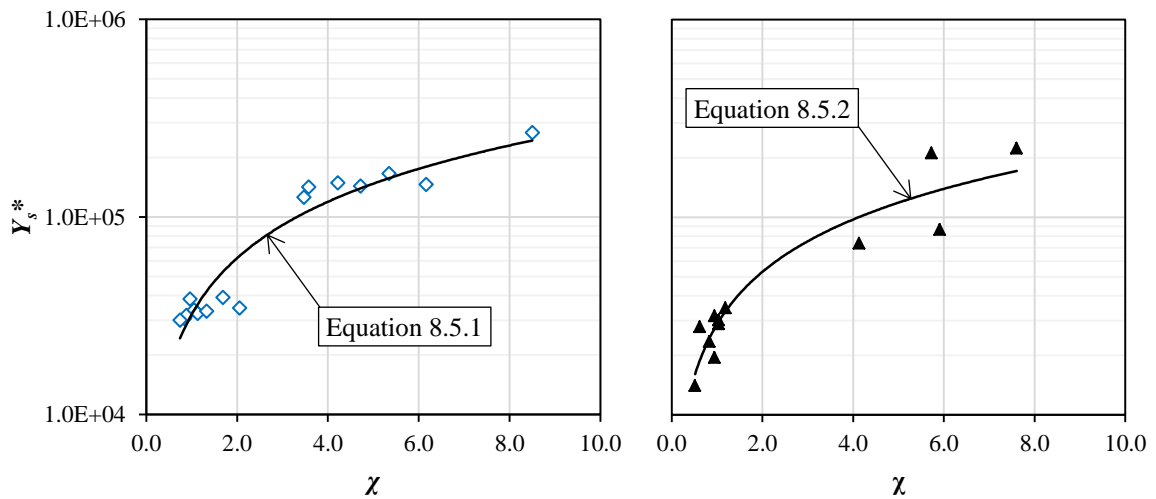
### ***Bed Load Yield Prediction with a Vegetation Patch***

The hydrograph descriptor variable,  $\chi$ , introduced in Chapter 6 and applied in Chapter 7 was used to develop predictive relationships for bed load yield from a sediment

bed with a vegetation patch. To maintain consistency with the patch mound adjustment model (Section 7.5.3), separate bed load yield relationships were derived for the sparse patch (Equation 8.5.1; Figure 8.5.3a) and dense patch (Equation 8.5.2; Figure 8.5.3b):

$$Y_s^* = 32,106\chi^{0.946} \quad (8.5.1)$$

$$Y_s^* = 28,767\chi^{0.880} \quad (8.5.2)$$



(a) Sparse patch yield ( $R^2 = 0.91$ ).

(b) Dense patch yield ( $R^2 = 0.90$ ).

**Figure 8.5.3.** Bed load yield prediction for patch-sediment data set.

These bed load yield prediction relationships provide broad estimates of expected yield for given hydrograph and channel characteristics. When compared with Equation 6.5.2, which predicted sediment yield without a patch, the patch yield predictions either increase or decrease bed load yield depending on the range in  $\chi$  (Figure 8.5.4). At small values of  $\chi$ , which represent low hydrograph work, unsteadiness, or coarser sediment, yield predictions are similar for the no patch and patch conditions. Above an approximate  $\chi$  value of 3.4, reductions in yield are predicted for the dense patch. A similar transition occurs for the sparse patch; for  $\chi$  values greater than approximately 15.5, the sparse patch

would be expected to reduce yield relative to a channel without a patch. In particular, the varying impact of the dense patch on sediment yield likely represents a transient effect in patch-adjacent scour as yield increases when these areas scour during initial flow events, but then decreases with subsequent flows as the bed approaches a more stable state at the patch location. Equations 8.5.1 and 8.5.2 are based on a finite number of data points and should be applied cautiously. However, they are the first relationships of their kind, offering predictions about how a vegetation patch influences bed load yield for different hydrographs and sediment types.

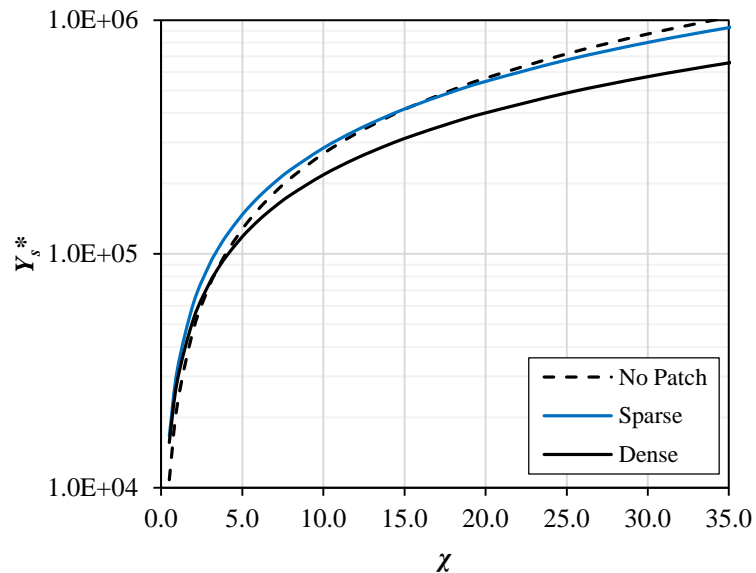


**Figure 8.5.4.** Comparison of bed load yield prediction curves.

### 8.5.2 Transport Hysteresis with a Vegetation Patch

Varying bed load hysteresis patterns were measured during hydrographs with a patch present. The conceptual framework presented in Chapter 6 (Table 6.5.1) for describing hysteresis in the context of bedform geometry was applied to the transport data with a vegetation patch in the sand/gravel and sand/silt channels. This framework was extended to include the six hydrographs in which no hysteresis was measured, which

was expected when bedform steepness remained unchanged prior to and after a hydrograph. The expanded conceptual framework fit with measured hysteresis patterns in 51.7% of hydrographs. While this is fair agreement, the bedform framework clearly does not fully describe hysteresis in vegetated channels.

In addition to bedform development and migration, bed surface patchiness or variations in sediment supply resulting from lags in transport distance along a reach can contribute to bed load hysteresis [e.g. *Lisle and Madej*, 1992]. When the vegetation patch was present, alterations in reach-scale hydraulics allowed distinct bed morphologies to develop within unsteady flow sequences (Chapter 7). The morphology of a channel prior to an unsteady flow event should influence temporal trends of sediment transport during a subsequent hydrograph. In these experiments, sediment accumulated as mound features downstream of patches and the area and volume of these patch mounds dynamically adjusted over a hydrograph sequence. In addition to the measurable change in bed topography after a hydrograph, hydraulics in the area around the patch would have caused further adjustments in the bed surface locally during the flow event. Thus, it is expected that changes in bed morphology around a vegetation patch may impact hysteresis patterns during individual hydrographs by providing a temporally variable sediment supply.

Data from the bed monitoring system were utilized to evaluate changes in the sediment bed during hydrographs. Best-fit linear trends in transducer load signals were determined for each four minute constant flow period during a hydrograph. Curves were developed from these time-variable relationships to approximate the cumulative change in weight over the first meter downstream of the patch (Figure 8.5.5). The first

downstream meter was selected because it is the area over which the flow field is most impacted by the patch, both downstream and adjacent to the patch location. The steady wake over mobile beds is contained within this 1 m distance (Section 7.5.1), which represents an area of reduced velocity and turbulence intensity, and within the first downstream meter, flow acceleration around the patch is greatest.

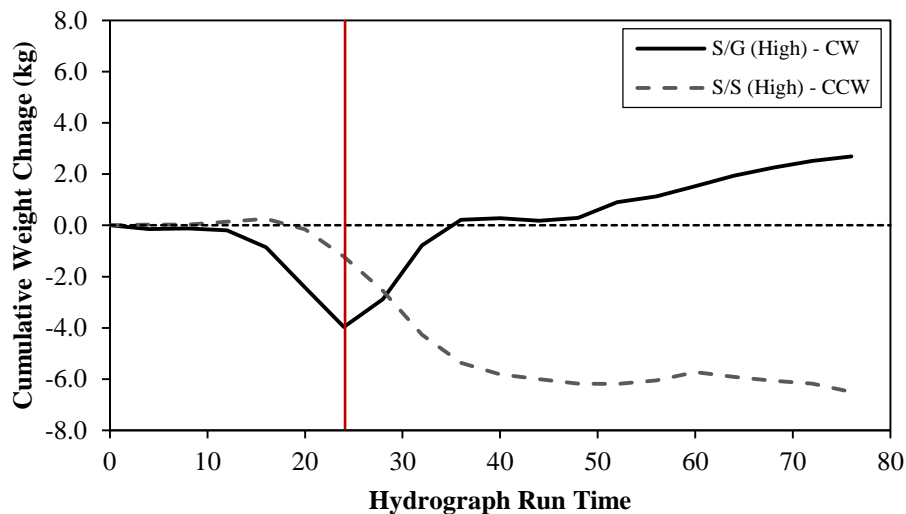


**Figure 8.5.5.** Sediment bed weight as indicator of patch induced transport hysteresis. Peak flow time is indicated by vertical red line.

These data were used to infer the patch influence on local bed morphology as a factor in reach-scale transport hysteresis by evaluating the timing and sign of cumulative weight changes. For instance, Figure 8.5.5 shows two cumulative weight curves for the first meter downstream of a dense patch in each of the two sediment mixtures. The solid black line shows that the downstream bed material decreased prior to the peak flow rate, indicating that more material in the vicinity of the patch was eroded out and transported downstream. After the peak flow, the weight of material in this segment increased, indicative of aggradation and lower sediment transport. Therefore, this trend suggests clockwise (CW) hysteresis. Conversely, the dashed gray line shows a reduction in bed

material around the patch following the peak flow, indicating that more material was transported out of this segment on the falling limb, or counterclockwise hysteresis.

These example transducer records agreed with the measured transport hysteresis for those particular hydrographs, patches, and sediment mixtures. Overall, cumulative bed weight changes around the patch were in agreement with measured hysteresis for approximately 48% of the hydrographs in which hysteresis was documented, with slightly better depictions for CW transport. For hydrographs of either magnitude with the dense patch in the sand/silt beds, transducer records agreed with measured hysteresis in all instances, highlighting the impact of increased flow blockage in a mobile substrate and its potential influence on transport hysteresis.

As with the bedform-hysteresis framework, this analysis does an adequate job in describing one of the potential causes of hysteresis in the presence of a vegetation patch but does not fully capture the process. Introduction of a vegetation patch into a channel alters the reach-scale hydraulics and channel morphology during unsteady flow regimes, adding complexity to the system that is reflected in the varying temporal patterns of sediment transport. Although bedforms and spatial variability of sediment supply appeared to influence transport hysteresis in a channel with a vegetation patch, it is hard to identify which factor was dominant because for some hydrographs both frameworks agreed with measured transport patterns, and for others, neither did. The likely scenario is a complex interaction between these two processes.

### **8.5.3 Sediment Transport Predictions with a Vegetation Patch**

#### ***Total Transport: Yang Equation with a Patch***

The Yang equation was used to predict transport rates across the range of flow,

sediment, and vegetation patch characteristics tested. Predictions were satisfactory for the sand/gravel mixture but were biased towards overprediction with a mean  $DR$  of 1.8. Prediction accuracy was impacted by patch density and flow magnitude as transport rates were more accurately predicted for the sparse patch and higher flow hydrographs. For the sand/silt mixture, the median  $DR$  of 1.1 suggested improved accuracy over for the sand/gravel beds, but there was increased scatter in the predictions (Figure 8.4.1), and a decreased percentage of predictions within desirable ranges (Table 8.4.2). Patch density was responsible for a large amount of the discrepancy in transport predictions (Figure 8.4.2), which indicated that the Yang equation was not able to account for the impact of the vegetation patch. With the influence of the patch, 92% of predictions were within an order of magnitude of the measured rates, suggesting that the Yang relationship can be applied to obtain broad estimates of transport with a patch present. However, this equation lacked strong predictive capacity for the patch conditions, which was expected given that it was not specifically developed for transport in a vegetated channel.

#### ***Fractional Transport: Dimensionless Bed Load Relationships with a Patch***

A dimensionless fractional bed load transport relationship was derived for the patch-sediment data set using non-linear regression of the Parker-Einstein (P-E) equation with modified coefficients (Equation 6.5.5), the separate limb transport approach introduced in Chapter 6, and the reference shear stresses given in Table 8.2.1. To account for the presence of a vegetation patch, separate relationships were developed for the rising and falling limbs of the sparse and dense patch runs. Thus, derived transport coefficients were specific to hydrograph limb and patch density, resulting in four unique transport equations for the patch-sediment data set (Table 8.5.1).

**Table 8.5.1.** Dimensionless transport coefficients with vegetation patch.

Patch Density	Hydrograph Limb	<i>a</i>	<i>b</i>
No Patch <sup>1</sup>	Rising	11.3	4.06
	Falling	11.7	3.98
Sparse	Rising	9.9	4.13
	Falling	9.8	4.37
Dense	Rising	10.1	3.82
	Falling	10.1	3.70

<sup>1</sup>Coefficients derived in Chapter 6.

The fractional transport relationships were used to predict unit transport rates for the unsteady flow data set with either a sparse or dense vegetation patch present in the channel. Prediction accuracy metrics indicated accurate estimates of transport rates (Table 8.5.2). In particular, 65% of the predictions were within a factor of 2.0 for the combined data set (i.e. both hydrograph limbs and patch densities), and the *NRMSE* was less than 8.0%. Figure 8.5.6 shows each respective transport relationship and data set.

**Table 8.5.2.** Dimensionless transport prediction results with vegetation patch.

Patch Density	Hydrograph Limb	<i>RMSE</i>	<i>NRMSE</i>	Median <i>DR</i>	$0.1 \leq DR \leq 10$	$0.5 \leq DR \leq 2.0$
Sparse	Rising	12.4	10.2%	1.0	95.8%	67.2%
	Falling	8.2	9.3%	1.0	94.6%	64.7%
	Both	10.0	8.2%	1.0	95.0%	65.6%
Dense	Rising	9.1	10.2%	1.0	85.7%	63.1%
	Falling	7.3	11.9%	1.0	92.4%	64.6%
	Both	9.3	10.5%	1.0	89.9%	64.0%
Both	Rising	11.1	9.1%	1.0	91.6%	65.5%
	Falling	7.8	8.9%	1.0	93.7%	64.7%
	Both	9.2	7.5%	1.0	92.9%	65.0%

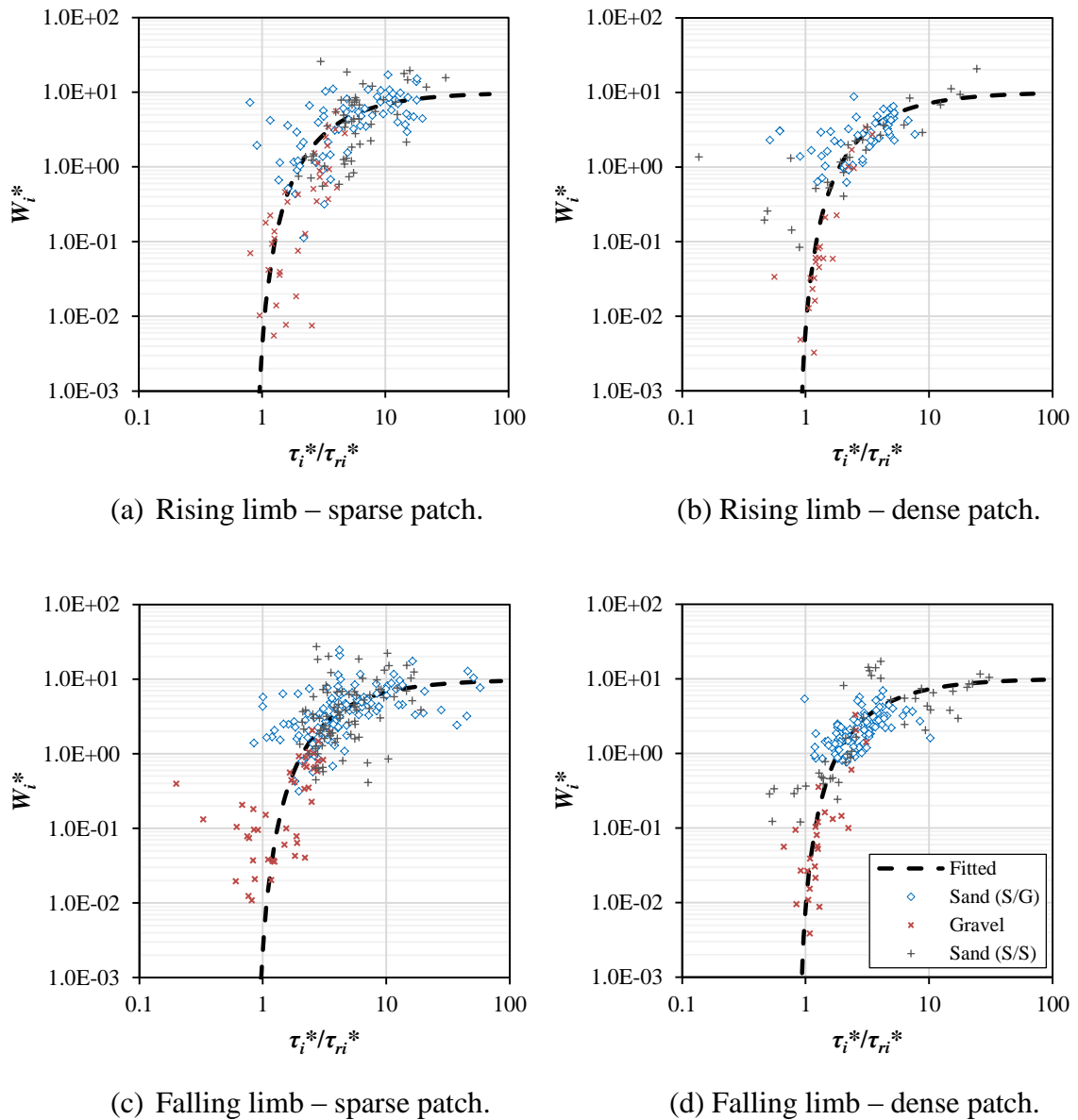


**Figure 8.5.6.** Dimensionless bed load transport relationships with patch. The legend given in (d) applies to all plots.

### *Comparison of Total and Fractional Transport Predictions*

The fractional transport equations gave more accurate predictions of transport rates than the Yang equation (Table 8.5.3), although neither relationship performed as well at lower flows. Total transport predictions obtained by combining fractional transport estimates showed less scatter and a higher percentage of predictions within a

factor of 2.0 of measured total transport rates across the full patch data set, which included two sediment mixtures. The Yang equation was developed with uniform sediment in channels without obstructions. Because the dimensionless fractional approach considered differences in grain entrainment and transport rates resulting from a sediment mixture and the presence of a vegetation patch in unsteady flows, it was able to more accurately model temporal variability in bed load transport.

**Table 8.5.3.** Prediction results for combined patch-sediment data set.

<b>Approach</b>	<b><i>RMSE</i></b>	<b><i>NRMSE</i></b>	<b>Median <i>DR</i></b>	<b><math>0.1 \leq DR \leq 10</math></b>	<b><math>0.5 \leq DR \leq 2.0</math></b>
Yang	17.3	14.2%	1.6	98.0%	53.5%
Separate limb (Modified P-E)	9.2	7.5%	1.0	92.9%	65.0%

### ***Discussion of Sediment Transport with a Vegetation Patch***

The fractional transport relationships developed for each limb and patch density indicate that higher transport rates should occur when a dense patch is present, as opposed to a sparse patch (Table 8.5.1). This is related to the changing hydraulics around and downstream of patches of varying stem density. Dense patches create greater flow blockage and divert more flow around the patch. This results in greater velocities around the patch, inducing scour and mobilizing sediment in these areas. Patch-scale turbulence is greater downstream of dense patches than sparse ones (Chapter 4), which is expected to create a flow field more conducive to sediment transport. The length-scales over which a dense patch impacts the flow field are shorter than for a sparse patch, focusing the kinetic energy in a limited area. Thus, when considering transport rates over a reach-scale, it is reasonable that higher transport rates occur for the patch density with a shorter

downstream influence on the mean flow field.

The dimensionless fractional transport relationships derived in this chapter and Chapter 6 predict that a patch of either stem density should reduce reach-scale transport rates relative to an unvegetated channel for the same excess shear stress. This is particularly true at higher shear stresses (Figure 8.5.7), which suggests that the effects of a vegetation patch on sediment transport rates extend to the higher flow conditions that may be found in unsteady flow regimes.

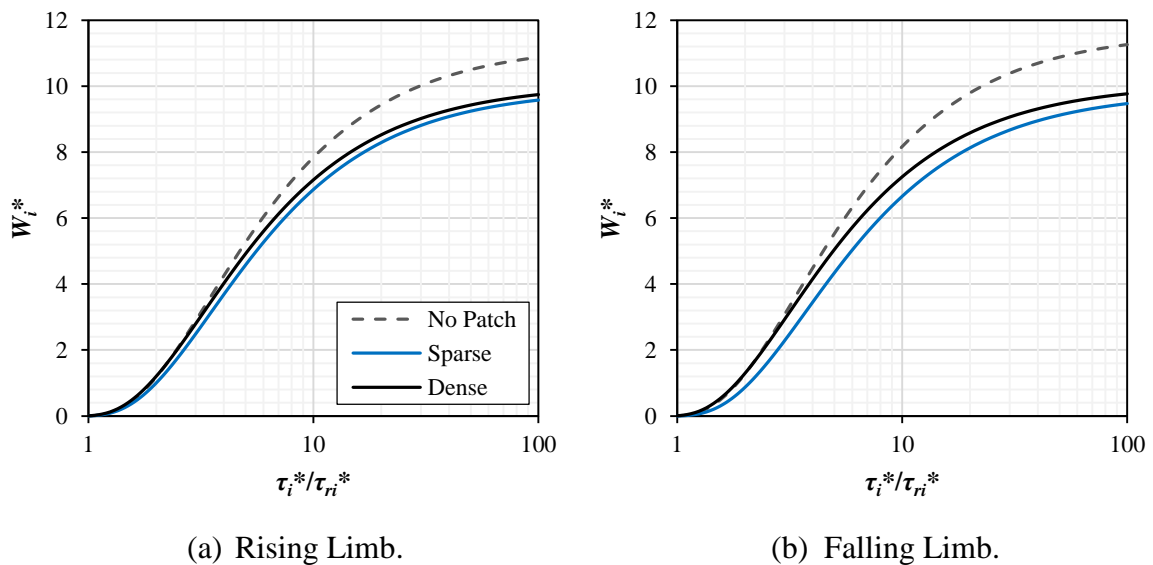


**Figure 8.5.7.** Dimensionless transport curves for patch and no patch flows. The plots are semi-log to more clearly illustrate differences in transport rates for each case.

The ratio of unit sediment transport rate in a channel with a patch to the rate in one without a patch,  $q_{s,p}/q_{s,np}$ , is expected to vary with the amount of excess shear stress generated by the flow, patch density, and hydrograph limb. The influence of excess shear stress,  $\tau_i^*/\tau_{ri}^*$ , should be minimized as the value increases and a constant difference in transport rates is approached at an excess stress equal to 100 (Figure 8.5.8). At these increased shear stresses, unit transport rate in a channel with a sparse vegetation patch is

predicted to be 12% and 16% less than in a channel with no patch for hydrograph rising and falling limbs, respectively. For a dense patch, reductions in unit transport rates are predicted to be 10.5% for the rising limb and 13% for the falling limb.

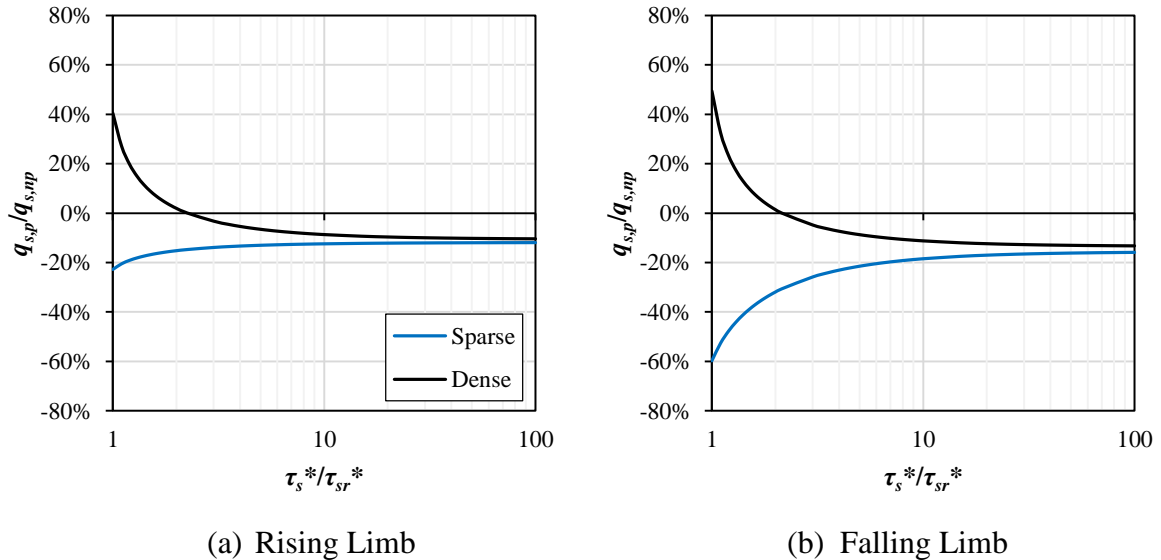


**Figure 8.5.8.** Differences in predicted sand transport rates for patch and no patch flows.

For the dense patch, there is a transition shear stress after which the patch begins to reduce transport rates relative to an unvegetated channel (Figure 8.5.8). When  $\tau_i^*/\tau_{ri}^* > 2.25$  for the rising limb and  $\tau_i^*/\tau_{ri}^* > 2.14$  for the falling limb, the transport rate is less than for a channel with no patch. This transition point from increased to reduced transport rates implies that the changes in hydraulics and bed morphology caused by a dense patch enhance transport at low flows. For increased flows and shear stresses, the patch influence on the flow field extends farther downstream and reduces transport rates at the reach-scale.

The dimensionless and fractional approach to bed load transport applied in this chapter utilized the separate limb methodology to incorporate much of the bed structure and transport complexity that occurs in unsteady flows. With the added complexity of a

vegetation patch in the channel, the modified Parker-Einstein fractional transport relationship was able to accurately predict bed load transport rates within acceptable ranges of uncertainty while discretely accounting for two different patch densities. Adding to these data sets by including additional sediment mixtures, patch configurations, or unsteady flow regimes (flow magnitudes, hydrograph shapes, timing, etc.), as well as inclusion of field data, would enhance the applicability of the transport relationships developed here. Regardless, the dimensionless, separate limb approach was effective for predicting transport rates with a vegetation patch in unsteady flows.

## **8.6 SUMMARY**

A vegetation patch impacted sediment yield, hysteresis, and transport rates depending on patch density and sediment mixture. In the sand/gravel beds, the presence of a patch increased hydrograph bed load yield, which was greatest for the sparse patch. Increased surface sand content and patchiness for these patch beds decreased reference shear stresses of the sand fraction relative to the no patch channels, which resulted in larger excess shear stresses and increased yields. For the dense patch, the surface sand content was not as high, which translated to higher reference shear stresses for the sand fraction and bed load yield that was less than the sparse patch, but still greater than the no patch conditions. For the sand/silt sediment mixture, patches of either stem density increased ripple heights which reduced the skin friction available for bed load transport and reduced sediment yield relative to the no patch channels. Separate predictive relationships for bed load yield were developed for the sparse and dense patches based on the hydrograph and channel descriptor variable,  $\chi$ . These relationships are unique in that

they provide initial hydrograph yield estimates when a channel contains an emergent vegetation patch.

Bed load hysteresis was measured in the majority of hydrographs with a patch present, but there was not a consistent pattern. The bedform-hysteresis framework proposed in Chapter 6 was applied to the patch-sediment data set and it was found to agree with measured hysteresis behavior in slightly more than half of the hydrographs. Data from the bed monitoring system for the first meter downstream of the patch was also used to evaluate the potential influence of a vegetation patch on transport hysteresis in terms of controlling local sediment supply. Changes in cumulative weight in this area were quantified and used to infer hysteresis patterns, but agreement with measured hysteresis was only found in approximately half of the hydrographs. Results from each analysis prevented identification of a dominant hysteresis indicator. The complexity in the flow field and bed morphology caused by a vegetation patch introduced large variability in transport patterns during unsteady flows making the likely cause of much of the hysteresis an interaction between changes in bed surface structure, supply, and bedform adjustment.

The Yang relationship overpredicted sediment transport rates for the patch-sediment data set. Prediction accuracy varied with patch density and sediment mixture, with the most accurate predictions occurring for the sparse patch in the sand/gravel beds. Because the Yang equation was developed for uniform sediment without consideration of a reach-scale flow obstruction like a vegetation patch, it should only be used for vegetated channels in unsteady flows to obtain broad transport estimates.

Dimensionless fractional transport relationships were developed using the

separate limb approach introduced in Chapter 6 and the Parker-Einstein equation with coefficients that were modified for the PS data set. Coefficients were derived for each hydrograph limb and patch density, resulting in four unique transport relationships. Transport predictions with these relationships showed good accuracy, as 65% were within a factor of two of measured rates. Because the data set was separated by hydrograph limb and patch density, the fractional transport relationships accounted for spatial complexities in reference shear stresses resulting from the presence of a patch, as well as temporal variability in bed load transport during unsteady flows. When compared to the predictive relationship for transport without a patch (Chapter 6), the sparse and dense patch equations each predicted reduced transport rates, with maximum reductions for the sparse patch on the order of 16% at larger excess shear stresses.

The analysis presented here suggests that the role of reference shear stress is paramount in evaluating sediment transport in unsteady flow regimes. Although lower transport rates were predicted for vegetated channels, reference shear stresses were lower when a patch was present in the sand/gravel beds, which produced larger hydrograph yields than with no patch. In the sand/silt beds, patch presence contributed to the formation of larger bedforms, which increased reference shear stresses and decreased sediment yield. Bed morphology greatly influenced sediment transport at the time-scales of repeated unsteady flow events, and the introduction of a vegetation patch further increased variability in sediment transport. Whether a vegetation patch is beneficial or detrimental to reach-scale transport rates is highly dependent on the bed sediment type and surface structure.

## CHAPTER 9

### *Conclusions and Recommendations*

---

---

The primary hypothesis of this work was that an in-channel patch of emergent vegetation alters flow patterns and bed morphology in a way that reduces sediment transport and promotes reach-scale channel stability over repeated unsteady flows. Three groups of flume experiments were conducted to test this main hypothesis. The first group focused on hydraulics downstream of a vegetation patch of varying stem density and configuration, measuring the velocity field around a patch without a sediment bed. The second group tested sediment beds of two different mixtures without a patch to investigate patterns of sediment transport and bed morphology in unsteady flows. The third group built on the first two by including a vegetation patch in a sediment bed, emphasizing the impact of vegetation on sediment transport and bed morphology changes over unsteady flow repetitions. This research is the first comprehensive study into how vegetation impacts sediment transport and channel morphology in unsteady flows. Focusing the analysis over extended temporal scales using repeated hydrographs provides for better connections to natural systems than has previously been done to evaluate the potential benefits of an emergent vegetation patch.

At the core of this work is the link between bed morphology and sediment transport, each of which was greatly impacted by a vegetation patch and the bulk bed sediment distribution. Patches of both sparse and dense stem density increased

topographic variability of all sediment beds, but in different ways depending on sediment mixture. For sand/gravel beds, a vegetation patch altered the spatial structure of the bed surface such that entrainment thresholds were lower than for the same conditions without a patch. This increased hydrograph bed load yields, particularly for the sparse patch which had the lowest reference shear stresses as a result of high sand content and patchiness on the surface. In the case of sand/silt beds, bedforms were the dominant bed feature. When a patch was present, larger ripples formed, which reduced skin friction and bed load yield relative to beds without a patch. Thus, how a vegetation patch affected overall sediment yield during hydrographs was primarily dictated by the sediment type and the degree to which the patch density affected the bed surface.

Dimensionless fractional bed load transport relationships were developed based on the concept of excess shear stress above a reference transport value. Coefficients of the Parker-Einstein relationship (Equation 6.5.4) were modified for the no patch and patch-sediment data sets. A separate limb transport approach was applied in which reference shear stresses were estimated for each limb of each individual hydrograph. This novel methodology was well suited for unsteady flow conditions because it implicitly accounted for temporal changes in channel surface complexity, bed structure, and sediment availability over an unsteady flow sequence through measurable changes in grain entrainment. Transport coefficients were derived specifically for hydrograph rising and falling limbs for no patch, sparse patch, and dense patch channels. Comparison of predictive relationships showed that vegetation patches reduce reach-scale transport rates as excess shear stress increases. Predictive relationships developed specifically for patch beds in unsteady flows were more accurate than the *Yang* [1973] transport equation,

capturing much of the temporal transport variability characteristic of unsteady flow conditions, as well as spatial bed surface variability created by the patches.

The role of a vegetation patch on channel stabilization was largely impacted by bed sediment distribution and patch density. Introduction of dynamic stability as a term to classify a reach as neither net aggradational nor net degradational over multiple flow events aided in the analysis of morphological adjustment. A unit bed adjustment parameter was proposed which enabled the use of DEM differencing to quantify dynamic stability at the reach-scale both with and without a patch. While vegetation is generally regarded to be a method for stabilizing bank sediment [e.g. *Tal and Paola, 2007; Braudrick et al., 2009*] and promoting zero net deposition at the reach-scale in low, steady flows [*Follett and Nepf, 2012*], the results presented here suggest a limited subset of patch, sediment, and unsteady flow conditions in which an in-channel emergent vegetation patch enhances channel stability. The most stable channel reach conditions were found when the sparse patch was in a bed of either sediment mixture that was subjected to the lower flow hydrograph sequences. In most cases for the sand/silt mixture, the patch location itself was subjected to extensive scour, indicating an erosive morphology around the patch that could promote patch removal. Thus, for unsteady flow regimes like those tested in these experiments, a vegetation patch was primarily detrimental to reach-scale stability.

The general application of emergent vegetation patches as an in-channel restoration measure remains inconclusive. Flow field alterations and topographic variability were measured over a wide range of values in this study, which would be beneficial in terms of habitat creation for a given restoration project. However, sediment

type and flow regime appear to dictate how much a vegetation patch can improve sediment retention and reach-scale stability. The somewhat contradictory results regarding patch sediment yield and transport rates highlights the importance of bed structure when considering an in-channel patch. Until a larger range of sediment, patch, and flow conditions are tested, in-channel vegetation patches should be used cautiously in restoration efforts, particularly when the primary goals are reductions in downstream sediment transport and channel stability.

### ***Recommendations for Future Work***

This research represents a foundation from which to develop an evaluative framework for assessment of an in-stream vegetation patch in stream restoration. Such a framework would necessarily include sediment transport and reach-scale stability impacts based on patch characteristics, unsteady flow regime, and bed sediment distribution. The current data set is based on repetition of hydrographs of the same flow magnitude, with two hour baseflow periods in between. This type of flow regime is representative of somewhat flashy conditions, with intermittent low flow periods only slightly longer than the hydrographs themselves. Thus, findings of this work should be extended through inclusion of different flow regimes, including variable hydrograph shapes, flow magnitudes, unsteadiness, and timing patterns. In particular, providing for prolonged low flow periods between hydrographs would further improve the link with natural river systems, adding the complexity of bed consolidation and stabilization between flood events that has been shown to alter sediment transport and hysteresis during a flood [e.g. Reid *et al.*, 1985].

Variable flow regimes and timing will likely have a large impact on the

morphological stability of a channel reach with a vegetation patch, including downstream sediment accumulation and longitudinal patch expansion. The patch mound adjustment model presented in Chapter 7 is based on cumulative flow work and therefore could be refined to include a range of hydrograph characteristics and timing sequences, as well as different patch densities. With extended low flow periods between hydrographs, it is hypothesized that patch mounds would accumulate material before decreasing in area with a flood event in similar fashion to what was measured here. Therefore, a cyclical type of behavior would be expected, where depending on the timing of flood events and growing season, patch mounds could increase and allow patch expansion or higher flows could limit mound accretion and patch growth. Unsteady flows add complexity to patch growth dynamics that could be better understood by expanding the patch mound dynamics model proposed in this work to accommodate a wider range of field conditions.

The separate limb transport approach applied in this study may also prove useful for deriving unsteady flow transport equations based on new data, or by re-analyzing past data sets to tweak current relationships. Because sediment transport hysteresis is widely observed both in the lab and field, it seems reasonable that any approach that accounts for temporal complexities in grain entrainment or sediment supply would provide better estimates of sediment transport during a flow event, either with or without a vegetation patch present.

## CHAPTER 10

### *References*

---

---

- Aberle, J. and G. M. Smart (2003). The influence of roughness structure on flow resistance on steep slopes, *J. Hydraul. Res.*, **41**, 259-269.
- Aberle, J. and V. Nikora (2006). Statistical properties of armored gravel bed surfaces, *Water Resour. Res.*, **42**(11), W11414.
- Abt, S., W. Clary, and C. Thornton (1994). Sediment deposition and entrapment in vegetated streambeds, *J. Irrigation Drainage Eng.*, **120**, 1098-1110.
- Ackers, P., and W. R. White (1973). Sediment transport: new approach and analysis, *J. Hydraul. Div. Am. Soc. Civ. Eng.*, **99**(HY11), 2041-2060.
- Afzalimehr, H., Dey, S. (2009). Influence of bank vegetation and gravel bed on velocity and Reynolds stress distributions, *Int. J. Sediment Research*, **24**(2), 236-246.
- Ahanger M. A., G. L. Asawa, and M. A. Lone (2008). Experimental study of sediment transport hysteresis, *J. Hydraul. Res.*, **46**(5), 628-635.
- Asaeda, T., T. Fujino, and J. Manatunge (2005). Morphological adaptations of emergent plants to water flow: a case study with *Typha angustifolia*, *Zizania latifolia* and *Phragmites australis*, *Freshwat. Biol.*, **50**, 1991-2001.
- Asaeda, T., L. Rajapakse, and M. Kanoh (2010). Fine sediment retention as affected by annual shoot collapse: *Sparganium erectum* as an ecosystem engineer in a lowland stream, *River Res. Applic.*, **26**, 1153-1169.

- Ashbridge, D. (1995). Processes of river bank erosion and their contribution to the suspended sediment load of the River Culm, Devon, in Foster, I. D. L., A. M. Gurnell, and B. W. Webb (Eds.), *Sediment and Water Quality in River Catchments*, Wiley, Chichester, pp 229-245.
- Asselman, N.E. (1999). Suspended sediment dynamics in a large drainage basin: the River Rhine, *Hydrol. Process.*, **13**, 1437-1450.
- Baatrup-Pedersen, A. and T. Riis (1999). Macrophyte diversity and composition in relation to substratum characteristics in regulated and unregulated Danish streams, *Freshwat. Biol.*, **42**(2), 375-385.
- Ball, B. J., P. K. Stansby, and N. Alliston (1996). Modeling shallow water flow around pile groups, *Proc. Inst. Civ. Eng. Water Marit. Energy*, 118, 226-236.
- Bennett, S. J., T. Piram, and B. D. Barkdoll (2002). Using simulated emergent vegetation to alter stream flow direction within a straight experiment channel, *Geomorph*, **44**(1-2), 115-126.
- Best, J. L. (2005). Kinematics, topology and significance of dune-related macro-turbulence: some observations from the laboratory and field, *Spec. Publs int. Ass. Sediment*, **35**, 41-60.
- Bombar, G., S. Elci, G. Tayfur, M. S. Guney, and A. Bor (2011). Experimental and numerical investigation of bed-load transport under unsteady flows, *J. Hydraul. Eng.*, **137**(10), 1276-1282.
- Bouma, T. J., L. van Duren, S. Temmerman, T. Claverie, A. Blanco-Garcia, T. Ysebaert, and P. Herman (2007). Spatial flow and sedimentation patterns within patches of

- epibenthic structures: combining field, flume and modeling experiments, *Cont. Shelf Res.*, **27**(8), 1020-1045.
- Bouma, T. J., M. Friedrichs, B. K. van Wesenbeeck, S. Temmerman, G. Graf, and P. M. J. Herman (2009). Density-dependent linkage of scale-dependent feedbacks: a flume study on the intertidal macrophyte *Spartina anglica*, *Oikos*, **118**(2), 260-268.
- Bouma, T. J., S. Temmerman, L. A. van Duren, E. Martini, W. Vandenbruwaene, D. P. Callaghan, T. Balke, G. Biermans, P. C. Klaassen, and P. van Steeg (2013). Organism traits determine the strength of scale-dependent bio-geomorphic feedbacks: A flume study on three intertidal plant species, *Geomorph.*, **180–181**, 57-65.
- Braudrick, C. A., W. E. Dietrich, G. T. Leverich, and L. S. Sklar (2009). Experimental evidence for the conditions necessary to sustain meandering in coarse-bedded rivers, *PNAS*, **106**(40), 16936-16941.
- Brown, C. B. (1950). Sediment transportation. In *Engineering Hydraulics*, Rouse H (ed.), John Wiley & Sons, New York, 769-857.
- Brownlie, W. R. (1981). Prediction of flow depth and sediment discharge in open channels, Report KH-R-43A, W. M. Keck Laboratory of Hydraulics and Water Resources Division of Engineering and Applied Science, California Institute of Technology, Pasadena, CA.
- Buffington, J. M., and D. R. Montgomery (1997). A systematic analysis of eight decades of incipient motion studies, with special reference to gravel-bedded rivers, *Water Resour. Res.*, **33**(8), 1993-2027.

- Carling, P. A., J. J. Williams, E. Golz, and A. D. Kelsey (2000). The morphodynamics of fluvial sand dune in the River Rhine, near Mainz Germany. I. Hydrodynamics and sediment transport, *Sedimentology*, **47**, 253-278.
- Chambers, P. and E. Prepas (1994). Nutrient dynamics in riverbeds: the impact of sewage effluent and aquatic macrophytes, *Water Res.*, **28**, 453-464.
- Chapman, J. and M. Blickenderfer (2011). "What is your confidence using bioengineering erosion control on Minnesota shorelines?" Presentation to the Minnesota Erosion Control Association, March 3, 2011.
- Chen, Z., A. Ortiz, L. Zong, and H. Nepf (2012). The wake structure behind a porous obstruction and its implications for deposition near a finite patch of emergent vegetation, *Water Resour. Res.*, **48**, W09517.
- Chesapeake Executive Council (CEC) (2003). Expanded riparian forest buffer goals, Directive 03-01, Chesapeake Bay Program.
- Clarke, S. J. (2002). Vegetation growth in rivers: influences upon sediment and nutrient dynamics, *Prog. Phys. Geogr.*, **26**(2), 159-172.
- Clarke, S. J. and G. Wharton (2001). Sediment nutrient characteristics and aquatic macrophytes in lowland English rivers, *Sci. Total Environ.*, **226**(1-3), 103-112.
- Cohen, H., J. B. Laronne, and I. Reid (2010). Simplicity and complexity of bed load response during flash floods in a gravel bed ephemeral river: a 10 year field study, *Water Resour. Res.*, **46**, W11542.
- Coops, H. and G. Van der Velde (1996). Effects of waves on helophyte stands: mechanical characteristics of stems of *Phragmites australis* and *Scirpus lacustris*, *Aquatic Botany*, **53**, 175-185.

- Corenblit, D., J. Steiger, A. M. Gurnell, E. Tabacchi, and L. Roques (2009). Control of sediment dynamics by vegetation as a key function driving biogeomorphic succession within fluvial corridors, *Earth Surf. Processes Landforms*, **34**(13), 1790-1810.
- Cotton, J. A., G. Wharton, J. Bass, C. M. Heppell, and R. S. Wotton (2006). The effects of seasonal changes to in-stream vegetation cover on patterns of flow and accumulation of sediment, *Geomorph.*, **77**, 320–334.
- Crowder, D. W. and P. Diplas (2000). Using two-dimensional hydrodynamic models at scales of ecological importance, *J. of Hydr.*, **230**, 172-191.
- Crowder, D. W. and P. Diplas (2002). Vorticity and circulation: spatial metrics for evaluating flow complexity in stream habitats, *Can. J. Fish. Aquat. Sci.*, **59**, 633-645.
- De Sutter, R., R. Verhoeven, and A. Krein (2001). Simulation of sediment transport during flood events: laboratory work and field experiments, *Hydrol. Sci. J.*, **46**(4), 599-610.
- Doomen, A. M. C., E. Wijma, J. J. G. Zwolsman, and H. Middelkoop (2008). Predicting suspended sediment concentrations in the Meuse River using a supply-based rating curve, *Hydrol. Process.*, **22**, 1846-1856.
- Einstein, H.A. (1942). Formula for the transportation of bed-load, *T. Am. Soc. Civ. Eng.*, **107**.
- Einstein, H. A. (1950). The bed-load function for sediment transportation in open channel flows, *Technical Bulletin No. 1026*, U.S. Department of Agriculture, Washington, D.C.
- Einstein, H. A., and N. Chien (1953). Transport of sediment mixtures with large ranges of grain size, Missouri River Division Sediment Series No. 2, U.S. Army Corps of

- Engineers Missouri River Division, University of California Institute of Engineering Research, Berkeley.
- Elci, S., R. Aydin, and P. A. Work (2009). Estimation of suspended sediment concentration in rivers using acoustic methods, *Environ. Monit. Assess.*, **159**, 255-265.
- Engelund, F., and E. Hansen (1967). *A Monograph on Sediment Transport in Alluvial Streams*, Technical University of Denmark, Lyngby, 62.
- Ettema, R., G. Constantinescu, and B. Melville (2011). Evaluation of bridge scour research: pier scour processes and predictions, Contractor's Final Report for NCHRP Project 24-27(01), Transportation Research Board of the National Academies.
- Follett, E. M. and H. M. Nepf (2012). Sediment patterns near a model patch of reedy emergent vegetation, *Geomorph.*, **179**, 141-151.
- French, T. D. and P. A. Chambers (1996). Habitat partitioning in riverine macrophyte communities, *Freshwat. Biol.*, **36**(3), 509-520.
- Gerstner, C. L. (1998). Use of substratum ripples for flow refuging by Atlantic cod, *Gadus morhua*, *Environ. Biol. Fish.*, **53**, 455-460.
- Goring, D. G. and V. I. Nikora (2002). Despiking acoustic Doppler velocimeter data, *J. Hydraul. Eng.*, **128**(1), 117-126.
- Graf, W.H. and L. Suszka (1985). Unsteady flow and its effect on sediment transport, *Proceedings, 21<sup>st</sup> IAHR Congress*, August 1985, Melbourne, Australia, 540-544.
- Gran, K., and C. Paola (2001). Riparian vegetation controls on braided stream dynamics, *Water Resour Res.*, **37**(12), 3275-3283.

- Griffiths, G. A., and A. J. Sutherland (1977). Bedload transport by translation waves, *J. Hydraul. Div. Am. Soc. Civ. Eng.*, **103**, 1279-1291.
- Guney, M. S., G. Bombar, and A. O. Aksoy (2013). Experimental study of the coarse surface development effect on the bimodal bed-load transport under unsteady flow conditions, *J. Hydraul. Eng.*, **139**(1), 12-21.
- Gurnell, A. M. and Petts, G. E. (2002). Island-dominated landscapes of large floodplain rivers, a European perspective, *Freshwater Biology*, **47**, 581-600.
- Gurnell, A. M., M. P. van Oosterhout, B. de Vlieger, and J. M. Goodson (2006). Reach-scale interactions between aquatic plants and physical habitat: River Frome, Dorset, *River Res. Applic.*, **22**(6), 1535-1467.
- Gurnell, A. M., J. M. O'Hare, M. T. O'Hare, M. J. Dunbar, and P. M. Scarlett (2010). An exploration of associations between assemblages of aquatic plant morphotypes and channel geomorphological properties within British rivers, *Geomorph*, **116**, 135-144.
- Hall, K. (2003). Recommended native plant species for stream restoration in North Carolina, North Carolina Stream Restoration Institute, North Carolina State University, Raleigh, NC.
- Hancock, G. S., J. W. Holley, and R. M. Chambers (2010). A field-based evaluation of wet retention ponds: how effective are ponds at water quantity control? *J. Am. Water Resour. As.*, **46**(6), 1145-1158.
- Hassan, M., R. Egozi, and G. Parker (2006). Experiments on the effect of hydrograph characteristics on vertical grain sorting in gravel bed rivers, *Water Resour. Res.*, **42**, W09408.

- Hearn, C. J. (2008). *The Dynamics of Coastal Models*, Cambridge University Press, New York.
- Hey, R. D. (1979). Flow resistance in gravel-bed rivers, *J. Hydraul. Div. Am. Soc. Civ. Eng.*, **105**(HY4).
- Hosseini, S. A., Shamsai, A. and B. Ataie-Ashtiani (2006). Synchronous measurements of the velocity and concentration in low density turbidity currents using an Acoustic Doppler Velocimeter, *Flow Meas. Instrum.*, **17**, 59-68.
- HR Wallingford (1990). Sediment transport, the Ackers and White theory revised, Report SR237, England.
- Humphries, R., J. G. Venditti, L. S. Sklar, and J. K. Wooster (2012). Experimental evidence for the effect of hydrographs on sediment pulse dynamics in gravel-bedded rivers, *Water Resour. Res.*, **48**, W01533.
- Hung, N. T., T. Asaeda, and J. Manatunge (2007). Modeling interactions of submersed plant biomass and environmental factors in a stream using structural equation modeling, *Hydrobiologia*, **583**(1), 183-193.
- Jadhav, R. S., and S. G. Buchberger (1995). Effects of vegetation on flow through free surface wetlands, *Ecol. Eng.*, **5**, 481-496.
- James, C. S., A. A. Jordanova, and C. R. Nicolson (2002). Flume experiments and modeling of flow-sediment-vegetation interactions, in *The Structure, Function and Management Implications of Fluvial Sedimentary Systems*, IAHS Publ. 276, edited by J. Dyer Fiona et al., pp. 3-9, Alice Springs, Australia.
- Jeng, R. I. 2006). NRCS (SCS) Synthetic curvilinear dimensionless unit hydrograph, *J. Irrig. Drain. E-ASCE*, **132**(6), 627-631.

- Jones, J. I., A. L. Collins, P. S. Naden, and D. A. Sear (2011). The relationship between fine sediment and macrophytes in rivers, *River Res. Applic.*, doi: 10.1002/rra.1486.
- Jordanova, A. A. and C. S. James (2003). Experimental study of bed load transport through emergent vegetation, *J. Hydr. Eng.*, **129**(6), 474-478.
- Julien, P. Y., and G. J. Klaassen (1995). Sand-dune geometry of large rivers during floods, *J. Hydraul. Eng.*, **121**(9), 657-663.
- Kamphuis, J. W. (1974). Determination of sand roughness for fixed beds, *J. Hydraul. Res.*, **12**(2).
- Karim, F. (1999). Bed form geometry in sand-bed flows, *J. Hydraul. Eng.*, 125(12), 1253-1261.
- Kemp, J. L., D. M. Harper, and G. A. Crosa (1999). Use of 'functional habitats' to link ecology with morphology and hydrology in river rehabilitation, *Aquatic Conserv: Mar. Freshw. Ecosyst.*, **9**, 159-178.
- Kemp, J. L., D. M. Harper, and G. A. Crosa (2000). The habitat-scale ecohydraulics of rivers, *Ecol. Eng.*, **16**, 17-29.
- Khorsandi, B., L. Mydlarski, and S. Gaskin (2012). Noise in turbulence measurements using acoustic Doppler velocimetry, *J. Hydraul. Eng.*, **138**(10), 829-838.
- Klein, M. (1984). Anti-clockwise hysteresis in suspended sediment concentration during individual storms: Holbeck catchment, Yorkshire, England, *Catena*, **11**(2-3), 251-257.
- Kleinhans, M. G., and L. C. Van Rijn (2001). Stochastic prediction of sediment transport in sand-gravel bed rivers, *J. Hydraul. Eng.*, **128**(4), 412-425.

- Kleinhans, M. G., A. W. E. Wilbers, A. Swaaf, and J. H. Van den Berg (2002). Sediment supply limited bedforms in sand-gravel bed rivers, *J. Sed. Res.*, **72**, 629-640.
- Kouwen, N. and T. Unny (1973). Flexible Roughness in Open Channels, *J. Hydraul. Div.* **99**(HY5), 713-727.
- Kuhnle, R. A. (1992). Bed load transport during rising and falling states on two small streams. *Earth. Surf. Processes Landforms*, **17**(2), 191-197.
- Kuhnle, R. A., J. K. Horton, S. J. Bennett, and J. L. Best (2006). Bed forms in bimodal sand-gravel sediments: laboratory and field analysis, *Sedimentology*, **53**, 631-654.
- Kundu, P. K. and I. M. Cohen (2008). *Fluid Mechanics, 4<sup>th</sup> Edition*, Academic Press.
- Lacey, R. W. J., and A. G. Roy (2007). A comparative study of the turbulent flow field with and without a pebble cluster in a gravel bed river, *Water Resour. Res.*, **43**, W05502.
- Laursen, E. (1958). The total sediment load of streams, *J. Hydr. Div.*, **84**(HY1), 1530-1 – 1530-36
- Lee, T. L., Y.- L. Liu, and K.- H. Cheng (2004). Experimental investigation of bedload transport processes under unsteady flow conditions, *Hydrol. Process.*, **18**(13), 2439-2454.
- Lenzi, M. A., and L. Marchi (2000). Suspended sediment load during floods in a small stream of the Dolomites (northeastern Italy), *Catena*, **39**, 267-282.
- Li, S. and R. Millar (2011). A two-dimensional morphodynamic model of gravel-bed river with floodplain vegetation. *Earth Surf. Processes Landforms*, **36**, 190-202.
- Liffen, T., A. M. Gurnell, M. T. O'Hare, N. Pollen-Bankhead, and A. Simon (2011). Biomechanical properties of the emergent aquatic macrophyte *Sparganium erectum*:

- implications for fine sediment retention in low energy rivers, *Ecol. Eng.*, **37**, 1925-1931.
- Lightbody, A. and H. M. Nepf (2006). Prediction of velocity profiles and longitudinal dispersion in emergent salt marsh vegetation. *Limnol. Ocean.*, **51**(1), 218-228.
- Lisle, T. E., and M. A. Madej (1992). Spatial variation in armoring in a channel with high sediment supply, in *Dynamics of Gravel-Bed Rivers*, edited by R. D. H. P. Billi, C. R. Thorne, and P. Tacconi, pp. 277-291, John Wiley, Chichester, U.K.
- Lopez, F. and M. Garcia (1998). Open-channel flow through simulated vegetation: suspended sediment transport modeling, *Water Resour. Res.*, **34**(9), 2341-2352.
- Madden, E. B. (1993). Modified Laursen method for estimating bed-material sediment load, *Contract Report HL-93-3*, U.S. Army Corps of Engineers, Waterways Experiment Station, Vicksburg, MS.
- Mao, L. (2012). The effect of hydrographs on bed load transport and bed sediment spatial arrangement, *J. Geophys. Res.*, **117**, F03024.
- Mars, M., M. Kuruvilla, and H. Goen (1999). The role of submergent macrophyte *Triglochin huegelii* in domestic greywater treatment, *Ecol. Eng.*, **12**, 57-66.
- Martin, R. L., and D. J. Jerolmack (2013). Origin of hysteresis in bed form response to unsteady flows, *Water Resour. Res.*, **49**, 1314-1333.
- Mays, L. W. (2011). *Water Resources Engineering*, 2nd Ed., John Wiley & Sons, Inc., USA.
- Meyer-Peter, E. and R. Muller (1948). Formula for bed-load transport, *Proceedings of the 2<sup>nd</sup> Meeting of the IAHR*, Stockholm, Sweden, 39-64.
- Micro-Epsilon (2008). *Instruction Manual: scanCONTROL 2800/2810*.

- Moog, D. B., and P. J. Whiting (1998). Annual hysteresis in bed load rating curves, *Water Resour. Res.*, **34**(9), 2393-2399.
- Mori, N. (2007). *Despiking*, MATLAB Central File Exchange. Retrieved July 6, 2012.
- Mudd, S. M., A. D'Alpaos, and J. T. Morris (2010). How does vegetation affect sedimentation on tidal marshes? Investigating particle capture and hydrodynamic controls on biologically mediated sedimentation, *J. Geophys. Res.*, **115**, F03029.
- Murray, A. B. and C. Paola (2004). Modeling the effect of vegetation on channel pattern in bedload rivers, *Earth Surf. Processes Landforms*, **28**, 131-143.
- Naden, P., P. Rameshwaran, O. Mountford, and C. Robertson (2006). The influence of macrophyte growth, typical of eutrophic conditions, on river flow velocities and turbulence production, *Hydrol. Proc.*, **20**, 3915-38.
- National Research Council (NRC) (2002). Riparian areas: functions and strategies for management, National Academy Press, Washington, D.C.
- National Resource Conservation Service (NRCS) (2007). National engineering handbook, Part 630: Hydrology, 210-VI-NEH, U.S. Department of Agriculture, Washington, D.C.
- Nelson, J. M., B. L. Logan, P. J. Kinzel, Y. Shimizu, S. Giri, R. L. Shreve, and S. R. McLean (2011). Bed form response to flow variability, *Earth Surf. Processes Landforms*, **26**(14), 1938-1947.
- Nepf, H. M. and E. R. Vivoni (2000). Flow structure in depth-limited, vegetated flow, *J. Geophys. Res.*, **105**(C12), 28547-28557.
- Nepf, H. M., J. A. Sullivan, and R. A. Zavistoski (1997). A model for diffusion within an emergent plant canopy, *Limnol. Oceanogr.*, **42**(8), 85-98.

- Nepf, H. M. (1999). Drag, turbulence, and diffusion in flow through emergent vegetation, *Water Resour. Res.*, **35**(2), 479-489.
- Ng, T. L., and J. W. Eheart (2008). A multiple-realizations chance-constrained model for optimizing nutrient removal in constructed wetlands, *Water Resour. Res.*, **44**, W04405.
- Nicolle, A., and I. Eames (2011). Numerical study of flow through and around a circular array of cylinders, *J. Fluid Mech.*, **679**, 1-31.
- Nikora, V. I., and D. G. Goring (1998). ADV measurements of turbulence: can we improve their interpretation? *J. Hydraul. Eng.*, **124**(6), 630-634.
- Nikora, V. I., D. G. Goring, and B. Biggs (1998). On gravel-bed roughness characterization, *Water Resour. Res.*, **34**(3), 517-527.
- Nikora, V. I., S. Larned, N. Nikora, K. Debnath, G. Cooper, and M. Reid (2008). Hydraulic resistance due to aquatic vegetation in small streams: field study, *J. Hydraul. Eng.*, **134**(9), 1326-1332.
- Noe, G., and C. Hupp (2009). Retention of riverine sediment and nutrient loads by coastal plain floodplains, *Ecosystems*, **12**, 728-746.
- Nortek (2009). *Vectrino Velocimeter User Guide*. Norway.
- Palmer, M. A., Bernhardt, E. S., Allan, J. D., Lake, P. S., Alexander, G., Brooks, S., Carr, J., Clayton, S, Dahm, C. N., Follstad-Shah, J., Galat, D. L., Loss, S. G., Goodwin, P., Hart, D. D., Hassett, B., Jenkinson, R., Kondolf, G. M., Lave, R., Meyer, J. L., O'Donnell, T. K., Pagano, L., Sudduth, E. (2005). Standards for ecologically successful river restoration. *Journal of Applied Ecology*, **42**, 208-217.

- Parker, G., M. Hassan, and P. R. Wilcock (2008). Adjustment of the bed surface size distribution of gravel-bed rivers in response to cycled hydrographs, in *Gravel Bed Rivers VI: From Process Understanding to River Restoration*, edited by H. Habersack, H. Piegay, and M. Rinaldi, pp. 241-285, Elsevier: New York.
- Parker, G. (1979). Hydraulic geometry of active gravel rivers, *J. Hydraul. Eng.*, **105**(9), 1185-1201.
- Persson, P. and G. Strang (2004). A simple mesh generator in MATLAB, *SIAM Review*, **46**(2), 329-345.
- Phillips, B. C., and A. J. Sutherland (1990). Temporal lag effect in bed load sediment transport, *J. Hydraul. Res.*, **28**(1), 5-23.
- Pollen, N. (2007). Temporal and spatial variability in root reinforcement of streambanks: Accounting for soil shear strength and moisture, *Catena*, **69**, 197-205.
- Pollen, N. and A. Simon (2005). Estimating the mechanical effects of riparian vegetation on stream bank stability using a fiber bundle model, *Water Res. Res.*, **41**, W07025.
- Pollen-Bankhead, N., and A. Simon (2010). Hydrologic and hydraulic effects of riparian root networks on streambank stability: Is mechanical root-reinforcement the whole story? *Geomorph.*, **116**(3-4), 353-362.
- Power, P. (1996). Effects of current velocity and substrate composition on growth of Texas wildrice (*Zizania texana*), *Aquat. Bot.*, **55**(3), 199-204.
- Proffitt, G. T. and A. J. Sutherland (1983). Transport of nonuniform sediments, *J. Hydraul. Res.*, **21**, 33-43.
- Qu, Z. (2002). Unsteady open-channel flow over a mobile bed, Ph.D. thesis, No. 2688, Ecole Polytechnique Federale de Lausanne, Lausanne, Switzerland.

- Recking, A., F. Liebault, C. Peteuil, and T. Jolimet (2012). Testing bedload transport equations with consideration of time scales, *Earth Surf. Processes Landforms*, **37**(7), 775-789.
- Reid, I., L. E. Frostick, and J. T. Layman (1985). The incidence and nature of bedload transport during flood flows in coarse-grained alluvial channels, *Earth Surf. Proc. Landforms*, **10**(1), 33-44.
- Richardson, E. V., and S. R. Davis (2001). Evaluating scour at bridges (4<sup>th</sup> ed.): Federal Highway Administration Hydraulic Engineering Circular (HEC) 18, Publication no. FHWA-NHI 01-001, 378 p.
- Robert, A. (1988). Statistical properties of sediment bed profiles in alluvial channels, *Math. Geol.*, **20**(3), 205-225.
- Robert, A. and K. S. Richards (1988). On the modeling of sand bedforms using the semivariogram, *Earth Surf. Processes Landforms*, **13**, 459-473.
- Rominger, J. T. and H. M. Nepf (2011). Flow adjustment and interior flow associated with a rectangular porous obstruction, *J. Fluid Mech.*, **680**, 636-659.
- Rominger, J. T., A. Lightbody, and H. M. Nepf (2010). The effects of vegetation on sand bar stability and stream hydrodynamics. *J. Hydraul. Eng.*, **136**(12), 994-1002.
- Roy, A. G., P. M. Biron, and M. F. Lapointe (1997). Implications of low-pass filtering on power spectra and autocorrelation functions of turbulent velocity signals, *Math. Geol.*, **29**(5), 653-668.
- Sand-Jensen, K. (1998). Influence of submerged macrophytes on sediment composition and near-bed flow in lowlands streams, *Freshwat. Biol.*, **39**, 663-679.

- Sand-Jensen, K. and T. V. Madsen (1992). Patch dynamics of the stream macrophyte, *Callitriche cophocarpa*, *Freshwat. Biol.*, **27**, 277-282.
- Sand-Jensen, K. and J. R. Mebus (1996). Fine-scale patterns of water velocity within macrophyte patches in streams. *Oikos*, **76**, 169-180.
- Sand-Jensen, K. and M. L. Pedersen (2008). Streamlining of plant patches in streams, *Freshwat. Biol.*, **53**, 714-726
- Schulz, M., H.-P. Kozerski, T. Pluntke, and K. Rinke (2003). The influence of macrophytes on sedimentation and nutrient retention in the lower River Spree (Germany), *Water Res.*, **37**, 569-578.
- Sharpe, R. G. and C. S. James (2006). Deposition of sediment from suspension in emergent vegetation, *Water S.A.*, **32**(2), 211-218.
- Shi, Z., J. S. Pethick, and K. Pye (1995). Flow structure in and above the various heights of a saltmarsh canopy: a laboratory flume study. *J. Coast. Res.*, **11**(4), 1204-1209.
- Shucksmith, J. D., J. B. Boxall, and I. Guymer (2010). Effects of emergent and submerged natural vegetation on longitudinal mixing in open channel flow, *Water Resour. Res.*, **46**, W04504.
- Smith, J. D., and S. R. McLean (1977). Spatially averaged flow over a wavy surface, *J. Geophys. Res.*, **82**, 1735-1746.
- Song, T. and W. H. Graf (1997). Experimental study of bed load transport in unsteady open-channel flow, *Int. J. Sediment Res.*, **12**(3), 63-71.
- Stern, D. A., R. Khanbilvardi, J. C. Alair, and W. Richardson (2001). Description of flow through a natural wetland using dye tracer tests, *Ecol. Eng.*, **18**(2), 173-184.

- Syvitski, J. P. M., M. D. Morehead, D. B. Bahr, and T. Mulder (2000). Estimating fluvial sediment transport: the rating parameters, *Water Resour. Res.*, **36**(9), 2747-2760.
- Takemura, T., and N. Tanaka (2007). Flow structures and drag characteristics of a colony-type emergent roughness model mounted on a flat plate in uniform flow, *Fluid Dyn. Res.*, **39**, 694-710.
- Tal, M. and C. Paola (2007). Dynamic single-thread channels maintained by the interaction of flow and vegetation, *Geological Soc. of America*, **35**:347-350.
- Tanaka, N., and J. Yagisawa (2010). Flow structures and sedimentation characteristics around clump-type vegetation, *J. Hydro-environ. Res.*, **4**(1), 15-25.
- Temmerman, S., T. J. Bouma, J. Van de Koppel, D. Van der Wal, M. B. De Vries, and P. M. J. Herman (2007). Vegetation causes channel erosion in a tidal landscape, *Geology*, **35**(4), 631-634.
- Tuijnder, A. P., J. S. Ribberink, and S. J. M. H. Hulscher (2009). An experimental study into the geometry of supply-limited dunes, *Sedimentology*, **56**, 1713-1727.
- van Katwijk, M., A. Bos, D. Hermus, and W. Suykerbuyk (2010). Sediment modification by seagrass beds: muddification and sandification induced by plant cover and environmental conditions. *Estuar. Coast. Shelf Sci.*, **89**(2), 175-181.
- Van Rijn, L. C. (1984a). Sediment transport, part I: bedload transport. *J. Hydraul. Eng.*, **110**(10), 1431-1457.
- Van Rijn, L. C. (1984b). Sediment transport, part III: bed forms and alluvial roughness, *J. Hydraul. Eng.*, **110**(12), 1733-1754.
- Vandenbruwaene, W., S. Temmerman, T. J. Bouma, P. C. Klaasen, M. B. de Vries, D. P. Callaghan, P. van Steeg, F. Dekker, L. A. van Duren, E. Martini, T. Balke, G.

- Biermans, J. Schoelynck, and P. Meire (2011). Flow interaction with dynamic vegetation patches: implications for biogeomorphic evolution of a tidal landscape, *J. Geophys. Res.*, **116**, F01008.
- Vanoni, V. A., and N. H. Brooks (1957). Laboratory studies of the roughness and suspended load of alluvial streams, Report E-68, Sedimentation Laboratory, California Institute of Technology, Pasadena, CA, 120.
- VanSickle, J., and R. L. Beschta (1983). Supply-based models of suspended sediment transport in streams, *Water Resour. Res.*, **19**, 768-778.
- Vereecken, H., J. Baetens, P. Viaene, F. Mostaert, and P. Meire (2006). Ecological management of aquatic plants: effects in lowland streams, *Hydrobiologia*, **570**, 205-210.
- Walling, D. E. (1974). Suspended sediment and solute yields from a small catchment prior to urbanization, in Gregory, K. J. and Walling, D. E. (Eds.), *Fluvial process in instrumented watersheds, Inst. Br. Geog. (Spec. Publ.)*, **6**, 169-192.
- Wharton, G., J. A. Cotton, R. S. Wotton, J. Bass, C. M. Heppell, M. Trimmer, I. A. Sanders, and L. L. Warren (2006). Macrophytes and suspension-feeding invertebrates modify flows and fine sediments in the Frome and Piddle catchments, Dorset (UK). *J. Hydrol.*, **330**, 171-184.
- Widdows, J., N. D. Pope, and M. D. Brinsley (2008). Effect of *Spartina anglica* stems on near-bed hydrodynamics, sediment erodability and morphological changes on an intertidal mudflat, *Mar. Ecol. Prog. Ser.*, **362**, 45-57.

- Wijbenga, J. H. A., and A. R. Van Nes (1986). Flow resistance and bed form dimensions for varying flow conditions; results of flume experiments with flood waves, *TOW Rivers Rep. R 567-XXV/M 1315 part XIII, WL/Delft Hydraulics*, Delft, Netherlands.
- Wilbers, A., and W. Ten Brinke (2003). The response of subaqueous dunes to floods in sand and gravel bed reaches of the Dutch Rhine, *Sedimentology*, **50**(6), 1013-1034.
- Wilcock, P. R., and S. T. Kenworthy (2002). A two-fraction model for the transport of sand/gravel mixtures, *Water Resour. Res.*, **38**(10), 1194.
- Wilcock, R., P. Champion, J. Nagels, G. Crocker (1999). The influence of aquatic macrophytes on the hydraulic and physicochemical properties of a New Zealand lowland stream, *Hydrobiologia*, **416**(1), 203-214.
- Williams, G. P. (1989). Sediment concentration versus water discharge during single hydrologic events in rivers, *J. Hydrol.*, **111**(1-4), 89-106.
- Wohl, E., P. L. Angermeier, B. Bledsoe, G. M. Kondolf, L. MacDonnell, D. M. Merritt, M. A. Palmer, N. L. Poff, and D. Tarboton (2005). River restoration, *Water Resour. Res.*, **41**, W10301.
- Wolman, M. G. (1954). A method of sampling coarse river-bed material, *Trans. Am. Geophys. Union*, **35**, 951-956.
- Wu, W., and Z. He (2009). Effects of vegetation on flow conveyance and sediment transport capacity, *Int. J. Sediment Res.*, **24**(3), 247-259.
- Wynn, T. and S. Mostaghimi (2006). Effects of riparian vegetation on stream bank subaerial processes in southwestern Virginia, USA. *Earth Surf. Processes Landforms*, **31**, 399-413.

- Yager, E. M., and M. W. Schmeeckle (2013). The influence of vegetation on turbulence and bed load transport, *J. Geophys. Res. Earth Surf.*, **118**, 1585-1601.
- Yalin, M. S. (1964). Geometrical properties of sand waves, *J. Hydraul. Div. Am. Soc. Civ. Eng.*, **90**(5).
- Yang, C. T. (1973). Incipient motion and sediment transport, *J. Hydr. Div.*, **99**(HY10), 1679-1704.
- Yang, C. T. (1984). Unit stream power equation for gravel, *J. Hydraul. Eng.*, **110**(12), 1783-1797.
- Yang, C. T. (1996). *Sediment Transport: Theory and Practice*, McGraw-Hill, Singapore.
- Yang, C. T. (2006). *Erosion and Sedimentation Manual*, U.S. Dep. of the Interior, Bureau of Reclamation, Denver, CO.
- Yen, C. L. and K. T. Lee (1995). Bed topography and sediment sorting in channel bend with unsteady flow, *J. Hydraul. Eng.*, **121**(8), 591-599.
- Yuill, B. T., and M. H. Nichols (2011). Patterns of grain-size dependent sediment transport in low-ordered ephemeral channels, *Earth Surf. Processes Landforms*, **36**, 334-346.
- Zierholz, C., I. P. Prosser, P. J. Fogarty, and P. Rustomji (2001). In-stream wetlands and their significance for channel infilling and the catchment sediment budget, Jugiong Creek, New South Wales, *Geomorph.*, **38**, 221-235.
- Zong, L. and H. M. Nepf (2010). Flow and deposition in and around a finite patch of vegetation, *Geomorph.*, **116**, 363-372.
- Zong, L. and H. M. Nepf (2011). Spatial distribution of deposition within a patch of vegetation, *Water Resour. Res.*, **47**(3), W03516.

Zong, L. and H. M. Nepf (2012). Vortex development behind a finite porous obstruction in a channel. *J. Fluid Mech.*, **691**, 368-391.

# APPENDIX A

## *Equipment Calibration*

---

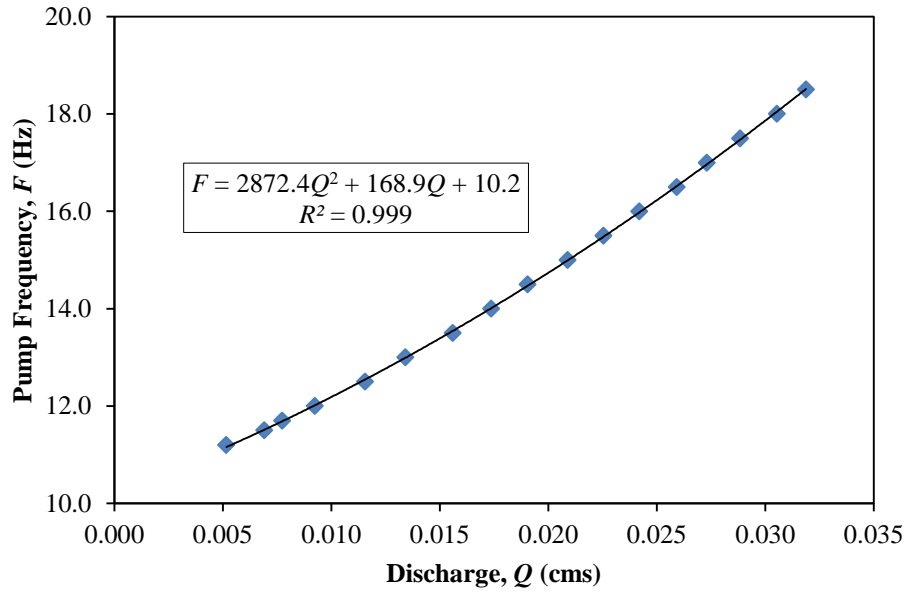
---

*A.1 Pump Calibration Curves*

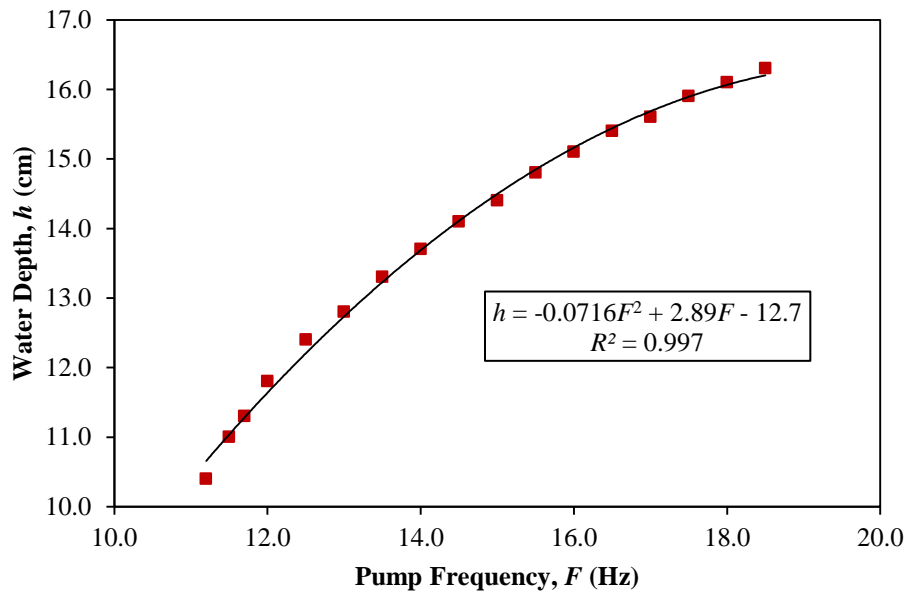
*A.2 Bed Monitoring System Calibration Curves*

## Appendix A.1 – Pump Calibration Curves

No Sediment Experiments, smooth flume bottom: baseflow  $Fr = 0.10$ ,  $h = 0.11$  m



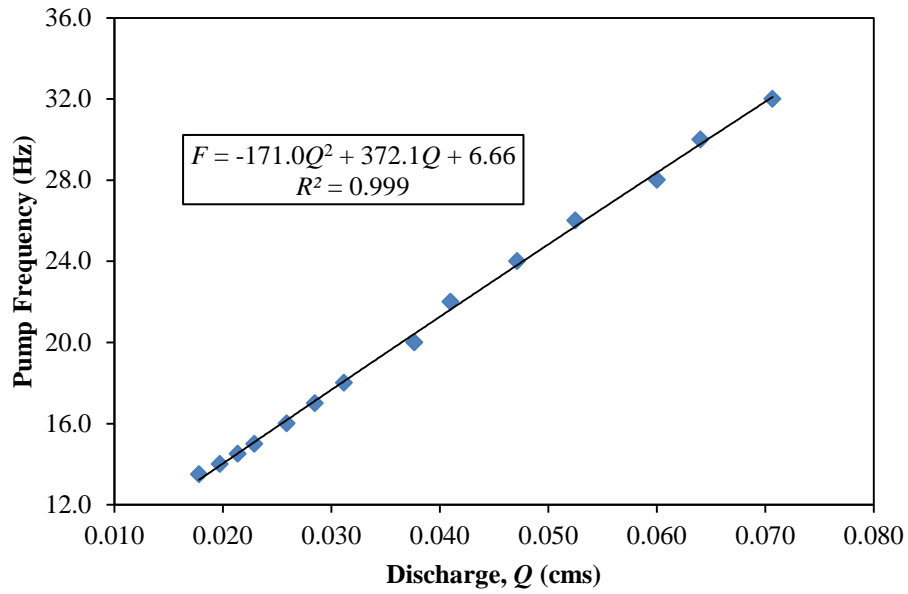
(a) Discharge-Pump Frequency\*



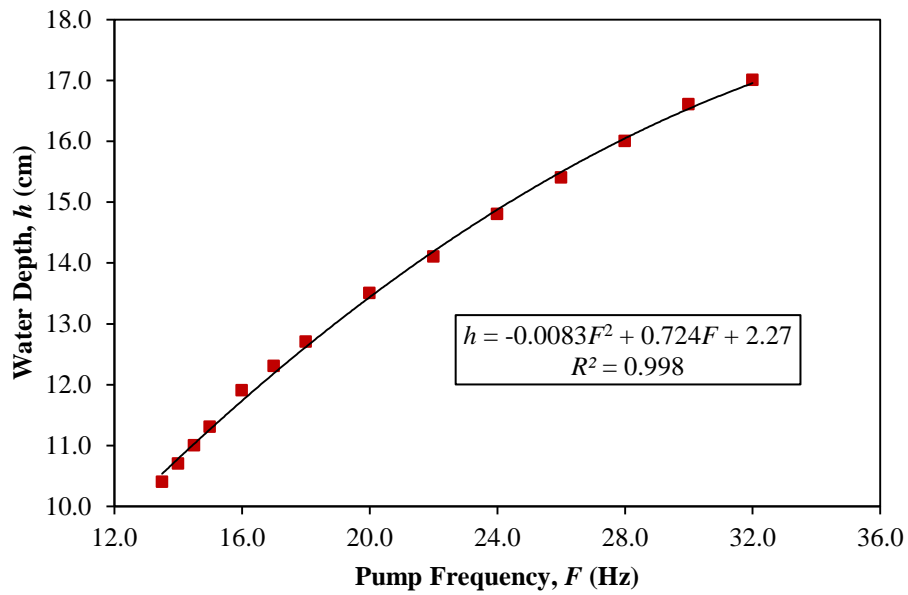
(b) Pump Frequency-Water Depth

\* Note: Discharge-pump calibration curves solved for pump frequency with known discharge because flows were specified through experimental design, and therefore, were independent variables.

No Sediment Experiments, smooth flume bottom: baseflow  $Fr = 0.31$ ,  $h = 0.11$  m

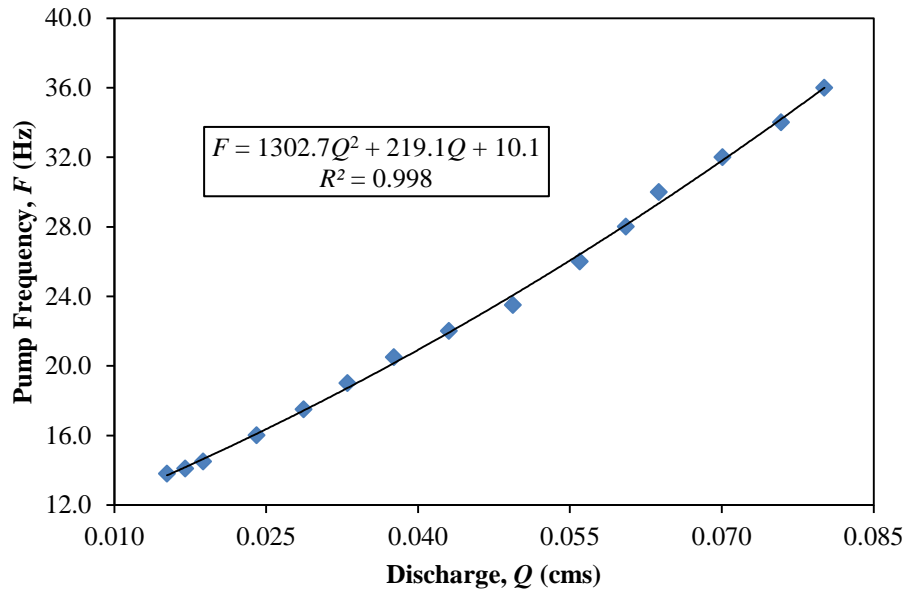


(c) Discharge-Pump Frequency

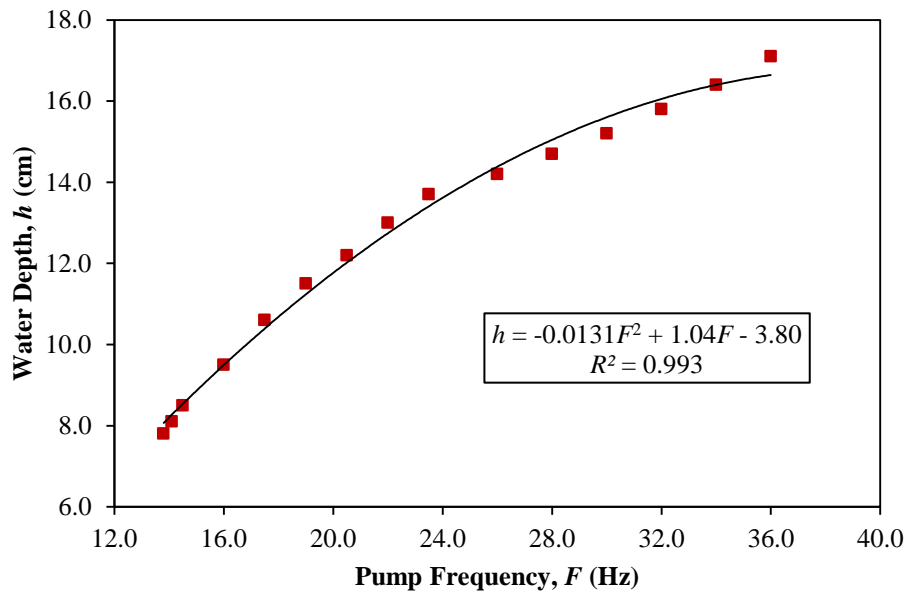


(d) Pump Frequency-Water Depth

*Sediment Experiments, rough/mobile flume bottom: baseflow  $Fr \sim 0.40$ ,  $h = 0.080$  m.*



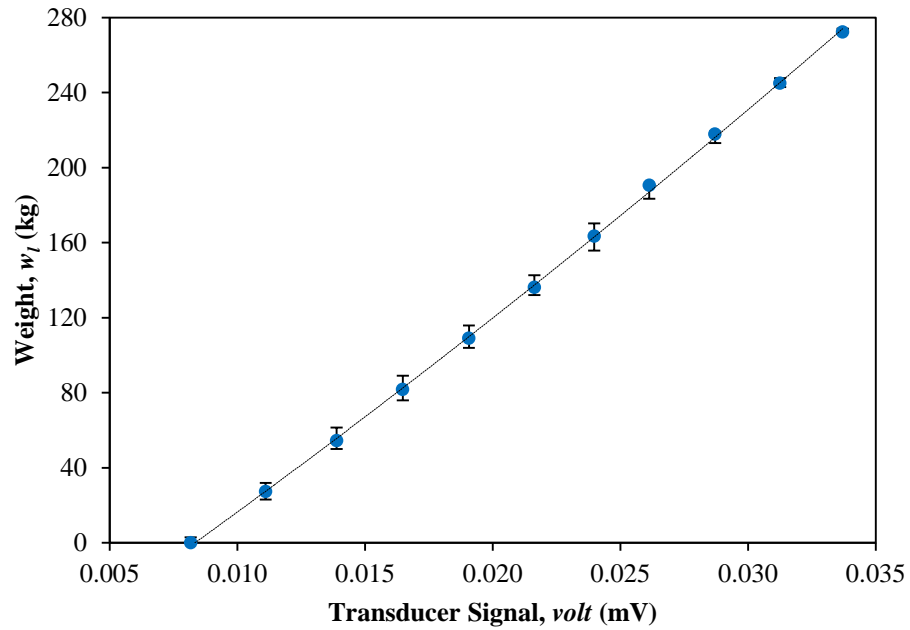
(e) Discharge-Pump Frequency



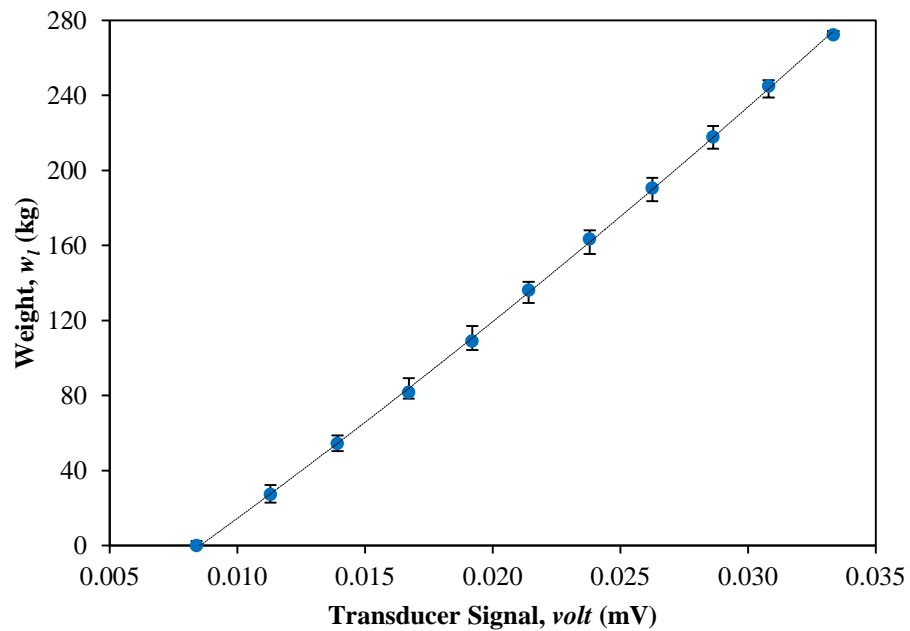
(f) Pump Frequency-Water Depth

### Appendix A.2 – Bed Monitoring System Calibration Curves

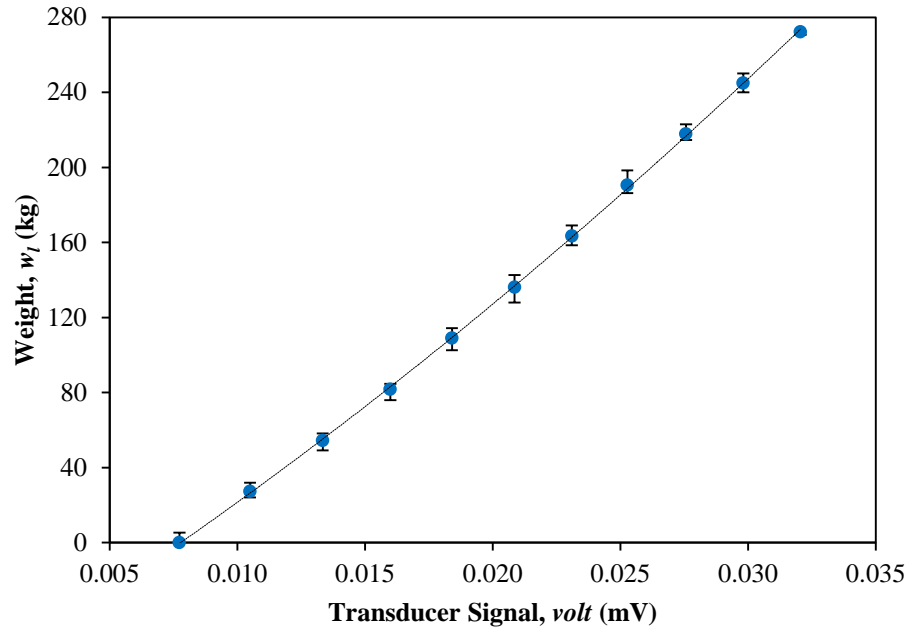
*First calibration only (prior to Patch-Sediment, Mix 1 experiments):* Blue points represent calibration data points; dashed black line is derived calibration curve; error bars denote values calculated with calibration relationship for upper and lower bound estimates



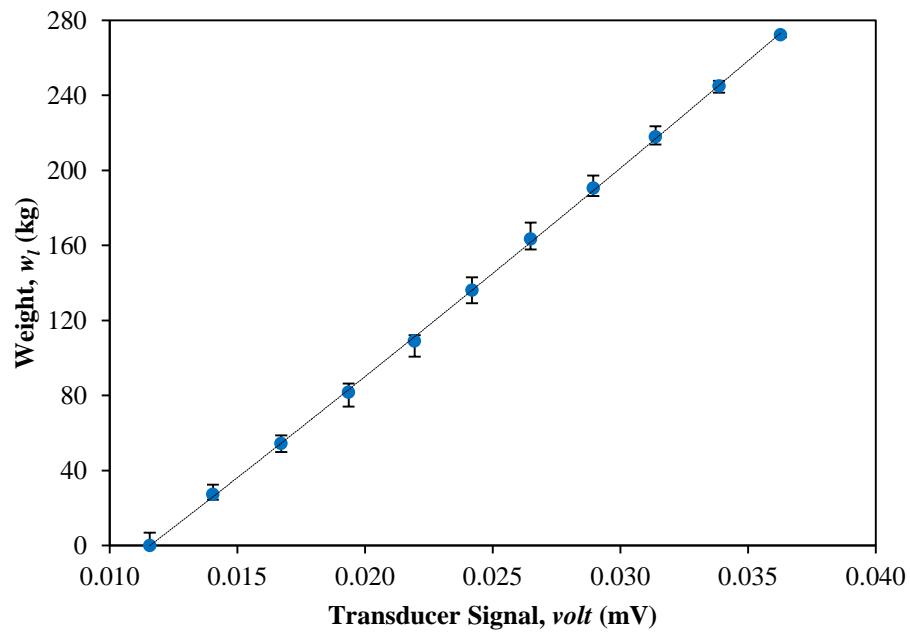
(a). Flume Segment 3m:  $w_l = 38,674(\text{volt})^2 + 9,175.2(\text{volt}) - 79.2$ ;  $R^2 = 0.9997$



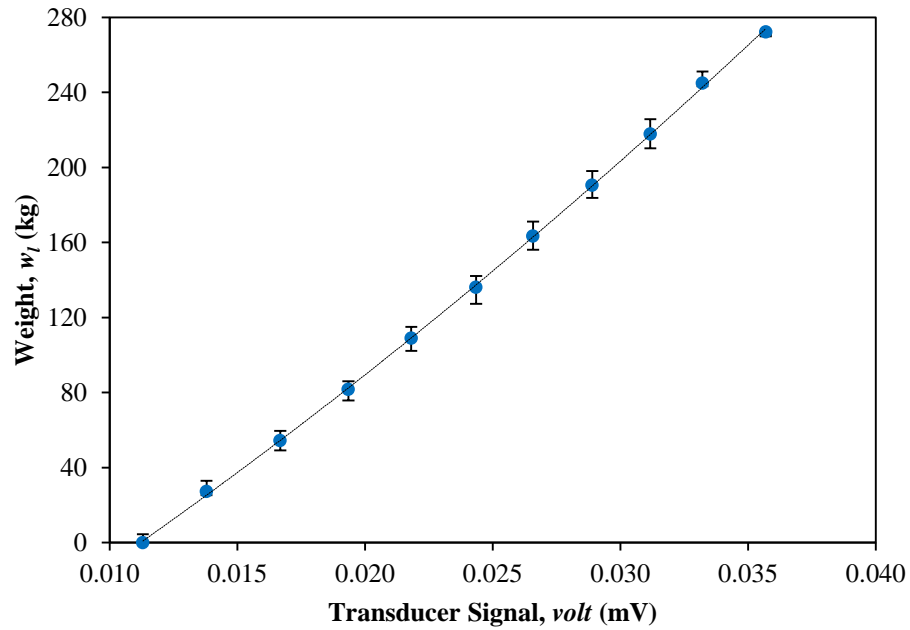
(b). Flume Segment 4m:  $w_l = 48,093(\text{volt})^2 + 9,039.9(\text{volt}) - 80.7$ ;  $R^2 = 0.9998$



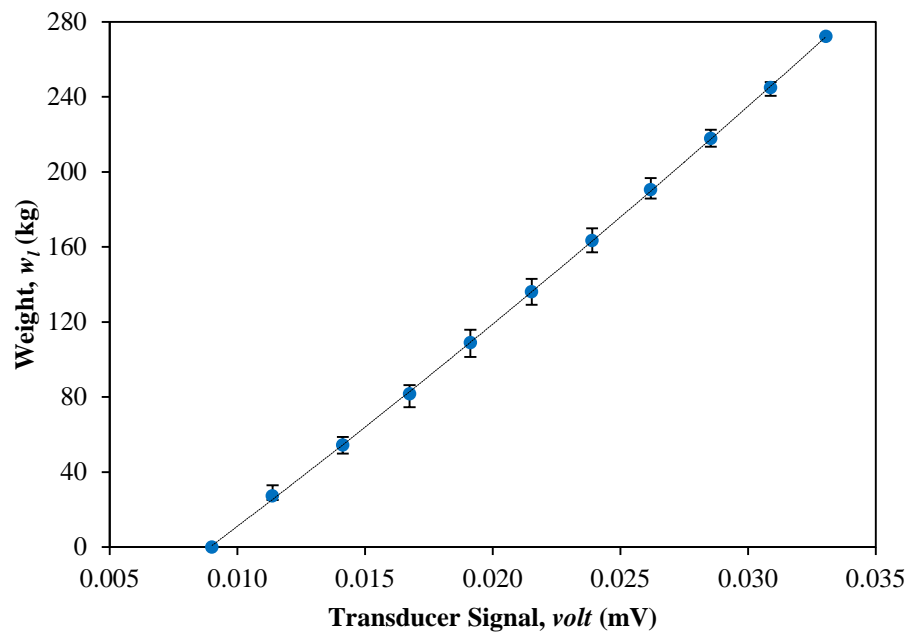
(c). Flume Segment 5m:  $w_l = 72,319(\text{volt})^2 + 8,392.8(\text{volt}) - 69.7$ ;  $R^2 = 0.9999$



(d). Flume Segment 6m:  $w_l = 22,328(\text{volt})^2 + 9,994.2(\text{volt}) - 118.8$ ;  $R^2 = 0.9998$



(e). Flume Segment 7m:  $w_l = 64,866(\text{volt})^2 + 8,144.5(\text{volt}) - 99.4$ ;  $R^2 = 0.9998$



(f). Flume Segment 8m:  $w_l = 41,550(\text{volt})^2 + 9,533(\text{volt}) - 88.4$ ;  $R^2 = 0.9999$

## **APPENDIX B**

### *Data Processing*

---

---

*B.1 ADV Processing MATLAB Code*

*B.2 Bed Scan Processing MATLAB Code*

*B.3 GIS Processing Flowcharts*

*B.4 Bed Monitoring System Converison MATLAB Code*

---

Appendix B.1 -- ADV Processing MATLAB Code

```

% ADV DATA PROCESSING: ADVprocess.m
%   Written by Kevin Waters (January 2013)
%   Revised by Kevin Waters (February 2013)

% Description:
% This script processes raw ADV data with the following tasks:
% (1) Import ADV data from text files
% (2) Despiked raw data with Goring and Nikora (2002) Method
% (3) Filter despiked data using specified correlation threshold
% (4) Apply 3rd order, low pass Butterworth filter
% (5) Calculate mean velocity from despiked, filtered data
% (6) Calculate turbulence intensities of despiked, filtered data
% (7) Combine velocity results into matrix form

%-----%
%%--- Define function and variables ---%%

function [velocity_results] = ADVprocess(~)

% Output parameters:
% velocity_results = full matrix of velocity results including:
%   umean      = mean streamwise velocity (m/s)
%   vmean      = mean lateral velocity (m/s)
%   wmean      = mean vertical velocity (m/s)
%   urms       = streamwise turbulence intensity (m/s)
%   vrms       = lateral turbulence intensity (m/s)
%   wrms       = vertical turbulence intensity (m/s)
%   ipd        = percentage of data points despiked (i.e.
%               number of spikes detected and interpolated)
%   ipc        = percentage of low correlation data points
%               removed

% Variable list:
% datlen      = number of data/measurement locations
% filename{k} = cell array of text file names
% ADVdata     = full raw data matrix from ADV (20 columns)
% u{k}        = streamwise velocity cell array (m/s)
% v{k}        = lateral velocity cell array (m/s)
% w{k}        = vertical velocity cell array (m/s)
% gx{k}       = signal correlation in x direction (%)
% gy{k}       = signal correlation in y direction (%)
% gz1{k},gz2{k} = signal correlations in z direction (%)
% gz{k}       = avg. signal correlation in z direction (%)
% ucorrfilter{k} = correlation threshold filtered u-vel (m/s)
% ipuc{k}     = number of filtered points from u-velocity
% vcorrfilter{k} = correlation threshold filtered v-vel (m/s)
% ipvc{k}     = number of filtered points from v-velocity
% wcorrfilter{k} = correlation threshold filtered w-vel (m/s)
% ipwc{k}     = number of filtered points from w-velocity
% udespike{k} = cell arrays of despiked u-velocity (m/s)
% vdespike{k} = cell arrays of despiked v-velocity (m/s)
% wdespike{k} = cell arrays of despiked w-velocity (m/s)

```

---

```

%   ufiltered{k}      = correlation filtered, despiked, low pass 3rd
%                       order Butterworth filtered u-vel (m/s)
%   vfiltered{k}      = correlation filtered, despiked, low pass 3rd
%                       order Butterworth filtered v-vel (m/s)
%   wfiltered{k}      = correlation filtered, despiked, low pass 3rd
%                       order Butterworth filtered w-vel (m/s)
%-----%
%%!--- Import ADV data ---%%

%Search directory for data files (.vna); count sampling locations
data = dir('*.*vna'); datlen = length(data);

% Preallocate cell arrays:
filename = cell(datlen,1); ADVdata = cell(datlen,1);
u = cell(datlen,1); v = cell(datlen,1);
w1 = cell(datlen,1); w2 = cell(datlen,1); w = cell(datlen,1);
gx = cell(datlen,1); gy = cell(datlen,1); gz = cell(datlen,1);
umean = cell(datlen,1); vmean = cell(datlen,1);
    wmean = cell(datlen,1);
urms = cell(datlen,1); vrms = cell(datlen,1);
    wrms = cell(datlen,1);

% Assign raw data to structures using loop
for k = 1:datlen
    filename{k} = data(k).name;
    ADVdata{k} = importdata(filename{k});
    u{k} = ADVdata{k}(:,5);
    v{k} = ADVdata{k}(:,6);
    w1{k} = ADVdata{k}(:,7);
    w2{k} = ADVdata{k}(:,8);
        % Average vertical velocities
        w{k} = (w1{k} + w2{k})./2;
    gx{k} = ADVdata{k}(:,17);
    gy{k} = ADVdata{k}(:,18);
    gz{k} = ADVdata{k}(:,19);
end

%-----%
%%!--- Despike raw ADV data ---%%

i_opt = 2; % Spike-removal method (interpolate w/cubic polynomial)
udespike = cell(datlen,1); % Preallocate for speed
vdespike = cell(datlen,1);
wdespike = cell(datlen,1);
ipd = cell(datlen,1);

% Loop over all sampling locations using despiking algorithm
for k = 1:datlen
    [udespike{k},vdespike{k},wdespike{k},ipd{k}] = ...
        func_despike_phasespace3d_3var(u{k},v{k},w{k},i_opt);
    ipd{k} = (length(ipd{k})/(3*length(u{k}))) * 100; % % of spikes
end

%-----%

```

---

```

%%--- Filter raw ADV data using correlation threshold ---%%

gs = 70;    % Correlation threshold in % (typically 70%)
ucorrfilter = cell(datlen,1);  % Preallocate for speed
ipuc = cell(datlen,1);
vcorrfilter = cell(datlen,1);
ipvc = cell(datlen,1);
wcorrfilter = cell(datlen,1);
ipwc = cell(datlen,1);

% Loop over all sampling locations using correlation filtering
% algorithm
for k = 1:datlen
    [ucorrfilter{k},ipuc{k}] = ...
        func_excludeoutlier_cor(udespike{k},gx{k},gs);
    % Percent filtered:
    ipuc{k} = (length(ipuc{k})/length(u{k}))*100;

    [vcorrfilter{k},ipvc{k}] = ...
        func_excludeoutlier_cor(vdespike{k},gy{k},gs);
    % Percent filtered:
    ipvc{k} = (length(ipvc{k})/length(v{k}))*100;

    [wcorrfilter{k},ipwc{k}] = ...
        func_excludeoutlier_cor(wdespike{k},gz{k},gs);
    % Percent filtered:
    ipwc{k} = (length(ipwc{k})/length(w{k}))*100;
end

% Combine correlation filter percentage results in one matrix:
ipc = [ipuc ipvc ipwc];

%-----%
%%--- Filter despiked data with low pass Butterworth filter ---%%

Fs = 25;    % Sampling frequency (Hz)
cutoff = Fs / 2.93;    % Cutoff frequency (Hz)
ord = 3;    % Third order Butterworth filter
unfiltered{k} = cell(datlen,1);    % Preallocate for speed
vfiltered{k} = cell(datlen,1);    % Preallocate for speed
wfiltered{k} = cell(datlen,1);    % Preallocate for speed

% Loop over all sampling locations using despiking algorithm
for k = 1:datlen
    unfiltered{k} = lowpass_butterworth(ucorrfilter{k},cutoff,Fs,ord);
    vfiltered{k} = lowpass_butterworth(vcorrfilter{k},cutoff,Fs,ord);
    wfiltered{k} = lowpass_butterworth(wcorrfilter{k},cutoff,Fs,ord);
end

%-----%
%%--- Calculate mean velocities from filtered data ---%%

% Loop over all sampling locations
for k = 1:datlen

```

---

---

```
    umean{k} = mean(ufiltered{k});
    vmean{k} = mean(vfiltered{k});
    wmean{k} = mean(wfiltered{k});
end

%-----%
%%!--- Calculate turbulence intensities from filtered data ---%%

% Loop over all sampling locations
for k = 1:datlen
    urms{k} = std(ufiltered{k});
    vrms{k} = std(vfiltered{k});
    wrms{k} = std(wfiltered{k});
end

%-----%
%%!--- Combine values to form results matrix ---%%

velocity_results = [umean vmean wmean urms vrms wrms ipd ipc];

%-----%
```

*Published with MATLAB® R2013a*

---

---

Appendix B.2 -- Bed Scan Processing MATLAB Code

```

% BED SCAN PROCESSING: scanprocess.m
%   Written by Kristen Cannatelli (2012)
%   Revised by Kevin Waters (April 2013)

% Description:
%   This script processes raw scanner data, combines data from
%   individual scans and writes .csv file for GIS post-processing

%-----%
%%--- Import raw scan data ---%%

% Import y and z data from different text files for each scan using
%   importscan.m function (populates empty cells with NaN)

y1 = importscan('y1-cut.txt'); z1 = importscan('z1-cut.txt');
y2 = importscan('y2-cut.txt'); z2 = importscan('z2-cut.txt');
y3 = importscan('y3-cut.txt'); z3 = importscan('z3-cut.txt');
y4 = importscan('y4-cut.txt'); z4 = importscan('z4-cut.txt');
y5 = importscan('y5-cut.txt'); z5 = importscan('z5-cut.txt');

% Determine # of profiles and # of points per profile
%   A,C,E,G,I = # of profiles in 1st, 2nd, 3rd, 4th, and 5th scans,
%               respectively
%   B,D,F,H,J = # of points per profile in 1st, 2nd, 3rd, 4th, and
%               5th scans, respectively (should match setting
%               specified when running LabVIEW program, i.e. 1024)

[A,B] = size(y1);   [C,D] = size(y2);   [E,F] = size(y3);
[G,H] = size(y4);   [I,J] = size(y5);

%-----%
%%--- Process scans individually ---%%

% Get y and z data into useable form and shift scan locations

% Shifts:
y1shift = 0.0;      y2shift = 0.12;      y3shift = 0.24;
y4shift = 0.36;      y5shift = 0.48;

% First scan:
y1 = y1'; y1 = y1(:); % Transpose, convert into column vectors
z1 = z1'; z1 = z1(:);
y1 = -0.001*y1; % Convert from mm to meters and flip direction
y1 = y1 + y1shift; % Shift scan to proper location

% Second scan:
y2 = y2'; y2 = y2(:); % Transpose, convert into column vectors
z2 = z2'; z2 = z2(:);
y2 = -0.001*y2; % Convert from mm to meters and flip direction
y2 = y2 + y2shift; % Shift scan to proper location

% Third scan

```

---

---

```

y3 = y3'; y3 = y3(:); % Transpose, convert into column vectors
z3 = z3'; z3 = z3(:);
y3 = -0.001*y3; % Convert from mm to meters and flip direction
y3 = y3 + y3shift; % Shift scan to proper location

% Fourth scan:
y4 = y4'; y4 = y4(:); % Transpose, convert into column vectors
z4 = z4'; z4 = z4(:);
y4 = -0.001*y4; % Convert from mm to meters and flip direction
y4 = y4 + y4shift; % Shift scan to proper location

% Fifth scan:
y5 = y5'; y5 = y5(:); % Transpose, convert into column vectors
z5 = z5'; z5 = z5(:);
y5 = -0.001*y5; % Convert from mm to meters and flip direction
y5 = y5 + y5shift; % Shift scan to proper location

%-----%
%%--- Calculate and assign x-coordinates ---%%

% X-coordinates derived from number of profiles recorded by scanner

% Scan length/distance along flume:
scanlen = 6.114; % Scan length (m)

% First scan:
x1 = linspace(0,scanlen,A);
x1 = repmat(x1',1,B);
x1 = x1';
x1 = x1(:);

% Second scan:
x2 = linspace(0,scanlen,C);
x2 = repmat(x2',1,D);
x2 = x2';
x2 = x2(:);

% Third scan:
x3 = linspace(0,scanlen,E);
x3 = repmat(x3',1,F);
x3 = x3';
x3 = x3(:);

% Fourth scan:
x4 = linspace(0,scanlen,G);
x4 = repmat(x4',1,H);
x4 = x4';
x4 = x4(:);

% Fifth scan:
x5 = linspace(0,scanlen,I);
x5 = repmat(x5',1,J);
x5 = x5';
x5 = x5(:);

```

---

---

```

%-----%
%%--- Combine coordinates to create and filter topo points---%%

% Remove points outside of scan coverage and above/below
% pre-specified threshold for high and low elevation points

% Elevation thresholds: update depending on scan information
zfilt_H = 200;      zfilt_L = 135;

% First scan:
topo1 = [x1,y1,z1];
topo1(any(isnan(topo1),2),:) = []; % Remove rows w/NaN points

condition_y1H = topo1(:,2) > y1shift + 0.075;
topo1(condition_y1H,:) = []; % Remove rows outside scan range

condition_y1L = topo1(:,2) < y1shift - 0.075;
topo1(condition_y1L,:) = []; % Remove rows outside scan range

condition_z1H = topo1(:,3) > zfilt_H; % High elevation filter
topo1(condition_z1H,:) = []; % Remove rows

condition_z1L = topo1(:,3) < zfilt_L; % Low elevation filter
topo1(condition_z1L,:) = []; % Remove rows

% Second scan:
topo2 = [x2,y2,z2];
topo2(any(isnan(topo2),2),:) = []; % Remove rows w/NaN points

condition_y2H = topo2(:,2) > y2shift + 0.075;
topo2(condition_y2H,:) = []; % Remove rows outside scan range

condition_y2L = topo2(:,2) < y2shift - 0.075;
topo2(condition_y2L,:) = []; % Remove rows outside scan range

condition_z2H = topo2(:,3) > zfilt_H; % High elevation filter
topo2(condition_z2H,:) = []; % Remove rows

condition_z2L = topo2(:,3) < zfilt_L; % Low elevation filter
topo2(condition_z2L,:) = []; % Remove rows

% Third scan:
topo3 = [x3,y3,z3];
topo3(any(isnan(topo3),2),:) = []; % Remove rows w/NaN points

condition_y3H = topo3(:,2) > y3shift + 0.075;
topo3(condition_y3H,:) = []; % Remove rows outside scan range

condition_y3L = topo3(:,2) < y3shift - 0.075;
topo3(condition_y3L,:) = []; % Remove rows outside scan range

condition_z3H = topo3(:,3) > zfilt_H; % High elevation filter
topo3(condition_z3H,:) = []; % Remove rows

```

---

```

condition_z3L = topo3(:,3) < zfilt_L; % Low elevation filter
topo3(condition_z3L,:) = []; % Remove rows

% Fourth scan:
topo4 = [x4,y4,z4];
topo4(any(isnan(topo4),2),:) = []; % Remove rows w/NaN points

condition_y4H = topo4(:,2) > y4shift + 0.075;
topo4(condition_y4H,:) = []; % Remove rows outside scan range

condition_y4L = topo4(:,2) < y4shift - 0.075;
topo4(condition_y4L,:) = []; % Remove rows outside scan range

condition_z4H = topo4(:,3) > zfilt_H; % High elevation filter
topo4(condition_z4H,:) = []; % Remove rows

condition_z4L = topo4(:,3) < zfilt_L; % Low elevation filter
topo4(condition_z4L,:) = []; % Remove rows

% Fifth scan:
topo5 = [x5,y5,z5];
topo5(any(isnan(topo5),2),:) = []; % Remove rows w/NaN points

condition_y5H = topo5(:,2) > y5shift + 0.075;
topo5(condition_y5H,:) = []; % Remove rows outside scan range

condition_y5L = topo5(:,2) < y5shift - 0.075;
topo5(condition_y5L,:) = []; % Remove rows outside scan range

condition_z5H = topo5(:,3) > zfilt_H; % High elevation filter
topo5(condition_z5H,:) = []; % Remove rows

condition_z5L = topo5(:,3) < zfilt_L; % Low elevation filter
topo5(condition_z5L,:) = []; % Remove rows

%-----%
%%--- Write text files ---%%

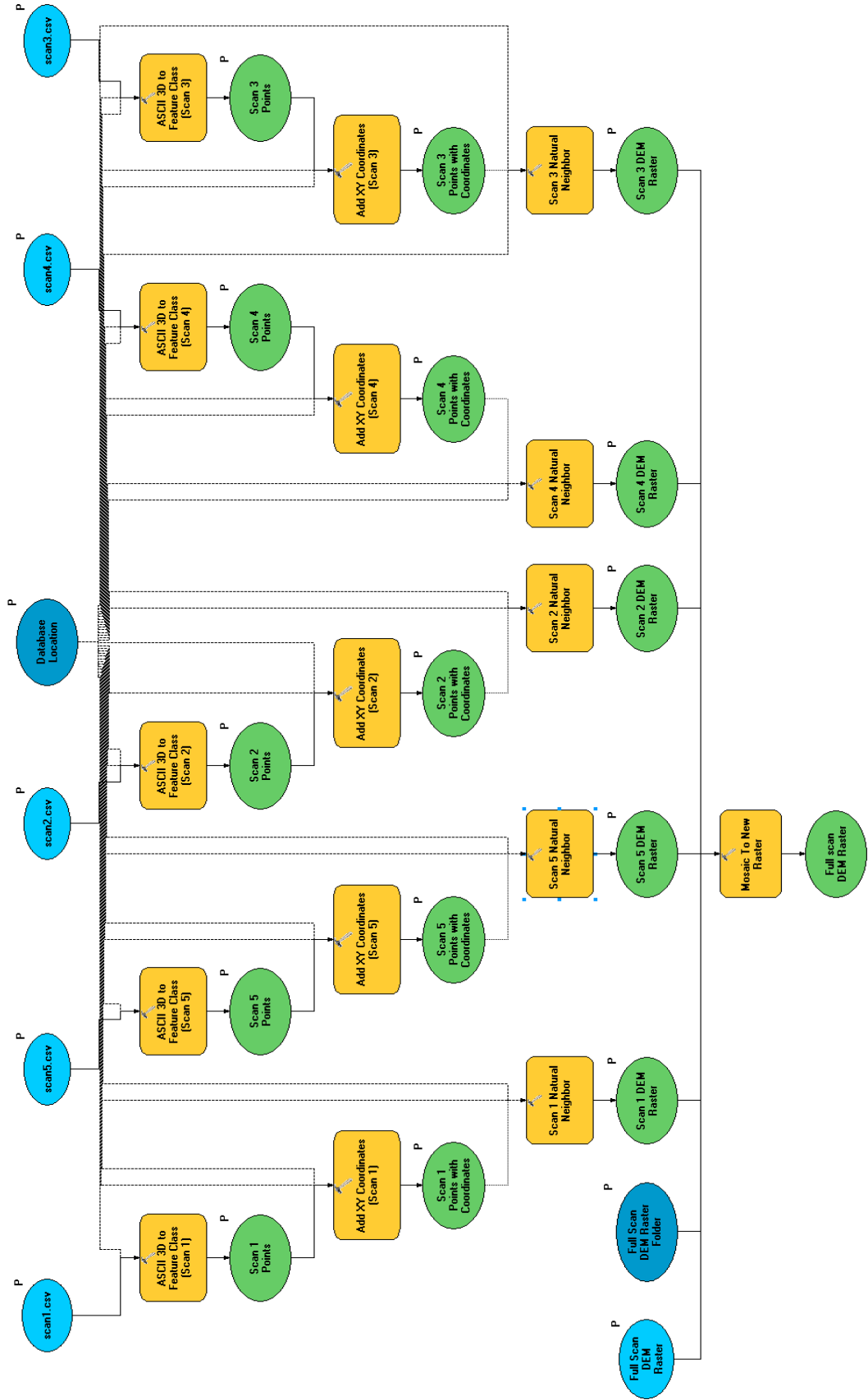
% Separate text file (comma-delimited) for each scan is saved for
% use with ArcGIS scan processing and analysis

dlmwrite('scan1.csv',topo1);    dlmwrite('scan2.csv',topo2);
dlmwrite('scan3.csv',topo3);    dlmwrite('scan4.csv',topo4);
dlmwrite('scan5.csv',topo5);

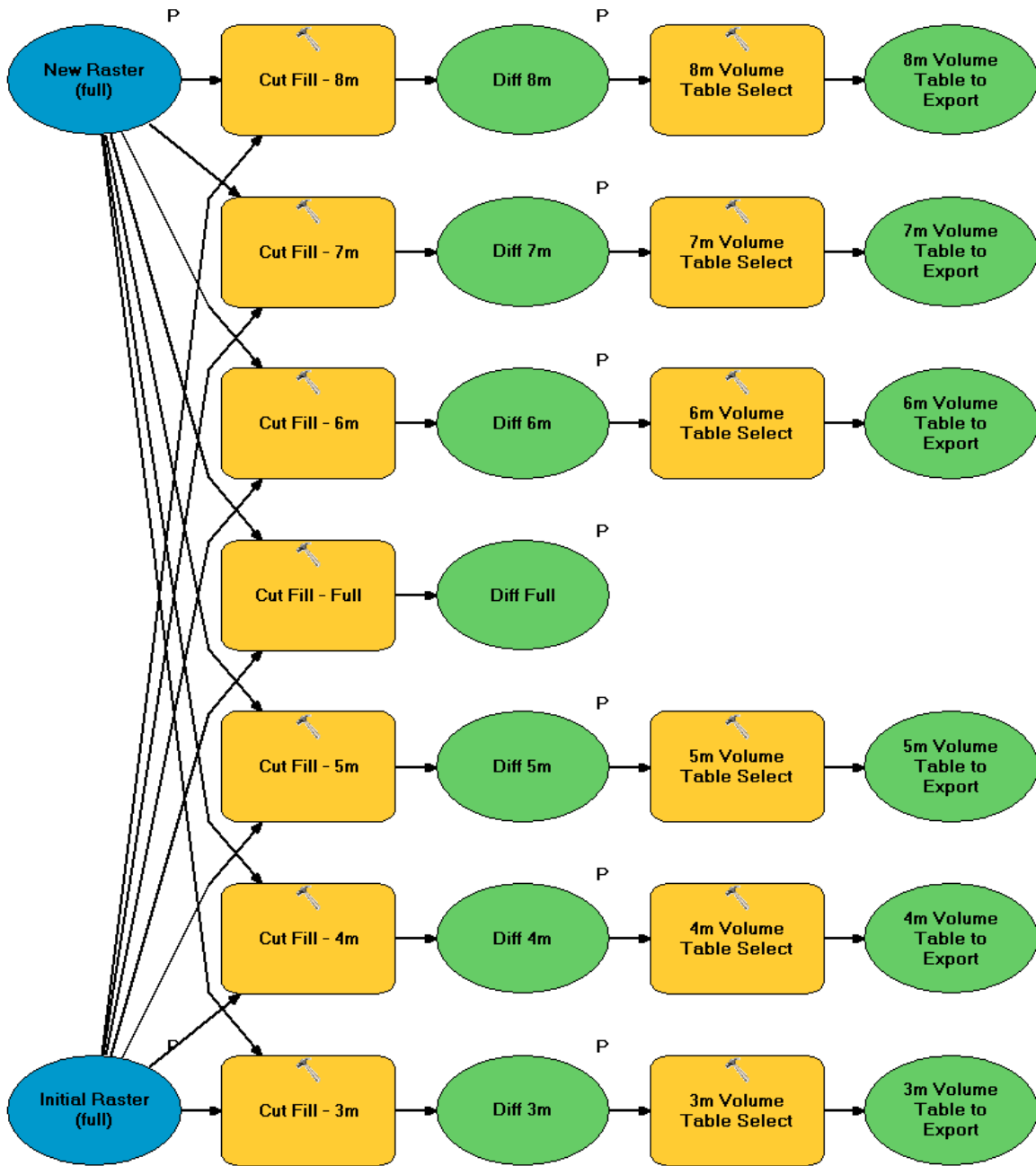
%-----%

```

Appendix B.3 – GIS Flowchart: Scan Processing



Appendix B.3 – GIS Flowchart: DEM Differencing



---

Appendix B.4 -- Bed Monitoring System Conversion MATLAB Code

```

% TRANSDUCER DATA PROCESSING: loadconverter.m
%   Written by Kevin Waters (April 2013)

% Description:
% This function converts transducer voltage data to load using
% manually developed calibration curves for each of six 1-m flume
% segments. Output is a tab-delimited text file and MATLAB plot of
% continuous weight time series for each flume segment.

%-----%
%%--- Define function and variables ---%%

function [t,w] = loadconverter(tm)

% Output parameters:
%   t   = time (s)
%   w   = total load (kg)

% Input variables:
%   tm  = total recording time (s)

%-----%
%%--- Import and treat voltage data ---%%

A = load('time_avg.txt'); % From transducer data text file

% Preallocate weight matrix w for speed
m = length(A);
n = 6; % Only flume segments 3-8 included in weight matrix
w = zeros(m,n);

% Calculate time array
t = 0:1:tm-1; t = t';
t = t./600; % Convert from seconds to minutes

%-----%
%%--- Calculate loads using quadratic calibration equations---%%

% Calibration #1 curves used:
% Meter 3:
w3m = 38674 .* (A(:,1).^2) + 9175.2 .* A(:,1) - 79.200;
w(:,1) = w3m; % Populate results matrix for flume meter 3

% Meter 4:
w4m = 48093 .* (A(:,2).^2) + 9039.9 .* A(:,2) - 80.681;
w(:,2) = w4m; % Populate results matrix for flume meter 4

% Meter 5:
w5m = 72319 .* (A(:,3).^2) + 8392.8 .* A(:,3) - 69.675;
w(:,3) = w5m; % Populate results matrix for flume meter 5

% Meter 6:

```

---

```

w6m = 22328 .* (A(:,4).^2) + 9994.2 .* A(:,4) - 118.78;
w(:,4) = w6m; % Populate results matrix for flume meter 6

% Meter 7:
w7m = 64866 .* (A(:,6).^2) + 8144.5 .* A(:,6) - 99.406;
w(:,5) = w7m; % Populate results matrix for flume meter 7

% Meter 8:
w8m = 41550 .* (A(:,8).^2) + 9533.0 .* A(:,8) - 88.434;
w(:,6) = w8m; % Populate results matrix for flume meter 8

%-----%
%%--- Plot results for each segment together ---%%

% Create figure
figure1 = figure;

% Create axes
axes1 = axes('Parent',figure1);
box(axes1,'on');
hold(axes1,'all');

% Plot load versus time
wplot = plot(t,w);

% Create axis labels
xlabel({'Time (min)'});
ylabel({'Sediment Weight (lb)'});

% Set data names
set(wplot(1),'DisplayName','3m');
set(wplot(2),'DisplayName','4m');
set(wplot(3),'DisplayName','5m');
set(wplot(4),'DisplayName','6m');
set(wplot(5),'DisplayName','7m');
set(wplot(6),'DisplayName','8m');

% Create legend
wlegend = legend(axes1,'show');
set(wlegend,'Location','EastOutside');

%-----%
%%--- Write output text file ---%%
dlmwrite('Transducer_loads.txt',w,'\t');

%-----%

```

## **APPENDIX C**

### ***Velocity Results***

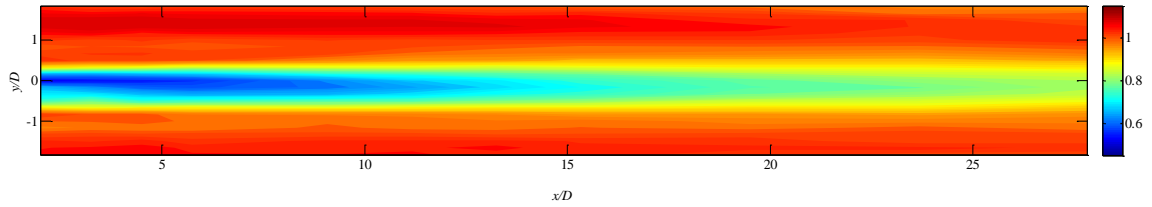
---

---

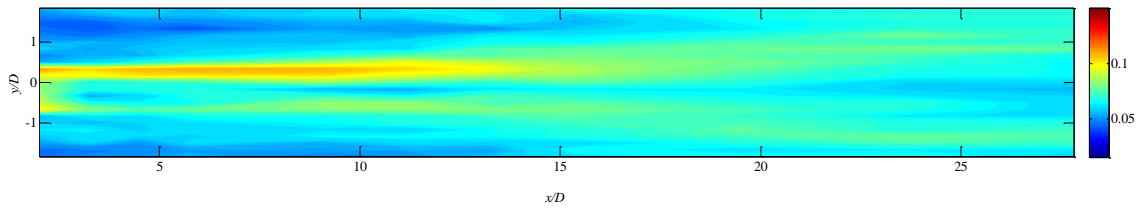
***C.1 Velocity and Turbulence Contour Plots (NS Experiments)***

***C.2 Velocity and Bed Centerline Profiles (PS Experiments)***

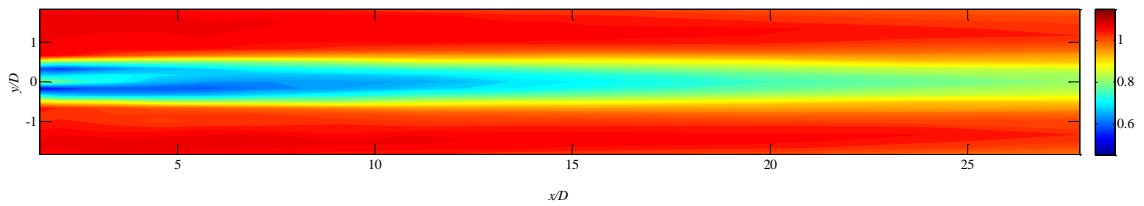
### Appendix C.1 – Velocity and Turbulence Contour Plots (NS Experiments)



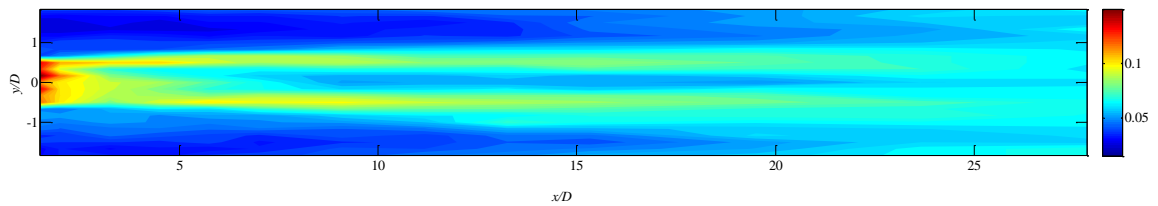
(a) NS-1A:  $u/U_0$  ( $Fr = 0.10$ ,  $\varphi = 0.03$ )



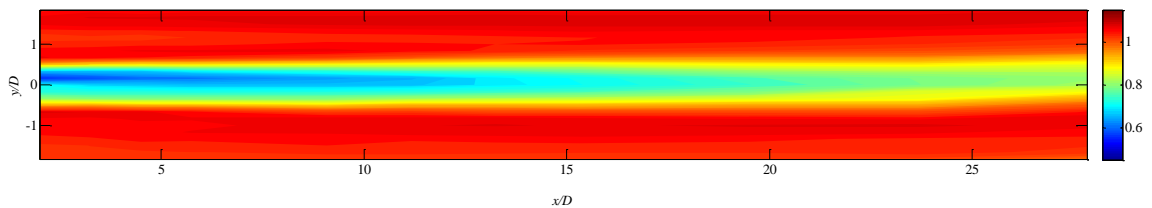
(b) NS-1A:  $u_{rms}/U_0$  ( $Fr = 0.10$ ,  $\varphi = 0.03$ )



(c) NS-1B:  $u/U_0$  ( $Fr = 0.10$ ,  $\varphi = 0.03$ )

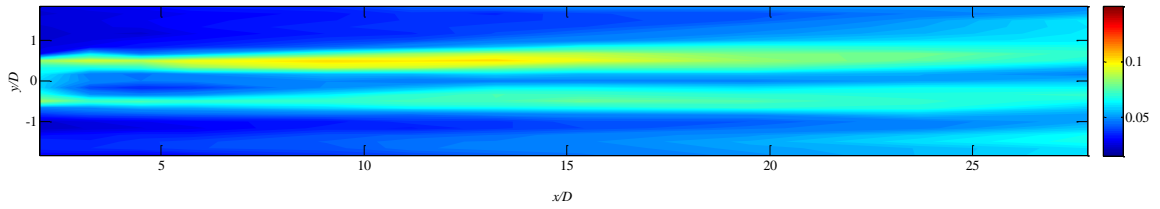
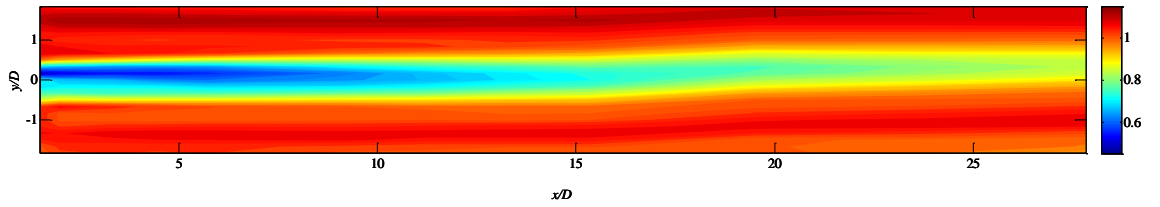
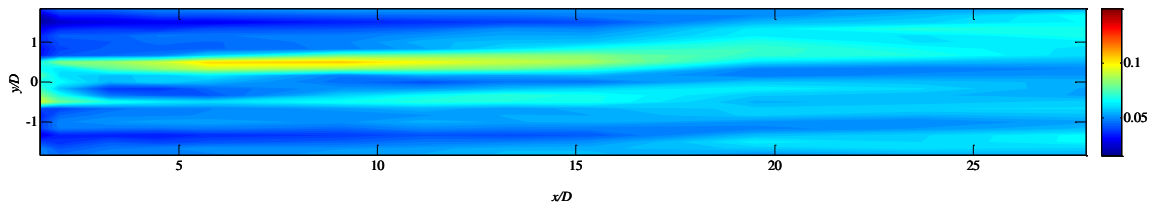
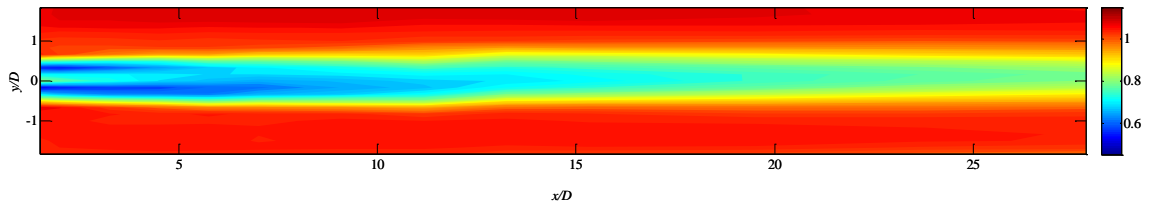
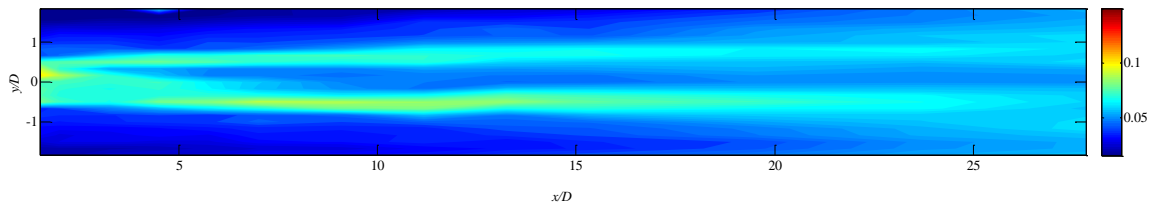


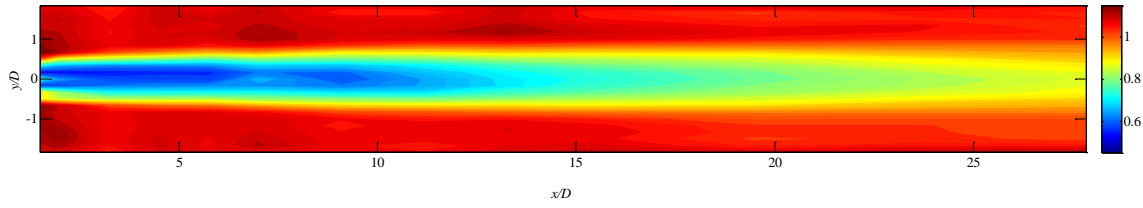
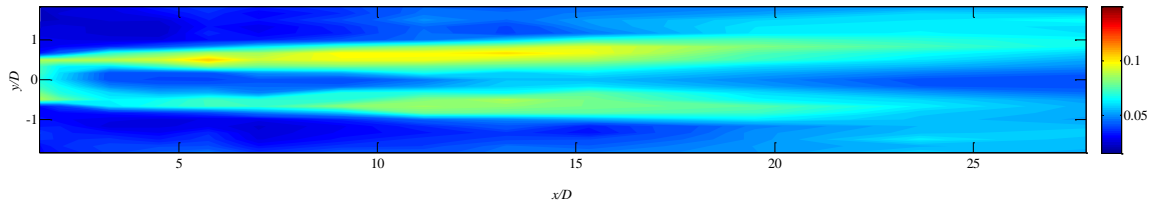
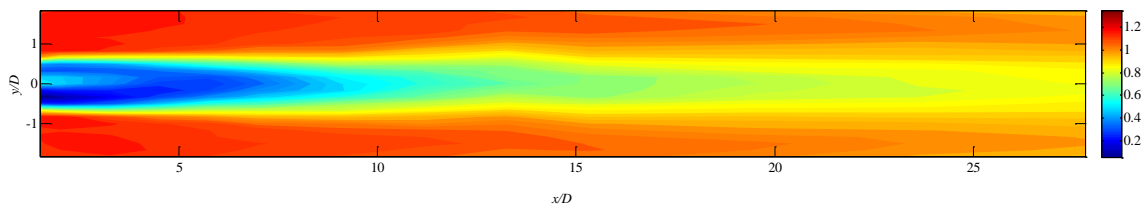
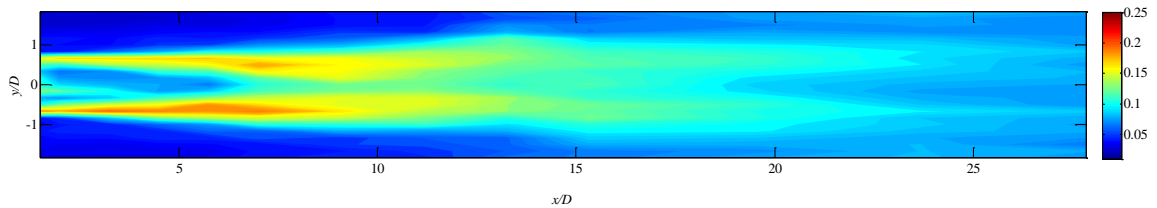
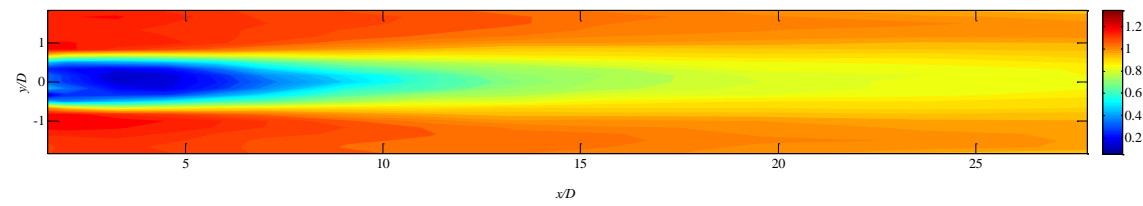
(d) NS-1B:  $u_{rms}/U_0$  ( $Fr = 0.10$ ,  $\varphi = 0.03$ )



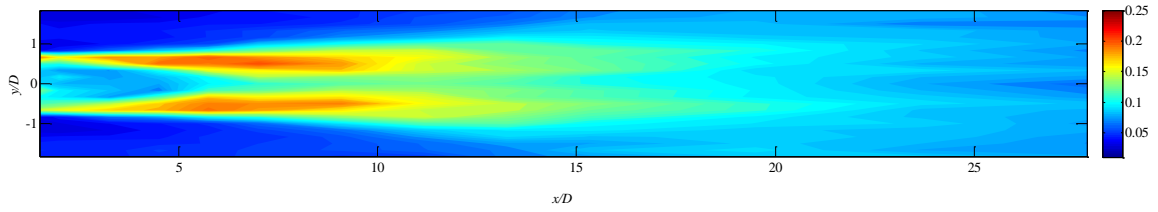
(e) NS-2:  $u/U_0$  ( $Fr = 0.22$ ,  $\varphi = 0.03$ )

Note: Patch ends at  $x/D = 1.0$ . Lateral patch extent is between  $y/D = -0.5$  and  $0.5$ . Flow is from left to right.

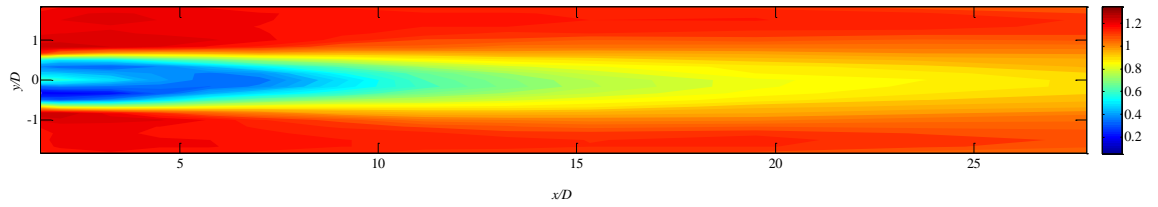
(f) NS-2:  $u_{rms}/U_0$  ( $Fr = 0.22$ ,  $\varphi = 0.03$ )(g) NS-3A:  $u/U_0$  ( $Fr = 0.31$ ,  $\varphi = 0.03$ )(h) NS-3A:  $u_{rms}/U_0$  ( $Fr = 0.31$ ,  $\varphi = 0.03$ )(i) NS-3B:  $u/U_0$  ( $Fr = 0.31$ ,  $\varphi = 0.03$ )(j) NS-3B:  $u_{rms}/U_0$  ( $Fr = 0.31$ ,  $\varphi = 0.03$ )

(k) NS-4:  $u/U_0$  ( $Fr = 0.47$ ,  $\varphi = 0.03$ )(l) NS-4:  $u_{rms}/U_0$  ( $Fr = 0.47$ ,  $\varphi = 0.03$ )(m) NS-5A:  $u/U_0$  ( $Fr = 0.10$ ,  $\varphi = 0.10$ )\*(n) NS-5A:  $u_{rms}/U_0$  ( $Fr = 0.10$ ,  $\varphi = 0.10$ )(o) NS-5B:  $u/U_0$  ( $Fr = 0.10$ ,  $\varphi = 0.10$ )

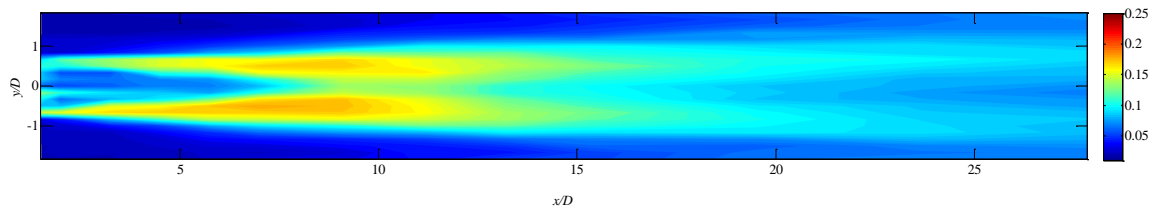
\*Note: color bar scales change for dense patches ( $\varphi = 0.10$ ) starting at (m).



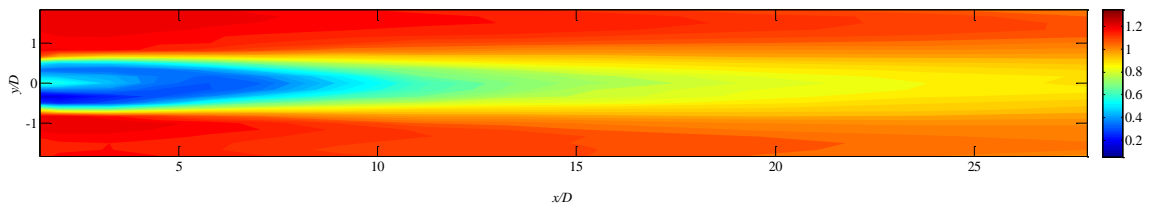
(p) NS-5B:  $u_{rms}/U_0$  ( $Fr = 0.10$ ,  $\varphi = 0.10$ )



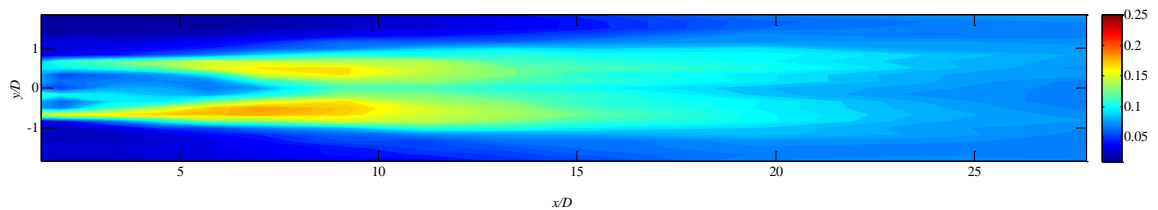
(q) NS-6:  $u/U_0$  ( $Fr = 0.21$ ,  $\varphi = 0.10$ )



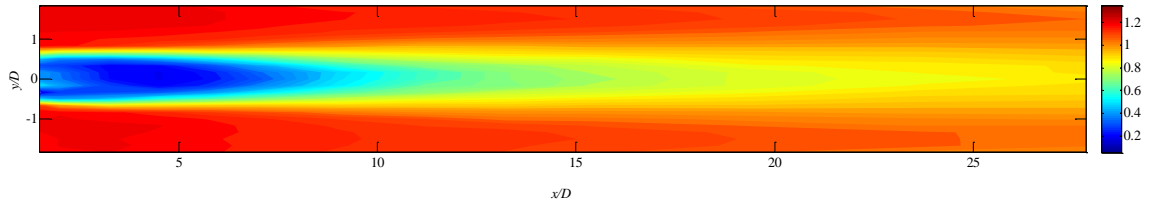
(r) NS-6:  $u_{rms}/U_0$  ( $Fr = 0.21$ ,  $\varphi = 0.10$ )



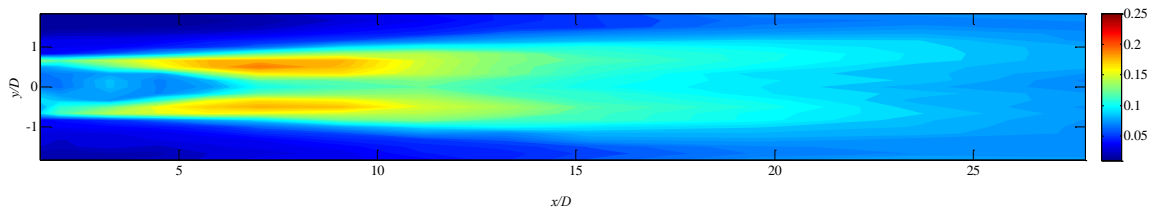
(s) NS-7A:  $u/U_0$  ( $Fr = 0.31$ ,  $\varphi = 0.10$ )



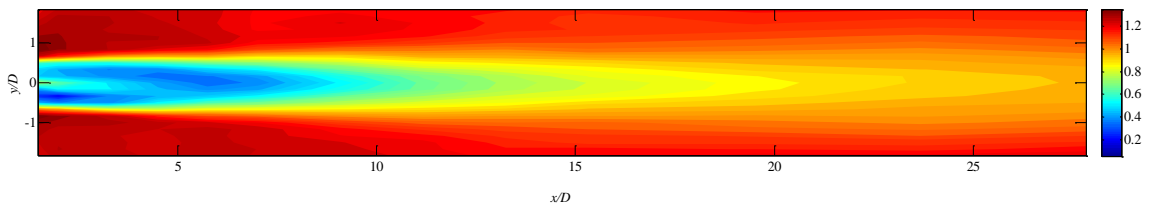
(t) NS-7A:  $u_{rms}/U_0$  ( $Fr = 0.31$ ,  $\varphi = 0.10$ )



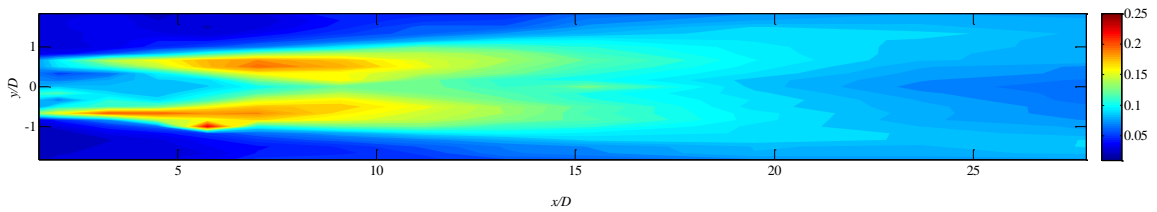
(u) NS-7B:  $u/U_0$  ( $Fr = 0.31$ ,  $\varphi = 0.10$ )



(v) NS-7B:  $u_{rms}/U_0$  ( $Fr = 0.31$ ,  $\varphi = 0.10$ )



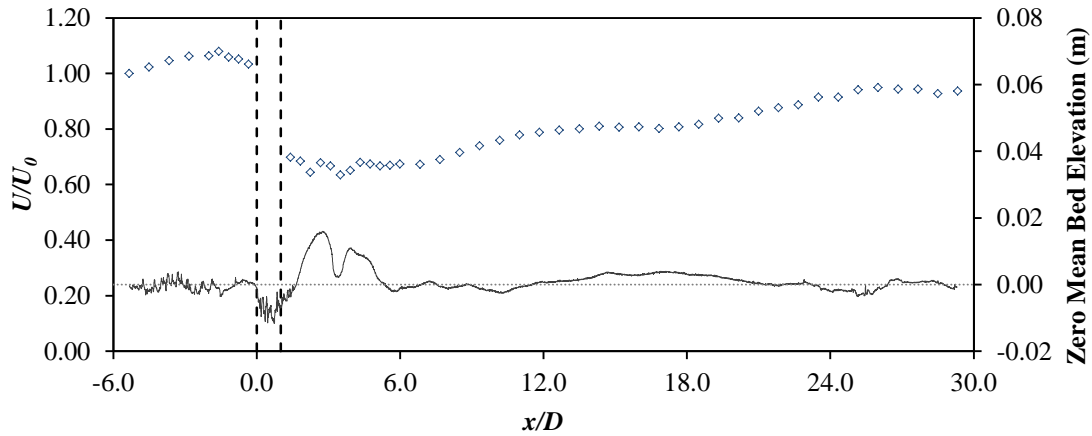
(w) NS-8:  $u/U_0$  ( $Fr = 0.44$ ,  $\varphi = 0.10$ )



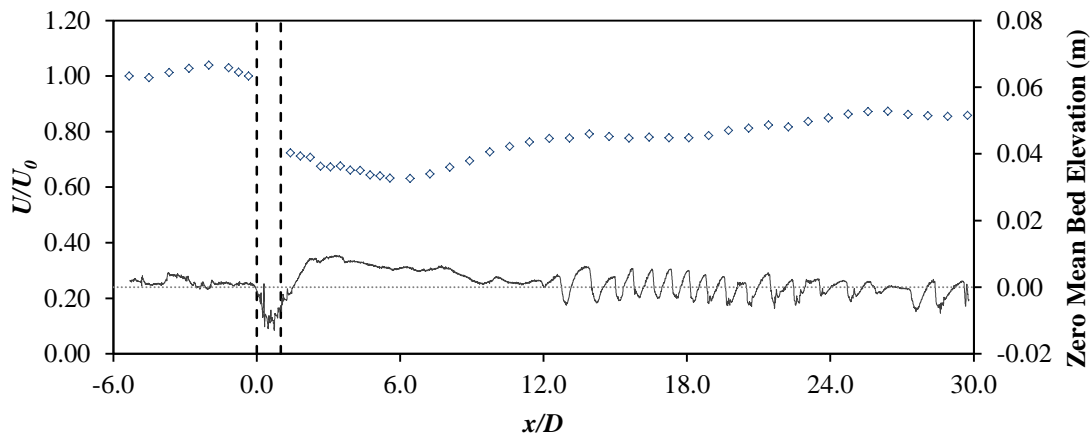
(x) NS-8:  $u_{rms}/U_0$  ( $Fr = 0.44$ ,  $\varphi = 0.10$ )

## Appendix C.2 – Velocity and Bed Centerline Profiles (PS Experiments)

### PS-1 (Sparse, Low flow, Mix 1)



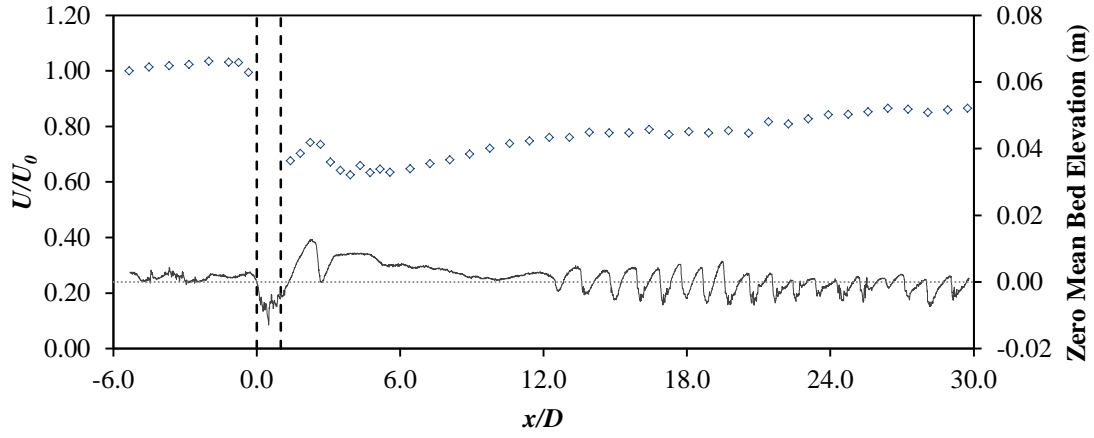
(a) Equilibrium Bed



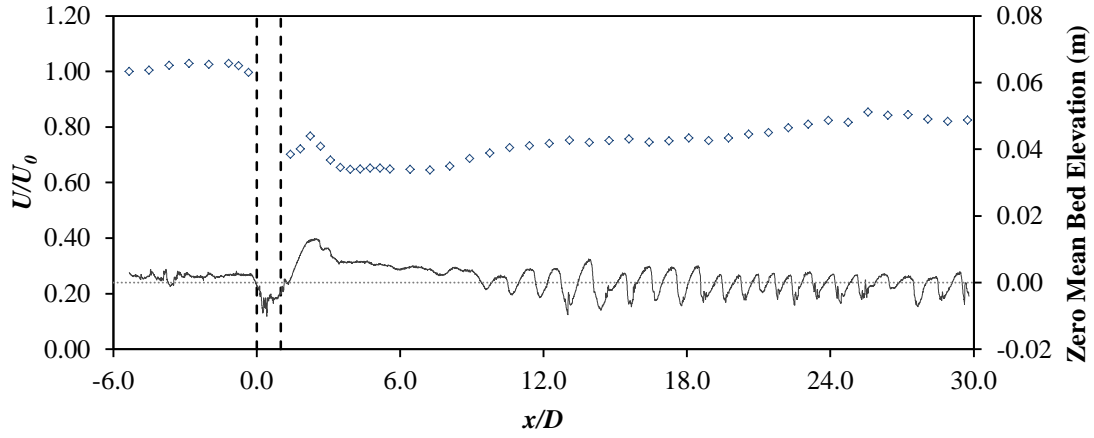
(b) Post Hydrograph 1

#### NOTES FOR ALL PROFILE PLOTS:

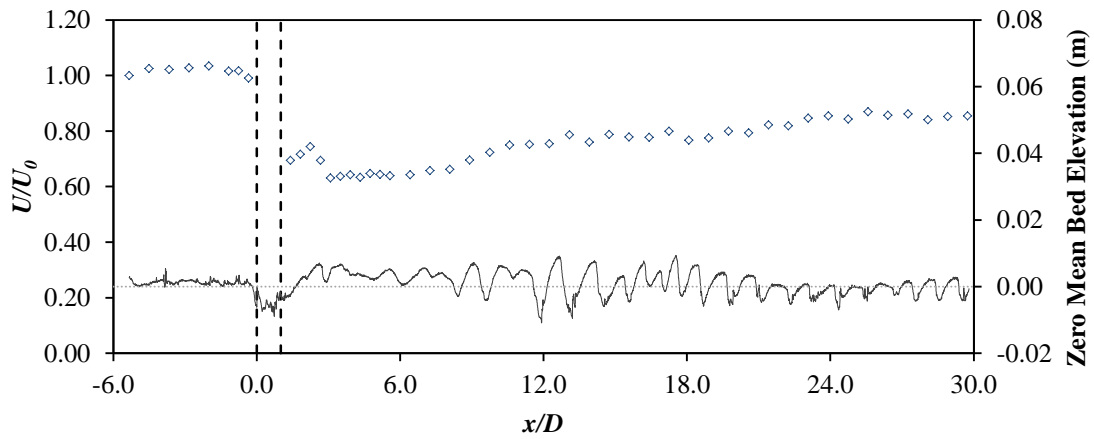
- Longitudinal distance ( $x$ ) is normalized by the patch diameter ( $D$ ) of 12 cm.
- Blue diamonds represent velocity measurements recorded along the longitudinal profile of the patch centerline (top portion of plots). Streamwise velocity ( $U$ ) is normalized by the velocity upstream of the patch ( $U_0$ ).
- Solid, dark gray lines represent centerline bed profiles extracted from DEMs, adjusted for a zero mean bed elevation (bottom portion of plots). The mean bed elevation is indicated by light dashed, horizontal line.
- Vertical dashed black lines represent the patch location, extending from  $x/D = 0$  to  $x/D = 1.0$ .



(c) Post Hydrograph 2



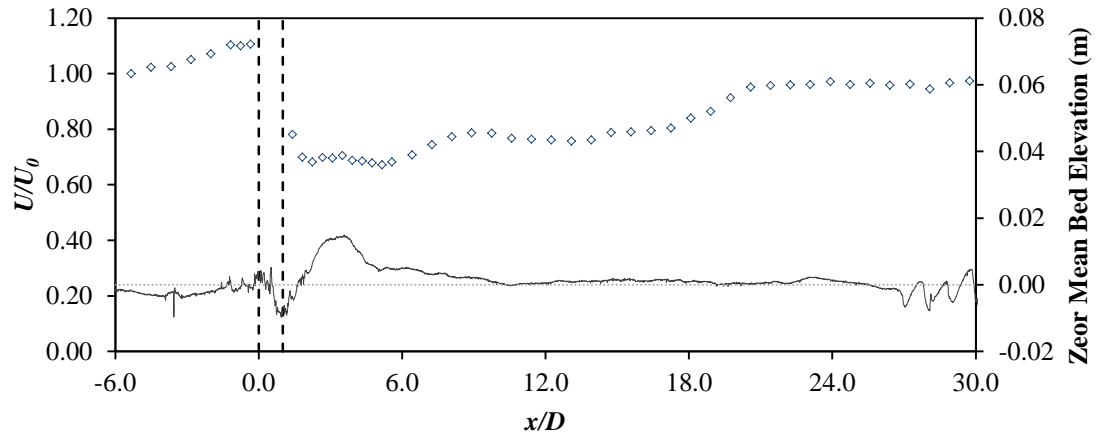
(d) Post Hydrograph 3



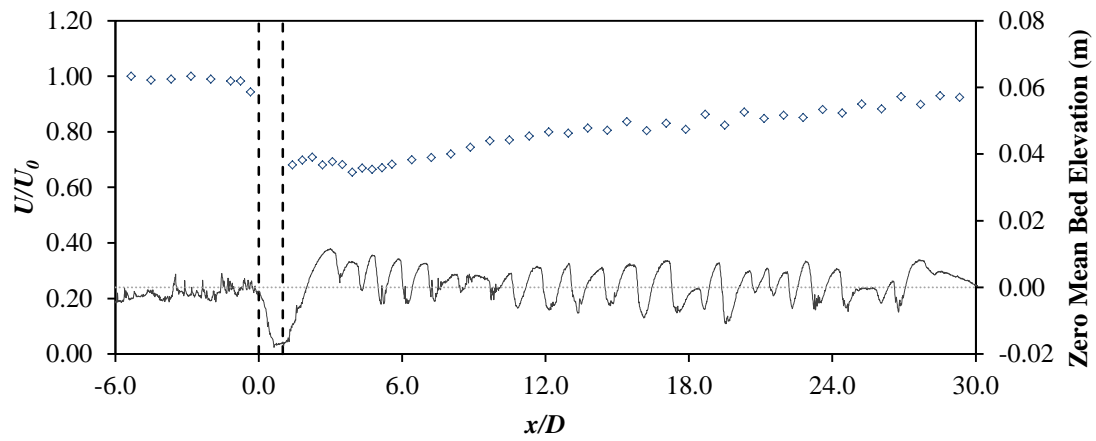
(e) Post Hydrograph 4

**PS-2 (Sparse, High flow, Mix 1)**

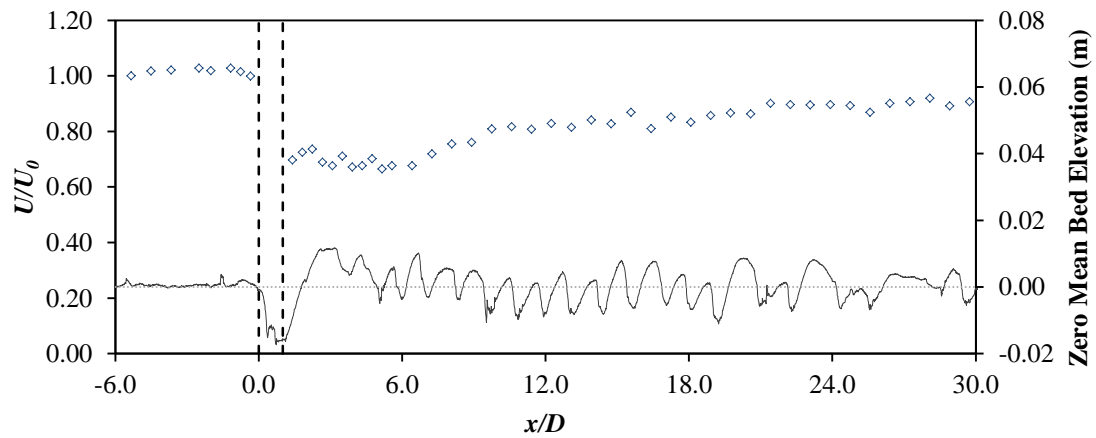

---



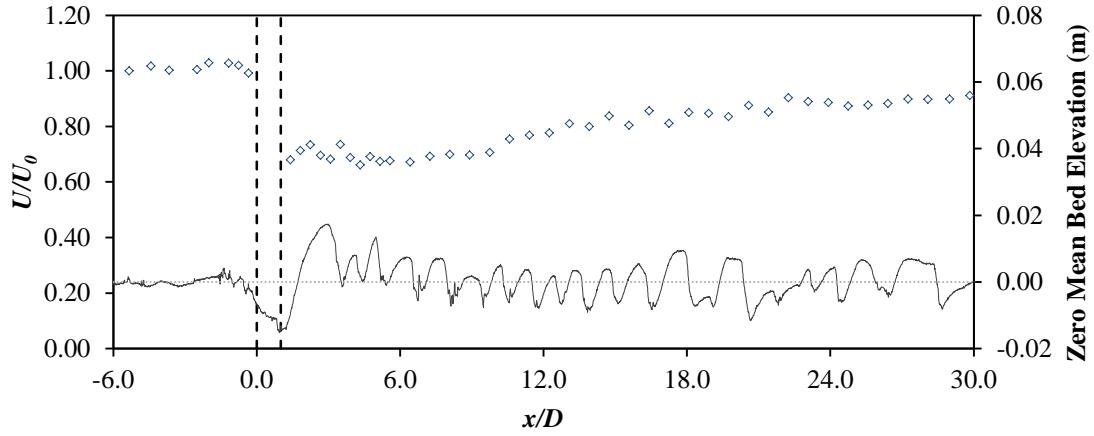
(a). Equilibrium Bed



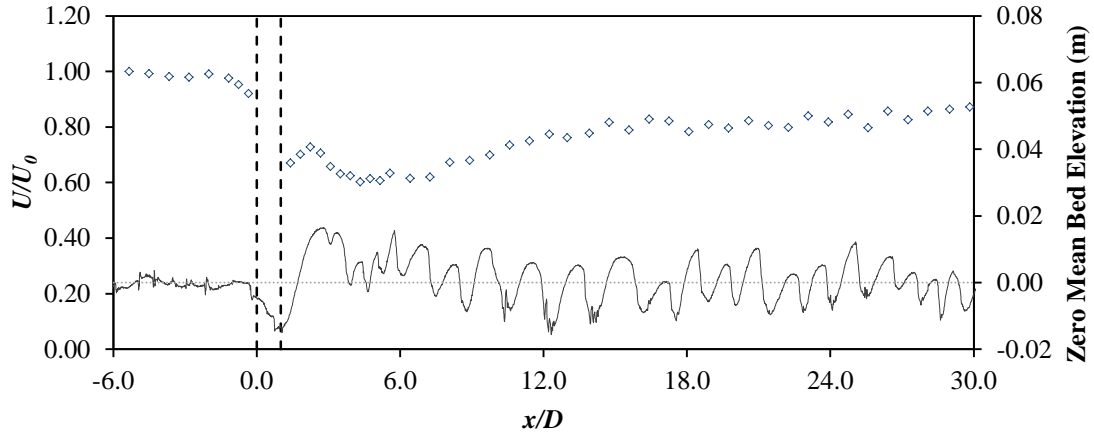
(b). Post Hydrograph 1



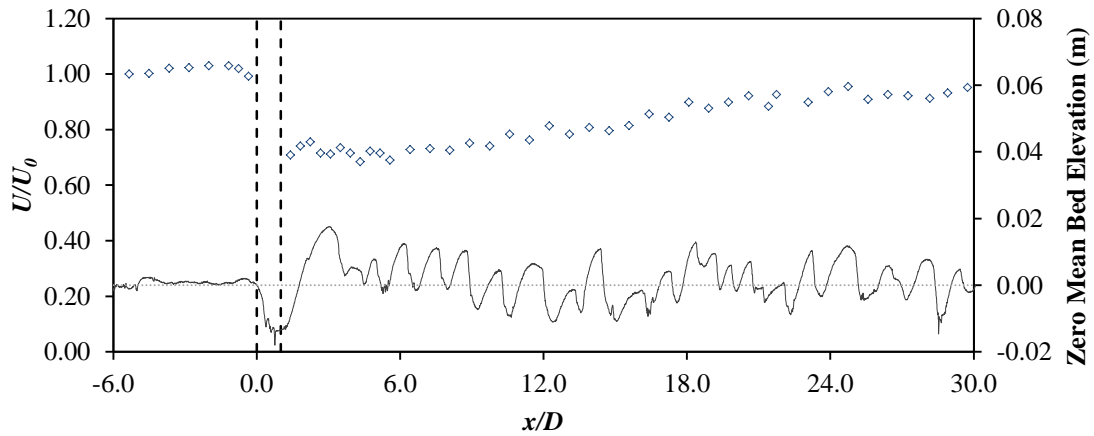
(c). Post Hydrograph 2



(d). Post Hydrograph 3

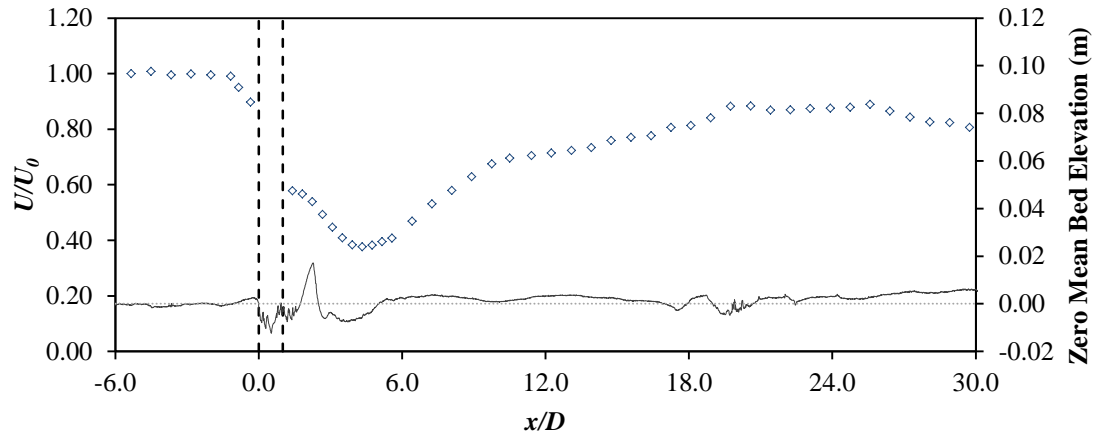


(e). Post Hydrograph 5 (Note: data collection failed Post Hydrograph 4)

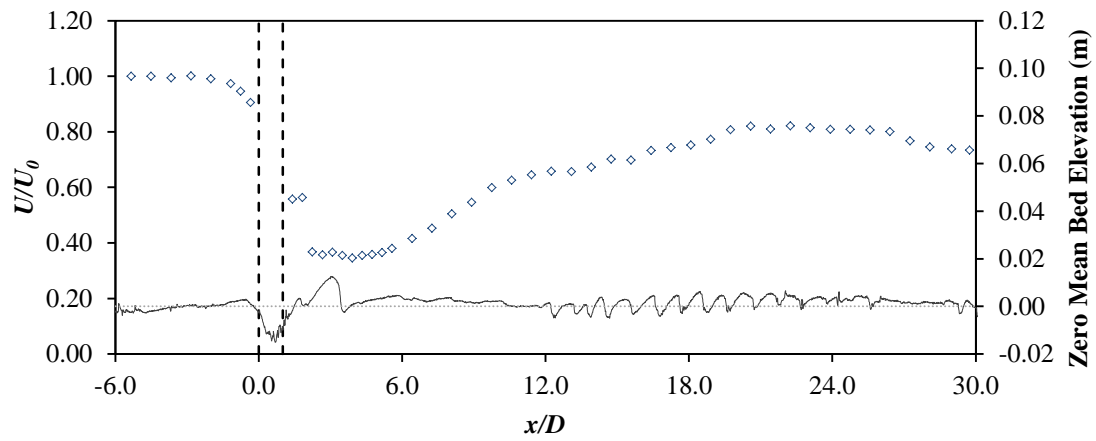


(f). Post Hydrograph 6

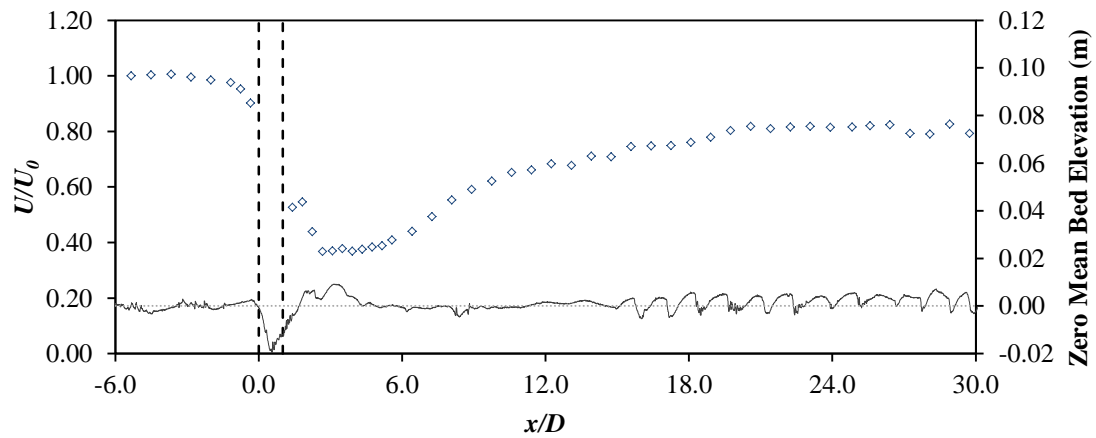
**PS-3 (Dense, Low flow, Mix 1)**



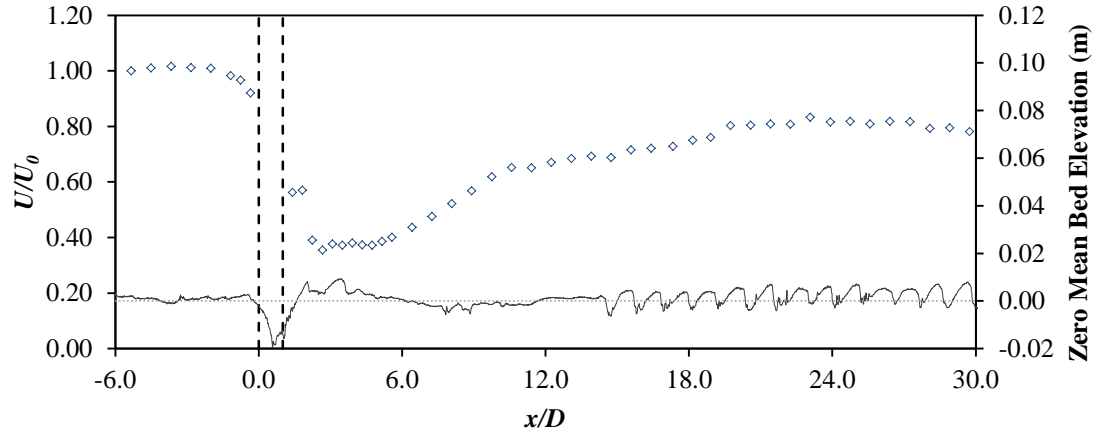
(a). Equilibrium Bed



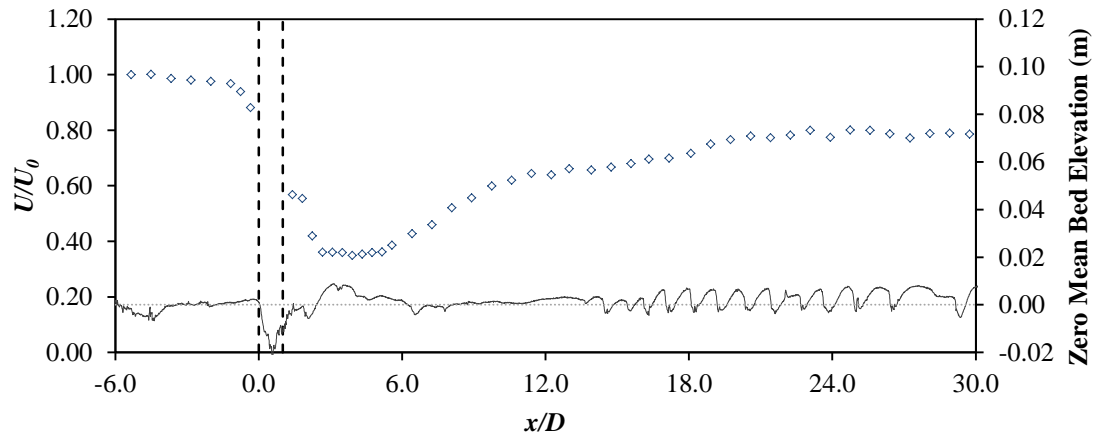
(b). Post Hydrograph 1



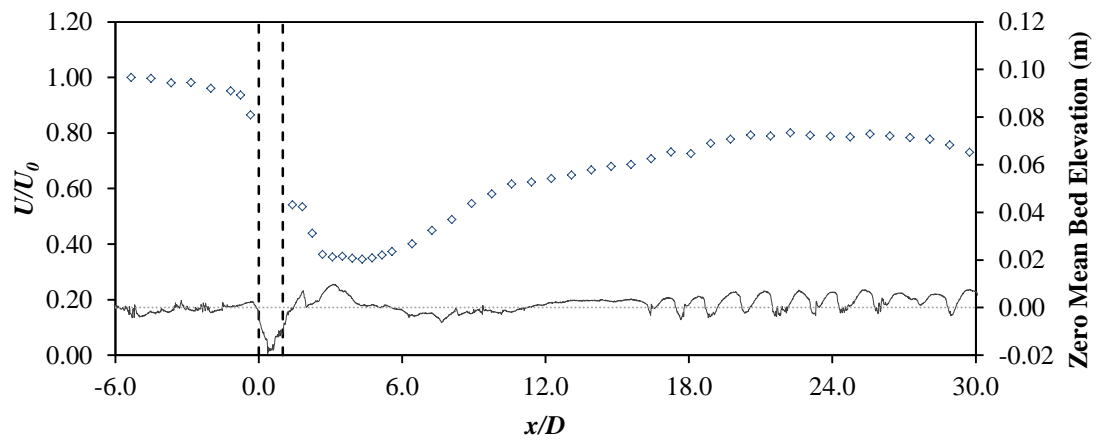
(c). Post Hydrograph 2



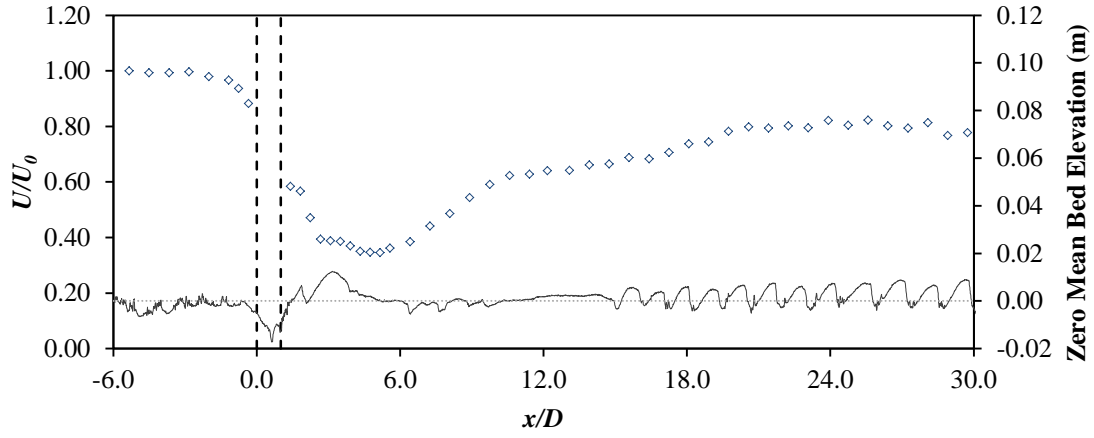
(d). Post Hydrograph 3



(e). Post Hydrograph 4



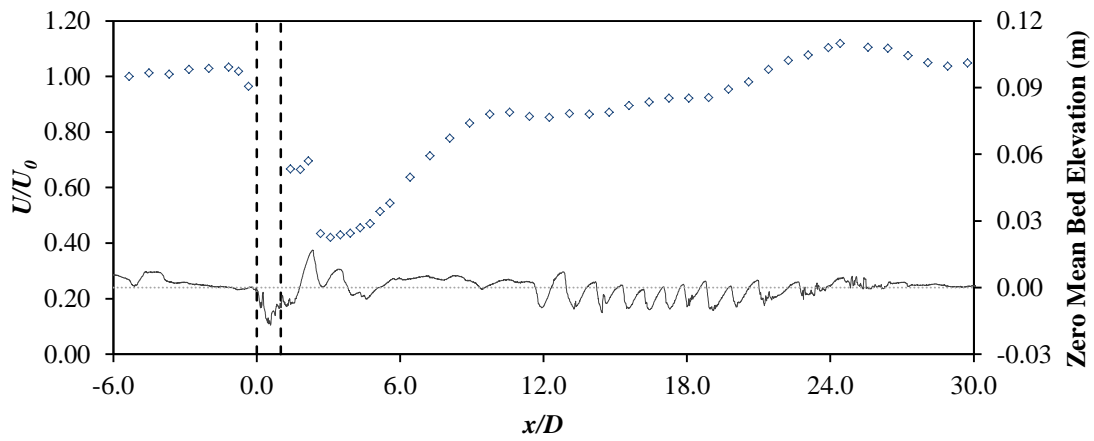
(f). Post Hydrograph 5



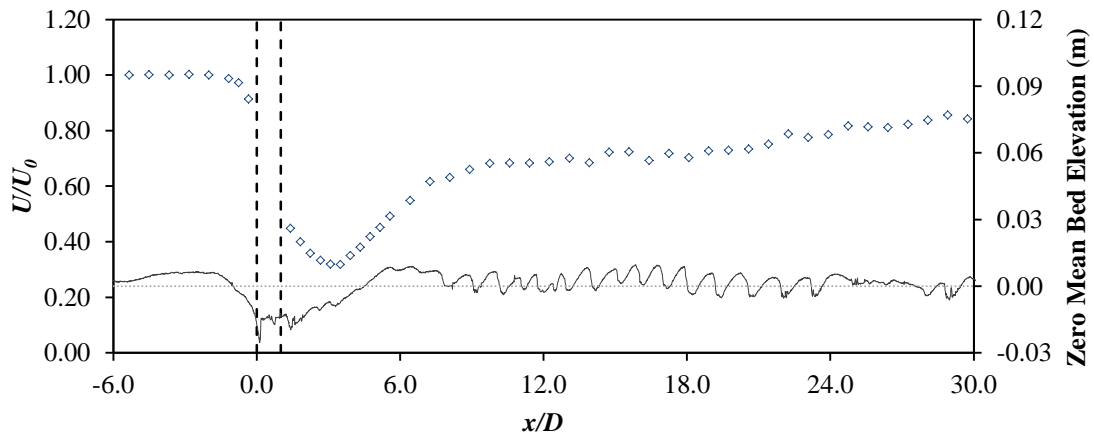
(g). Post Hydrograph 6

**PS-4 (Dense, High flow, Mix 1)**

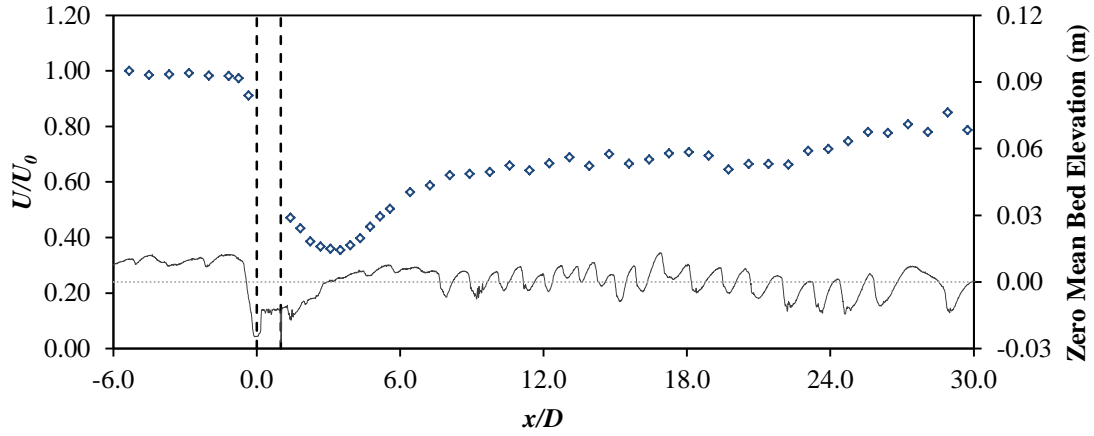
---



(a). Equilibrium Bed

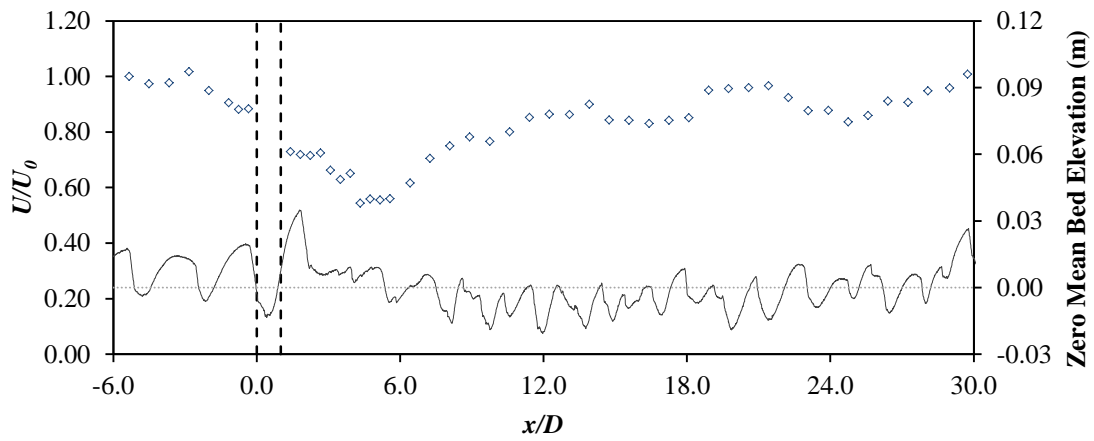


(b). Post Hydrograph 1

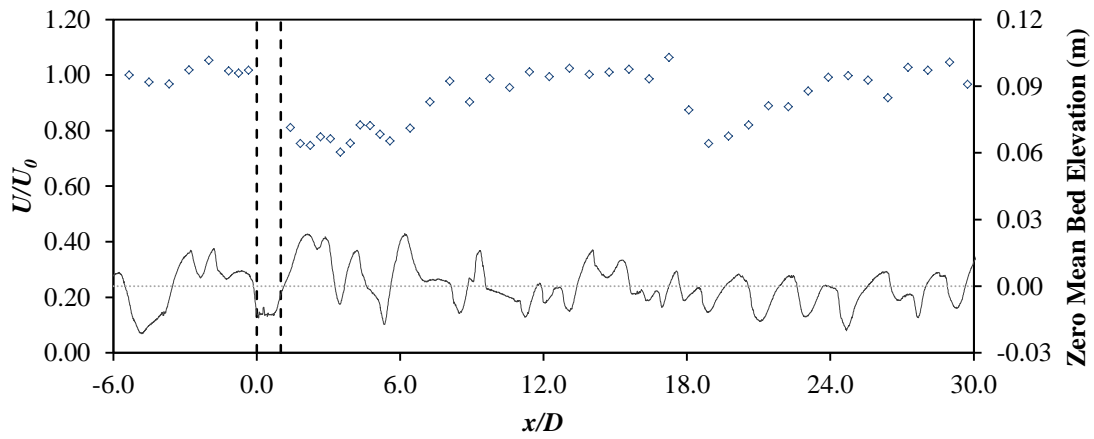


(c). Post Hydrograph 2

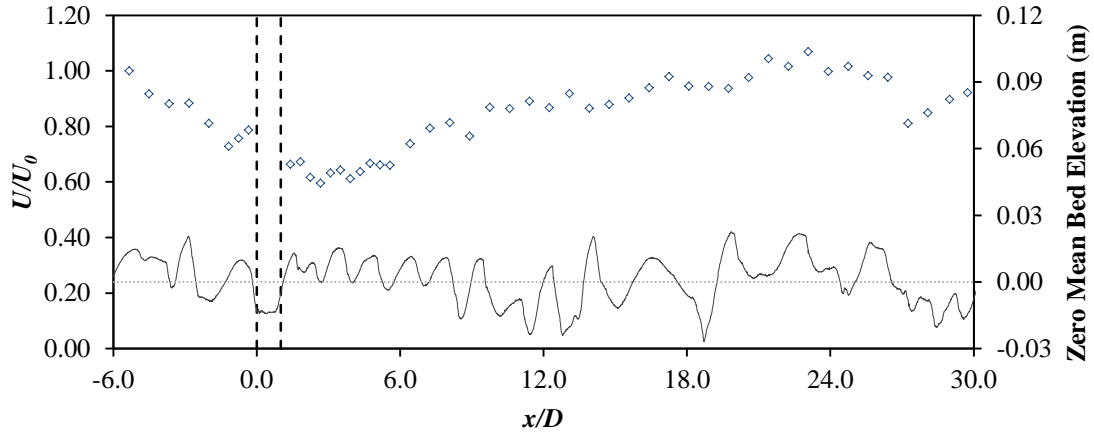
**PS-5 (Sparse, Low flow, Mix 2)**



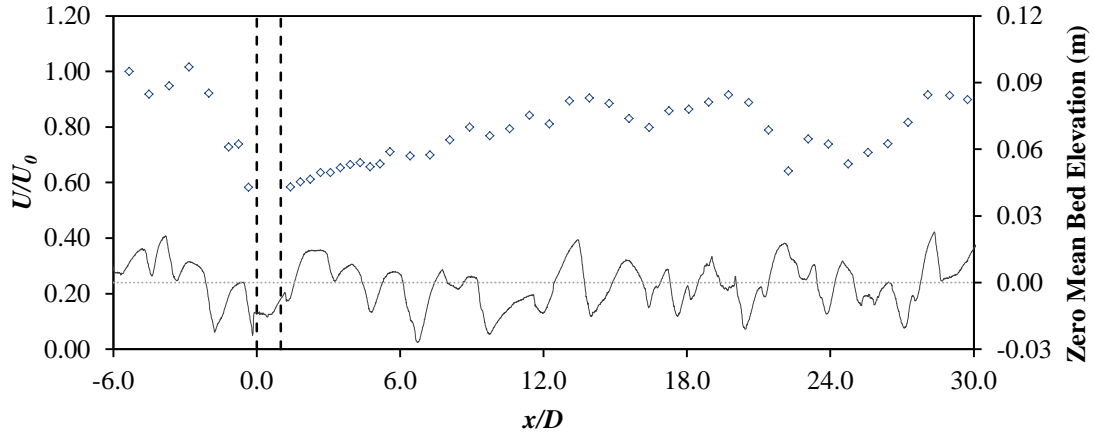
(a). Post Hydrograph 1 (Note: data collection failed for Equilibrium bed)



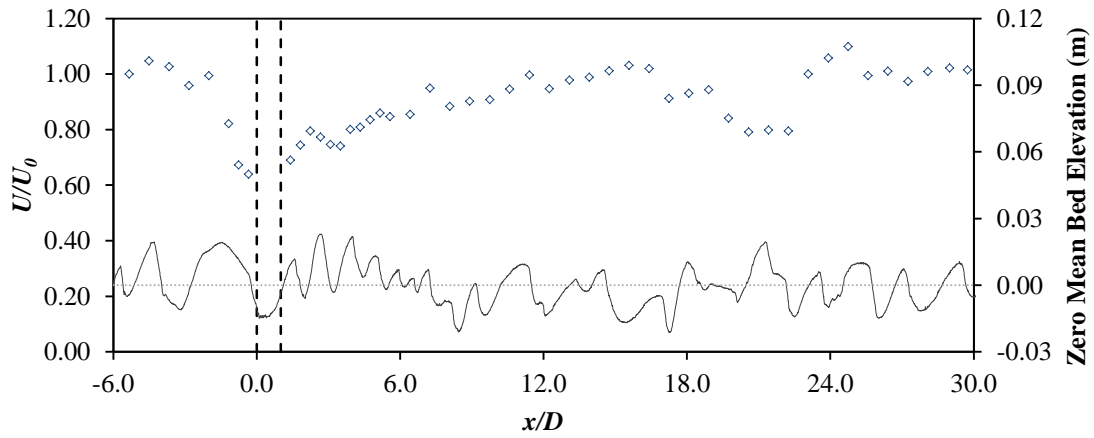
(b). Post Hydrograph 2



(c). Post Hydrograph 3

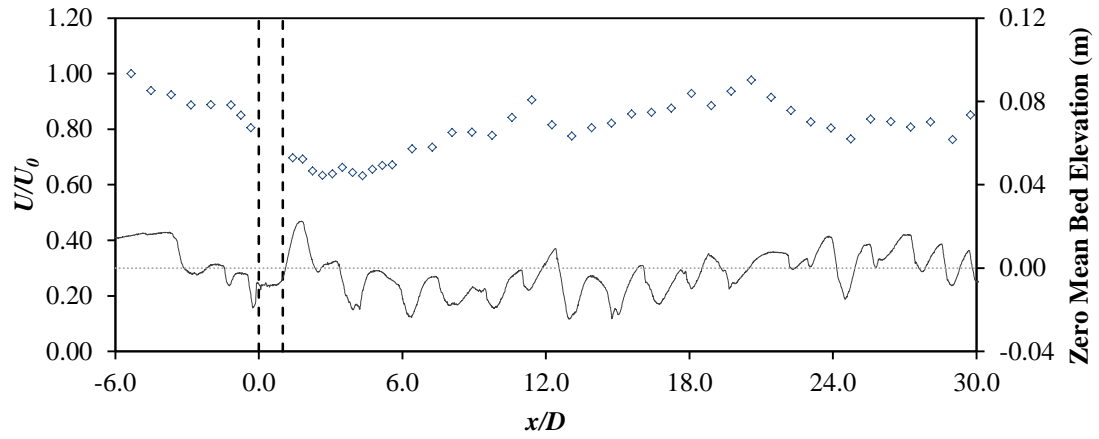


(d). Post Hydrograph 4

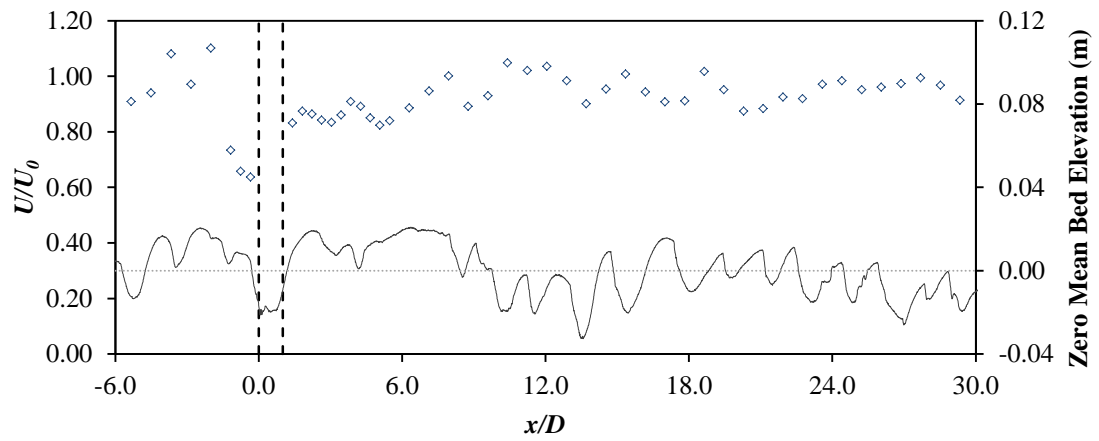


(e). Post Hydrograph 5

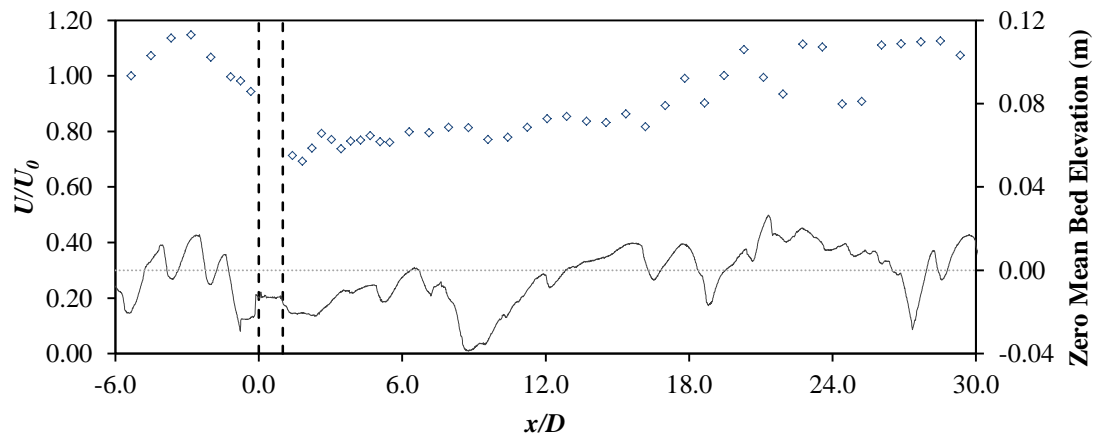
**PS-6 (Sparse, High flow, Mix 2)**



(a). Equilibrium Bed

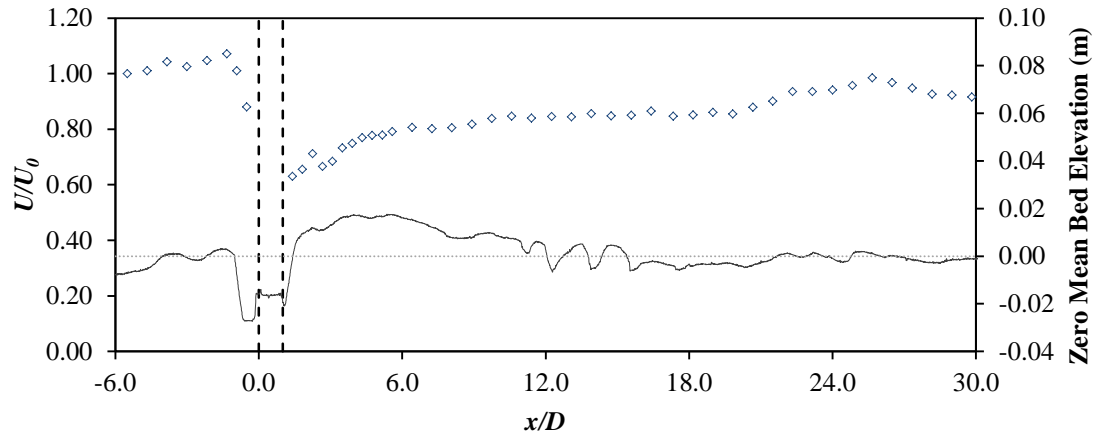


(b). Post Hydrograph 1

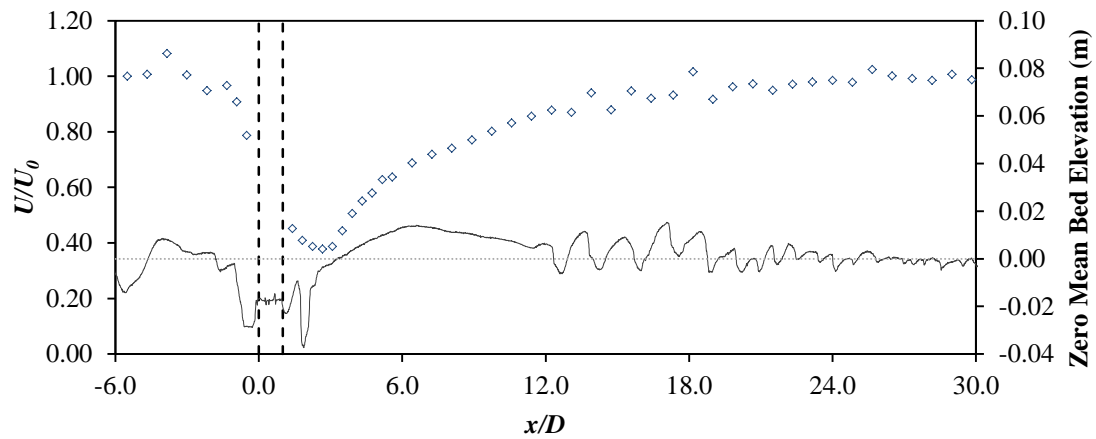


(c). Post Hydrograph 2

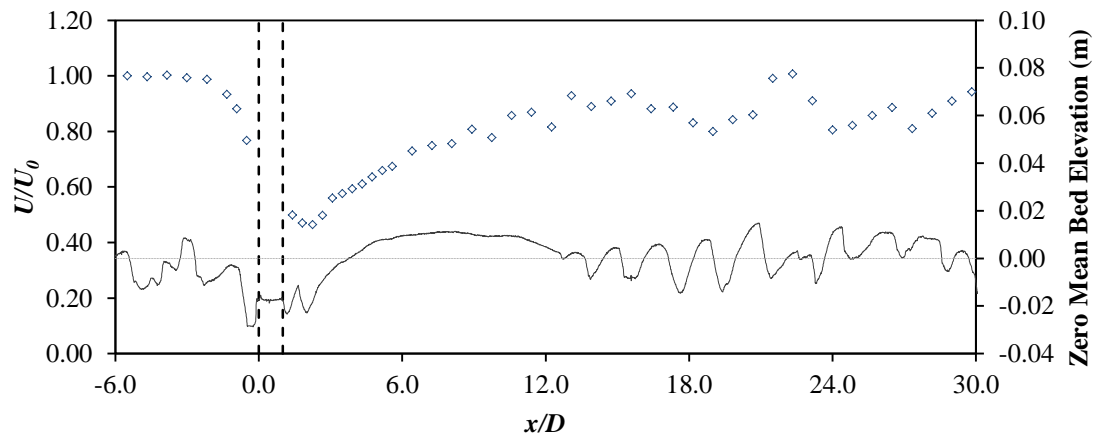
## PS-7 (Dense, Low flow, Mix 2)



(a). Equilibrium Bed



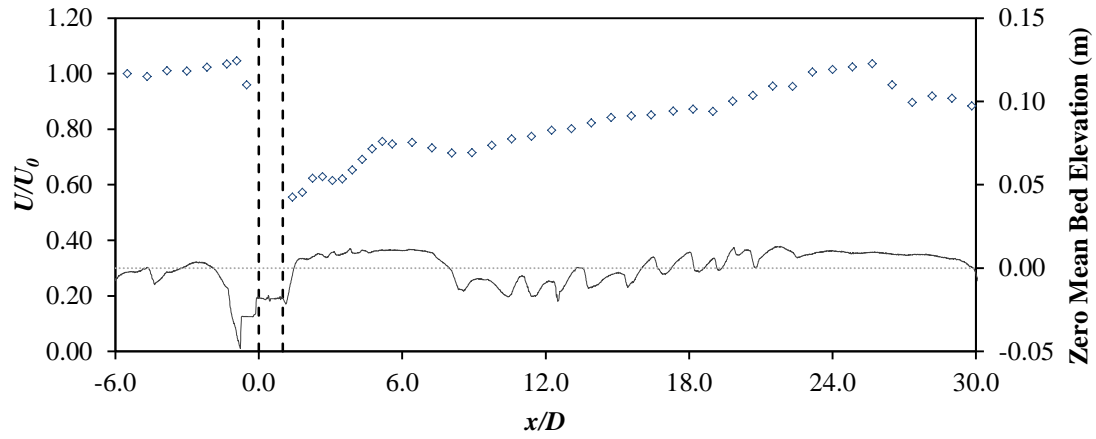
(b). Post Hydrograph 1



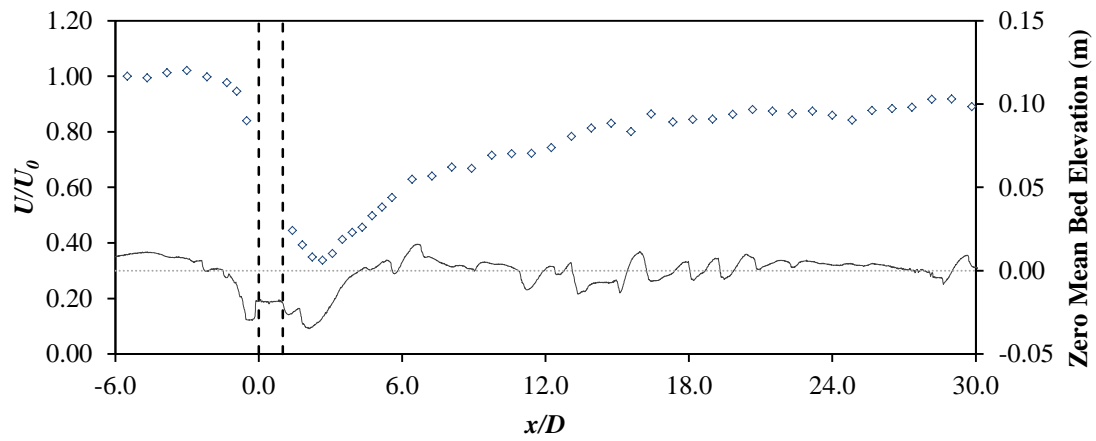
(c). Post Hydrograph 2

**PS-8 (Dense, High flow, Mix 2)**

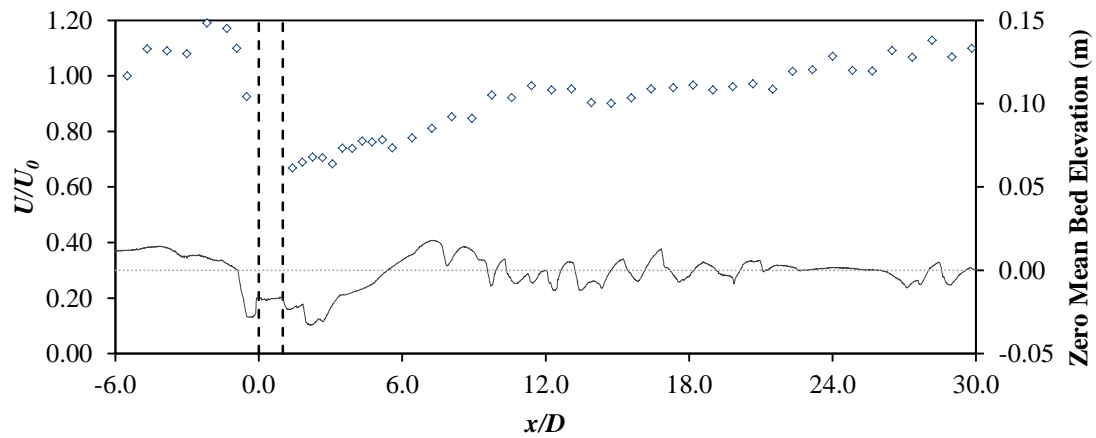

---



(a). Equilibrium Bed



(b). Post Hydrograph 1



(c). Post Hydrograph 2

## **APPENDIX D**

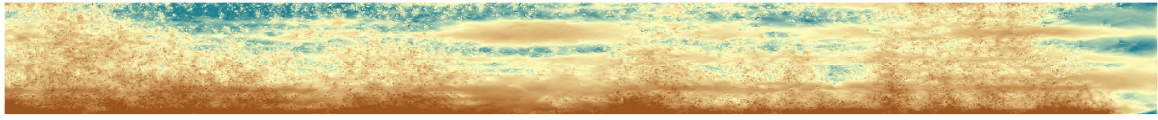
### ***DEMs, Bed Change Maps, Panoramic Bed Photos***

---

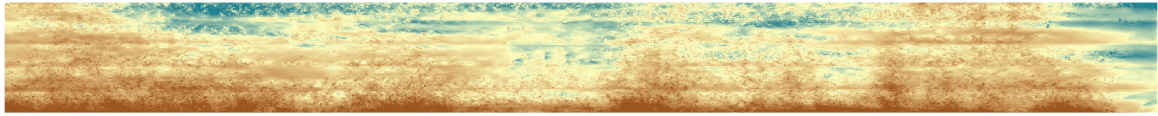
***D.1 No Patch (NP) Experiments***

***D.2 Patch Sediment (PS) Experiments***

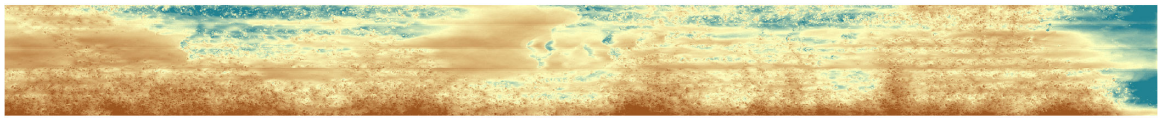
Appendix D.1 -- DEMs: NP-1 (No patch, Low flow, Mix 1)



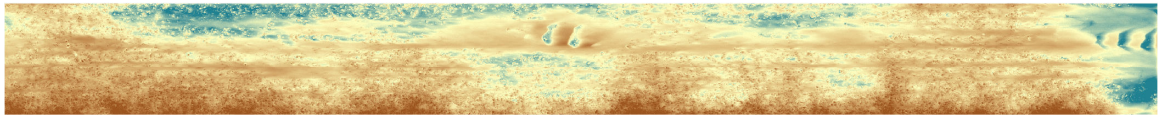
(a) Equilibrium Bed



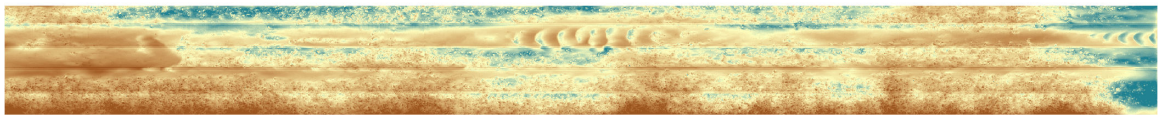
(b) Post Hydrograph 1



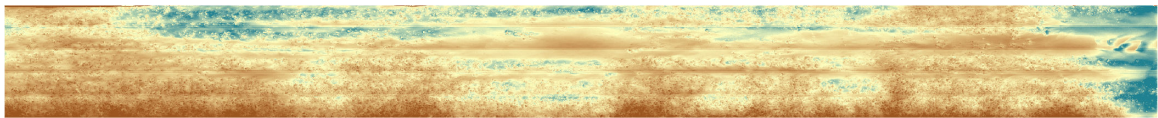
(c) Post Hydrograph 2



(d) Post Hydrograph 3

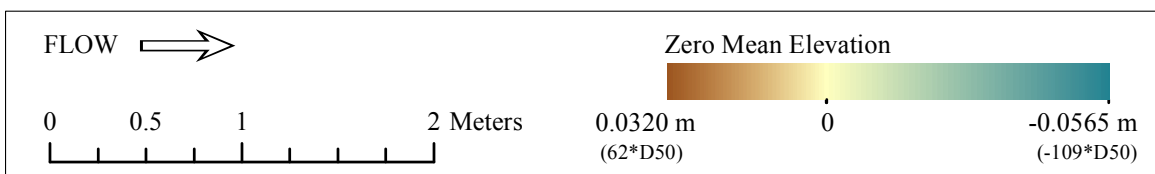


(e) Post Hydrograph 4

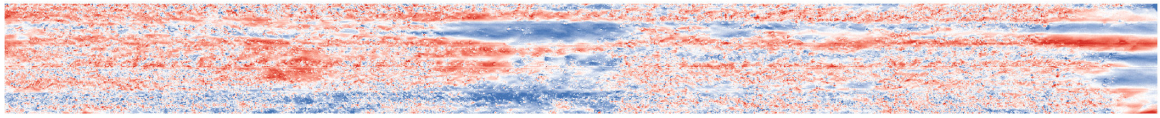


(f) Post Hydrograph 5

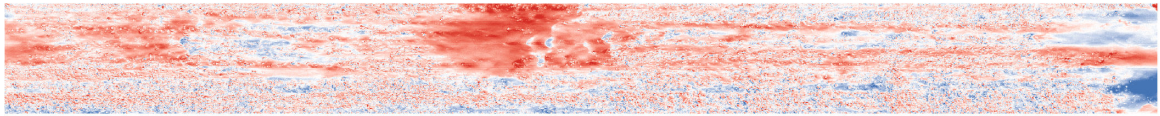
**NOTES**



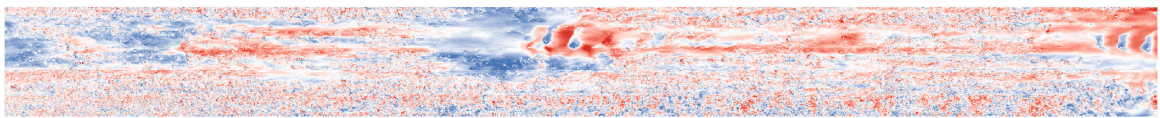
Appendix D.1 -- Bed Change Maps: NP-1 (No patch, Low flow, Mix 1)



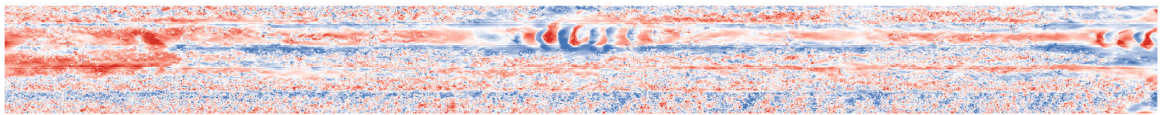
(a) Equilibrium Bed to Post Hydrograph 1



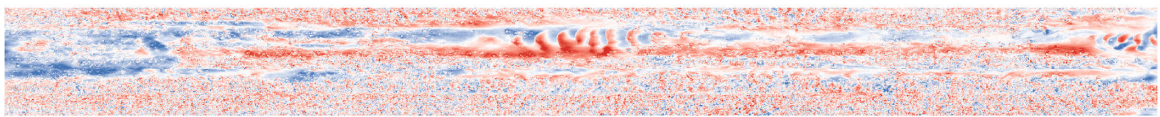
(b) Post Hydrograph 1 to Post Hydrograph 2



(c) Post Hydrograph 2 to Post Hydrograph 3

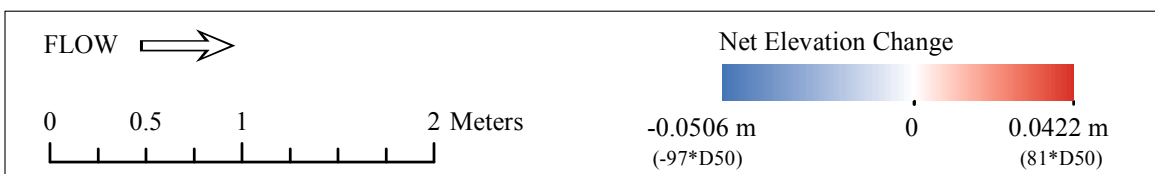


(d) Post Hydrograph 3 to Post Hydrograph 4



(e) Post Hydrograph 4 to Post Hydrograph 5

**NOTES**



Appendix D.1 – Panoramic bed photos: NP-1 (No patch, Low flow, Mix 1)



(a) Equilibrium Bed



(b) Post Hydrograph 1



(c) Post Hydrograph 2



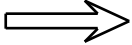
(d) Post Hydrograph 3



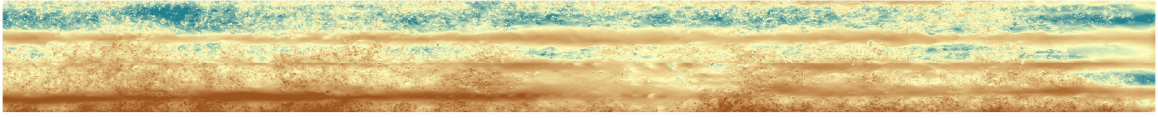
(e) Post Hydrograph 4



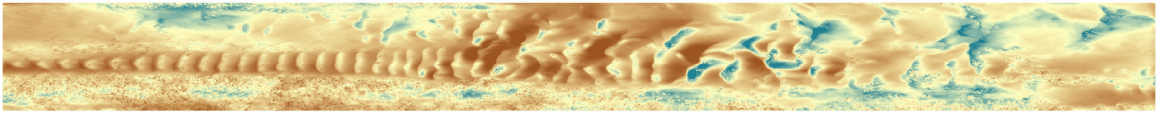
(f) Post Hydrograph 5

FLOW 

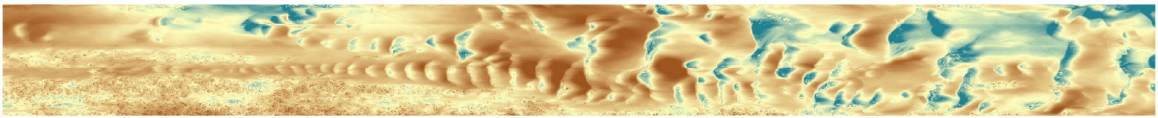
Appendix D.1 -- DEMs: NP-2 (No patch, High flow, Mix 1)



(a) Equilibrium Bed

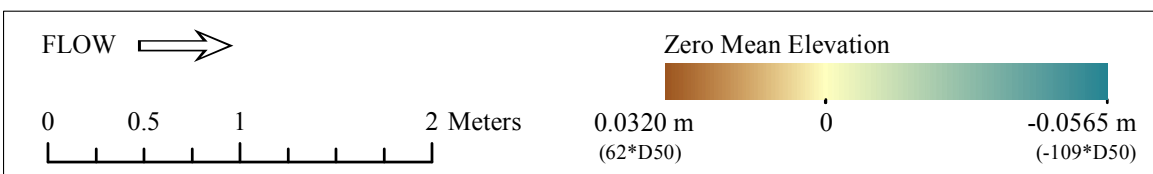


(b) Post Hydrograph 1

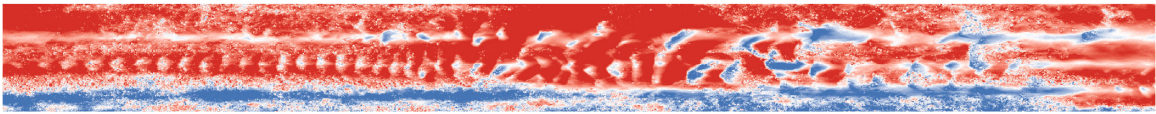


(c) Post Hydrograph 2

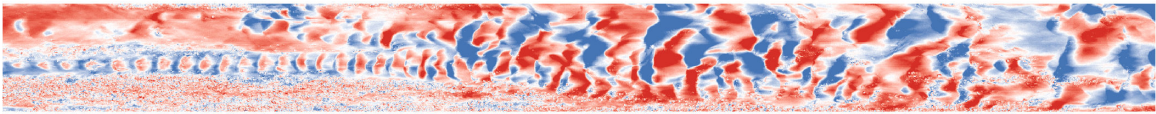
**NOTES**



Appendix D.1 -- Bed Change Maps: NP-2 (No patch, High flow, Mix 1)

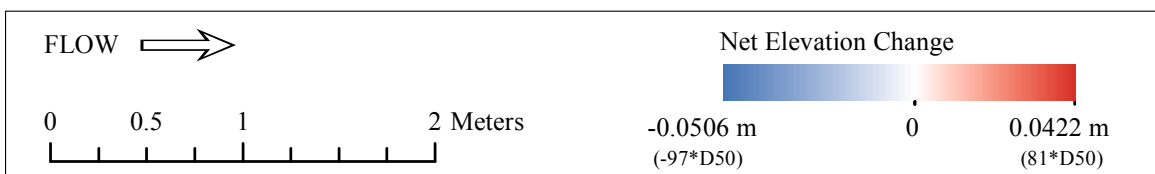


(a) Equilibrium Bed to Post Hydrograph 1



(b) Post Hydrograph 1 to Post Hydrograph 2

**NOTES**



Appendix D.1 – Panoramic bed photos: NP-2 (No patch, High flow, Mix 1)



(a) Equilibrium Bed



(b) Post Hydrograph 1



(c) Post Hydrograph 2

FLOW 

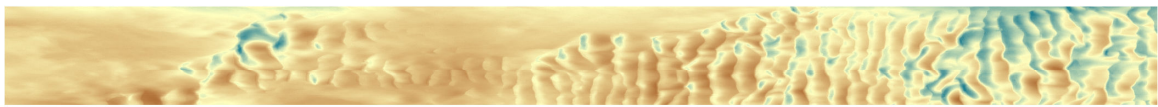
Appendix D.1 -- DEMs: NP-3 (No patch, Low flow, Mix 2)



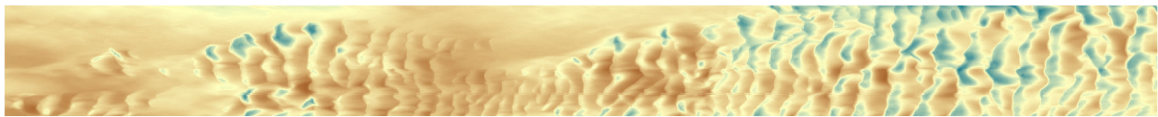
(a) Equilibrium Bed



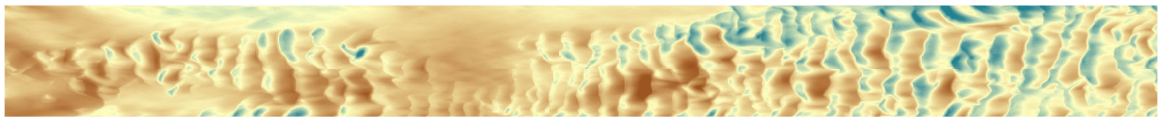
(b) Post Hydrograph 1



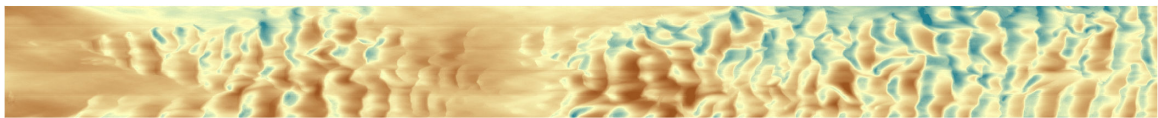
(c) Post Hydrograph 2



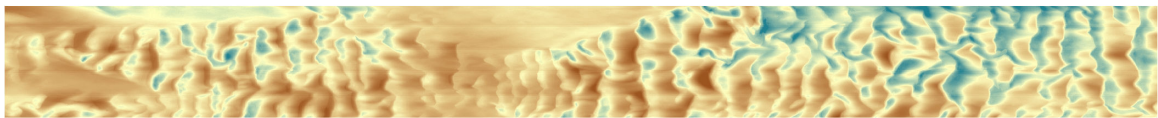
(d) Post Hydrograph 3



(e) Post Hydrograph 4

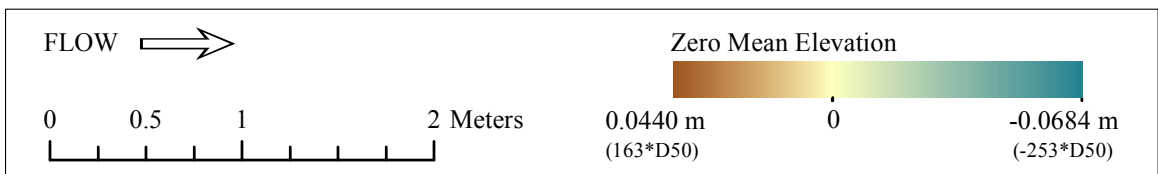


(f) Post Hydrograph 5



(g) Post Hydrograph 6

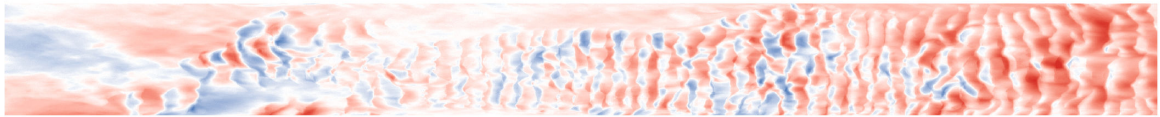
**NOTES**



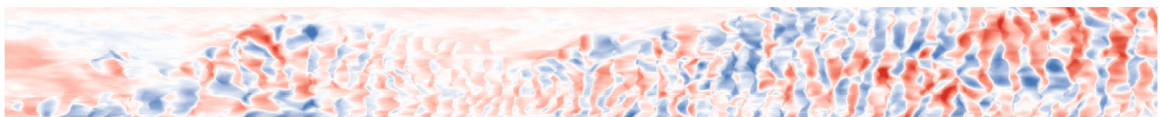
Appendix D.1 -- Bed Change Maps: NP-3 (No patch, Low flow, Mix 2)



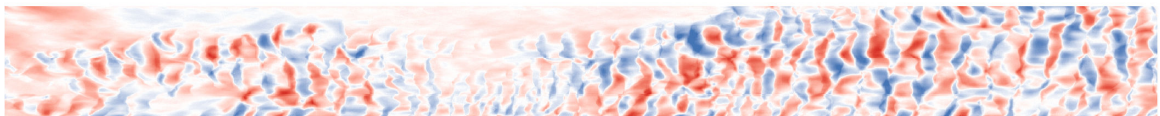
(a) Equilibrium Bed to Post Hydrograph 1



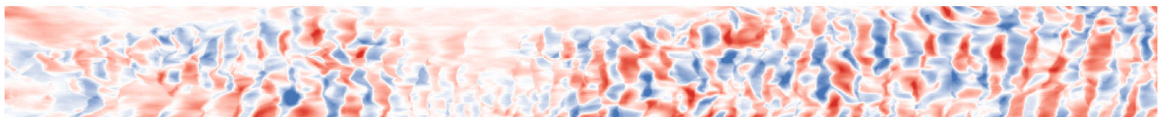
(b) Post Hydrograph 1 to Post Hydrograph 2



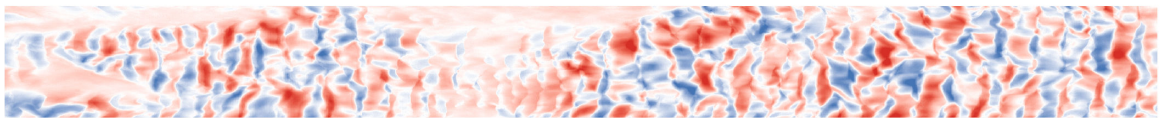
(c) Post Hydrograph 2 to Post Hydrograph 3



(d) Post Hydrograph 3 to Post Hydrograph 4

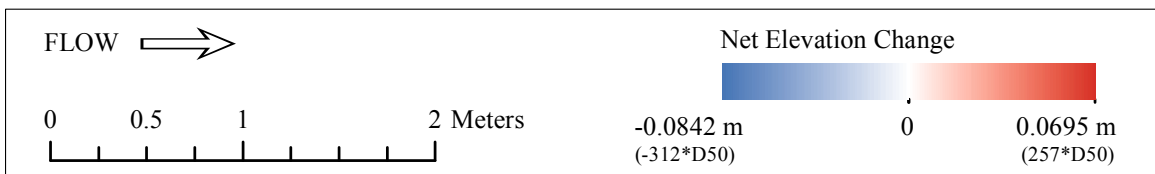


(e) Post Hydrograph 4 to Post Hydrograph 5



(f) Post Hydrograph 5 to Post Hydrograph 6

**NOTES**



Appendix D.1 – Panoramic bed photos: NP-3 (No patch, Low flow, Mix 2)



(a) Equilibrium Bed



(b) Post Hydrograph 1



(c) Post Hydrograph 2



(d) Post Hydrograph 3



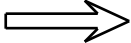
(e) Post Hydrograph 4



(f) Post Hydrograph 5



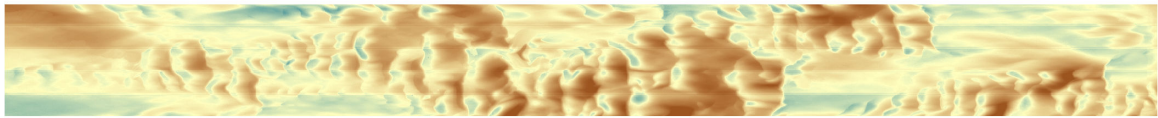
(g) Post Hydrograph 6

FLOW 

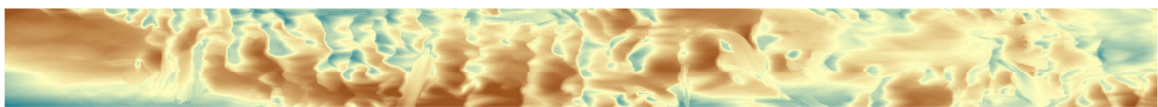
Appendix D.1 -- DEMs: NP-4 (No patch, High flow, Mix 2)



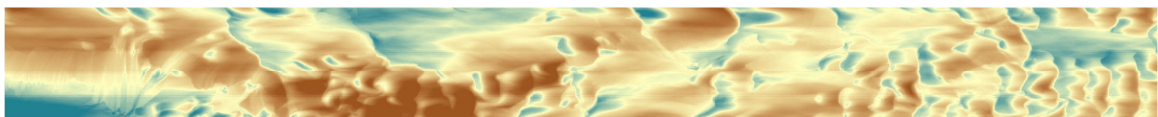
(a) Equilibrium Bed



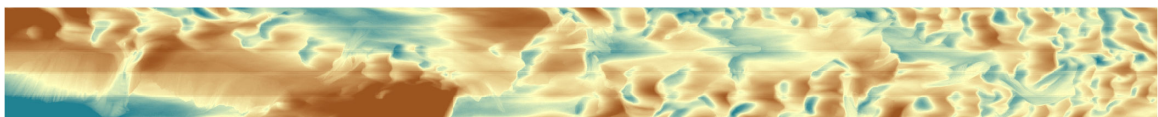
(b) Post Hydrograph 1



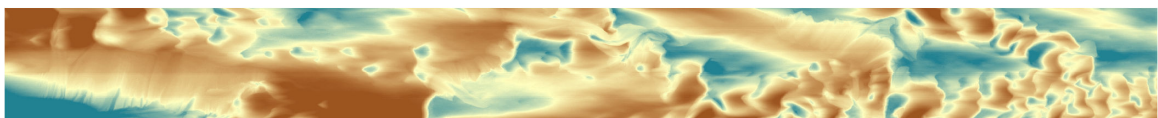
(c) Post Hydrograph 2



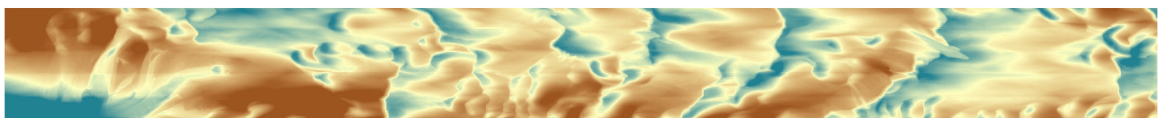
(d) Post Hydrograph 3



(e) Post Hydrograph 4

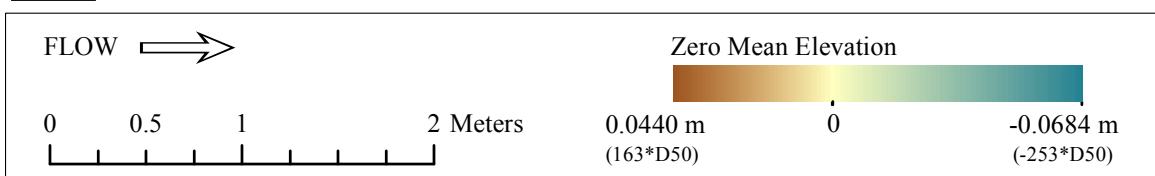


(f) Post Hydrograph 5

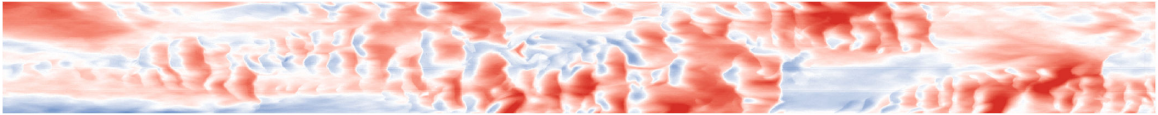


(g) Post Hydrograph 6

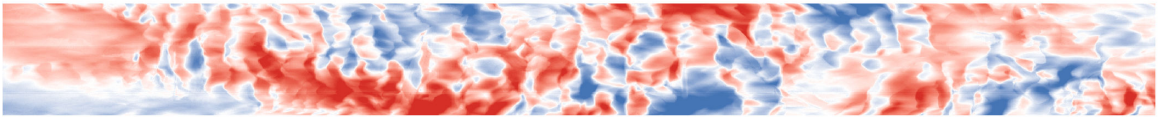
**NOTES**



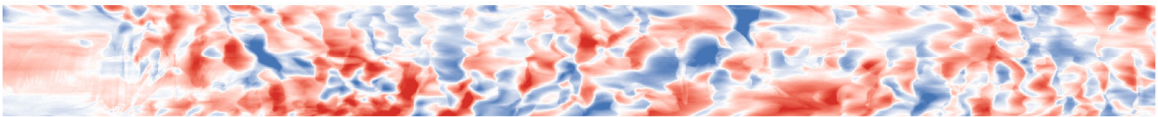
Appendix D.1 -- Bed Change Maps: NP-4 (No patch, High flow, Mix 2)



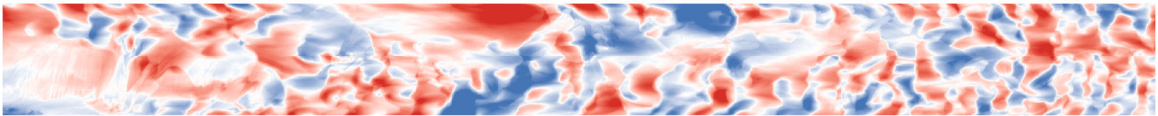
(a) Equilibrium Bed to Post Hydrograph 1



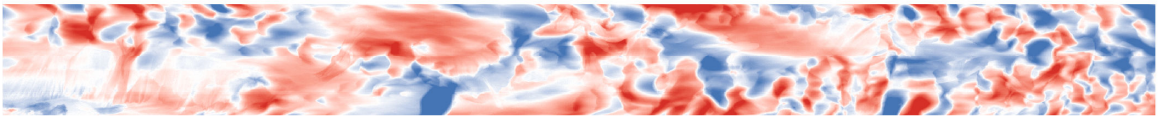
(b) Post Hydrograph 1 to Post Hydrograph 2



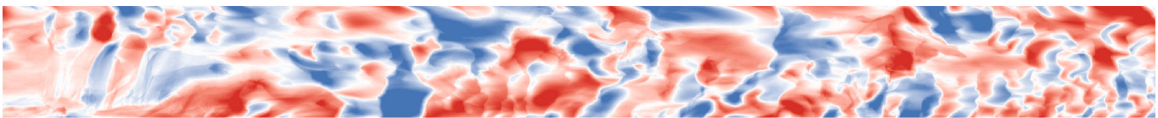
(c) Post Hydrograph 2 to Post Hydrograph 3



(d) Post Hydrograph 3 to Post Hydrograph 4

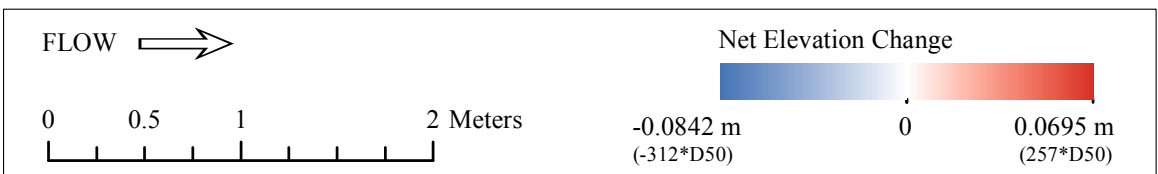


(e) Post Hydrograph 4 to Post Hydrograph 5



(f) Post Hydrograph 5 to Post Hydrograph 6

**NOTES**



Appendix D.1 – Panoramic bed photos: NP-4 (No patch, High flow, Mix 2)



(a) Equilibrium Bed



(b) Post Hydrograph 1



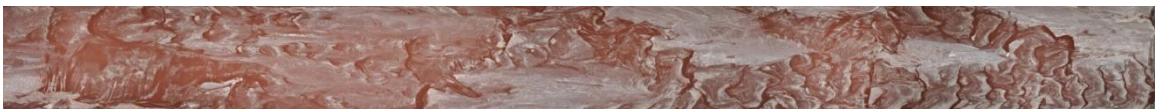
(c) Post Hydrograph 2



(d) Post Hydrograph 3



(e) Post Hydrograph 4



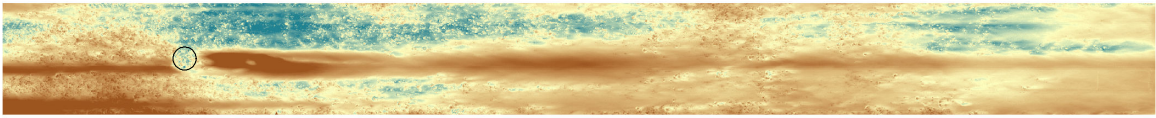
(f) Post Hydrograph 5



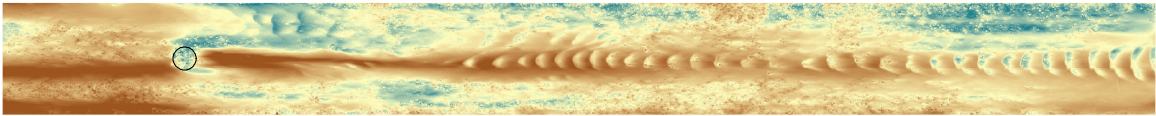
(g) Post Hydrograph 6

FLOW 

Appendix D.2 -- DEMs: PS-1 (Sparse patch, Low flow, Mix 1)



(a) Equilibrium Bed



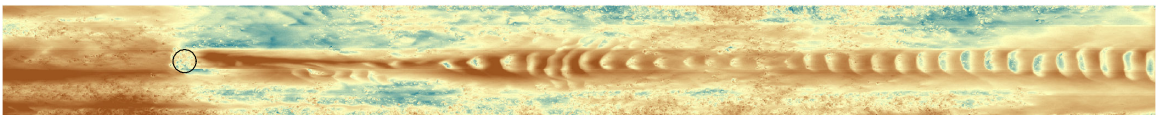
(b) Post Hydrograph 1



(c) Post Hydrograph 2

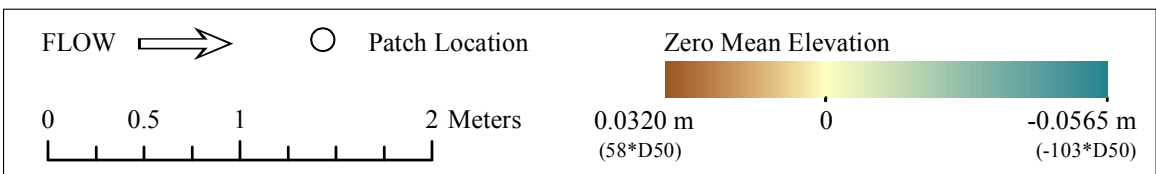


(d) Post Hydrograph 3

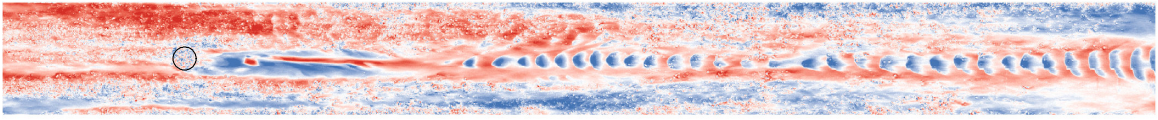


(e) Post Hydrograph 4

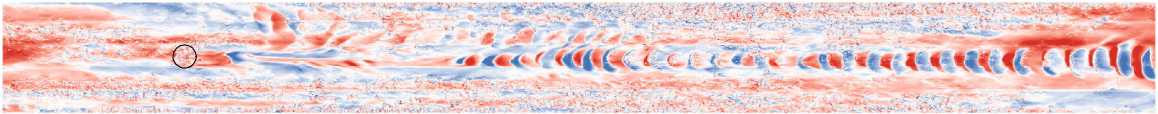
**NOTES**



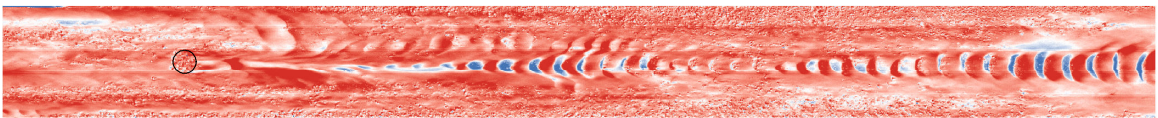
Appendix D.2 -- Bed Change Maps: PS-1 (Sparse patch, Low flow, Mix 1)



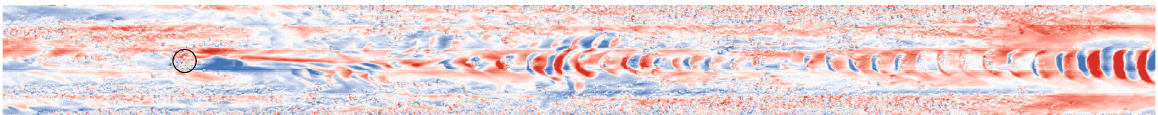
(a) Equilibrium Bed to Post Hydrograph 1



(b) Post Hydrograph 1 to Post Hydrograph 2

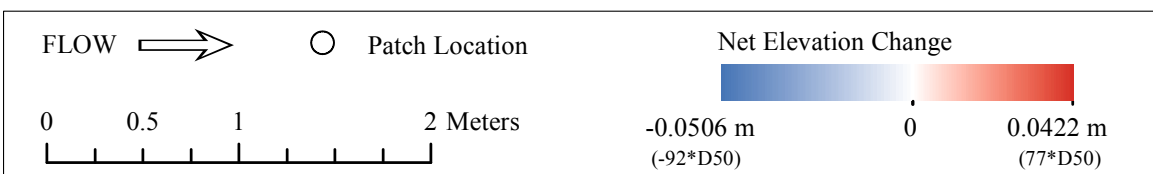


(c) Post Hydrograph 2 to Post Hydrograph 3



(d) Post Hydrograph 3 to Post Hydrograph 4

**NOTES**



Appendix D.2 – Panoramic bed photos: PS-1 (Sparse patch, Low flow, Mix 1)



(a) Equilibrium Bed



(b) Post Hydrograph 1



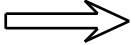
(c) Post Hydrograph 2



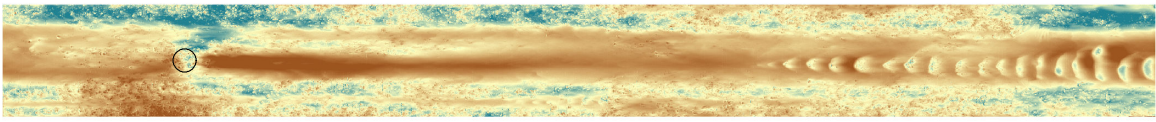
(d) Post Hydrograph 3



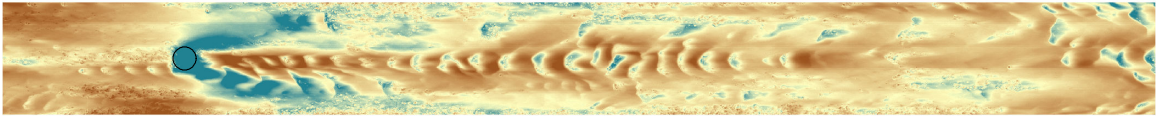
(e) Post Hydrograph 4

FLOW 

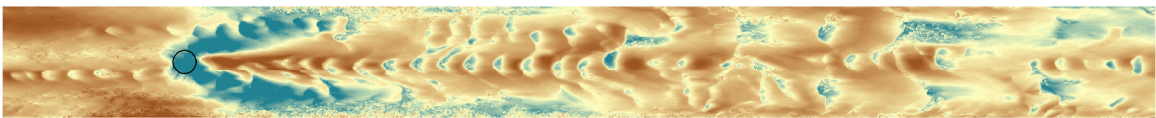
Appendix D.2 -- DEMs: PS-2 (Sparse patch, High flow, Mix 1)



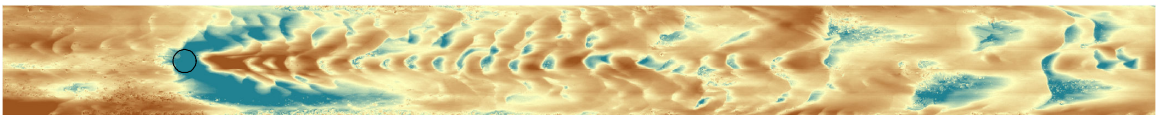
(a) Equilibrium Bed



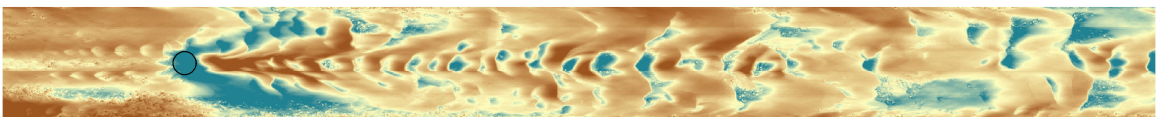
(b) Post Hydrograph 1



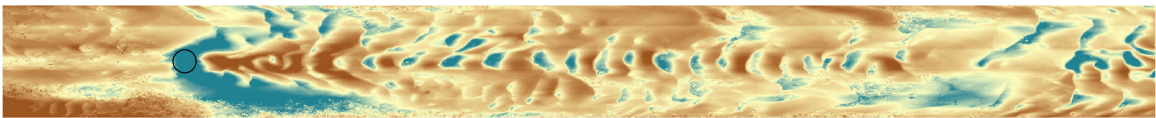
(c) Post Hydrograph 2



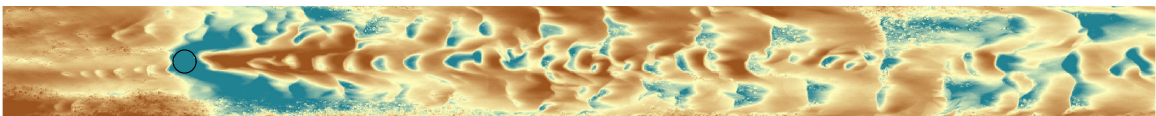
(d) Post Hydrograph 3



(e) Post Hydrograph 4

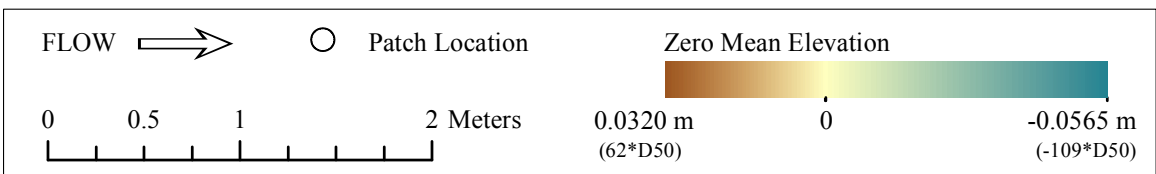


(f) Post Hydrograph 5

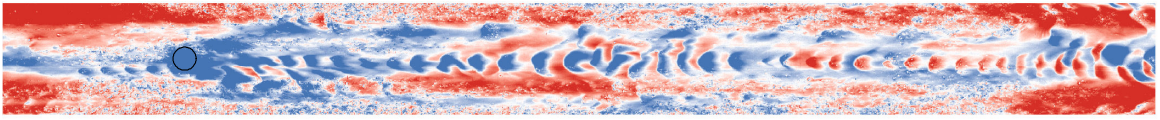


(g) Post Hydrograph 6

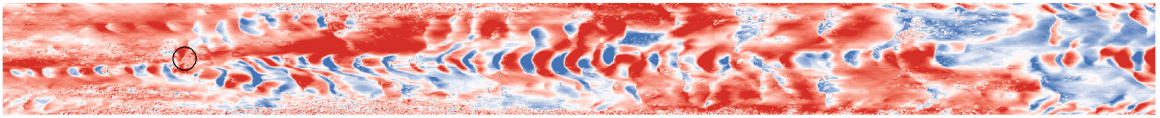
**NOTES**



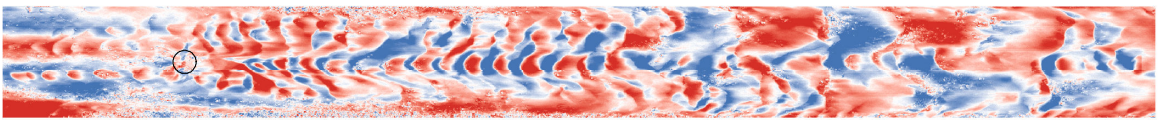
Appendix D.2 -- Bed Change Maps: PS-2 (Sparse patch, High flow, Mix 1)



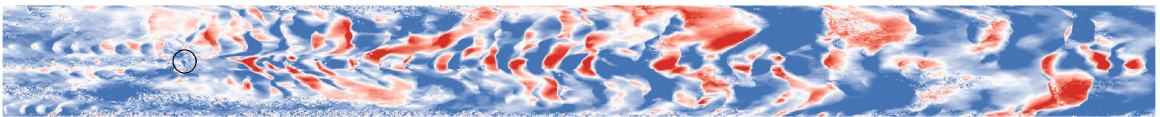
(a) Equilibrium Bed to Post Hydrograph 1



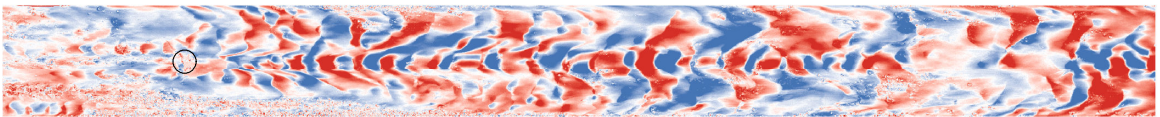
(b) Post Hydrograph 1 to Post Hydrograph 2



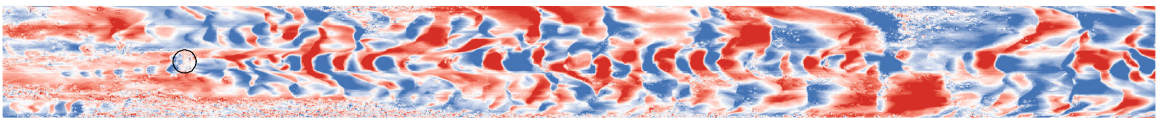
(c) Post Hydrograph 2 to Post Hydrograph 3



(d) Post Hydrograph 3 to Post Hydrograph 4

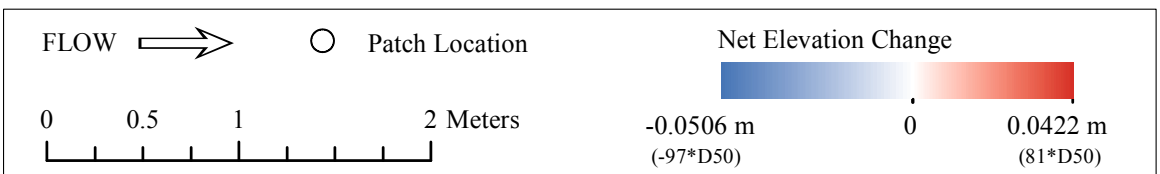


(e) Post Hydrograph 4 to Post Hydrograph 5



(f) Post Hydrograph 5 to Post Hydrograph 6

**NOTES**



Appendix D.2 – Panoramic bed photos: PS-2 (Sparse patch, High flow, Mix 1)



(a) Equilibrium Bed



(b) Post Hydrograph 1



(c) Post Hydrograph 2



(d) Post Hydrograph 3



(e) Post Hydrograph 4



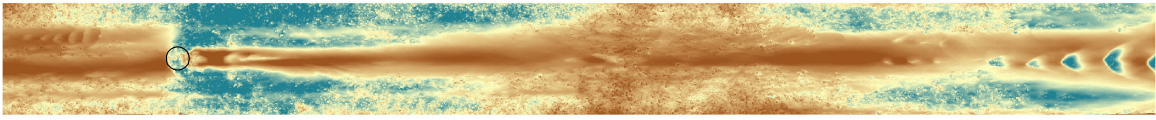
(f) Post Hydrograph 5



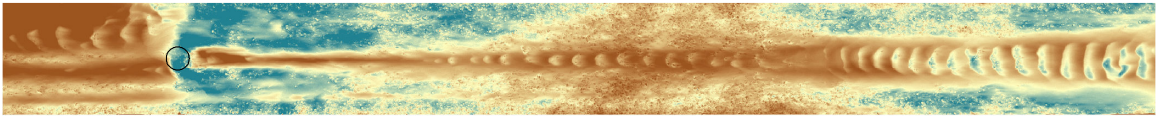
(g) Post Hydrograph 6

FLOW 

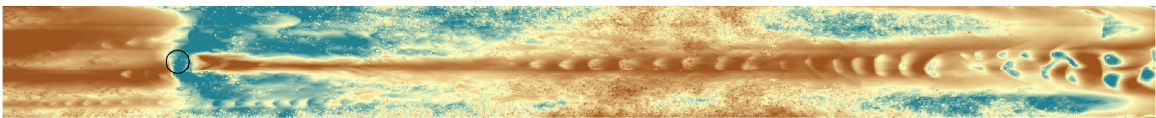
Appendix D.2 -- DEMs: PS-3 (Dense patch, Low flow, Mix 1)



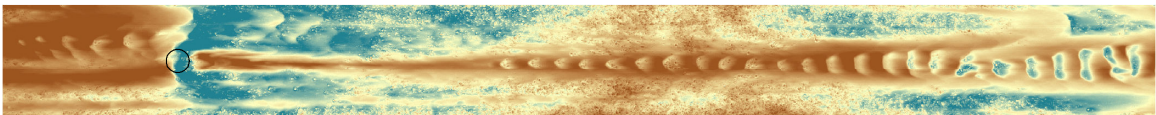
(a) Equilibrium Bed



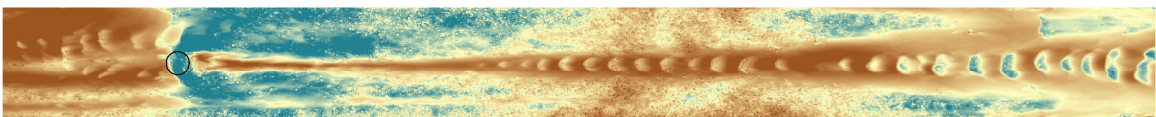
(b) Post Hydrograph 1



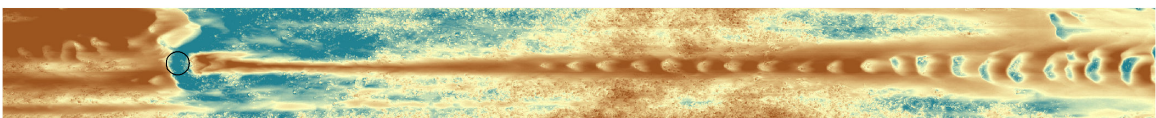
(c) Post Hydrograph 2



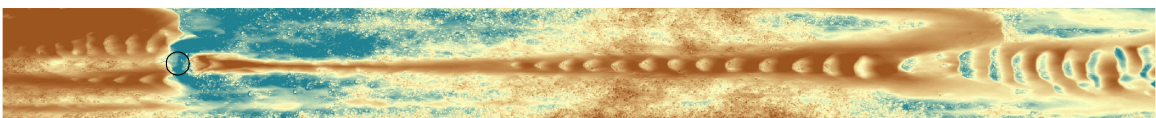
(d) Post Hydrograph 3



(e) Post Hydrograph 4

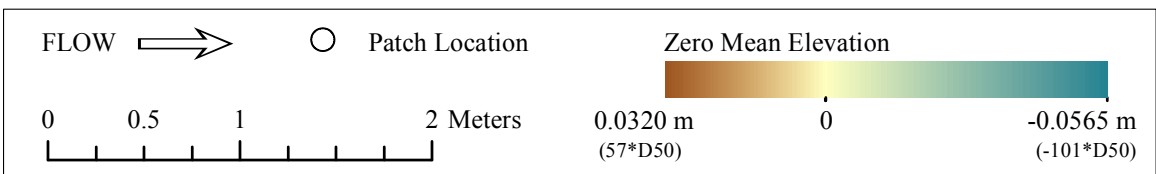


(f) Post Hydrograph 5

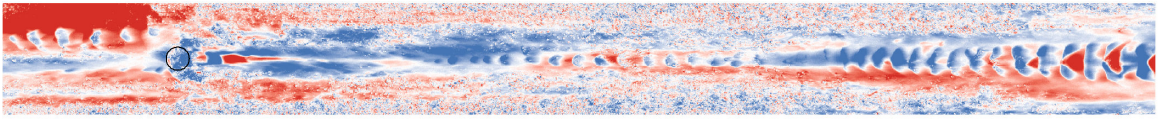


(g) Post Hydrograph 6

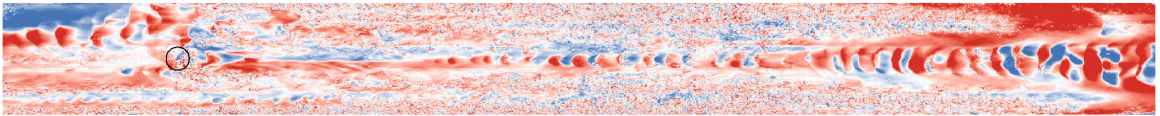
**NOTES**



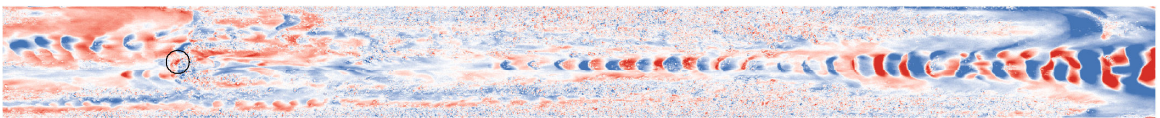
Appendix D.2 -- Bed Change Maps: PS-3 (Dense patch, Low flow, Mix 1)



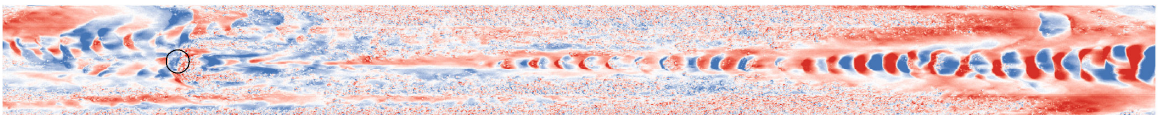
(a) Equilibrium Bed to Post Hydrograph 1



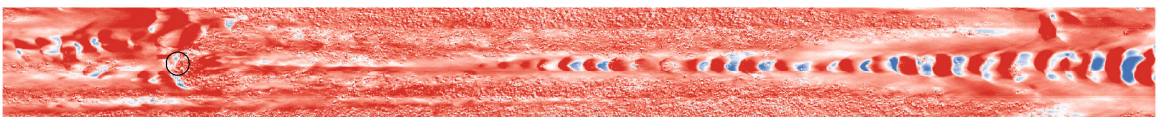
(b) Post Hydrograph 1 to Post Hydrograph 2



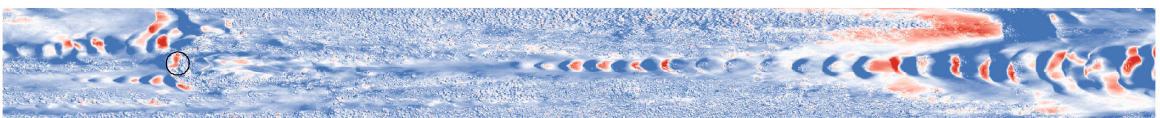
(c) Post Hydrograph 2 to Post Hydrograph 3



(d) Post Hydrograph 3 to Post Hydrograph 4

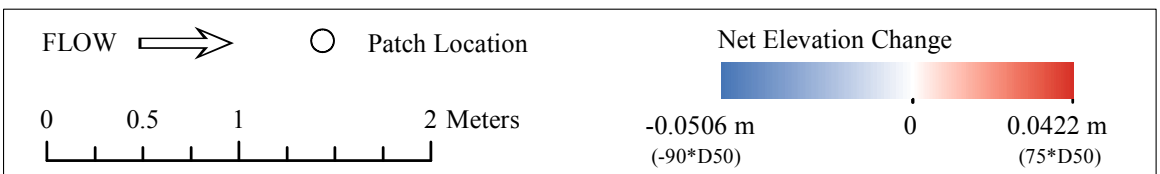


(e) Post Hydrograph 4 to Post Hydrograph 5



(f) Post Hydrograph 5 to Post Hydrograph 6

**NOTES**



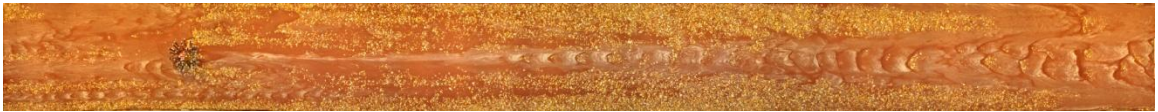
Appendix D.2 – Panoramic bed photos: PS-3 (Dense patch, Low flow, Mix 1)



(a) Equilibrium Bed



(b) Post Hydrograph 1



(c) Post Hydrograph 2



(d) Post Hydrograph 3



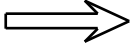
(e) Post Hydrograph 4



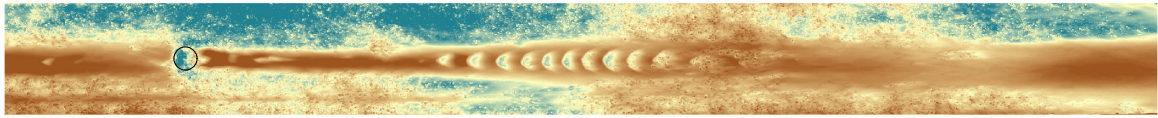
(f) Post Hydrograph 5



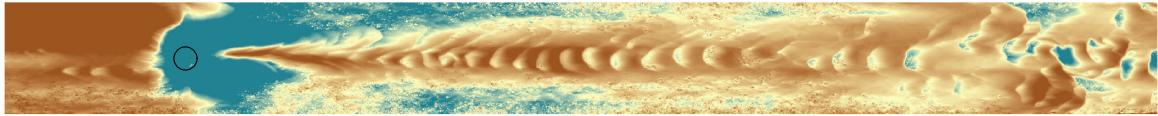
(g) Post Hydrograph 6

FLOW 

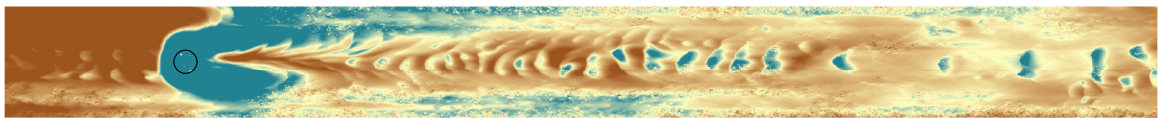
Appendix D.2 -- DEMs: PS-4 (Dense patch, High flow, Mix 1)



(a) Equilibrium Bed

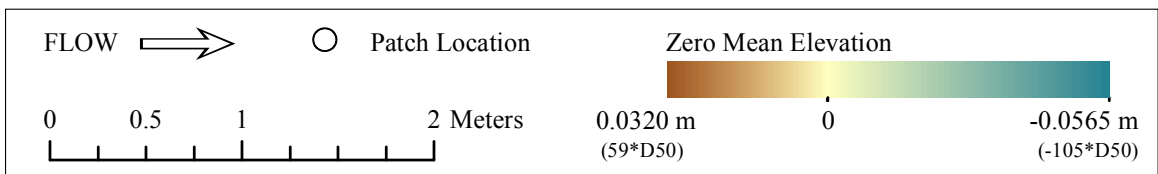


(b) Post Hydrograph 1

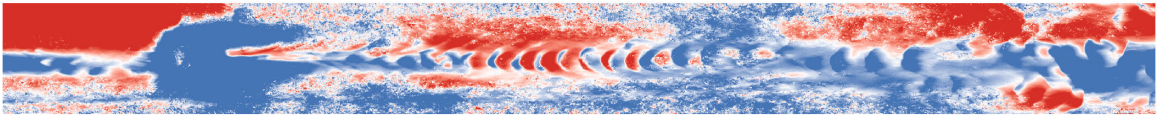


(c) Post Hydrograph 2

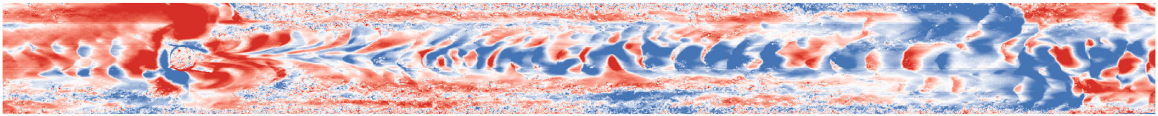
**NOTES**



Appendix D.2 -- Bed Change Maps: PS-4 (Dense patch, High flow, Mix 1)

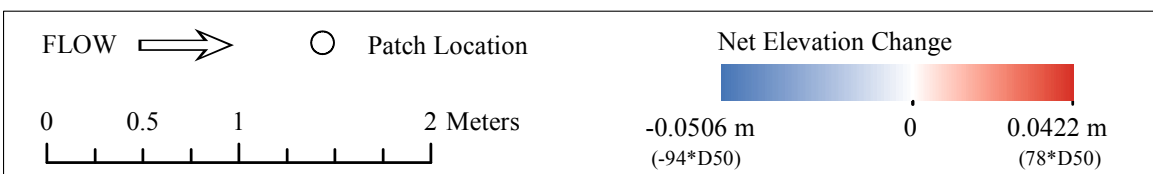


(a) Equilibrium Bed to Post Hydrograph 1



(b) Post Hydrograph 1 to Post Hydrograph 2

**NOTES**



Appendix D.2 – Panoramic bed photos: PS-4 (Dense patch, High flow, Mix 1)



(a) Equilibrium Bed



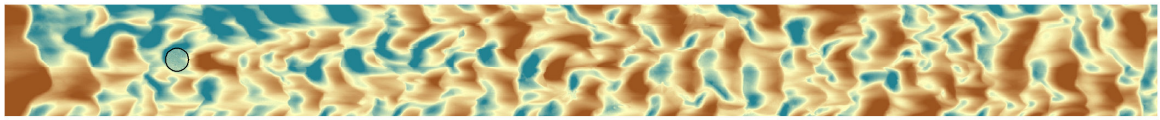
(b) Post Hydrograph 1



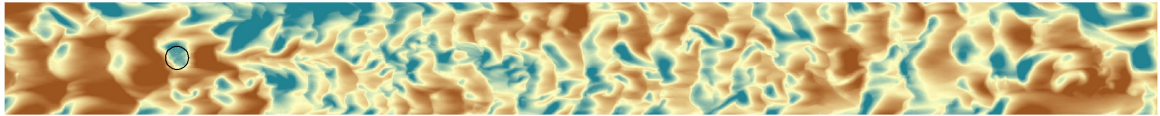
(c) Post Hydrograph 2

FLOW 

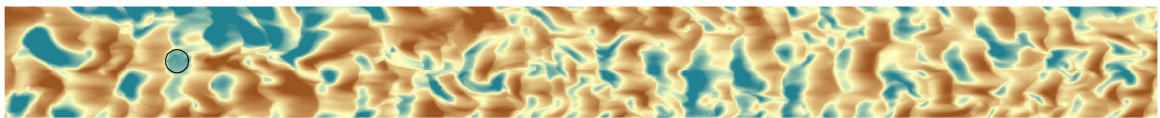
Appendix D.2 -- DEMs: PS-5 (Sparse patch, Low flow, Mix 2)



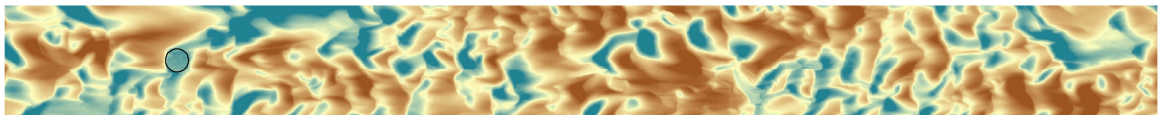
(a) Equilibrium Bed



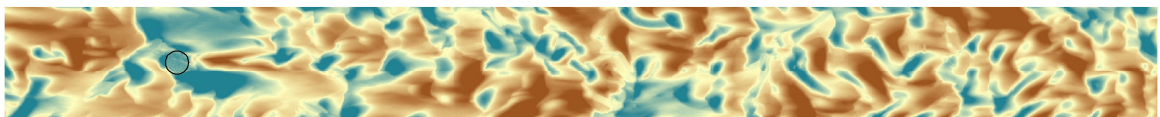
(b) Post Hydrograph 1



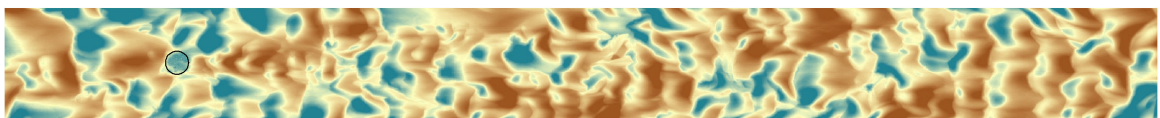
(c) Post Hydrograph 2



(d) Post Hydrograph 3

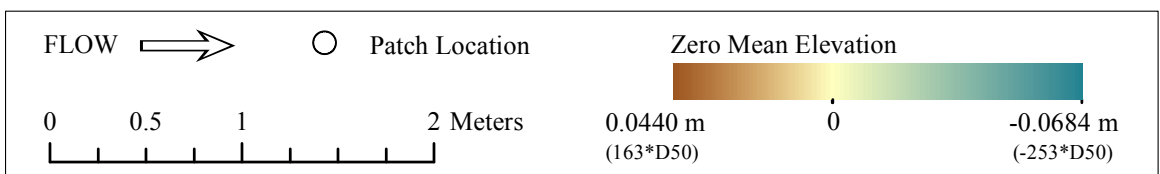


(e) Post Hydrograph 4

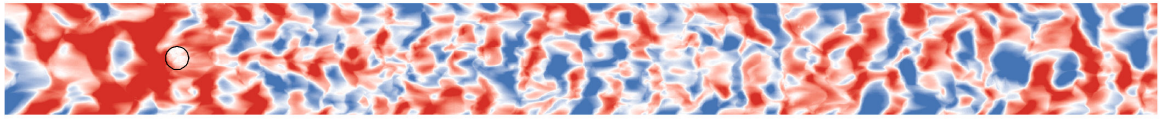


(f) Post Hydrograph 5

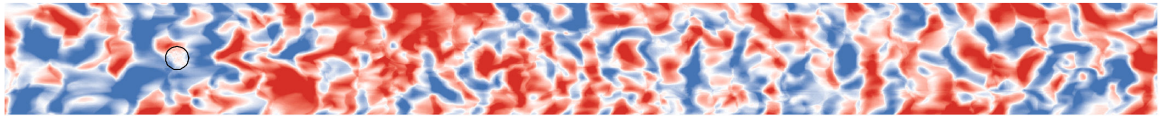
**NOTES**



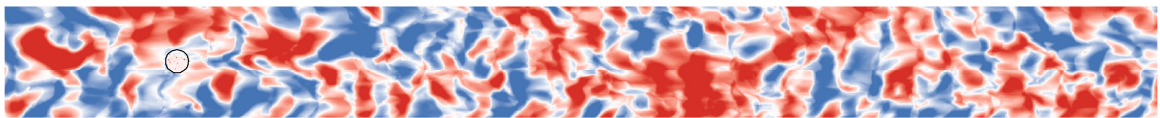
Appendix D.2 -- Bed Change Maps: PS-5 (Sparse patch, Low flow, Mix 2)



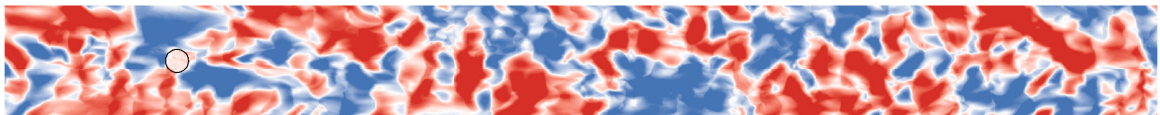
(a) Equilibrium Bed to Post Hydrograph 1



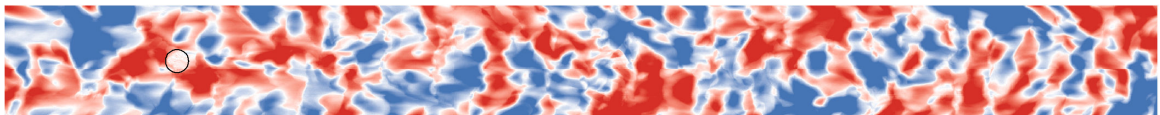
(b) Post Hydrograph 1 to Post Hydrograph 2



(c) Post Hydrograph 2 to Post Hydrograph 3

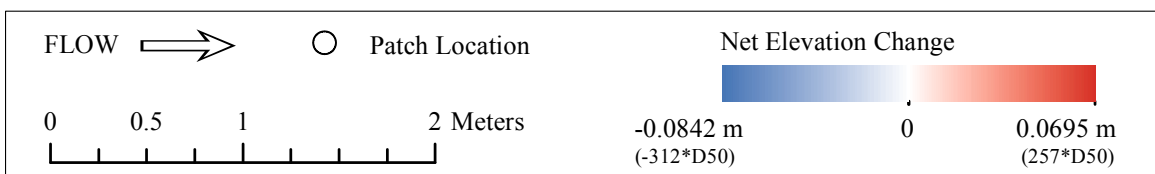


(d) Post Hydrograph 3 to Post Hydrograph 4



(e) Post Hydrograph 4 to Post Hydrograph 5

**NOTES**



Appendix D.2 – Panoramic bed photos: PS-5 (Sparse patch, Low flow, Mix 2)



(a) Equilibrium Bed



(b) Post Hydrograph 1



(c) Post Hydrograph 2



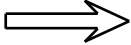
(d) Post Hydrograph 3



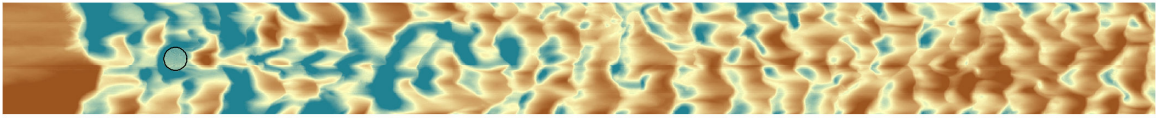
(e) Post Hydrograph 4



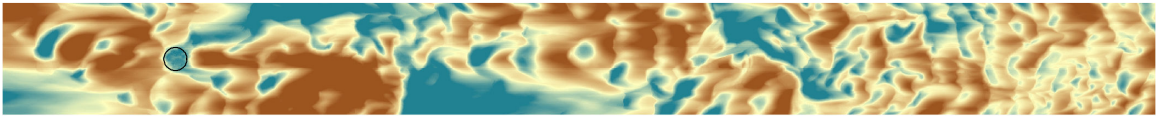
(f) Post Hydrograph 5

FLOW 

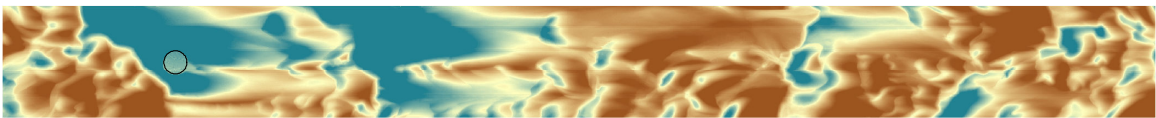
Appendix D.2 -- DEMs: PS-6 (Sparse patch, High flow, Mix 2)



(a) Equilibrium Bed

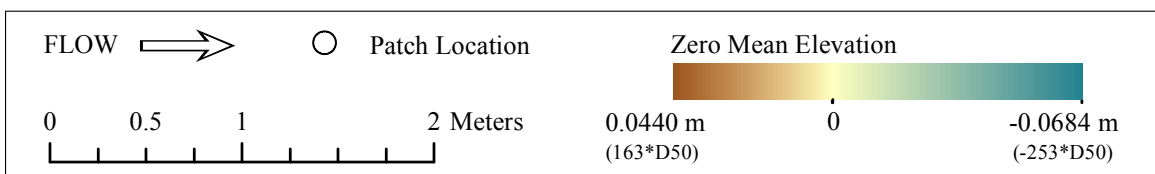


(b) Post Hydrograph 1

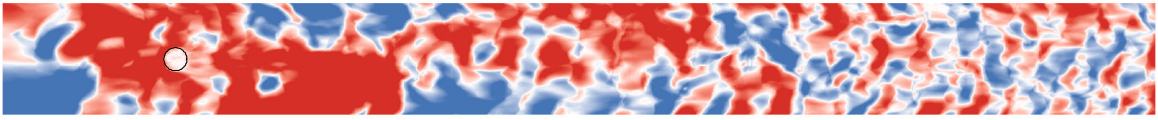


(c) Post Hydrograph 2

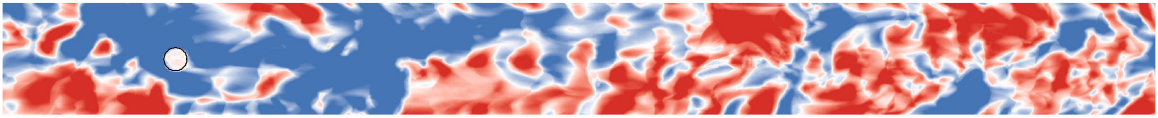
**NOTES**



Appendix D.2 -- Bed Change Maps: PS-6 (Sparse patch, High flow, Mix 2)

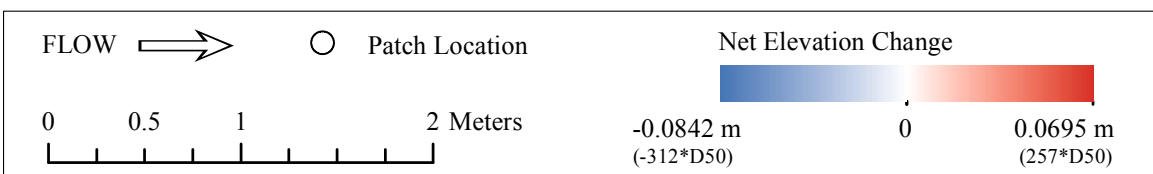


(a) Equilibrium Bed to Post Hydrograph 1



(b) Post Hydrograph 1 to Post Hydrograph 2

**NOTES**



Appendix D.2 – Panoramic bed photos: PS-6 (Sparse patch, High flow, Mix 2)



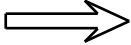
(a) Equilibrium Bed



(b) Post Hydrograph 1



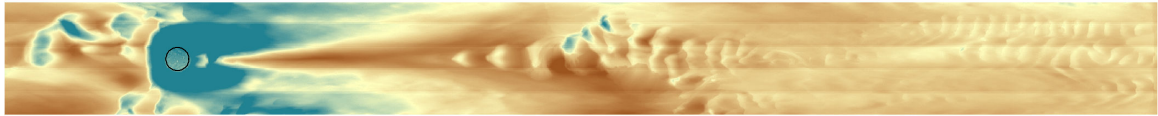
(c) Post Hydrograph 2

FLOW 

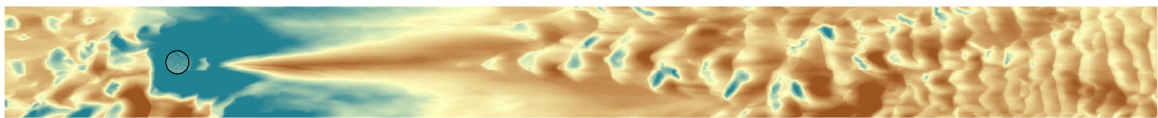
Appendix D.2 -- DEMs: PS-7 (Dense patch, Low flow, Mix 2)



(a) Equilibrium Bed

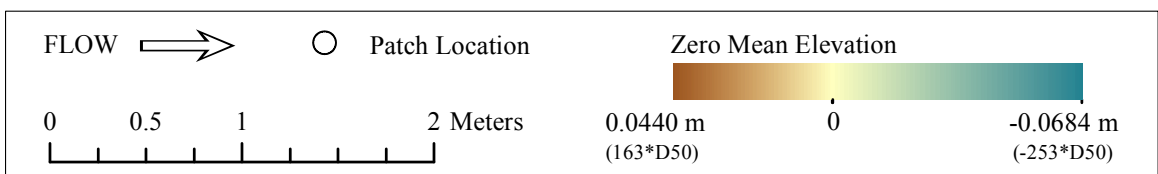


(b) Post Hydrograph 1

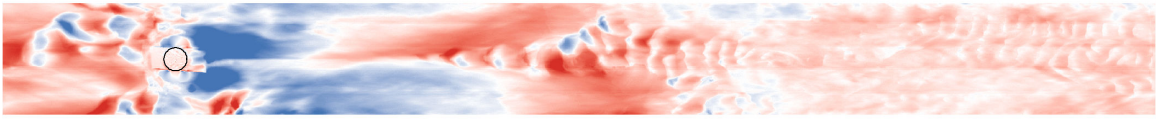


(c) Post Hydrograph 2

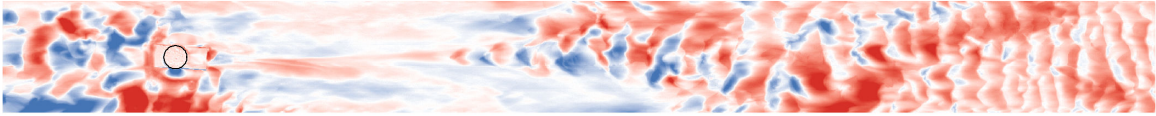
**NOTES**



Appendix D.2 -- Bed Change Maps: PS-7 (Dense patch, Low flow, Mix 2)

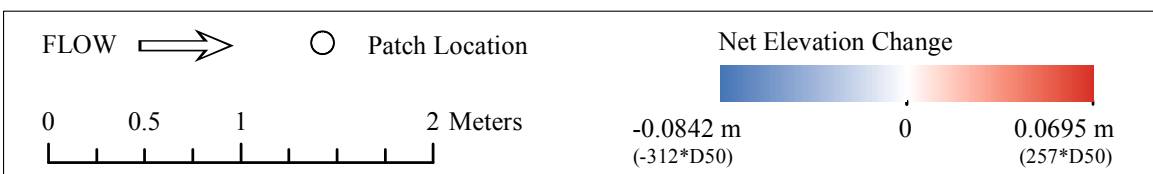


(a) Equilibrium Bed to Post Hydrograph 1



(b) Post Hydrograph 1 to Post Hydrograph 2

**NOTES**



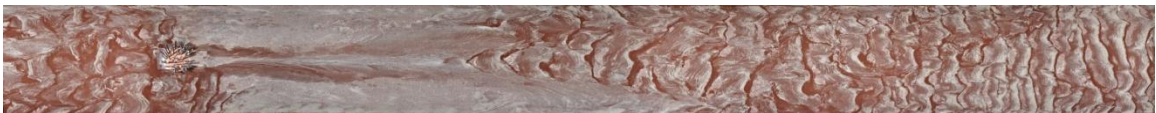
Appendix D.2 – Panoramic bed photos: PS-7 (Dense patch, Low flow, Mix 2)



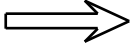
(a) Equilibrium Bed



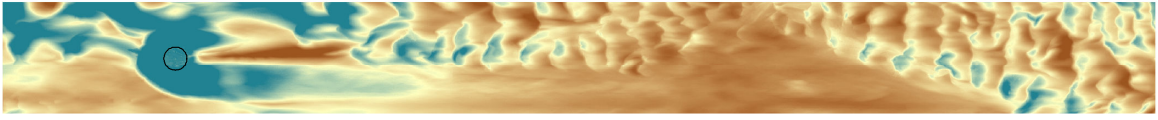
(b) Post Hydrograph 1



(c) Post Hydrograph 2

FLOW 

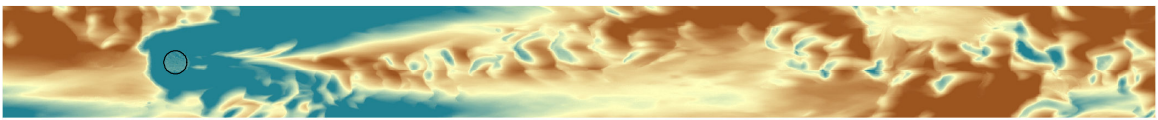
Appendix D.2 -- DEMs: PS-8 (Dense patch, High flow, Mix 2)



(a) Equilibrium Bed

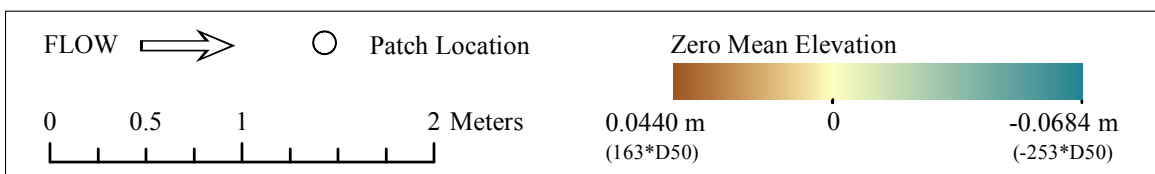


(b) Post Hydrograph 1

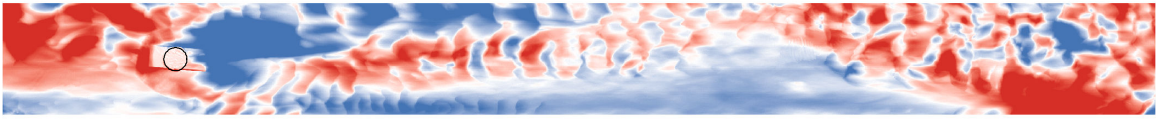


(c) Post Hydrograph 2

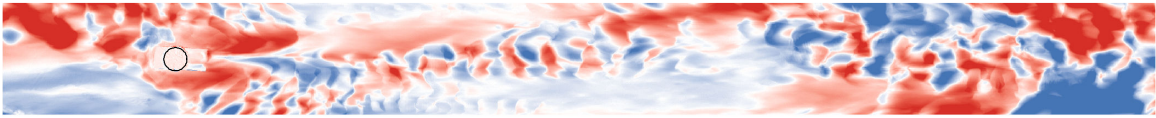
**NOTES**



Appendix D.2 -- Bed Change Maps: PS-8 (Dense patch, High flow, Mix 2)

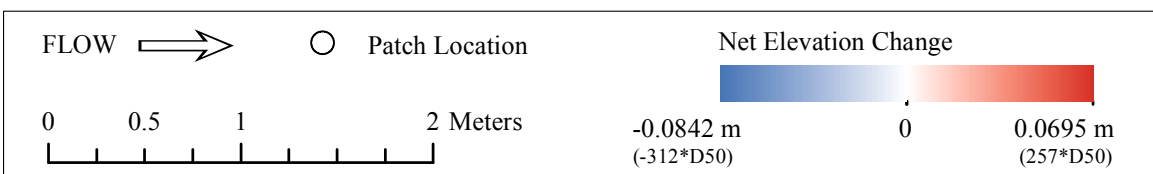


(a) Equilibrium Bed to Post Hydrograph 1



(b) Post Hydrograph 1 to Post Hydrograph 2

**NOTES**



Appendix D.2 – Panoramic bed photos: PS-8 (Dense patch, High flow, Mix 2)



(a) Equilibrium Bed



(b) Post Hydrograph 1



(c) Post Hydrograph 2

FLOW 